Thermoplastic Active Fiber Composites for Structural Actuation

by

CHRISTOPHER T. DUNN

B.S., Aerospace Engineering
The Pennsylvania State University, 1995

S.M., Astronautical Engineering
Massachusetts Institute of Technology, 2000

Submitted to the Department of Aeronautical and Astronautical Engineering
in Partial Fulfillment of the Requirements for the Degree of

Doctor of Science in Aeronautical and Astronautical Engineering
At the
MASSACHUSETTS INSTITUTE OF TECHNOLOGY

June 2002

Signature of Author.....
Department of Aeronautical and Astronautical Engineering
May #, 2002

Certified by .....
Nesbitt W. Hagood IV
Principal Research Engineer of Aeronautics and Astronautics
Thesis Supervisor

Certified by .....
John Dugundji
Professor Emeritus of Aeronautics and Astronautics

Certified by .....
Yet-Ming Chiang
Professor of Materials Science and Engineering

Certified by .....
Anna Pavlova
Assistant Professor of Finance

Accepted by .....
Wallace E. Vander Velde
Professor of Aeronautics and Astronautics
Chair, Departmental Committee on Graduate Students

Thermoplastic Active Fiber Composites for Structural Actuation

by

CHRISTOPHER T. DUNN

Submitted to the Aeronautical and Astronautical Engineering
on May 31, 2002 in Partial Fulfillment of the
Requirements for the Degree of Doctor of Science in
Aeronautical and Astronautical Engineering

ABSTRACT

The integration of piezoelectric actuators into a structure can lead to an active structural surface that can adapt by bending or straining to different operational conditions. This can be used to tune desired properties of the active system to their optimal levels. Due to their fast response time, high bandwidth, and the level of force that the actuator can apply, it has been proposed that monolithic piezoelectric materials be used for active structural control. Monolithic piezoelectric materials for planar actuation have several drawbacks including: (a) use of the lower *3-1* actuation for planar actuation, (b) low strain before failure, (c) inability to conform to curved surfaces.

Active Fiber Composites (AFCs) have been developed to address some of these shortcomings of monolithic piezoceramic materials. AFCs are thin composite plies comprised of unidirectional piezoelectric fibers imbedded in a thermoset matrix. An electric field is supplied to the fibers by use of an interdigitated electrode pattern adhered to either side of the AFC. The benefits of AFCs include: the interdigital electrode design uses *3-3* actuation offering increased levels of actuation, AFCs allows for anisotropic planar actuation, the AFCs matrix provides load transfer and load distribution, AFCs allows for coverage of curved shapes. A major drawback of the AFCs with PZT-5A fibers is that the level of actuation is 60% lower than that of the *3-3* actuation of monolithic PZT-5A. This is due primarily to a small layer of low dielectric matrix material that is trapped between the electrodes and the high dielectric fibers during manufacturing. This dielectric mismatch causes a large voltage drop in the matrix thereby reducing actuation. A method that has been developed to reduce this matrix gap, and thus increasing actuation, is to transfer the electrode pattern onto plastic sheets, and heat and press the sheets around the fibers to make Thermoplastic Active Fiber Composites (tmAFCs). tmAFCs also have simpler processing when compared to AFCs and are reshapeable.

The focus of this research is to analyze, manufacture, and test tmAFCs to be used in structural control applications with the goal of producing high quality and high performance actuators.

Thesis Supervisor: Nesbitt W. Hagood IV
Title: Principal Research Engineer of Aeronautics and Astronautics

i. Acknowledgements

The author would like to acknowledge DARPA under the Active Fiber Composite Consortium (AFCC, # 49620-97-0527) with program monitors Dr. William Coblenz and Dr. Spencer Wu.

ii. Table of Contents

iii. List of Figures

iv. List of Tables

v. Nomenclature

Nomenclature and abbreviations:

Symbol	Description	Units
A	Area	m^2
A_i	Area of i^{th} material	m^2
B	Electric susceptance	S
C	Capacitance	F
Cp	Parallel Capacitance	F
$\underline{\underline{c}}$	Matrix of stiffness	Pa
c_{ij}	i,j component of matrix of stiffness	Pa
D	Dissipation factor	-
$\underline{D}$	Electric displacement vector	C/m^2
D_i	i component of the electric displacement	C/m^2
d	Displacement	m
$\underline{\underline{d}}$	"Strain" piezoelectric matrix	m/V
d_{ij}	i,j component of "Strain" piezoelectric matrix	m/V
E	Young's modulus for an isotropic non-piezoelectric material	Pa
$\underline{E}$	Electric field vector	V/m
E_i	i component of electric field	N/m V
$\underline{\underline{e}}$	"Stress" piezoelectric matrix	N/m V
e_{ij}	i,j component of "Stress" piezoelectric matrix	m/V

f	Frequency	Hz
G	Electrical conductance	S
$\underline{\underline{g}}$	"Voltage" piezoelectric matrix	V m /N
g_{ij}	*i,j* component of "Voltage" piezoelectric matrix	V m /N
H	Additional constant in Rambergs-Osgood relationship	Pa
h	Thickness of an AFC/tmAFC	m
h_A	Thickness of the active area of an AFC/tmAFC	m
h_F	Thickness of an electrode finger of an AFC/tmAFC	m
$\underline{\underline{I}}$	Identity matrix	-
i	Current	A
$\hat{i}, \hat{j}, \hat{k}$	Direction vectors in the *X*, *Y*, and *Z* directions respectively	-
$\underline{J}_f$	Vector of conduction current density	A/m^2
$\left(J_f\right)_{ij}$	*i,j* component of conduction current density	A/m^2
j	Square root of negative one	-
K	Relative dielectric	-
k_{ij}	*i,j* coupling coefficient	-
L	Length	m
L	Length of an AFC/tmAFC	m
L_A	Length of the active area of an AFC/tmAFC	m
L_F	Length of the electrode finger of an AFC/tmAFC	m
$\mathcal{L}$	Electrode finger spacing in an AFC/tmAFC	m
LF	Line fraction of fibers in an AFC/tmAFC	%
m	Mass	kg
N_F	Number of fingers	-
N_{Fibers}	Number of fibers	-
n	Strain hardening constant in Rambergs-Osgood relations	-
$\hat{n}$	Normal vector	-
P	Real average power	W

$\underline{P}$	Electric polarization	C/m^2
P_i	i component of the electric polarization	C/m^2
Q	Reactive power	W
q	Charge	C
R	Fiber radius	m
R	Electric resistance	Ω
S	Apparent power	W
$\underline{S}$	Engineering strain vector	m/m
S_{ij}	i,j component of engineering strain vector	m/m
$\underline{\underline{s}}$	Matrix of compliance	m^2/N
s_{ij}	i,j component of matrix of compliance	m^2/N
$\underline{T}$	Stress vector	Pa
T_{ij}	i,j component of stress vector	Pa
T_g	Glass transition temperature	°C
t	Time	sec
u, v, w	Displacement in the X, Y, and Z directions respectively	m
V	Applied voltage	V
V_0	Applied DC voltage	V
V_{PP}	Peak to peak applied sinusoidal voltage	V
W	Width of AFC/tmAFC	m
$\mathcal{W}$	Width of a volume element surrounding a single fiber of a AFC/tmAFC	m
W_A	Width of active area of AFC/tmAFC	m
X,Y,Z	Coordinate axes in AFC/tmAFC	-
x,y,z	Coordinate axes in a single AFC/tmAFC fiber	-
X	Electric reactance	Ω
Y	Admittance	S
Y_{ii}	i,i Young's modulus for a piezoelectric material	Pa
Z	Impedance	Ω

$1,2$	Coordinate axes aligned perpendicular to remnant polarization direction in a piezoelectric material	-
3	Coordinate axes aligned parallel to remnant polarization direction in a piezoelectric material	-
$\hat{1},\hat{2},\hat{3}$	Unit vectors aligned with the *1*,*2* and *3* axes respectively	-
$\underline{\Phi}$	Vector relating measured charge and applied stress in an AFC/tmAFC	C/Pa
Φ_{ij}	Constant relating measured charge and applied *ij* stress in an AFC/tmAFC	C/Pa
$\underline{\Gamma}$	Vector relating measured strain and applied voltage in an AFC/tmAFC	1/V
Γ_{ij}	Constant relating measured *ij* strain and applied voltage in an AFC/tmAFC	1/V
$\underline{\Lambda}$	Vector relating measured charge and applied strain in an AFC/tmAFC	C
Λ_{ij}	Constant relating measured charge and *ij* applied strain in an AFC/tmAFC	C
θ	Temperature	K
Ξ	Ratio of extensional stiffness of a structure to the extensional stiffness of the actuator	-
$\underline{\Psi}$	Vector relating measured stress and applied voltage in an AFC/tmAFC	Pa/V
Ψ_{ij}	Constant relating measured *ij* stress and applied voltage in an AFC/tmAFC	Pa/V
$\underline{\underline{\beta}}$	Impermittivity matrix	m/F
β_{ij}	*i,j* component of impermittivity matrix	m/F
$\underline{\underline{\varepsilon}}$	Permittivity matrix	F/m
ε_{ij}	*i,j* component of permittivity matrix	F/m
ε_0	Permittivity of free space	F/m
γ	The closest distance between the inside of the electrode finger ($y = h_A - h_F$) and the fiber ($y = R$) for a single fiber	m
φ	Electric potential	V
ρ	Density	kg/m^3
σ	Poisson's ratio	-

$\underline{\underline{\sigma}}$	Conductivity matrix	S/m
σ_{ij}	*i*,j component of conductivity matrix	S/m
σ_F	Free charge per unit area	C/m^2
ω	Radial frequency	rad/sec
ξ	The closest distance between the electrode fingers and the plane $y=0$ divided by the fiber radius for a single fiber	-

Notation	Description
$\underline{X},\{X\}$	Vector "*X*"-
$\lfloor X \rfloor$	Transpose of vector "*X*"
$\widehat{X}$	Unit vector "*X*"
$\underline{\underline{X}},[X]$	Matrix "*X*"
$\overline{X}$	Amplitude of X
X^*	Complex conjugate of X

Superscript	Description
D	Material constant measured at constant electric displacement
E	Material constant measured at constant electric field
i	Material constant measured at constant current
S	Material constant measured at constant strain
T	Material constant measured at constant stress
V	Material constant measured at constant voltage

Subscript	Description
A	Material constant is for active area of AFC/tmAFC
A	Material constant is for actuator
AFC	Material constant is for entire AFC
DC	Constant value
E	Material constant is for a e-glass laminated to an AFC/tmAFC
F	Material constant is for a single fiber volume element of an AFC/tmAFC
G	Parameter is for the matrix region between the electrode and fiber

I	Quantity is the imaginary portion of a parameter
K	Material constant is for the Kapton or the outer layer of matrix
LAM	Material constant is for laminated AFC/tmAFC
M	Material constant is for the matrix
PP	Peak to Peak value
R	Quantity is the real portion of a parameter
S	Material constant is for passive structure
t	Transpose of matrix
tmAFC	Material constant is for entire tmAFC

Abbreviation	**Description**
ACX	Active Control eXperts, Inc.
AFC	Active Fiber Composite
CP	Continuum Photonics, Inc
cpAFC	conductive polymer Active Fiber Composites
GNPT	Guaranteed non-porous Teflon
LaRC-MFC	The NASA Langley Research Center Macro-Fiber Composite actuator
MIT	Massachusetts Institute of Technology
MEK	Methyl ethyl ketone
MFC	Macro-Fiber Composite actuator
mpAFC	magnetic particle Active Fiber Composite
PVDF	Polyvinylidene Fluoride
PZT	Lead Zirconate Titanate
tmAFC	thermoplastic matrix Active Fiber Composite

Renamed Items	**Description**
Polymer Gap	The closest distance between the electrode surface and the interface between the polymer and the high dielectric material for an interdigitated block
Piezo	Piezoelectric Material
Shell Epoxy	EPON resin 9405/ EPI-CURE curing agent 9470 epoxy

1. Background

1.1 Background and Motivation

The integration of smart materials into a structure can lead to an active structural surface that can adapt by bending or straining to different operational conditions. This can be directly used to tune desired properties of the active system to their optimal levels. Smart materials are defined in many different ways:[1]

1. Materials functioning as both sensing and actuating

2. Materials which have multiple responses to one stimulus in a coordinated fashion

3. Passively smart materials with self-repairing or stand-by characteristics to withstand sudden changes

4. Actively smart materials utilizing feedback

5. Smart materials and systems reproducing biological functions in load bearing structural systems

One example of a smart material is a piezoelectric material, such as PZT (Lead Zirconate Titanate). Piezoelectric materials behave in two different modes. Sensors can be designed using the direct piezoelectric effect, which is charge generated from an applied external stress. Using the converse piezoelectric effect, which is strain in response to applied electric field, an actuator can be built.

For actuation of beams or plates, actuators can be used in two modes, discrete and distributed actuators, as shown in Figure 1.1.

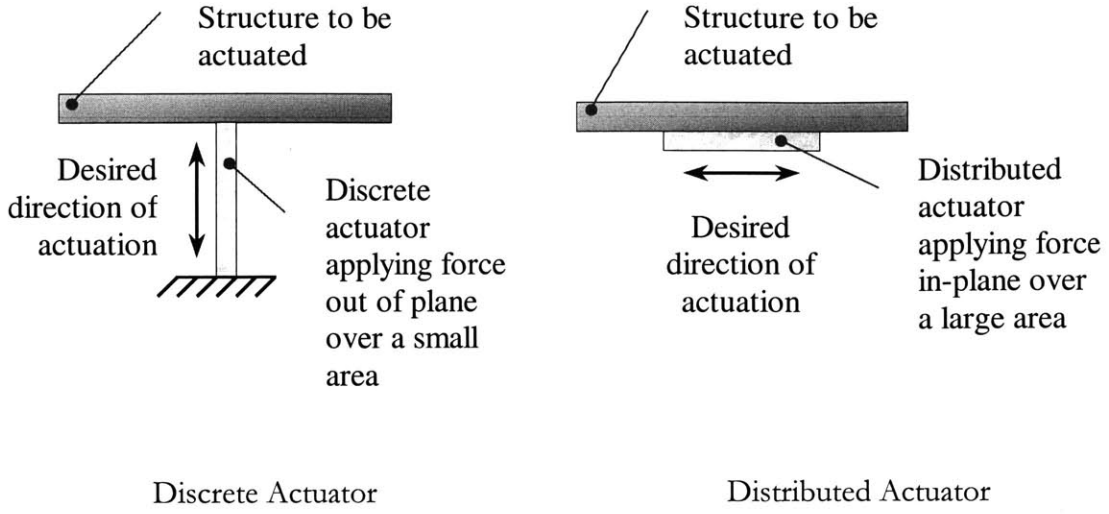

Figure 1.1 Illustration of a Discrete Actuator and a Distributed Actuator

Discrete actuators act over a small area to generate an out-of-plane displacement. Displacement for distributed actuators (or strain actuators) primarily occurs in-plane. Distributed actuators typically have the geometry of thin wafer or plies and are characterized by a relatively large contact area. Because a thin structure is typically characterized by a smaller out-of-plane stiffness compared to the in-plane stiffness, typically a single discrete actuator will generate a larger out of plane displacement than several distributed actuators. However, distributed actuators can be embedded into a structure without changing the surface of the structure and can be placed into locations where a discrete actuator cannot be placed. For example, embedded actuators can be used to perform shape control of rotor blades without changing the aerodynamic shape of the unactuated blade, where as a discrete actuator could be used to actuate a flap and thus change the aerodynamic shape of the blade.

The use of distributed actuators has been proposed as the solution to many active control problems. For example, it has been proposed to use distributed actuators to suppress the vibration due to buffeting in a F/A-18 tail empennage.[2] The use of distributed actuators has been investigated to suppress the vibration of the helicopter rotor blades.[3,4,5,6] The role that distributed actuators can play in the reduction of radiated noise in aircraft has been investigated.[7,8,9,10] Acoustic control of torpedoes[11] has been investigated. Active Control eXperts (ACX)[2] in conjunction with other companies have used distributed actuators to dampen the vibration levels in sports equipment including skis[12], water-skis[13], snow boards[14], baseball bats[15], and bicycle forks[16].

An excellent description of the technology overview of active materials including monolithic piezoceramic materials and Active Fiber Composites is given in Reference [17].

1.2 Piezoceramic Actuator Background

The three main types of distributed piezoceramic actuators include monolithic piezoceramic materials, interdigitated electrode monolithic piezoceramic actuators, and Active Fiber Composites. Thermoplastic Active Fiber Composites are an improvement to the Active Fiber Composite design. The benefits and drawbacks of each as actuators will be discussed in turn. Many references regarding standard notation of piezoelectric materials exist.[18,19,20,21,22,23,24,25]

1.2.1 Planar Monolithic Piezoceramic Actuators

The direct piezoelectric effect is defined as a change in the electric polarization with a change in applied stress. The converse piezoelectric effect is a change in strain for a free material with a change in applied field. By applying a voltage to a piezoelectric material and using the converse piezoelectric effect, actuators can be constructed. Materials displaying piezoelectric behavior will have the following constitutive relations in engineering matrix notation as:[18]

$$\begin{aligned} \underline{D} &= \underline{\underline{\varepsilon}}^{T}\,\underline{E} + \underline{\underline{d}}\,\underline{T} \\ \underline{S} &= \underline{\underline{d}}_{t}\,\underline{E} + \underline{\underline{s}}^{E}\,\underline{T} \end{aligned} \tag{1.1}$$

Where $\underline{T}$ is the stress vector, $\underline{S}$ is the engineering strain vector, E is the electric field vector, $\underline{D}$ is the electrical displacement vector, $\underline{\underline{s}}$ is the matrix of compliance, $\underline{\underline{\varepsilon}}$ is the dielectric matrix, and $\underline{\underline{d}}$ is the piezoelectric "strain" matrix. The T superscript indicates measured at constant stress, the E superscript indicates measured at constant electric field, and the t subscript indicates the transpose. For example for a Hexagonal Crystal – Class 6 mm poled ferroelectric with the polarization direction in the *3* direction, Equation 1.1 can be written as:

$$\left\{\begin{matrix} D_1 \\ D_2 \\ D_3 \\ \hdashline S_1 \\ S_2 \\ S_3 \\ S_4 \\ S_5 \\ S_6 \end{matrix}\right\} = \left[\begin{array}{ccc:ccccccc} \varepsilon_{11}^{T} & 0 & 0 & 0 & 0 & 0 & 0 & d_{15} & 0 \\ 0 & \varepsilon_{11}^{T} & 0 & 0 & 0 & 0 & d_{15} & 0 & 0 \\ 0 & 0 & \varepsilon_{33}^{T} & d_{31} & d_{31} & d_{33} & 0 & 0 & 0 \\ \hdashline 0 & 0 & d_{31} & s_{11}^{E} & s_{12}^{E} & s_{13}^{E} & 0 & 0 & 0 \\ 0 & 0 & d_{31} & s_{12}^{E} & s_{11}^{E} & s_{13}^{E} & 0 & 0 & 0 \\ 0 & 0 & d_{33} & s_{13}^{E} & s_{13}^{E} & s_{33}^{E} & 0 & 0 & 0 \\ 0 & d_{15} & 0 & 0 & 0 & 0 & s_{44}^{E} & 0 & 0 \\ d_{15} & 0 & 0 & 0 & 0 & 0 & 0 & s_{44}^{E} & 0 \\ 0 & 0 & 0 & 0 & 0 & 0 & 0 & 0 & s_{66}^{E} \end{array}\right] \left\{\begin{matrix} E_1 \\ E_2 \\ E_3 \\ \hdashline T_1 \\ T_2 \\ T_3 \\ T_4 \\ T_5 \\ T_6 \end{matrix}\right\} \tag{1.2}$$

"The microscopic origin of the piezoelectric effect is the displacement of ionic charges within a crystal structure. In the absence of external mechanical stress the charge distribution within the crystal is symmetric and the net electric dipole moment is zero. However, when an external stress is applied, the charges are displaced and the charge

distribution is no longer symmetric. A net polarization develops and results in an internal electric field. Each unit cell within a material has a net polarization vector. A region of equally oriented polarization vectors within a material is called a domain. Ideally, polarization vectors of all unit cells would add up forming one large domain within the crystal. However, most commercially available piezoceramics for use as actuators are polycrystalline. The sum of all polarization vectors of all unit cells results in an electrically neutral samples as vectors cancel each other out due to their random statistical distribution of directions." (Reference 17 pages 21-23) The electrical domains of a piezoceramic material can be aligned using a poling process. Piezoelectric materials are "poled" under elevated temperatures and high electric fields aligning the domains of the material with the poling field. As can be seen in Equation 1.2, Hexagonal Crystal – Class 6 mm poled ferroelectrics with the polarization direction in the *3* direction are transversely isotropic with the axis of anisotropy in the *3* direction. The *3* direction is the direction of the net electrical polarization or the poling direction. Due to the transverse isotropy, s_{66}^{E} in Equation 1.2 is not independent of the other material properties.

$$s_{66}^{E} = 2\left(s_{11}^{E} - s_{12}^{E}\right) \tag{1.3}$$

Equation 1.1 can be written in several forms, two of which will be used throughout this document:

$$\begin{aligned} \underline{D} &= \underline{\underline{\varepsilon}}^{S}\,\underline{E} + \underline{\underline{e}}\,\underline{S} \\ \underline{T} &= -\underline{\underline{e}}_{t}\,\underline{E} + \underline{\underline{c}}^{E}\,\underline{S} \end{aligned} \tag{1.4}$$

$$\begin{aligned} \underline{E} &= \underline{\underline{\beta}}^{T}\,\underline{D} - \underline{\underline{g}}\,\underline{T} \\ \underline{S} &= \underline{\underline{g}}_{t}\,\underline{D} + \underline{\underline{s}}^{D}\,\underline{T} \end{aligned} \tag{1.5}$$

Where $\underline{\underline{c}}$ is the matrix of stiffness, $\underline{\underline{\beta}}$ is the impermittivity matrix, $\underline{\underline{e}}$ is the piezoelectric "stress" matrix, and $\underline{\underline{g}}$ is the piezoelectric "voltage" matrix. The *S* superscript indicates measured at constant strain, while the *D* superscript indicates measured at constant electric displacement. Equation 1.1 is used for piezoelectric materials for testing under stress free conditions. Equation 1.4 is used for piezoelectric materials under strain free conditions, or in analyses where displacement and voltage degrees of freedom are assumed, such as finite element analyses. Equation 1.5 is typically used in power generation applications, and when performing piezoelectric composite analyses. The material parameters in Equations 1.4 and 1.5 can be derived from Equation 1.1 by:

$$\underline{\underline{\varepsilon}}^{S} = \underline{\underline{\varepsilon}}^{T} - \underline{\underline{e}}\,\underline{\underline{d}}_{t} \qquad \underline{\underline{c}}^{E} = \left(\underline{\underline{s}}^{E}\right)^{-1} \qquad \underline{\underline{e}} = \underline{\underline{d}}\,\underline{\underline{c}}^{E} \tag{1.6}$$

$$\underline{\underline{\beta}}^{T} = \left(\underline{\underline{\varepsilon}}^{T}\right)^{-1} \qquad \underline{\underline{s}}^{D} = \underline{\underline{s}}^{E} - \underline{\underline{d}}_{t}\,\underline{\underline{g}} \qquad \underline{\underline{g}} = \underline{\underline{\beta}}^{T}\,\underline{\underline{d}} \tag{1.7}$$

It should be noted that throughout the text the following non-standard piezoelectric symbols will be used:

$$K_{ij}^{T} = \frac{\varepsilon_{ij}^{T}}{\varepsilon_0} \qquad K_{ij}^{S} = \frac{\varepsilon_{ij}^{S}}{\varepsilon_0} \tag{1.8}$$

$$Y_{ii}^{E} = \frac{1}{s_{ii}^{E}} \qquad Y_{ii}^{D} = \frac{1}{s_{ii}^{D}} \tag{1.9}$$

$$\sigma_{ij}^{E} = -\frac{s_{ij}^{E}}{s_{ii}^{E}} \qquad \sigma_{ij}^{E} = -\frac{s_{ij}^{D}}{s_{ii}^{D}} \qquad i \neq j \tag{1.10}$$

Where K is the relative dielectric, ε_0 is the permittivity of free space (ε_0 = 8.854 × 10^{-12} F / m), Y is the Young's modulus, and σ is the Poisson's ratio. Using Equations 1.9 and 1.10, the compliance matrix at constant electric field in Equation 1.1 can be rewritten as:

$$\underline{\underline{s}}^{E} = \begin{bmatrix} \frac{1}{Y_{11}^{E}} & -\frac{\sigma_{21}^{E}}{Y_{11}^{E}} & -\frac{\sigma_{31}^{E}}{Y_{33}^{E}} & 0 & 0 & 0 \\ -\frac{\sigma_{12}^{E}}{Y_{11}^{E}} & \frac{1}{Y_{11}^{E}} & -\frac{\sigma_{31}^{E}}{Y_{33}^{E}} & 0 & 0 & 0 \\ -\frac{\sigma_{13}^{E}}{Y_{11}^{E}} & -\frac{\sigma_{13}^{E}}{Y_{11}^{E}} & \frac{1}{Y_{33}^{E}} & 0 & 0 & 0 \\ 0 & 0 & 0 & s_{44}^{E} & 0 & 0 \\ 0 & 0 & 0 & 0 & s_{44}^{E} & 0 \\ 0 & 0 & 0 & 0 & 0 & \frac{2\left(1-\sigma_{21}^{E}\right)}{Y_{11}^{E}} \end{bmatrix} \tag{1.11}$$

$$\sigma_{12}^{E} = \sigma_{21}^{E} \tag{1.12}$$

From Ohm's law, the conduction current density, $\underline{J}_f$ for a piezoelectric material is given by:

$$\underline{J}_f = \underline{\underline{\sigma}}\,\underline{E} \tag{1.13}$$

Where $\underline{\underline{\sigma}}$ is the conductivity matrix. Although not much data exists, for a Hexagonal Crystal – Class 6 mm poled ferroelectric with the polarization direction in the *3* direction, Equation 1.13 is assumed to be written as:

$$\begin{Bmatrix} (J_f)_1 \\ (J_f)_2 \\ (J_f)_3 \end{Bmatrix} = \begin{bmatrix} \sigma_{11} & 0 & 0 \\ 0 & \sigma_{11} & 0 \\ 0 & 0 & \sigma_{33} \end{bmatrix} \begin{Bmatrix} E_1 \\ E_2 \\ E_3 \end{Bmatrix} \tag{1.14}$$

Where the conductivity matrix is the same as an electrically othotropic material. For most piezoceramic materials, the conductivity is very small compared to many non-ceramic materials ($\sigma \cong$ 1-100 pS/m). Resistance measurement for conductivities this low is typically

difficult due to parasitics, resistive heating, and the fact that some current that appears due to resistance is due to lags in the permittivity. It is currently unknown if the conduction current is a function of the stress or strain state of the material, however there is some research that may be conducted in this field.[26] Due to the low conductivity of piezoceramic materials, typically when modeling and analyzing piezoceramic materials it is assumed that the conductivity is zero, and thus all charge and current is due to the capacitance of the material.

The electroelastic equations of equilibrium under electrostatic conditions are presented in Appendix I.

The Military Standard for Piezoelectric Ceramics Materials and Measurements defines six standard piezoelectric ceramic types, known as type I - type VI.[25] In order for a manufacturer to be able to call its material by the type I- type VI designation each material type must conform to certain material property specifications. Manufactures are then free to manufacture lead zirconate-titanate materials using their own proprietary manufacturing processes that have small variations in material properties with respect to their competitors. and sell them to the military as a standard material. One of the standard ceramic types defined in the Military Standard is type II, also referred to in some literature as Navy type II. Type II is "A hard lead zirconate-titanate composition modified to yield higher charge sensitivity, but one that is not suitable for high electric drive due to dielectric heating. This material is more suitable for passive devices such as hydrophones. Advantages include better time stability" (Reference 25 page 5). Material properties for PZT-5A[27] a material manufactured by Morgan Electro Ceramics, which conforms to the type II standard, can be found in Table 1.1.

Table 1.1 Military Type II Material Property Specifications[25] and PZT-5A Material Properties Manufactured by Morgan Electro Ceramics[28]

Material Property	**Military Type II Material Property Specifications**	**PZT-5A Value**
K_{33}^T	1725 ± 12.5%	1700
K_{31}^T	-	1730
d_{33}	390 ± 15% pC / N	374 pC / N
d_{31}	-	-171 pC / N
k_p	-0.60 ± 8%	-0.60
s_{11}^E	-	16.4 pm^2 / N
s_{33}^E	-	18.8 pm^2 / N
Conductivity at 25 °C (77 °F), σ		< 10 pS / m
Density, ρ	≥ 7600 kg / m^3	7750 kg / m^3

PZT-5A is the most commonly referred to type II material. The chemical composition of another type II material is given by $Pb_{0.988}(Ti_{0.48}Zr_{0.52})_{0.96}Nb_{0.024}O_3$.[29] It should be noted that there are many other piezoelectric materials that do not conform to the Military Standard for Piezoelectric Materials and that the Military Standard has been canceled without replacement.[30]

Consider a thin planar piezoceramic actuator poled in the *3* direction electoded on the positive and negative *3* faces as shown below:

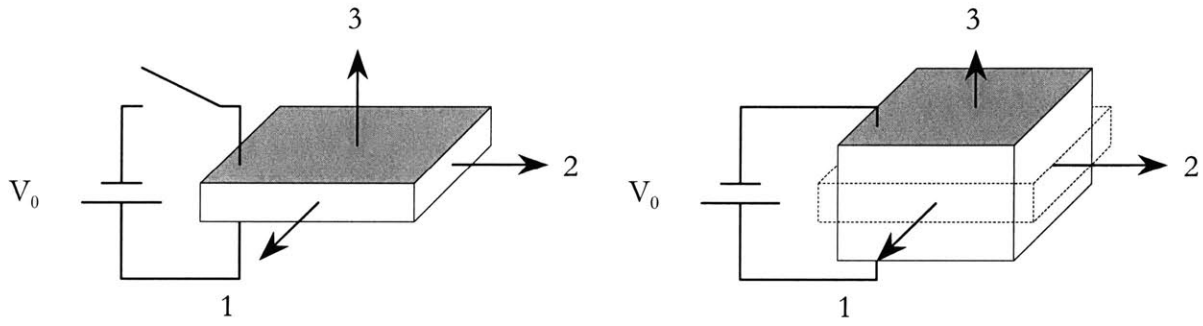

Before application of voltage After application of voltage

Figure 1.2 Illustration of *3-3* and *3-1* Actuation of a Piezoceramic Actuator

When a voltage, V_0, is applied to the piezoceramic creating an electric field in the *3* direction, the piezoceramic undergoes a positive strain in the *3* direction. This actuation is known as *3-3* actuation. The piezoceramic also undergoes *3-1* actuation, a negative strain in the *1* and *2* directions due to the application of an electric field in the *3* direction. It should be noted that for all PZT based actuator systems *3-3* actuation is roughly 2 to 2.5 times greater than *3-1* actuation (average of d_{33} / d_{31} for PZT in Reference 28). In order to induce strains in PZT piezoceramics on the order of magnitude of 1000 με an electric field on the order of several thousand V/mm is required. This limits the thickness of PZT actuators to be a few millimeters to keep the driving voltages to a reasonable level (kilovolt range). Because of the limit on actuator thickness, for planar actuation the *3-1* mode is used.

An example of a planar monolithic piezoceramic actuator is the QuickPack[31] actuator manufactured by ACX. "The QuickPack actuator packages piezoelectric materials in a protective skin with pre-attached electrical leads, producing a highly reliable component with no soldered wires. The QuickPack actuator's protective skin also provides electrical insulation and defense against humidity and harsh contaminants."[32] A picture of a single piezoceramic and a four piezoceramic QuickPacks are shown in Figure 1.3.

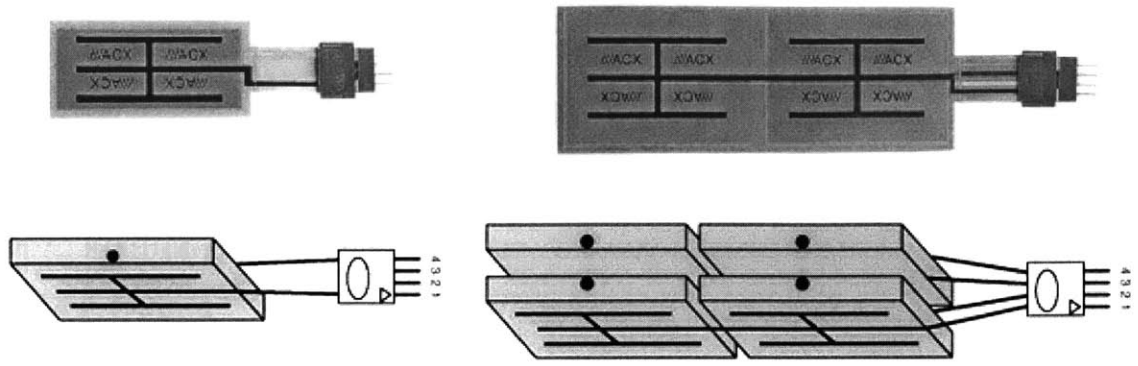

QuickPack QP10N QuickPack QP45W

Figure 1.3 QuickPack Monolithic Piezoceramic Actuators [33]

QuickPacks are manufactured from PZT-5A for extensional actuators and PZT-5H (Reference 27) for bimorph actuators and are poled through the thickness. QuickPacks can be made to actuate in extension or bending and can be custom made to meet customers needs. Properties of standard off the shelf extension mode QuickPacks are shown in Table 1.2.

Table 1.2 Properties of Standard Extension Mode QuickPacks and the Single Wafer QuickPack QP10N[32]

Material Property	**Range of All QuickPack Actuators**	**QuickPack QP10N**
Piezoceramic wafer material	PZT-5A	PZT-5A
Electrode material	Nickel	Nickel
Piezoceramic wafer thickness	127-254 μm (5-10 mil)	254 μm (10 mil)
QuickPack thickness	254-762 μm (10-30 mil)	381 μm (15 mil)
Piezoceramic wafer configurations (length x width)	2 x 2, 1 x 2, 1 x 1	1 x 1
Capacitance	60-165 nF	60 nF
Maximum strain	225-280 με	262 με
Maximum voltage	100 – 200 V	200 V
High field d_{31} (see note below)	-286 to -356 pm/V	-333 pm/V
Maximum electric field	0.79 kV/mm	0.79 kV/mm
Maximum operating power	20 W rms	20 W rms
Maximum operating temperature	100 °C (212 °F)	100 °C (212 °F)

It should be noted that in Table 1.2 d_{31} is the high field d_{31} and was determined by multiplying the maximum operating strain times the wafer thickness and dividing by the maximum voltage. d_{31} for the QuickPacks at low electric fields cannot be exceed that of the piezoceramic material d_{31} = -171 pm / V (Table 1.1). It should also be noted that the difference in thickness between the QuickPack and the wafer is due to a 63-127 μm (2.5 – 5 mil) thick electrically insulating layer bonded to either side of the QuickPack. The actuation properties of the single wafer *3-1* planar actuator QP10N QuickPack are shown in Figure 1.4:

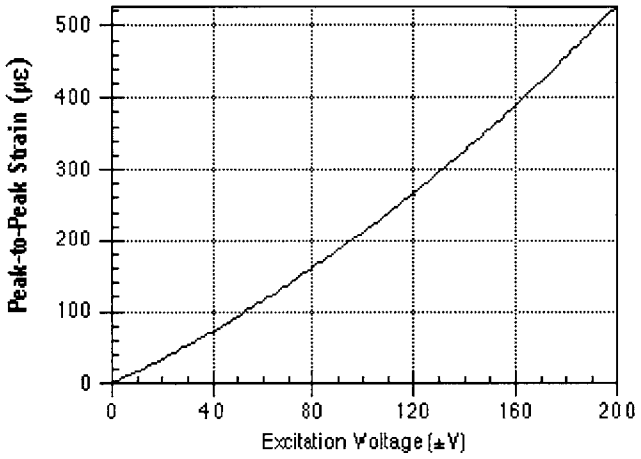

Figure 1.4 Actuation of a Single Wafer *3-1* Planar Actuator QP10N QuickPack

The greatest drawback to using planar monolithic piezoceramic materials as actuators is their brittleness. Piezoelectric materials can tolerate very low levels of strain before failure. For example, PZT-5H has a maximum strain of 1300 $\mu\varepsilon$[34], and is very susceptible to cracking. Due to their high stiffness piezoelectric materials cannot conform to curved surfaces and must be machined to fit curved shapes.

An excellent description of the technology overview of piezoceramic distributed actuator systems is given in Reference [35].

1.2.2 Interdigitated Electrode Monolithic Piezoceramic Actuators

In order to increase the actuation properties of planar monolithic piezoceramic actuators, planar interdigitated electrode actuators have been developed which use *3-3* actuation instead of *3-1* actuation, providing coupling efficiency and higher strain output. Unlike the *3-1* planar actuator which strains equally in the length and width direction, the *3-3* planar actuators strain more in the direction of the applied electric field (typically the length direction) than in the width or thickness directions, thus providing anisotropic actuation. An illustration of an interdigitated electrode monolithic piezoceramic actuator is shown in Figure 1.5:

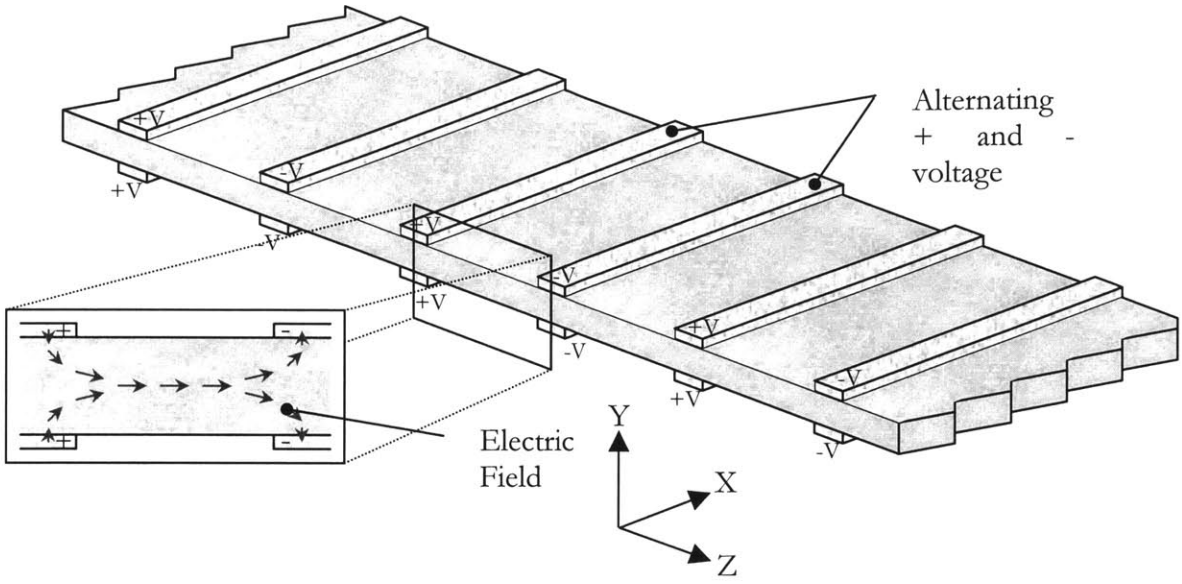

Figure 1.5 Illustration of an Planar Interdigitated Electrode Monolithic Piezoceramic Actuator

In Figure 1.5, the electrode is bonded to either side of the piezoceramic. A voltage of alternating sign is applied to the electrodes giving an electric field in the piezoceramic that alternates in direction. Directly beneath the electrodes, the field is perpendicular to the surface, however between the electrodes the field is primarily in the *Z* direction. It should be noted that the electrodes bonded to the planar interdigitated electrode actuator can be used to pole the piezoceramic. Thus the electric field is always in the *3* direction, however this direction is not always aligned with the *Z* direction.

An example of a planar interdigitated electrode actuator is the PowerAct[36] strain actuator manufactured by Midé Technology and the QuickPack IDE Strain Actuator model number QP10Ni[37] manufactured by ACX. A picture of a QuickPack IDE Strain Actuator is shown in Figure 1.6:

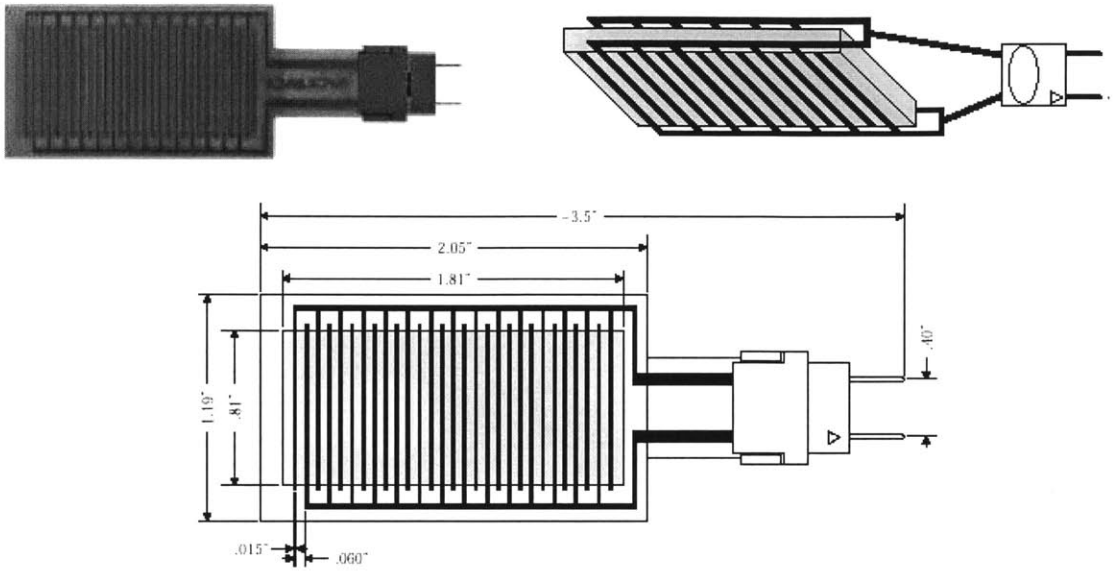

Figure 1.6 QuickPack IDE Strain Actuator (Dimensions in inches)

Material properties for the QuickPack IDE Strain Actuator model number QP10Ni are given in Table 1.3

Table 1.3 QuickPack IDE Strain Actuator model number QP10Ni Material Properties[38]

Property	**Value**
Size	52.1 x 30.2 x 0.38 mm (2.05 x 1.19 x 0.015 in)
Electrode spacing (center to center)	1.52 mm (60 mil)
Electrode width	0.38 mm (15 mil)
Capacitance	1.02 nF
Maximum *Z* strain	347 με
Maximum *X* strain	123 με
Maximum voltage	1200 V
High field d_{33} (see note below)	440 pm/V
High field d_{31} (see note below)	156 pm/V

It should be noted that in Table 1.3 d_{33} and d_{31} are the high field d_{33} and d_{31} and was determined by multiplying the maximum operating strain times the center to center electrode spacing and dividing by the maximum voltage. d_{33} for the QuickPacks at low electric fields cannot be exceed that of the piezoceramic material d_{33} = 374 pm / V (Table 1.1). It should also be noted that the strain in the *3-3* direction is 180° out of phase with the strain in the *3-*

1 direction as was shown in Figure 1.2. The strain versus applied field is for a QP10Ni IDE strain actuator and a *3-1* strain actuator, QP10N is compared in Figure 1.7:

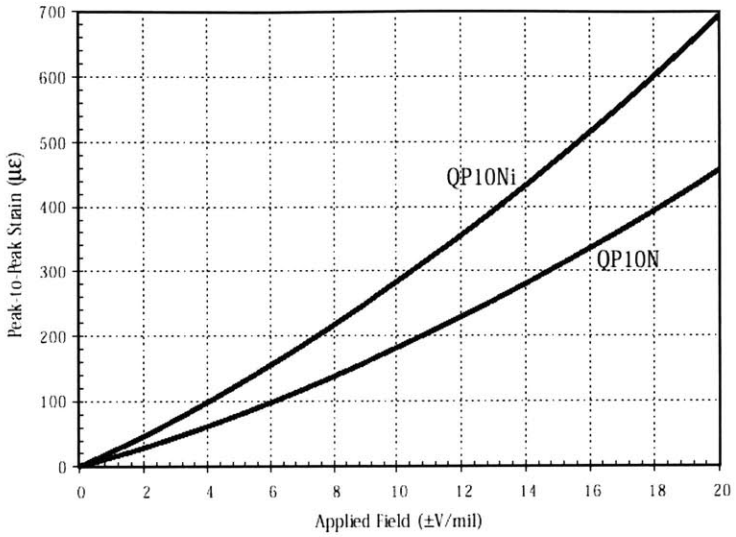

Figure 1.7 Comparison of the Actuation of a QP10Ni IDE Strain Actuator a *3-1* Strain Actuator, QP10N

As can be seen in Figure 1.7, the actuation of the QP10Ni IDE strain actuator is greater than that of the QP10N actuation for a given applied field. At the maximum electric field the strain in the IDE actuation is 1.3 times greater that the stain in the *3-1* actuator. This is less than the theoretical maximum of $d_{33} / d_{31} = 2.2$ (see Table 1.1) due to several reasons. First, only the volume between the electrodes in the *Z* direction actuates using *3-3* actuation in the *Z* direction. The volume between the electrodes represents 75% (1 – 15 mil/ 60 mil) the total length of the active length of the actuator. The *3* direction and the electric field beneath the electrodes are both perpendicular to the electrode. Thus, when the actuator actuates, the material beneath the electrode actuates using *3-1* strain in the *Z* direction. This actuation is 180° out of phase with the actuation in between the electrodes in the *Z* direction, and thus cancels out some of the strain due to the *3-3* actuation.

Like planar monolithic piezoceramic actuator, planar interdigitated electrode actuators have low failure stress and cannot conform to a curved surface due to their large stiffness.

1.2.3 Active Fiber Composites (AFCs)

AFCs are thin composite plies comprised of unidirectional piezoelectric fibers imbedded in a thermoset matrix. An electric field is supplied to the fibers by use of an interdigitated electrode pattern adhered to either side of the fibers. An example of an AFC is illustrated in Figure 1.8. The benefits of AFCs include: the interdigital electrode design uses *3-3* actuation offering increased levels of actuation, the AFC allows anisotropic planar

actuation, the AFCs matrix provides load transfer and load distribution, AFCs allows for coverage of curved shapes, and the electrical connections are independent of ceramic damage.

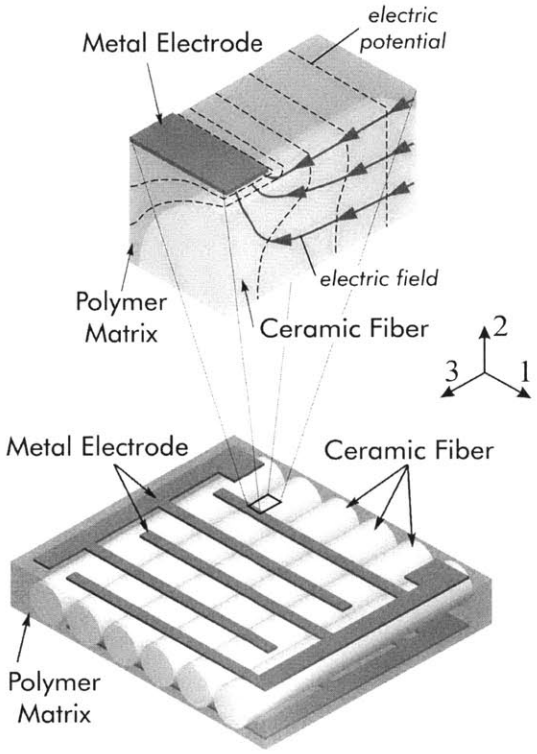

Figure 1.8 Illustration of an Active Fiber Composite

Active Fiber Composites were first developed at the Massachusetts Institute of Technology by Aaron Bent and Professor Nesbitt Hagood IV.[34,39,40] AFCs are being commercially developed at Continuum Photonics, Inc[41] (CP) under the trade name PiezoFlex. Table 1.4 gives the performance data for PiezoFlex AFCs with PZT-5A fibers.

Table 1.4 PiezoFlex Properties[42]

Property	**Value**
IDE Electrode Substrate Material	Kapton[43]
IDE Electrode Ink	Silver
Matrix	Thermosetting Epoxy Film Adhesive
Fiber Material	PZT-5A Manufactured By CeraNova[44]
Fiber Diameter	250 Microns
Thickness	330 Microns
Line Fraction	85 – 90 %
s_{33}	4.00 x 10^{-11} m^2 / N
d_{33} (low field)	150 pm/V

It should be noted that PiezoFlex actuators can be custom made to meet customers needs and Table 1.4 gives only sample material properties. An illustration of the wet lay-up manufacturing process for AFCs[34] used at the Massachusetts Institute of Technology is shown in Figure 1.9:

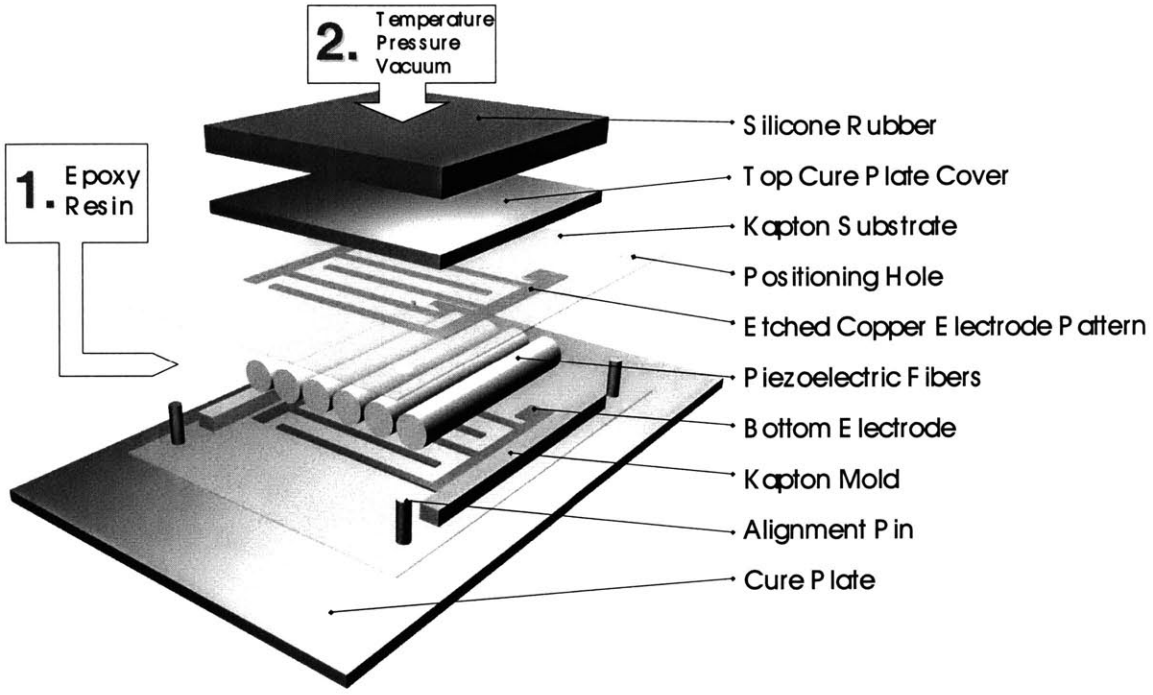

Figure 1.9 Illustration of the Wet Lay-Up Manufacturing Process for AFCs[45]

Much work was done at the Massachusetts Institute of Technology to perfect the manufacturing process, including work performed by the author not listed in this presentation. Currently PiezoFlex AFCs are manufactured at CP using a thermosetting film adhesive matrix using a proprietary manufacturing process.

A major drawback of the AFCs with PZT-5A fibers is that the level of actuation is 60% lower than that of the *3-3* actuation of monolithic PZT-5A giving the AFCs about the same actuation as planar monolithic piezoceramic materials. (see Table 1.1 and Table 1.4). This is due primarily to the fact that a small layer of low dielectric matrix material is trapped between the electrodes and the high dielectric fibers due to manufacturing. This dielectric mismatch causes a large voltage drop in the matrix thereby reducing the available voltage for actuation. Another drawback to the AFC design is that the maximum voltage that can be applied to the AFC is limited to the dielectric breakdown strength of the polymer material, which is typically much lower than that of the piezoceramic fiber. A third draw back of the PiezoFlex design is the that it is comprised of an epoxy thermosetting matrix that requires a

cure time of about 5 minutes,[46] thus limiting the rate at which PiezoFlex AFCs can be manufactured.

An excellent description of the technology overview of Active Fiber Composites Technologies is given in Reference [47].

1.2.4 NASA Langley Research Center Macro-Fiber Composite Actuator (LaRC-MFC)

The NASA Langley Research Center Macro-Fiber Composite actuator (LaRC-MFC), manufactured by the NASA Langley Research Center is a low-cost, flexible, planar actuator, with an intedigitated electrode that is very similar to a traditional AFC.[48,49] "The LaRC-MFC retains the most advantageous features of active fiber composite actuators, namely, high strain energy density, directional actuation, conformability and durability, yet incorporates several new features, chief among these being the use of low-cost fabrication processes that are uniform and repeatable. The actuator uses interdigitated electrodes for poling and subsequent actuation of an internal layer of machined piezoceramic fibers. The fiber sheets are formed from monolithic piezoceramic wafers and conventional computer controlled wafer-dicing methods." [48] The primary difference between the PiezoFlex AFC and the LaRC-MFC is the AFC uses piezoceramic fibers and the LaRC-MFC uses a diced piezoceramic wafer. "The fabrication and use of fiber sheets allows precise handling and alignment of piezoceramic fibers during subsequent phases of actuator assembly." [48] A picture of a LaRC MFC is shown in Figure 1.10:

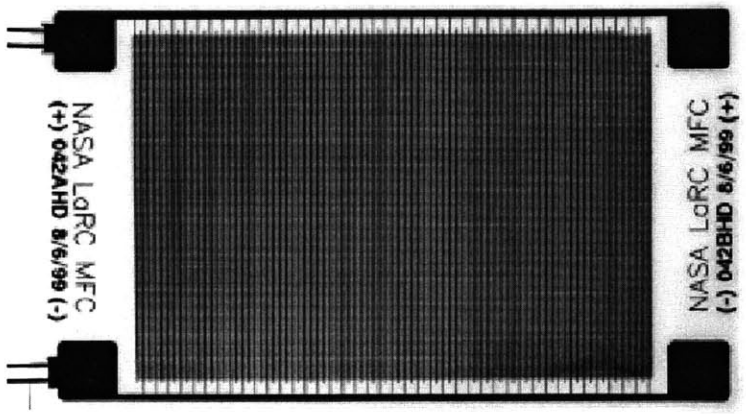

Figure 1.10 Langley Research Center Macro-Fiber Composite Actuator[48]

Properties of the LaRC-MFC actuator are given in Table 1.5.

Table 1.5 Properties of the LaRC-MFC Actuator[50]

Property	Value
IDE electrode substrate material	LF7062 film
Matrix	Hysol E-120HP Epoxy
Wafer material	PZT 3195HD[51]
Average thickness	254 microns
Shorted Longitudinal Young's modulus (fiber axis)	29.0 GPa
Transverse Young's modulus	17.9 GPa
Effective d_{33} (see note below)	530 pm / V
Effective d_{31} (see note below)	-210 pm / V
Poled capacitance per unit area (1 kHz, 25 C)	155 pC/cm^2
Maximum operation free strain	1000 με
Limit longitudinal mechanical strain (piezoelectric fiber failure)	3000 με
Recommended operational temperature limit	66 °C

The wafer material for the MFCs is PZT 3195[51] which is equivalent to PZT-5A sold by Morgan Electroceramics (Reference 27). For PZT 3195, d_{33} = 390 pm/V, d_{31} = -190 pm/V, Y_{33}^{E} = 53 GPa, K_{33}^{T} = 1900, and k_{33} = 0.72.[52] It should be noted that in Table 1.5 d_{33} and d_{31} are the high field d_{33} and d_{31}. For this actuator, the high field d was determined from the maximum peak-to-peak strain divided by the maximum electric field (Reference 50). The d's for the MFC will be lower at lower electric field levels. A comparison of the LaRC-MFC and other interdigitated electrode piezoceramic actuators is shown in Figure 1.11.

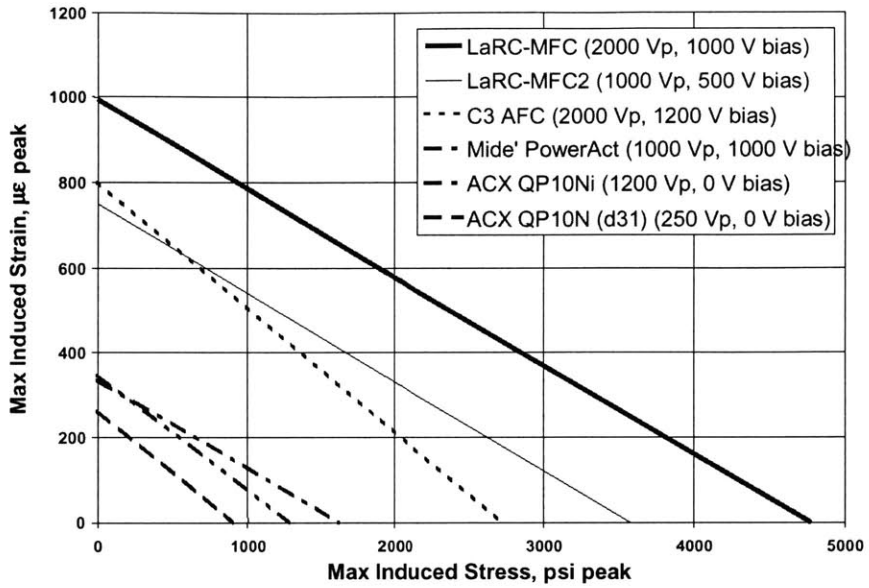

Figure 1.11 Comparison of the LaRC-MFC and other Interdigitated Electrode Piezoceramic Actuators[48]

It should be noted that in Figure 1.11 the maximum induced stress is the maximum free induced stress and was calculated by multiplying the stiffness of the respective actuator by the maximum free strain. In addition, the data in Figure 1.11 does not match the data in Table 1.5 because the data in Figure 1.11 is not the most current data.

The LaRC-MFC also suffers from the same problems as the AFCs. That is a small layer of low dielectric matrix material is trapped between the electrodes and the high dielectric fibers due to manufacturing. This dielectric mismatch causes a large voltage drop in the matrix thereby reducing the available voltage for actuation. In addition, like the AFC design, the maximum voltage that can be applied to the LaRC-MFC is limited to the dielectric breakdown strength of the polymer material.

1.2.5 Magnetic Particle Active Fiber Composites (mpAFCs)

In order to reduce the eliminate the voltage drop due to the layer of matrix trapped between the electrode and the fibers, a different concept for AFC manufacture was investigated, magnetic particle Active Fiber Composites (mpAFCs).[45,53] "To manufacture mpAFCs, a polymer matrix material (uncured liquid epoxy) is doped with small ferromagnetic, electrically conductive particles (nickel powder). During the curing process, these particles would de-mix from the epoxy and were aligned using a magnetic field to create a three-dimensional electrically conductive network that is frozen into the matrix

when it is cured" (Reference 45 pages 3 and 4). An illustration of the manufacturing process of an mpAFC is shown in Figure 1.12.

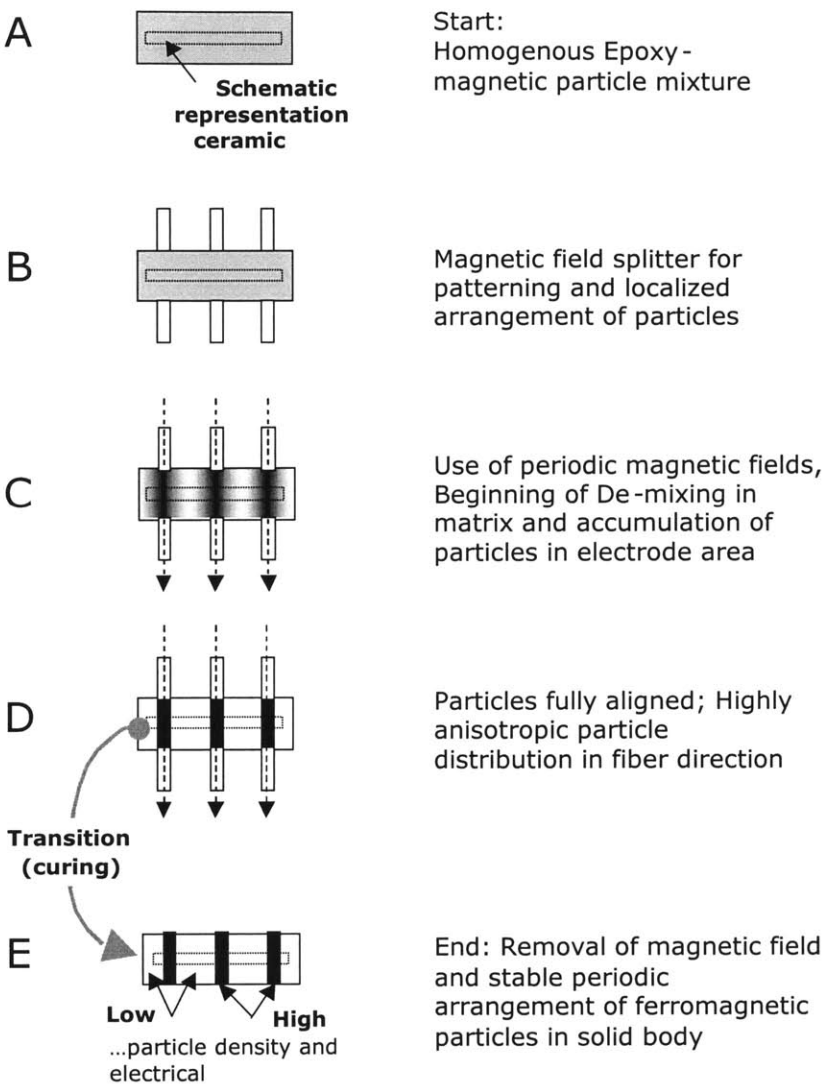

Figure 1.12 Illustration of the Manufacturing Process of a Magnetic Particle Active Fiber Composite (Reference 45 page 44)

This electrical network of nickel particles provides direct electrical contact between the voltage source and the piezoelectric fibers. A picture of an mpAFC is shown in Figure 1.13:

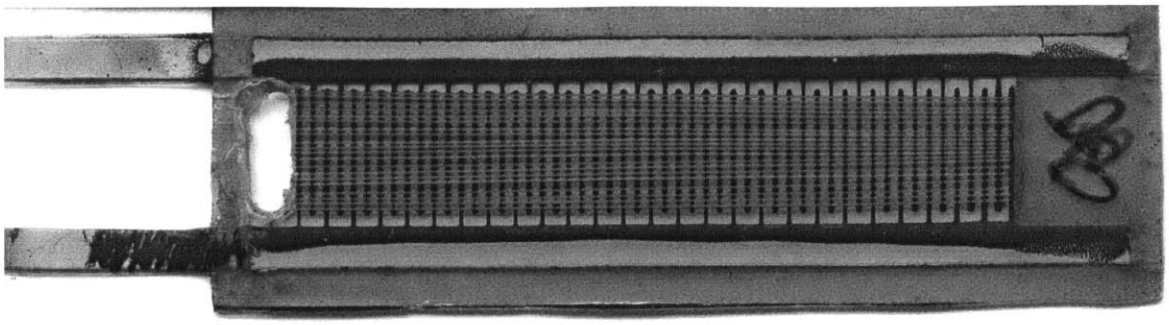

Figure 1.13 Magnetic Particle Active Fiber Composite (Reference 45 pages 166)

Alignment of the magnetic field was supplied using a magnetic template that was embedded into the curing plate. The magnetic template was constructed using Permalloy 80 in the shape of the electrode pattern. The magnetic template was placed in the center of the cure plate and epoxy was pored between the fingers of the magnetic template to provide a cure plate with a flush surface as illustrated in Figure 1.14.

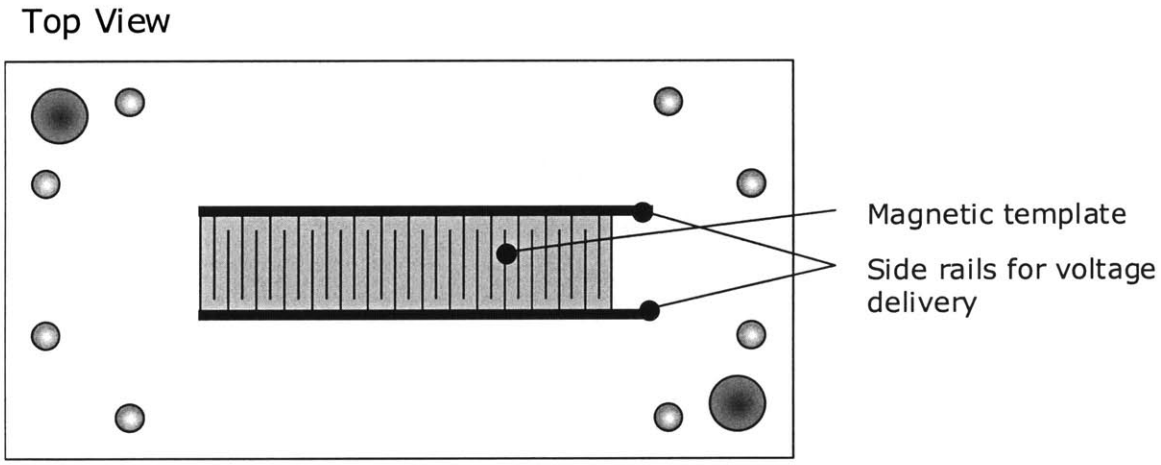

Figure 1.14 Illustration of mpAFC Cure Plate with Magnetic Template (Reference 45 page 131)

In Figure 1.15 the actuation properties of a single mpAFC are compared to the actuation properties of three PiezoFlex AFCs:

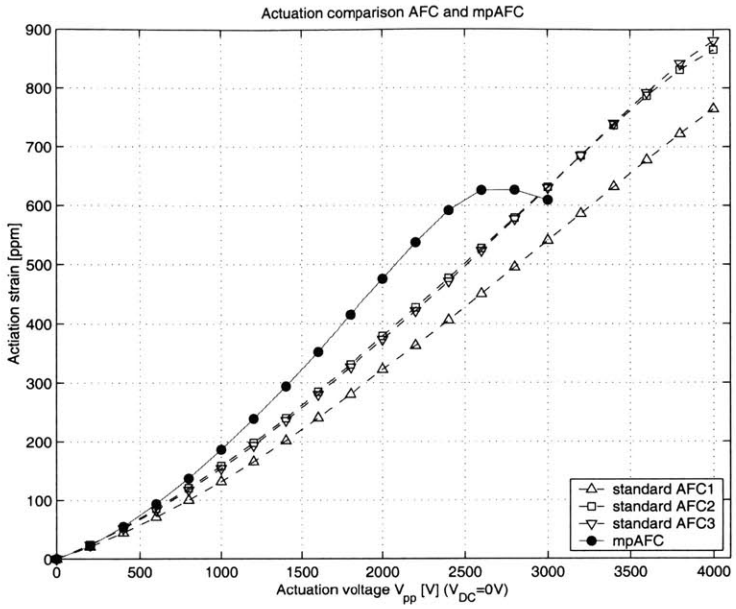

Figure 1.15 Actuation Properties of a Single mpAFC Compared to Three PiezoFlex AFCs (Reference 45 page 225)

It should be noted that a direct comparison between the two different actuators is difficult because the materials used and the thickness for the two actuators are different, and thus the stiffness of the two actuators is different. It should be noted that the material surrounding the mpAFC in Figure 1.15 is much thicker and had less fibers per width than the PiezoFlex and therefore the mpAFC is a better actuator. The greater actuation of the mpAFC compared to the PiezoFlex AFC can be attributed to the fact that the electrodes are in direct electrical contact with the fibers, and thus there is no voltage drop attributed to the a layer of matrix trapped between the electrode and the fibers which is present in the PiezoFlex AFCs.

Several problems exist with the current manufacturing process of mpAFCs. Budget concerns limited the strength of the electromagnets used to generate the magnetic field. In addition, the heat of the magnets was used to cure the epoxy matrix. Due to the low magnetic field, the magnets could generate and the low temperature that the magnets could generate, and epoxy was selected such that it had a low viscosity at room temperature and a low curing temperature 100 °C (212 °F). A low viscosity epoxy was necessary because, during the de-mixing process, the particles had a tendency to not fully de-mix, thus leaving particles between the electrode fingers. This lowered the dielectric breakdown strength between the electrode fingers, thus limiting the maximum voltage of the mpAFC. Thus, in order to increase the dielectric strength an epoxy with a low viscosity was selected so that the magnetic particles would encounter as little resistance during the de-mixing phase of the manufacturing. The viscosity of the epoxy was further lowered using an epoxy modifier.

The low viscosity of the epoxy was not enough to eliminate the magnetic particles between the electrode fingers during the de-mixing, and therefore the line fraction (the number of fibers per unit active electrode width) was reduced (41%) compared to a standard PiezoFlex AFC (85-95%). This reduction in the fiber line fraction limited the maximum actuation strain of the mpAFCs. The low fiber line fraction could be eliminated by purchasing stronger (more expensive) electromagnets. In addition, due to low cure temperature of the epoxy, mpAFCs could most likely not survive curing in a composite host structure cured at 176 °C (350 °F). This greatly limits the possible number of structures and environments that the mpAFCs could be used in. Higher temperature epoxies could be used for curing if the temperature of curing was supplied not by the magnets, but by a separate heating method such as inline heaters embedded into the curing mold. It should be noted that like PiezoFlex AFCs, the rate that mpAFCs are manufactured is given by the cure time of the thermosetting matrix material.

1.2.6 Conductive Polymer Active Fiber Composites (cpAFCs)

In order to reduce the driving voltages for AFCs, another concept for AFC manufacturing was being perused, conductive polymer Active Fiber Composites (cpAFCs).[54] cpAFCs are manufactured by placing the piezoelectric fibers between two sheets of an intrinsically conductive polymer, and heating and pressing the three layers together. Intrinsically conductive polymers are a new class of polymers that can be made selectively conductive or non-conductive by using a doping process. In order to establish better contact between the fibers and the electrodes an electrode pattern would be doped into the intrinsically conductive polymer either before or after bonding to the fibers. This would result in direct electrical contact between the fibers and the electrodes and thus result in lower driving voltages. cpAFCs would have similar actuation levels and driving voltages as mpAFCs. A schematic of a cpAFC is shown in Figure 1.16.

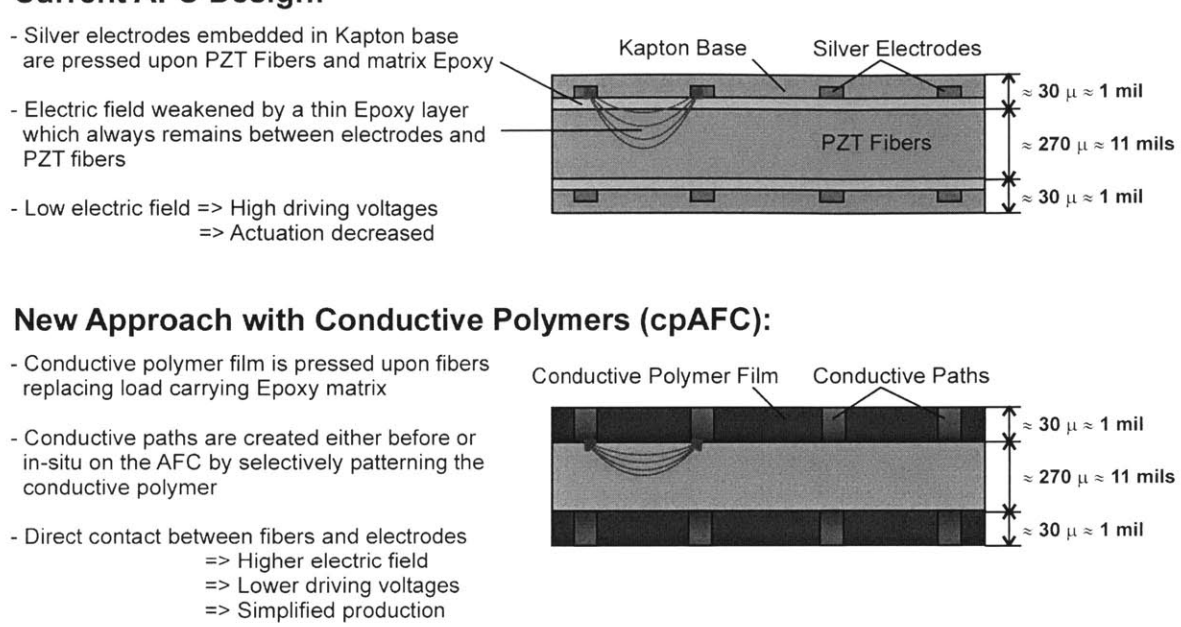

Figure 1.16 Illustration of a Conductive Polymer Active Fiber Composite (Reference 54 page 22)

Mr. Mueller (Author of Reference 54) performed a feasibility study of cpAFC manufacturing in the Summer and Fall of 2000. After determining the material requirements for a cpAFC, several intrinsically conductive polymers were selected to be tested. Polymers were doped using UV-light and were doped chemically. It was shown that conductive patterning of the electrode was generally feasible, and that the polymer would bind to the fibers, and thus a cpAFC was possible.

In the Spring of 2001, work on cpAFCs was continued by Ms. Hernandez, an undergraduate in Center for Materials Science and Engineering at the Massachusetts Institute of Technology, with some assistance by the author of the present work. Ms. Hernandez helped conduct research into cpAFCs with the Mr. Mueller in the Summer and Fall of 2000. Manufactures of intrinsically conductive polymers were contacted and were asked to provide samples of intrinsically conductive polymers that met more stringent and more realistic material requirements for an AFC matrix material than used in Reference 54. These minimum requirements for an AFC matrix material are listed in Section 4.2. After talking with many sales people, researchers, and professors, it was Ms. Hernandez conclusion that the field of intrinsically conductive polymers were still in the research and development stage, and that no material currently existed that could meet the needs of an cpAFC matrix material.[55] Ms. Hernandez and the author of the present work felt that further research should not be pursued until the field of intrinsically conductive polymers had time to mature.

1.2.7 Thermoplastic Active Fiber Composites (tmAFCs)

Thermoplastic matrix Active Fiber Composites (tmAFCs) are being developed in order to address some of the shortcomings of AFCs. The primary difference between tmAFCs and AFCs is that tmAFCs have a matrix that is comprised of a thermoplastic material and not a thermosetting material. tmAFCs have several advantages over AFCs including: tmAFCs have faster processing times because the matrix does not need to be cured, tmAFCs can be reshaped after manufacture, and tmAFC have nearly direct electrical contact between the electrodes and fibers because the electrodes can be printed onto matrix prior to processing. The nearly direct electrical contact between the fibers and the matrix allows for higher actuation levels of tmAFCs compared to AFCs.

Research into tmAFCs was performed by Mr. Patrick Trapa, who was an undergraduate at the time, in the Active Materials and Structures Laboratory at the Massachusetts Institute of Technology. His unpublished research, which will be described in the beginning of Chapter 4, started in the Summer of 1997 and continued until about June of 1999. The author of this present work started working on tmAFCs in January of 1999, assisting in and eventually continuing Mr. Trapa's research.

1.2.8 Objectives

The objective of this research is to analyze, manufacture, and test tmAFCs to be used in structural control applications with the goal of producing high quality and high performance actuators.

2. tmAFC Introduction

2.1 Introduction

The relation between dielectric, stiffness, and Poisson's ratio of the matrix material on tmAFC performance is not clearly understood. In order to determine the effect that the matrix has on the stiffness and the actuation performance of tmAFCs, finite element models of a CP PiezoFlex AFCs were constructed and the matrix material properties were varied. These analyses will be presented in Chapter 3. This chapter presents the supporting information for the analyses in Chapter 3. First, the notation used for the subsequent analyses is introduced. Then an average estimate of the material properties and standard deviations for engineering polymers is presented. Finally, the material properties for PiezoFlex AFCs and PZT-5A are presented.

2.2 tmAFC Geometry and Notation

A tmAFC is comprised of four basic materials, the piezoelectric fibers, the matrix, the electrode, and layers of material with high dielectric breakdown strength. The piezoelectric fibers provide the actuation authority and carry the majority of the load in the Z direction due to their stiffness. The compliant matrix acts as a load transfer mechanism around fiber breaks. The metal electrode provides an electric field to the fibers in the Z direction. The layers of materials with high dielectric breakdown strength provide electrical protection for the surrounding host structure. A schematic of a tmAFC is shown in Figure 2.1.

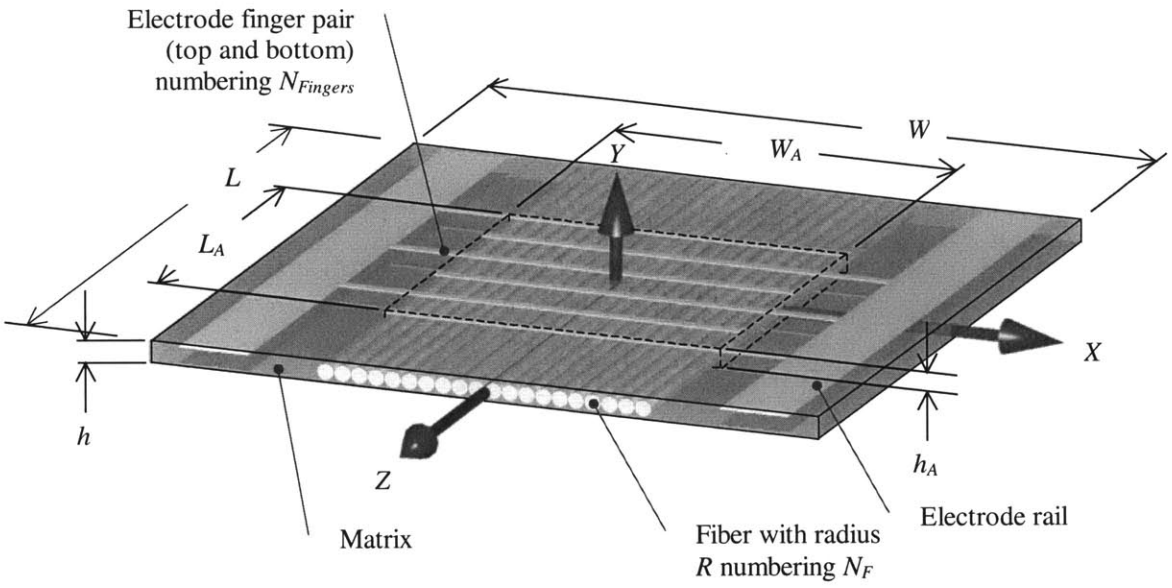

Figure 2.1 tmAFC Diagram

In Figure 2.1, the X axis is aligned transverse to the fibers in plane, the Y axis is aligned out of plane of the tmAFC, and the Z axis are aligned with the fibers. L, W, and h is length, width, and height of the entire tmAFC respectively. L_A, W_A, and h_A is length, width, and height of the active area of the tmAFC respectively, which will be described in detail below. $N_{Fingers}$ is the total number of electrode fingers divided by two. In Figure 2.1 there are four pairs of electrodes. Both electrodes on the left are electrically connected to each other. Both electrodes on the right are electrically connected to each other. In Figure 2.1 there exists a layer with a high dielectric breakdown strength on either side of the tmAFC in the Y direction.

The geometry of one of the electrodes for the tmAFCs is shown in Figure 2.2 with the important parameters used throughout this document in Table 2.1.

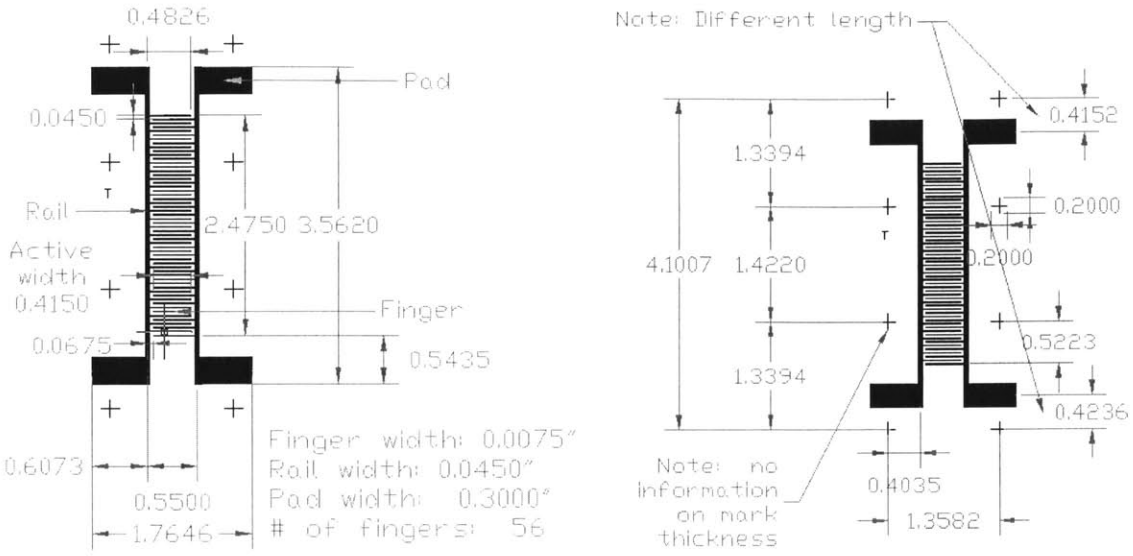

Figure 2.2 tmAFC Electrode Geometry (In Inches)

Table 2.1 tmAFC Electrode Geometry

Parameter	**Value**
L_A (center to center)	6.286 cm (2.475")
W_A	1.054 cm (415 mil)
l	1.143 mm (45 mil)
L_F	191 μm (7.5 mil)
$N_{Fingers}$	56

It should be noted that two electrode types were used for the AFCs/tmAFCs, copper and silver electrodes on a Kapton substrate. The copper electrodes are approximately 5 μm (0.197 mil) thick with a Kapton substrate thickness of either 12.7 or 25.4 μm (0.5 or 1 mil). The copper electrodes had a smooth surface, and appeared to be manufactured using a sputtering or etching process. The silver electrodes are 25.4 μm (1 mil) thick with a Kapton substrate thickness of 25.4 μm (1 mil). The electrode is screen printed onto a Kapon substrate using a silver based conductive ink. Not much information is known about the electrodes because the electrodes were purchased prior to the author starting this research.

There are three important pieces of the electrode geometry illustrated in Figure 2.2, the pads, the rails, and the fingers. The electrode pads are the large rectangular areas on either end of the electrodes. The voltage leads from the voltage source are connected to the pads using alligator clips, solder, or silver epoxy. The electrode fingers are the name given to

the many pieces of the electrode that are running horizontally in Figure 2.2. The electrode rails are the pieces of electrode running vertically in Figure 2.2. The electrode rails connect the electrode fingers to the electrode pads. As can be seen in Figure 2.2, there are electrode pads on either end of the electrode rails, however these are not shown in Figure 2.1 to increase clarity. It should be noted that in Figure 2.1, W is the width of the actuator across the area with electrode fingers.

Consider a DC voltage source connected to a tmAFC as illustrated in Figure 2.3. Positive charge from the high side of the voltage source rushes down the wire and deposits itself on the electrodes on the left hand side. Positive charge on the electrodes on the right hand side is attracted to the low side of the voltage source and thus a negative charge builds up on the electrodes on the right hand side.

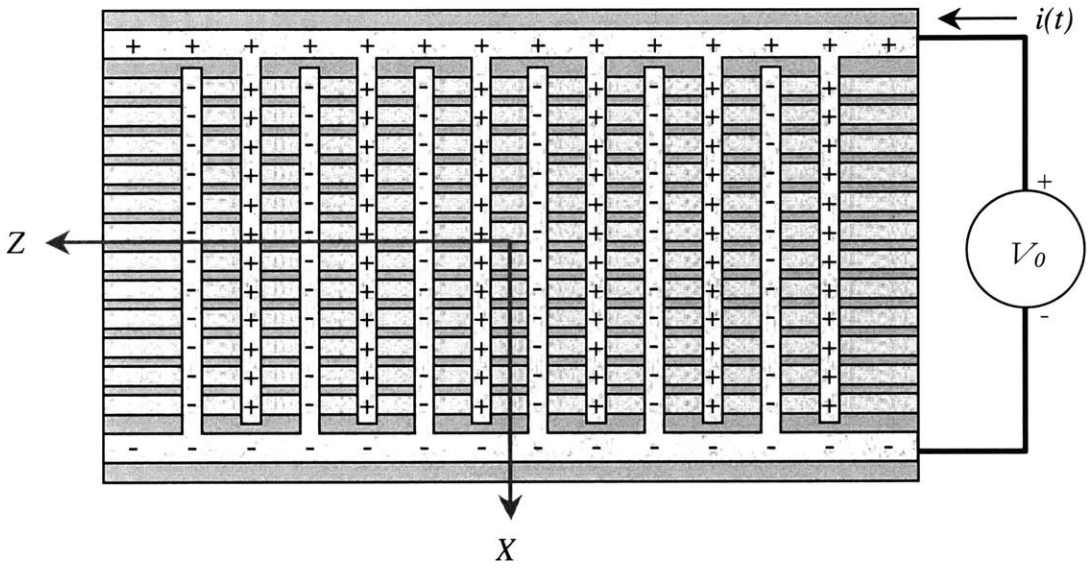

Figure 2.3 Illustration of the Electrode Potential for an Applied Voltage of $V(t)$

In Figure 2.3, an electric field exists in the Z direction in the fibers due to the intedigitated electrode pattern due to the separation of charge. The direction of the electric field is the direction a positive charge would travel, and thus extends from the positive electrode to the negative electrode. The electric field in a tmAFC is illustrated in Figure 2.4.

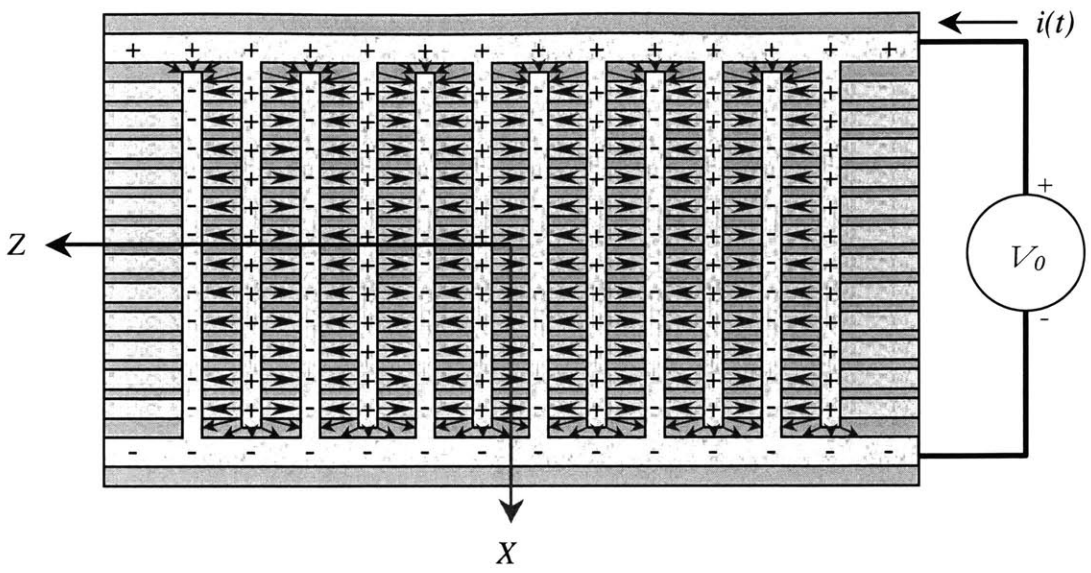

Figure 2.4 Illustration of the Electric Field in a tmAFC

In Figure 2.4, arrows indicate the average direction of the electric field. The electric field exists at $Y = 0$ between the electrodes, however to increase clarity the field is shown to be on the surface of the tmAFC. In the fibers, this electric field alternates in the positive and negative Z direction between the electrode fingers. This electric field is the field that causes actuation in the fibers. Except for poorly manufactured tmAFCs, all fibers will be under the electrodes and thus all fibers will contribute to actuation. Outside of the fibers, fringing of the electric field occurs between the tips of the electrode fingers and the rails. The distance between the tip of the electrode finger and the rail is greater than that between parallel electrode fingers. Thus, the average electric field (voltage / length) is smaller for the fringing field than between the parallel electrodes. The charge on the lower electrode, and some of the axes were removed in Figure 2.4 to increase the clarity of the electric field.

A term that will be used commonly throughout this thesis is the "active area". The active area is the rectangular volume indicated in Figure 2.1 by the dotted line and is indicated with an "A" subscript. The active area is bounded by ends of the electrode fingers in the X direction ($X = \pm W_A / 2$), bounded by the outermost dimension of the electrode fingers in the Y direction ($Y = \pm h_A / 2$), and bounded by the center of the first and last electrode finger in the Z direction ($Z = \pm L_A / 2$). The dimension h_A will best be illustrated in Figure 2.5. The active area surrounds the electric field that causes the fibers to actuate.

Another term that will be used commonly throughout this thesis is the "passive area". The passive area is any volume in the AFC outside of the active area. Within the passive area electric field fringing occurs, however no actuation of the fibers occurs.

Consider a single fiber between two electrodes as shown in Figure 2.5:

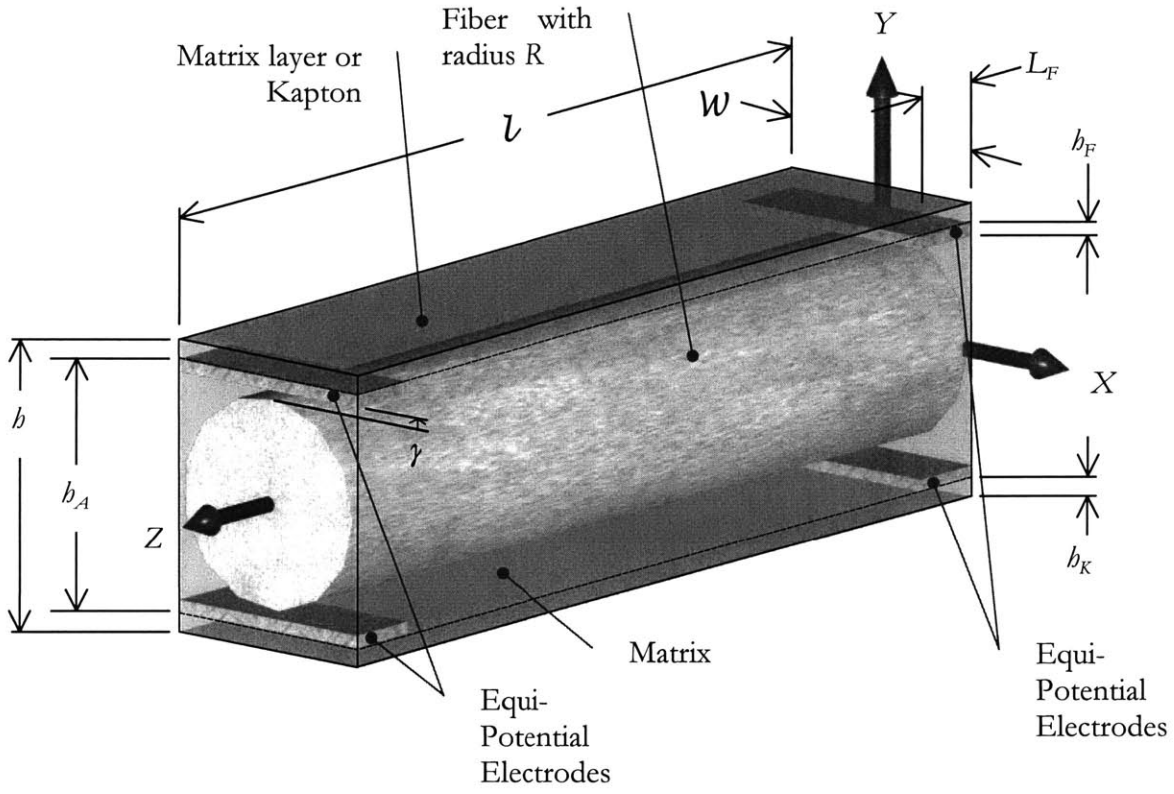

Figure 2.5 Single Fiber in a tmAFC Cross Section

In Figure 2.5, the x-axis is aligned in the direction of the electrode finger, the y-axis is aligned out of plane of the tmAFC, the z-axis is aligned with the direction of the fiber. The F subscripts refer to the electrode finger. L_F is the electrode finger width and l is the spacing between the electrode fingers center to center. The geometry is symmetric in Figure 2.5 about the $x = 0$ plane, the $y = 0$ plane, and the $z = l/2$ plane. The relationship between L_A and l is given by:

$$L_A = l\left(1 - N_{Fingers}\right) \tag{2.1}$$

It should be noted that in Figure 2.5 there exists on the outside of the electrode fingers either a layer with a high dielectric breakdown strength such as Kapton[43] (for an AFC), or a layer of matrix (for a tmAFC) that prevents breakdown of the air when a large voltage is applied to the AFC/tmAFC.

Another important relationship is given by:

$$\gamma = \frac{h_A}{2} - h_F - R \qquad \left(-R \le \gamma \le \frac{h_A}{2} - R\right) \tag{2.2}$$

Where γ is the closest distance between the inside of the electrode finger ($y = h_A - h_F$) and the fiber ($y = R$). γ is positive when h_A / 2– $h_F > R$, that is when the electrode finger does not touch the fiber. γ is zero when the electrode barely touches the fibers. γ is negative when the electrode wraps around the fiber. For a magnetic particle AFC, or a conductive polymer AFC, γ is equal to –R.

The closest distance between the electrodes and the plane $y = 0$ divided by the fiber radius is defined as ξ, were ξ is given by:

$$\xi = \frac{R+\gamma}{R} = 1 + \frac{\gamma}{R} \qquad (\xi \geq 0\%) \tag{2.3}$$

Where ξ is expressed as a percentage greater than or equal to zero. ξ and γ are illustrated for an AFC/tmAFC in the following Figure:

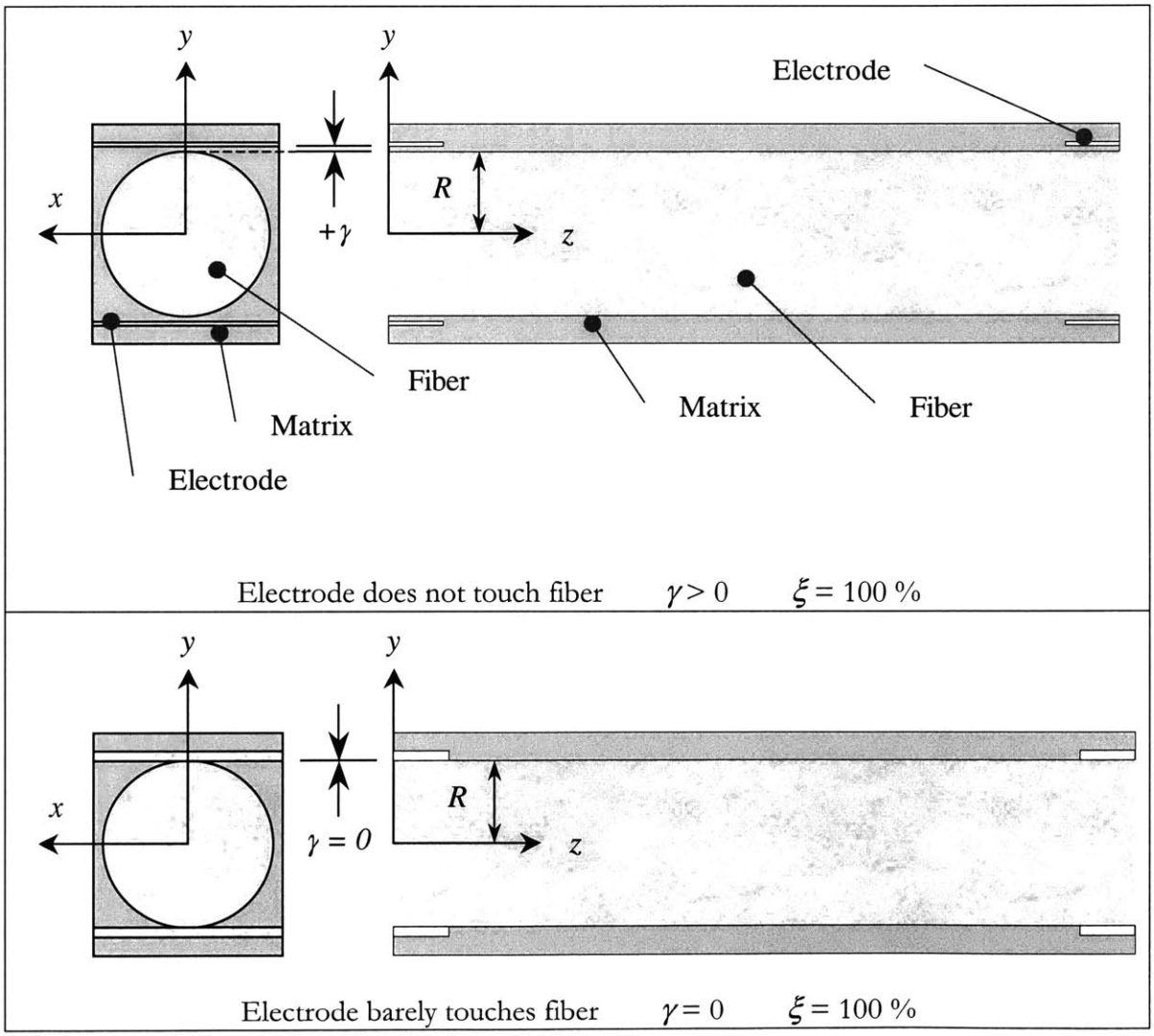

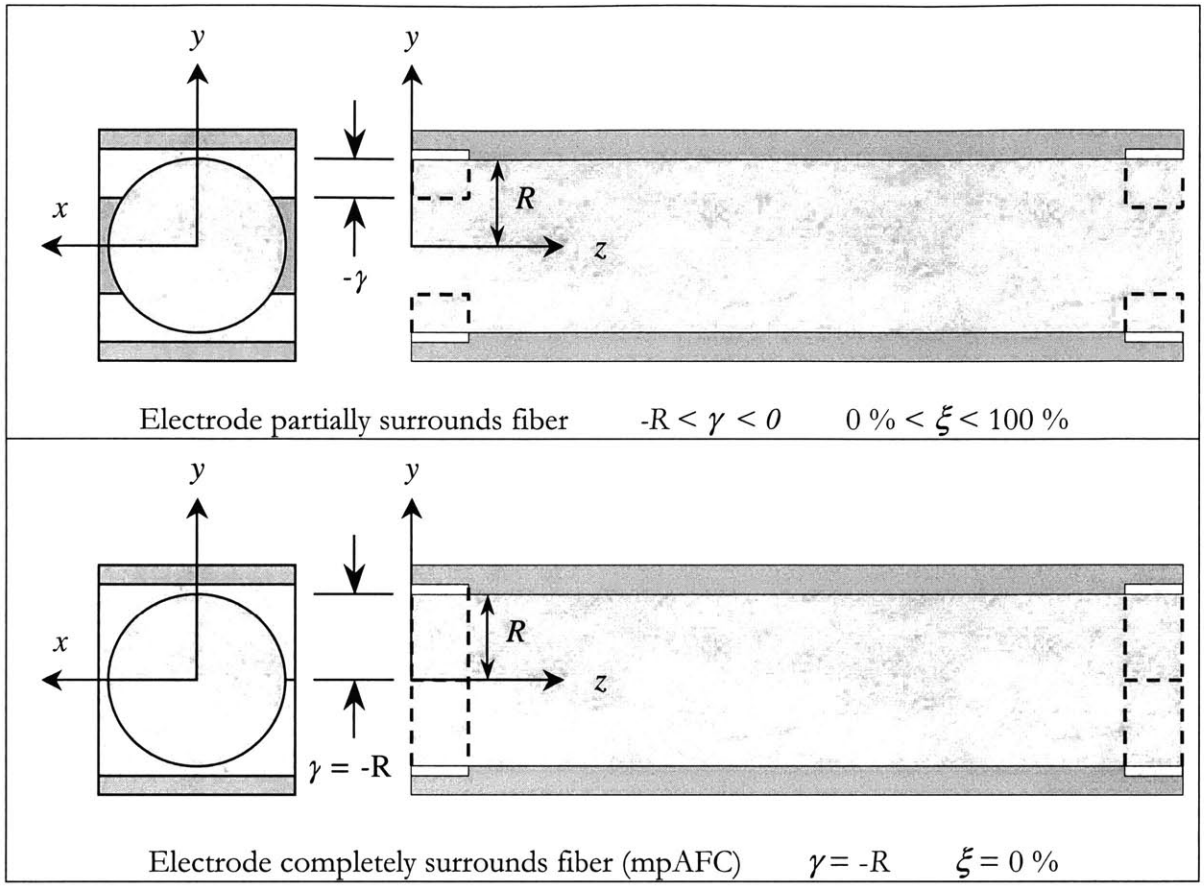

Figure 2.6 Illustration of ξ and γ in an AFC/tmAFC

A term that will be used throughout this thesis is the line fraction of the fibers. The line fraction is defined as:

$$LF = 2\frac{N_{Fibers}\,R}{W_A} \tag{2.4}$$

Where LF is the line fraction and N_{Fibers} is the number of fibers in the active area. If it is assumed that the fibers are evenly spaced apart with spacing W, we can write W as:

$$W = \frac{2R}{LF} \qquad \text{(Even fiber spacing)} \tag{2.5}$$

2.3 Properties of AFC/tmAFC Materials

The relation between dielectric, stiffness, and Poisson's ratio of the matrix material on AFC/tmAFC performance is not clearly understood. In order to determine the effect that the matrix has on the stiffness and the actuation performance of tmAFCs, finite element models of a CP PiezoFlex AFC were constructed and the matrix material properties were varied. Because the composition of the matrix material for the PiezoFlex AFC is proprietary, the material properties for the matrix material had to be determined from testing or estimated. The dielectric, the Young's modulus, and the Poison's ratio had to be

determined before a finite element model could be made of the AFC. First, the average relative dielectric and Young's modulus for a polymer is determined by using a search engine on the internet. Then the known material properties for the PiezoFlex AFC are presented. Finally, the assumed material properties for the PZT-5A fibers for AFCs and tmAFCs are presented.

2.3.1 Average Material Properties for an Engineering Polymer

There is no accepted definition of an engineering polymer. One definition is "a broad term covering all plastics, with or without fillers or reinforcements, which have mechanical, chemical and thermal properties suitable for use, in construction, machine components and chemical processing equipment".[56] Typically, the phrase "engineering polymer" refers to a structural polymer (relatively stiff and/or relatively high tensile strength). Engineering polymers are usually characterized by material properties that are relatively stable with respect to changes in temperature, stress, and applied field. The AFC/tmAFC is to be embedded into a host structure that will be in use in a relatively high load environment and the polymer for the AFC/tmAFC matrix material must survive these load environments. The AFC/tmAFC matrix will be also subjected to unknown temperatures and loads during service. Because of this high load environment with a possibly fluctuating temperature and applied stress, it was assumed that the matrix material for the AFC/tmAFC should be an engineering polymer.

A search was done on the Internet on the website http://www.matweb.com on November 11, 2000 to determine the average relative dielectric for a polymer. On this website there is a search engine that allow the user to search material properties for various types of materials, however the search engine cannot discern between unfilled polymers and polymers filled with particles such as glass or graphite. For polymers with a relative dielectric between 0 and 10 a search was performed in increments of 1. Between a relative dielectric of zero and ten, 3760 polymers were found and above a relative dielectric of ten, 97 polymers were found. Figure 2.7 shows the results from the search.

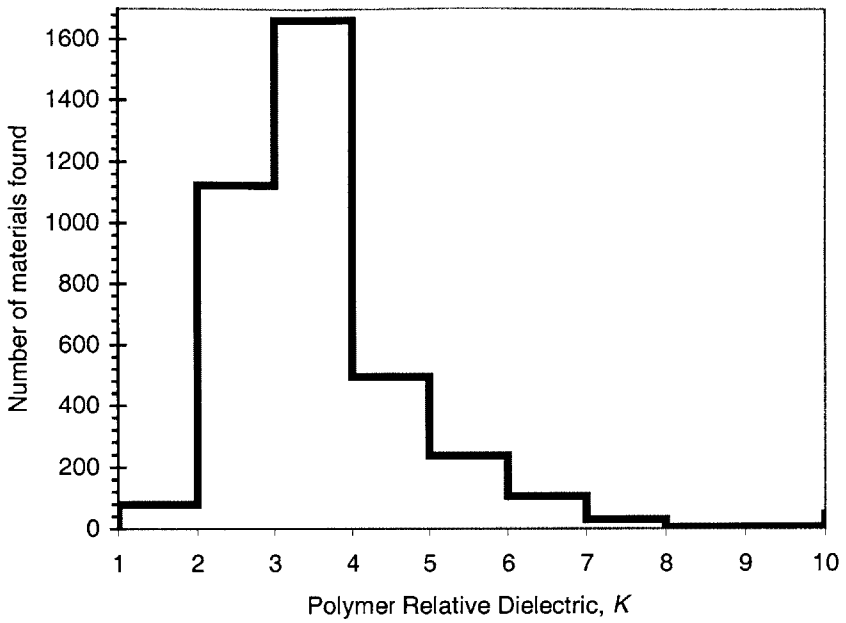

Figure 2.7 Number of Plastics versus Relative Dielectric Found on http://www.matweb.com

It was seen that the majority of the higher dielectric materials we filled with either graphite or glass. From the above plot, assuming that all the material found were unfilled, (which is not true) the average relative dielectric for a polymer is about 3.6 with a variance of $\sigma^2 = 1.2$. The values are assumed to be the average relative dielectric and the variance in the relative dielectric of an engineering polymer.

The Poisson's ratio for an engineering polymer was estimated by averaging the Poisson's ratios for polymers in Reference.[57] This yields an average Poisson's Ratio of 0.35 with an approximate range of 0.3 to 0.4.

Engineering polymers have a Young's modulus in the range of about 1 to 5 GPa. This is the approximate range of the Young's modulus of the unfilled polymers in Reference 57 (page 158). A search was done on the Internet on the website http://www.matweb.com on August 28, 2001 to determine the average Young's modulus for a polymer. As mentioned previously, the search engine cannot discern between unfilled polymers and polymers filled with particles such as glass or graphite. For polymers with a Young's modulus between 0 GPa and 5.4999 GPa a search was performed in increments of 0.5 GPa. Between a Young's modulus of 1 GPa and 5.499 GPa, 4146 polymers were found. Figure 2.8 shows the results of the search.

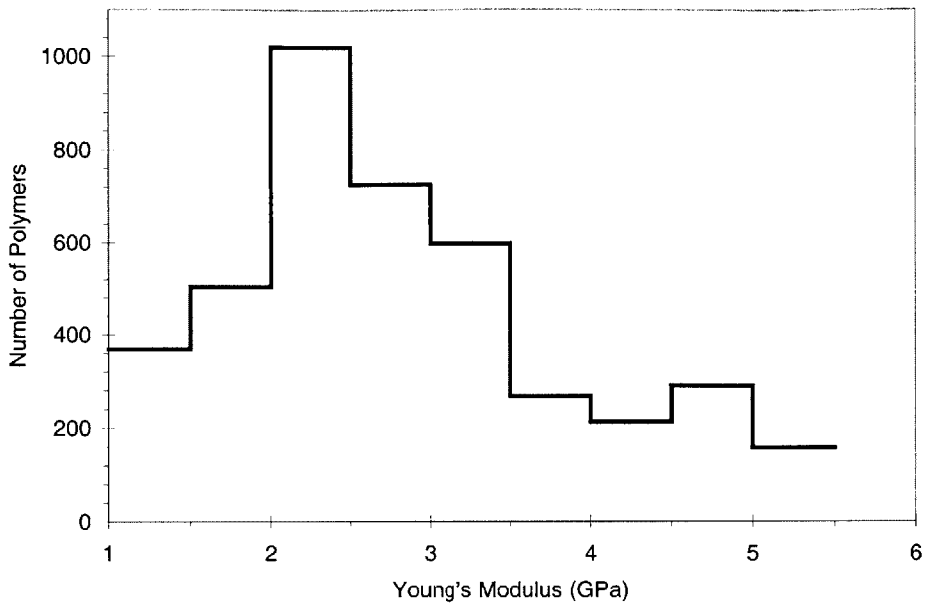

Figure 2.8 Number of Plastics versus Young's Modulus Found on http://www.matweb.com

Assuming that all the materials found were unfilled (which is not true) the average Young's modulus for an engineering polymer is about 2.8 GPa with a variance of $\sigma^2 = 1.1$ GPa^2. The values are assumed to be the average Young's modulus and the variance in the Young's modulus of an engineering polymer. It should be noted that above 5.5 GPa all the materials found appeared to be filled polymers. As the Young's modulus is increased from 0 GPa to 5.5 GPa the percentage of the polymers found that was filled increased. It should be noted that the search engine gave results for the maximum tensile Young's modulus of each material. Thus for example for carbon fiber reinforced polymers, the search engine gave the results for the tensile Young's modulus in the fiber direction.

In Section 3.8, finite element analyses are preformed on a CP PiezoFlex AFC to determine the effect of matrix material properties on AFC performance. To accomplish this, the matrix material properties were varied to numerically determine the partial derivative of the AFC material properties with respect to the matrix material properties. As discussed in Section 2.3.3, the properties of the matrix material of a CP PiezoFlex AFC are very close to the values determined in the above material search for an average engineering polymer. The amount that the matrix material properties are varied are the standard deviations determined for an average engineering polymer, as discussed in Section 2.3.3. Using the data in Section 3.8 allows one to determine the effect of changing matrix material properties on the performance of an AFC. Because the matrix material properties were varied by one standard deviation, the designer of the AFC can be confidant that the changes in AFC material properties represent the bounds on performance for most engineering polymers.

2.3.2 Known PiezoFlex Material Properties

In order to determine the effect that the matrix has on the stiffness and the actuation performance of tmAFCs, the performance CP PiezoFlex AFC was analyzed in Chapter 3. PiezoFlex AFCs have been tested extensively by CP and MIT.[58] As mentioned in Section 1.2, PiezoFlex AFCs have PZT-5A fibers embedded in a thermoset matrix. On either side of the fibers is a layer of Kapton 100 HN[43] to prevent dielectric breakdown of the air during actuation. On the interior side of the Kapton, a silver electrode pattern is screen-printed. Table 1.4 and Table 2.2 summarize the known material properties for PiezoFlex AFCs.

Table 2.2 Known PiezoFlex Material Properties

Material Property	Value	Test Method	Source
Kapton type 100 HN nominal thickness, h_K	25.4 μm (1 mil)	ASTM D-374-94	DuPont bulletin GS-96-7 (Reference 59)
Kapton type 100 HN minimum thickness	21.6 μm (0.85 mil)	ASTM D-374-94	DuPont bulletin GS-96-7
Kapton type 100 HN maximum thickness	29.2 μm (1.15 mil)	ASTM D-374-94	DuPont bulletin GS-96-7
Kapton type 100 HN film Young's modulus, E_K	2.5 GPa	ASTM D-882-91	DuPont (8/95) 231302B datasheet (Reference 60)
Kapton type 100 HN film Poisson's ratio, ν_K	0.34		Average of three samples elongated at 5%, 7%, 10%, DuPont (8/95) 231302B datasheet
Kapton type 100 HN film relative dielectric constant, K_K	3.4	ASTM D-150-92 at 1 kHz.	DuPont (8/95) 231302B datasheet
Kapton type 100 HN film density, ρ_K	1420	ASTM D-1505-90	DuPont (8/95) 231302B datasheet
Fiber diameter, 2 R	270 μm (10.6 mil)		Reference 44
PiezoFlex thickness, h	343 μm (13.5 mil)		Reference 58 page 42
Number of fibers for AFC test coupon in Reference 58, N_{Fibers}	30		Reference 58 page 50
Active width for AFC test coupon in Reference 58, W_A	8.64 mm (340 mil)		Reference [61]
Fiber line fraction, LF	93.8 %		Equation 2.4
Active length (finger center to finger center) for AFC test coupon in Reference 58, L_A	9.94 cm (3.915")		Reference 61
Active width (finger tip to finger tip) for AFC test coupon in Reference 58, W_A	8.64 mm (0.340")		Reference 61

Finger width for AFC test coupon in Reference 58, L_F	191 μm (7.5 mil)		Reference 61
Finger spacing (finger center to finger center) for AFC test coupon in Reference 58, l	1.14 mm (45 mil)		Reference 61
Number of fingers for AFC test coupon in Reference 58, $N_{Fingers}$	88		Reference 61
AFC width for AFC test coupon in Reference 58, W	13.2 mm (520 mil)		Reference 58 page 50
Open circuit chord modulus in the fiber direction of the active area 100 με to 500 με	39.3 GPa	ASTM D-3039	Reference 58 page 71

It should be noted that some discrepancies exist between Table 1.4 and Table 2.2. The data in Table 1.4 was listed in Reference 42 and is an average of the many types of PiezoFlex actuators. The material properties for AFCs in Table 2.2 were taken from actuators measured in Reference 58 and will be used for comparison purposes. . It should also be noted that much scatter existed in the data for the unlaminated open circuit chord modulus for PiezoFlex AFCs due to the fact that the tensile specimens were not straight prior to loading. Less scatter existed in the data when the AFCs were laminated with e-glass and then tested.[62] The additional stiffness of the e-glass was subtracted off using the Rule of Mixtures,[63] which is presented in Appendix III. Thus, this is not a direct measurement of the material stiffness and therefore has some uncertainty associated with it.

2.3.3 Assumed PiezoFlex AFC Matrix Material Properties

PiezoFlex AFCs are manufactured using a dry film resin matrix material (Reference 58 page 38). The matrix material trade name and matrix material properties of PiezoFlex AFCs are proprietary information of Continuum Photonics. Previously,[34] AFCs were manufactured using a thermoset epoxy, EPON resin 9405/ EPI-CURE curing agent 9470 epoxy manufactured by Shell Chemicals,[64] which will henceforth be referred to as the "Shell epoxy". Table 2.3 summarizes the material properties of EPON resin 9405/ EPI-CURE curing agent 9470 epoxy.

Table 2.3 Material Properties of EPON Resin 9405/ EPI-CURE Curing Agent 9470 Epoxy

Material Property	Value	Test Method and Notes
Tensile Young's Modulus	2.8 GPa	Reference [65]: Cured at 212 °F for 1 hour and then 4 hours at 250 °F, 37% mix ratio
Ultimate Failure Strain	7.5 %	Reference 65: Cured at 212 °F for 1 hour and then 4 hours at 250 °F, 37% mix ratio
Relative Dielectric	4.4	Reference 89 page 101 at 23 °C (73 °F)
Glass Transition Temperature	107 °C (225 °F)	DTA measurement by the author: Cured at 15 min at 170 °F and then 4 hours at 250 °F, 37% mix ratio

It should be noted that in Table 2.3 the test standard for the tensile stiffness and ultimate failure strain were not given. The measurement of the relative dielectric did not conform to any test standard nor was the cure cycle given. The testing standard ASTM E1356-98[66] was used as a guideline to measure the glass transition temperature, however the DTA used did not have controlled cooling and thus the standard could not be followed exactly.

Although the matrix for PiezoFlex AFCs is proprietary, the matrix material properties are approximately the same as the properties for the Shell epoxy.[67] The matrix material properties used for matrix material properties for the analysis of a PiezoFlex AFC in Chapter 3 are given in Table 2.4.

Table 2.4 Assumed PiezoFlex Matrix Material Properties

Material Property	**Value**	**Source**	**Possible Range**	**Source**
Young's modulus, E_M	2.9 GPa	Reference 58 page 51	1.9-3.9 GPa	$E_M \pm \sigma$ using analyses in Section 2.3.1
Poisson's ratio, σ_M	0.35	Section 2.3.1	0.3-0.4	Section 2.3.1
Relative dielectric, K_M	3.6	Section 2.3.1	2.5-4.7	$K_M \pm \sigma$ using analyses in Section 2.3.1
Glass Transition Temperature	107 °C (225 °F)	Table 2.3	-	-

2.3.4 CeraNova PZT-5A Fiber Material Properties

PZT-5A fibers with diameters of 140 and 270 microns (5.5 and 10.6 mil) were purchased from CeraNove for use in the tmAFCs. Five fibers from five different 270 micron fiber batches were selected to determine the variation in the diameter. The fibers came from batches 410-0867, 410-0868, 410-0869, 410-0870, and 410-0872. The average fiber diameter was 270 microns (10.6 mil) with a standard deviation of 3 microns (0.12 mil) and a range of 264 – 274 microns (10.4 – 10.8 mil). The measurement agrees with the approximate range quoted by an employee of CeraNova, that the range in the diameters of the fibers is approximately 255-275 microns (10.0 – 10.8 mil)

The low field material properties of bulk PZT-5A are well known,[28] however due to the difficulty in testing CeraNova fibers due to their small size, not much is known about Cera Nova fibers properties. As an approximation, the material properties of CeraNova PZT-5A fibers are assumed to be the same as bulk PZT-5A. The material properties

presented in Table 2.5 are the low field material properties of the constitutive relations presented in Equations 1.1, 1.4, and 1.5.

Table 2.5 Bulk PZT-5A Material Properties (Assumed Material Properties for CeraNova PZT-5A Fibers)

Material Property	Value	Notes	Reference
Transverse or lateral coupling factor, k_{31}	-0.344	$k_{31} = d_{31} / \sqrt{\varepsilon_{33}^T s_{11}^E}$	68
Longitudinal coupling factor, k_{33}	0.705	$k_{33} = d_{33} / \sqrt{\varepsilon_{33}^T s_{33}^E}$	28, 68
Shear coupling factor, $k_{15} = k_{24}$	0.685	$k_{15} = k_{24} = d_{15} / \sqrt{\varepsilon_{11}^T s_{44}^E}$	28, 68
Planar coupling factor, k_p	-0.60	$k_P = \sqrt{2}\, k_{31} / \sqrt{1-\sigma^P}$	28, 68
Invariant coupling factor with electric field parallel to polar axis, k_{i3}	0.715	$k_{i3} = \sqrt{1 - \frac{\varepsilon_{33}^S}{\varepsilon_{33}^T}}$	68, 69,70,[71]
Invariant coupling factor with electric field perpendicular to polar axis, k_{i1}	0.685	$k_{i1} = k_{15} = k_{24} = \sqrt{1 - \frac{\varepsilon_{11}^S}{\varepsilon_{11}^T}}$	68, 69
$\varepsilon_{11}^T / \varepsilon_0 \left(K_{11}^T\right)$	1730		28, 68
$\varepsilon_{11}^S / \varepsilon_0 \left(K_{11}^S\right)$	916	$K_{11}^S = K_{11}^T \left(1 - k_{15}^2\right)$	28, 68
$\varepsilon_{33}^T / \varepsilon_0 \left(K_{33}^T\right)$	1700		28, 68
$\varepsilon_{33}^S / \varepsilon_0 \left(K_{33}^S\right)$	830		28, 68
s_{11}^E	16.4 pm² / N		28, 68
s_{11}^D	14.4 pm² / N	$s_{11}^D = s_{11}^E \left(1 - k_{31}^2\right)$	28, 68
c_{11}^E	121 GPa		28, 68 page 5
s_{12}^E	-5.74 pm²/N		68
s_{12}^D	-7.71 pm²/N	$s_{12}^D = s_{12}^E - s_{11}^E k_{31}^2$	68
c_{12}^E	75.4 GPa		68 page 5
s_{13}^E	-7.22 pm²/N		68
s_{13}^D	-2.98 pm²/N	$s_{13}^D = s_{13}^E + k_{31} k_{33} \sqrt{s_{11}^E s_{33}^E}$	68

c_{13}^{E}	75.2 GPa		68 page 5
s_{33}^{E}	18.8 pm² / N		28, 68
s_{33}^{D}	9.46 pm² / N	$s_{33}^{D} = s_{33}^{E}\left(1-k_{33}^{2}\right)$	28, 68
c_{33}^{E}	111 GPa		28, 68 page 5
Y_{11}^{E}	61.0 GPa	$Y_{11}^{E} = 1/s_{11}^{E}$	28, 68
Y_{11}^{D}	69.4 GPa	$Y_{11}^{D} = 1/s_{11}^{D} = Y_{11}^{E}/\left(1-k_{31}^{2}\right)$	28, 68
Y_{33}^{E}	53.2 GPa	$Y_{33}^{E} = 1/s_{33}^{E}$	28, 68
Y_{33}^{D}	106 GPa	$Y_{33}^{D} = 1/s_{33}^{D} = Y_{33}^{E}/\left(1-k_{33}^{2}\right)$	28, 68
Shorted 12 and 21 Poisson's Ratio	0.35	$\sigma^{P} = \sigma_{12}^{E} = \sigma_{21}^{E} = -s_{12}^{E}/s_{11}^{E}$	
Shorted 13 and 23 Poisson's Ratio	0.44	$\sigma_{13}^{E} = \sigma_{23}^{E} = -s_{13}^{E}/s_{11}^{E}$	
Shorted 31 and 32 Poisson's Ratio	0.38	$\sigma_{31}^{E} = \sigma_{32}^{E} = -s_{13}^{E}/s_{33}^{E}$	
Open circuit 12 and 21 Poisson's Ratio	0.54	$\sigma_{12}^{D} = \sigma_{21}^{D} = -s_{12}^{D}/s_{11}^{D}$	
Open circuit 13 and 23 Poisson's Ratio	0.21	$\sigma_{13}^{D} = \sigma_{23}^{D} = -s_{13}^{D}/s_{11}^{D}$	
Open circuit 31 and 32 Poisson's Ratio	0.32	$\sigma_{31}^{D} = \sigma_{32}^{D} = -s_{13}^{D}/s_{33}^{D}$	
s_{44}^{E}	47.5 pm2/N	$s_{44}^{E} = 1/c_{44}^{E}$	28, 68
s_{44}^{D}	25.5 pm2/N	$s_{44}^{D} = s_{44}^{E}\left(1-k_{15}^{2}\right)$	68
c_{44}^{E}	21.1 GPa	$c_{44}^{E} = 1/s_{44}^{E}$	28, 68 page 5
s_{66}^{E}	44.3 pm2/N	$s_{66}^{E} = 1/c_{66}^{E} = 2\left(s_{11}^{E} - s_{12}^{E}\right)$	28, 68
c_{66}^{E}	22.6 GPa	$c_{66}^{E} = 1/s_{66}^{E} = 1/\left(2\left(s_{11}^{E} - s_{12}^{E}\right)\right)$	28. 68 page 5
d_{31}	-171 pC / N	$d_{31} = e_{31}\left(s_{11}^{E} + s_{12}^{E}\right) + e_{33}\, s_{13}^{E}$	28, 68
e_{31}	-5.4 C/m²	$e_{31} = d_{31}\left(c_{11}^{E} + c_{12}^{E}\right) + d_{33}\, s_{13}^{E}$	28, 68
d_{33}	374 pC / N	$d_{33} = 2\, e_{31}\, s_{13}^{E} + e_{33}\, s_{33}^{E}$	28, 68
e_{33}	15.8 C/m²	$e_{33} = 2\, d_{31}\, c_{13}^{E} + d_{33}\, c_{33}^{E}$	28, 68

d_{15}	584 pC / N	$d_{15} = e_{15}\, s_{44}^{E}$	28, 68
e_{15}	12.3 C/m^2	$e_{15} = d_{15}\, c_{44}^{E}$	28, 68
g_{33}	0.00248 m^2 / C	$g_{33} = d_{33} / \varepsilon_{33}^{T}$	68
g_{33}	0.00249 m^2 / C	$g_{33} = d_{33} / \varepsilon_{33}^{T}$	28
Density, ρ	7750 kg/m^3		28, 68 page 5
Static tensile strength	75.8 MPa (11,000 psi)		28, 68 page 7
Compression strength	517 MPa (75,000 psi)		68 page 7
Polarization field	2.0 kV/mm – 3.9 kV/mm (50 V/mil - 100 V/mil)	Material Type 5A4E Industry Type 5A, Navy Type II	72
Polarization field	1.6 kV/mm (40 V/mil)	Morgan Electro Ceramics[73]	74
Polarization temperature	130-140 °C (266-284 °F)	Morgan Electro Ceramics	74
Depolarization field	-0.5 kV/mm	Material Type 5A4E Industry Type 5A, Navy Type II	72
Compressive depolarization stress	30~50 MPa (4400~ 7300 psi)		75
Maximum rated compressive stress 25 °C (77 °F)	14~21 MPa (2000~ 3000 psi)		68 page 7
Maximum rated compressive stress 100 °C (212 °F)	21 MPa (3000 psi)		68 page 7
Curie temperature	365 °C (689 °F)		28, 68 page 2
Volume conductivity at 25 °C (77 °F)	< 10 pS / m		68 page 6
Volume conductivity at 100 °C (212 °F)	10 pS / m		68 page 6
Volume conductivity 200 °C (392 °F)	100 pS / m		68 page 6
Polarization	380 C / cm^2		28, 68 page 7
Coercive Field	1.2 kV/mm		68 page 7

	(30 V/mil)		
AC depoling field at 25 °C (77 °F)	~0.7 kV/mm rms (18 V/mil rms)		28, 68 page 7

It should be noted that:

1. The allowed material property range for Navy type II materials such as PZT-5A can be large, as shown in Table 1.1. In addition, the material properties in Table 2.5 are dependant on the degree of poling. If the fibers are not fully poled then the material properties will differ than those given in Table 2.5.[76]

2. For all the above elastic constants, Reference 28 and Reference 68 agree, except in two instances. In Reference 68 k_{31} is listed to three decimal places where Reference 28 lists k_{31} to two decimal places. In Reference 68 and Reference 28 g_{33} is different by a small amount, 10 m^2 / MC.

3. Due to the difficulty in measuring the force in a zero strain condition, most likely, the $\underline{e}$ data was calculated from the $\underline{d}$ and $\underline{\varepsilon}$ data, and small measurement errors in the $\underline{d}$ and $\underline{\varepsilon}$ data can cause large errors in the $\underline{e}$ data.

4. The open circuit 12 and 21 Poisson's ratio is greater than ½, however this does violate the constraint that the sum of the work done by all the stress components must be positive to avoid creation of energy during loading (Reference 63 pages 37-45).

$$2\sigma_{21}\sigma_{32}\sigma_{13} \le 1-\sigma_{12}\sigma_{21}-\sigma_{13}\sigma_{31}-\sigma_{23}\sigma_{32} \le 1 \qquad (2.6)$$

Where in Equation 2.6, either the open circuit Poisson's ratio is used for all terms, or the short circuited Poisson's ratio is used for all terms.

5. In the reference given for the static tensile strength, (Reference 68), the static tensile strength was obtained from bending tests on thin bimorph structures. However, no details were presented boundary conditions (shorted or open circuit) for the test articles.

6. The coupling coefficient (or coupling factor) are "nondimensional coefficients which are useful for the description of a particular stress and electric field configuration for

conversion of stored energy to mechanical or electric work." (Reference 23 pages 38-39) Consider a piezoelectric material that is free to deform with no charge applied to it. An electrical source (such as a battery) is connected to the piezoelectric material resulting in a stress free mechanical deformation. The coupling factor, k, for static or quasistatic conditions in Reference 23 is usually defined by its squared, k^2, as:

$$k^2 = \frac{\text{Work delivered to the mechanical load}}{\text{Work delivered to the mechanical load + Energy unavailable to the mechanical load}} \quad (2.7)$$

This is the case of an actuator where electrical energy is supplied to the actuator in order to generate mechanical energy. The electrical energy supplied to the piezoelectric material is given by the denominator of Equation 2.7.

If mechanical energy is supplied to a piezoelectric material, under the right conditions an electric field is generated, and the coupling factor, k, for static or quasistatic conditions is defined as:

$$k^2 = \frac{\text{Work done on the electrical load}}{\text{Work done on the electrical load + Energy unavailable to the electric load}} \quad (2.8)$$

This is the case of a transducer where mechanical energy is supplied to the piezoelectric material in order to generate electrical energy. The mechanical energy supplied to the piezoelectric material is given by the denominator of Equation 2.8. In both cases (Equations 2.7 and 2.8) k^2 is equal. Thus, k^2 is a measure of the efficiency of the electromechanical conversion of the piezoelectric material. If the material is not piezoelectric then k^2 is zero. If the material is piezoelectric then k^2 must be less than one due to conservation of energy. Further information on the coupling coefficient and its meaning can be found in References [77] and [78].

7. In Table 2.5, two coupling factors exist which are not defined in Reference 23, k_{i1} and k_{i3}. These are the invariant piezoelectric coupling factor. "For a given electric field there is a certain condition of elastic stress which will lead to the highest piezoelectric coupling factor. These coupling factors may be termed invariant or eigen coupling factors."[79] The original derivation for the invariant coupling factors is found in Reference [80]. For each crystallographic orientation there are 3 invariant coupling factors. (Reference 79).

For a Hexagonal Crystal – Class 6 mm poled ferroelectric with the polarization direction in the *3* direction, the first invariant coupling factor requires one to apply $E_1 = E_2 = 0, E_3 \neq 0$, yielding the invariant coupling factor k_{i3}

$$k_{i3} = \sqrt{1 - \frac{\varepsilon_{33}^S}{\varepsilon_{33}^T}} \tag{2.9}$$

In order to achieve the coupling factor in Equation 2.9, the following stresses must be applied:[81]

$$\begin{gathered} T_1 = T_2 = \frac{d_{33}\, s_{13}^E - d_{31}\, s_{33}^E}{2 d_{31}\, s_{33}^E - d_{33}\left(s_{11}^E + s_{12}^E\right)} T_3 \\ T_3 \neq 0 \\ T_4 = T_5 = T_6 = 0 \end{gathered} \tag{2.10}$$

The second coupling factor requires one to apply $E_2 = E_3 = 0, E_1 \neq 0$, yielding the invariant coupling factor k_{i1}:

$$k_{i1} = \sqrt{1 - \frac{\varepsilon_{11}^S}{\varepsilon_{11}^T}} = \frac{d_{15}}{\sqrt{\varepsilon_{11}^T\, s_{44}^E}} \tag{2.11}$$

Where in order to achieve the coupling factor in Equation 2.11, the following stresses must be applied:

$$\begin{gathered} T_1 = T_2 = T_3 = T_4 = T_6 = 0 \\ T_5 \neq 0 \end{gathered} \tag{2.12}$$

The third coupling factor is for $E_1 = E_3 = 0, E_2 \neq 0$, however it equals k_{i1} except with $T_1 = T_2 = T_3 = T_5 = T_6 = 0, T_4 \neq 0$.

In order to avoid the positive creation of energy, it can be shown (Reference 81) that two of the nine requirements for the piezoelectric constitutive relations for a Hexagonal Crystal – Class 6 mm poled ferroelectric with the polarization direction in the *3* direction are that k_{i3}^2 and k_{i1}^2 are thermodynamically constrained to be less than 1:

$$k_{i3}^2 < 1 \tag{2.13}$$

$$k_{i1}^2 < 1 \tag{2.14}$$

Because the invariant coupling factor are the maximum coupling factors for a given electric field, all other coupling factors squared must be less than 1, and the absolute value of the coupling coefficients must be less than absolute value of the invariant coupling factors.

8. Material coefficients can be expressed as complex coefficients to account for losses in the piezoelectric materials:[24,83,82]

$$\begin{aligned} s^E &= \left(s^E\right)^R - j\left(s^E\right)^I \\ d &= d^R - j\,d^I \\ \varepsilon^T &= \left(\varepsilon^T\right)^R - j\left(\varepsilon^T\right)^I \end{aligned} \tag{2.15}$$

Where the R superscript represent the real terms, the I superscript represents the imaginary terms, and j is the square root of –1. It can be shown that by requiring the power dissipation to be positive:[83]

$$\left(s_{11}^E\right)^I, \left(s_{33}^E\right)^I, \left(s_{44}^E\right)^I, \left(s_{66}^E\right)^I, \left(\varepsilon_{11}^T\right)^I, \left(\varepsilon_{33}^T\right)^I \geq 0 \tag{2.16}$$

$$\left(s_{11}^E\right)^I \geq \left|\left(s_{12}^E\right)^I\right| \tag{2.17}$$

$$\left(s_{11}^E\right)^I \left(s_{33}^E\right)^I \geq \left(\left(s_{13}^E\right)^I\right)^2 \tag{2.18}$$

$$\left(s_{11}^E\right)^I \left(\varepsilon_{33}^T\right)^I \geq \left(\left(d_{31}\right)^I\right)^2 \tag{2.19}$$

$$\left(s_{33}^E\right)^I \left(\varepsilon_{33}^T\right)^I \geq \left(\left(d_{33}\right)^I\right)^2 \tag{2.20}$$

$$\left(s_{44}^E\right)^I \left(\varepsilon_{11}^T\right)^I \geq \left(\left(d_{15}\right)^I\right)^2 \tag{2.21}$$

$$\left(s_{33}^E\right)^I \left(\left(s_{11}^E\right)^I + \left(s_{12}^E\right)^I\right) \geq 2\left(\left(s_{13}^E\right)^I\right)^2 \tag{2.22}$$

9. In many common PZT piezoceramics (Navy type I, II, III, V and VI) the following approximate relations hold:[84]

$$\begin{aligned} k_{33} &\cong 2.0\,k_{31} \\ d_{33} &\cong 2.22\,d_{31} \\ s_{33}^E &\cong 1.05\,s_{31}^E \end{aligned} \tag{2.23}$$

The values for PZT-5A were mostly taken from data measured by MorganElectro Ceramics. In order to determine if this material data differed greatly from other

manufactures, some of the data in Table 2.5 was compared to data from three other manufactures.

Table 2.6 Comparison of *33* values of Navy type II Materials between Manufactures

Manufacturer	**Material Name**	k_{33}	d_{33} (pm/V)	K_{33}^{T}	Y_{33}^{E} (GPa)	Y_{33}^{D} (GPa)	**Reference**
Sensor Technology Limited	BM500	0.72	365	1750	53	110*	[85]
Staveley NDT Technologies	EBL#2	0.72	380	1725	55*	114*	[86]
Piezo Systems, Inc	5A4E	0.72	390	1800	52	108*	[87]
Average		0.72	377	1740	53	110	
MorganElectro Ceramics	PZT-5A	0.705	374	1700	53.2	106	28, 68
Percent Difference		2.1%	1.1%	3.3%	0.2%	4.2%	

* Denotes calculated from k_{33} and other data

As can be seen in Table 2.6, the MorganElectro Ceramics PZT-5A material data differs form the average data of the other manufactures by a small amount. The percent difference was calculated by subtracting the PZT-5A data from the average data and dividing it by the average data. Therefore, the PZT-5A data in Table 2.5 from Reference 28 and 68 is assumed to be correct. Other data which is taken from a single source and is difficult to measure, such as the compressive depolarization stress, and the author has much less confidence in its value.

3. tmAFC Analysis

3.1 Introduction

The relationship between the material properties of the materials in an AFC/tmAFC, the geometry, and the response of due to stimulus of the AFC/tmAFC is poorly understood. This is due primarily to the fact that the poling direction of the AFC/tmAFC follows a curvilinear path, which cannot be determined using analytical methods, and the combination of the rectangular geometry and the cylindrical fiber makes electrical analysis difficult. Some back of the envelope calculations exist to determine AFC performance (Reference 34 pages 79-106) however they make assumptions that ignore the length of the electrode compared to distance between the electrode fingers, and yield AFC stiffness that are incompatible with the Rule of Mixtures for composites.[63] In order to determine the effect of the matrix material properties on the tmAFC, the relationship between material properties, geometry, and the response of an AFC/tmAFC is revisited.

First, the requirements for optimally performing distributed actuators are presented. The electric field and electric potential in an interdigitated block is presented next to help illustrate the electric field and potential in an AFC/tmAFC. Then the electric field and potential in an AFC/tmAFC is discussed. Approximate relationships between material properties, geometry, and the response of an AFC is derived next. A finite element analysis of representative volume elements is presented next showing the effect of the matrix material properties on the AFC. An AFC was chosen to be analyzed instead of a tmAFC because as will be discussed in Chapter 4, various thicknesses of polymer were used for manufacturing, and thus there did not exist a uniform geometry that could be analyzed for a tmAFC. It should be noted that although the analysis was performed on an AFC, the results determined for an AFC remain true for a tmAFC. This is because many tmAFC have a similar geometry and similar matrix properties to PiezoFlex AFCs.

3.2 Desirable Attributes for a Distributed Actuator

Given the diversity of active material applications listed in Section 1.1, it is desirable to define the "best" properties for a longitudinal actuator. In order to determine the best properties that a longitudinal actuator can have, consider two distributed actuators of length L_A bonded to the root of a thin passive isotropic cantilevered beam, as shown in Figure 3.1.

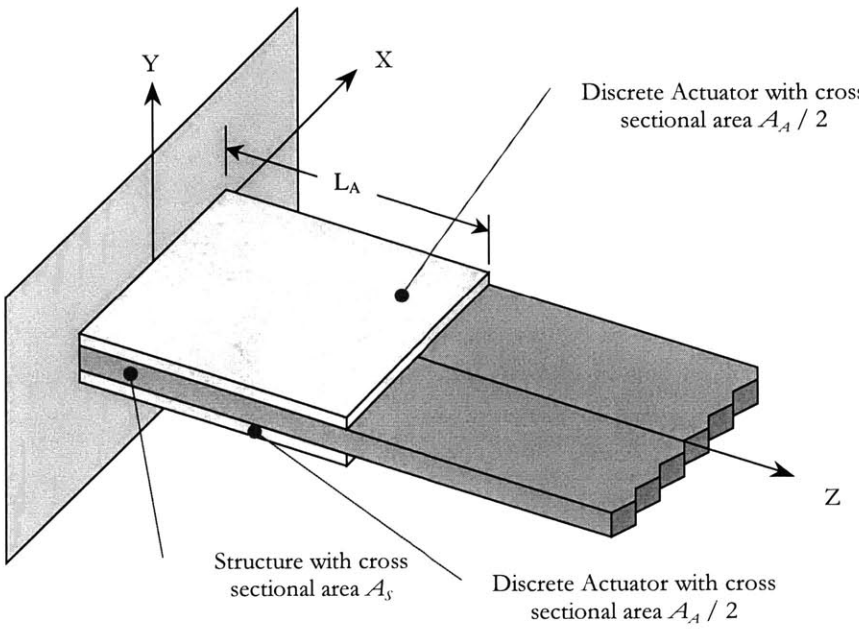

Figure 3.1 Distributed Actuator Bonded to the Root of a Cantilevered Beam

Let us assume that the actuators are of the same material and are poled and actuated in the Z direction. The actuators are actuated in such a way that the structure is actuated quasi-statically in extension and not in bending. Let us also assume that the two discrete longitudinal actuators have constitutive relations given by Equation 1.2 where the "*3*" subscript is replaced with "*Z*". The structure is comprised of a passive orthotropic material with a constitutive relationship given by:

$$\begin{Bmatrix} S_{XX} \\ S_{YY} \\ S_{ZZ} \end{Bmatrix} = \begin{bmatrix} s_{XX} & s_{XY} & s_{XZ} \\ s_{XY} & s_{YY} & s_{YZ} \\ s_{XZ} & s_{YZ} & s_{ZZ} \end{bmatrix} \begin{Bmatrix} T_{XX} \\ T_{YY} \\ T_{ZZ} \end{Bmatrix} \tag{3.1}$$

If the thickness and width of the beam and the actuators is small compared to the length of the beam and the actuators, then the stress in the XX and YY directions can be assumed to be zero:

$$T_{XX} = T_{YY} = 0 \tag{3.2}$$

We can also make the assumption that because the structure is so thin that the strain and the stress in the ZZ direction beneath the actuators is independent of X and Y and the ZZ strain in the actuators are the same. Using Equations 1.2, 3.1, and 3.2, and assuming that the electric field in the X and Y directions in zero, the strain in the ZZ direction is given by:

$$S_{ZZ} = s_{ZZ}\left(T_{ZZ}\right)_S = s^E_{ZZ}\left(T_{ZZ}\right)_A + d_{ZZ}\,E_Z \tag{3.3}$$

Where the S subscript and the A subscript refer to the structure and the actuator respectively. If the structure is cut in the X-Y plane, the total force in the Z direction must be zero:

$$\begin{gathered}\sum F_Z = 0 \\ A_S\left(T_{ZZ}\right)_S + A_A\left(T_{ZZ}\right)_A = 0\end{gathered} \tag{3.4}$$

Where F_Z is the force in the Z direction. Solving Equation 3.3 for the stress and substituting it into Equation 3.4 and the solving for the strain yields:

$$S_{ZZ} = \frac{A_A\, s_{ZZ}\, d_{ZZ}}{A_S\, s^E_{ZZ} + A_A\, s_{ZZ}} E_Z = \frac{d_{ZZ}}{1 + \dfrac{A_S\, s^E_{ZZ}}{A_A\, s_{ZZ}}} E_Z \tag{3.5}$$

Equation 3.5 can be rewritten using the Young's modulus of the materials instead of the compliance, where the Young's modulus of the two materials is given by.

$$Y_{ZZ} = \frac{1}{s_{ZZ}} \qquad Y^E_{ZZ} = \frac{1}{s^E_{ZZ}} \tag{3.6}$$

Where Y is the Young's modulus. Substituting in the definitions in Equation 3.6 into Equation 3.5:

$$S_{ZZ} = \frac{d_{ZZ}}{1 + \dfrac{A_S\, Y_{ZZ}}{A_A\, Y^E_{ZZ}}} E_Z = \frac{d_{ZZ}}{1 + \Xi} E_Z \tag{3.7}$$

Where Ξ is the ratio of the extensional stiffness of the structure to the extensional stiffness of the actuator:

$$\Xi = \frac{A_S\, Y_{ZZ}}{A_A\, Y^E_{33}} \tag{3.8}$$

Where Ξ is a positive number greater than zero. The function $1 / (1 + \Xi)$ is maximized at Ξ equals zero, and monotonically decreases as Ξ becomes larger. $1 / (1 + \Xi)$ can be thought of as the reduction in the actuation of the actuator due to the stiffness of the structure. Let us consider two cases. First, let us consider the limiting case where Ξ is very small, but d_{ZZ} and E_Z is finite. This is the case where the extensional stiffness of the actuator, $A_A\, Y^E_{ZZ}$, is infinitely greater than the extensional stiffness of the structure, $A_S\, Y_{ZZ}$. Therefore, Equation 3.7 can be written as:

$$\lim_{\Xi \to 0} S_{ZZ} = d_{ZZ} E_Z \tag{3.9}$$

This is the solution for an actuator operating under stress free conditions.

Let us consider the opposite limiting case, where Ξ is infinite but both d_{ZZ} and E_Z are finite. This second case occurs when the extensional stiffness of the structure is infinitely greater than the extensional stiffness of the actuator. Therefore, Equation 3.7 can be written as:

$$\lim_{\Xi \to \infty} S_{ZZ} = 0 \tag{3.10}$$

If d_{ZZ} and E_Z are finite, however Ξ is infinite, no amount of force that the actuator applies to the structure will deform the structure.

Let us consider an actuator that has a stiffness in the Z direction that is much greater than that in the stiffness in the off diagonal terms. Let us also assume that when actuated in a stress free condition the actuation in the Z direction is much greater than the actuation in the other two directions. For this case, as will be shown in Equation 3.50, $e_{33} \cong Y^E_{33} d_{33}$. Equation 3.7 can then be written as:

$$S_{ZZ} = \frac{d_{ZZ} A_A Y^E_{ZZ}}{A_A Y^E_{ZZ} + A_S Y_{ZZ}} E_Z \cong \frac{e_{ZZ} A_A}{A_A Y^E_{ZZ} + A_S Y_{ZZ}} E_Z \tag{3.11}$$

If the case arises such that the extensional stiffness of the structure is infinitely greater than the extensional stiffness of the actuator then Equation 3.11 can be written as:

$$\lim_{A_A Y^E_{ZZ} \to 0} S_{ZZ} \cong \frac{A_A e_{ZZ}}{A_S Y_{ZZ}} E_3 \tag{3.12}$$

In this case, to maximize the strain in the ZZ direction and actuation should be chosen such that e_{ZZ} is maximized.

It should be noted that in Equation 3.7 the actuator is assumed to be a piezoelectric actuator. The previous derivation holds true for any active material with a strain linearly proportional to a field variable, assuming one substitutes the appropriate material properties into Equation 3.7.

From the above cases we can see that if one wanted to maximize the tip displacement of the structure it would be desirable to have a large Y^E_{ZZ}, and large stress free actuation ($d_{ZZ} E_Z$). In the second case, one could either maximize d_{ZZ} or use an actuator with a smaller d_{ZZ} but with a larger allowable electric field. Depending on the application, if one wanted to maximize the tip displacement per unit volt it would be desirable to have an actuator with a large shorted Young's modulus, and a large d_{ZZ}. Applications could exist where it is desirable to maximize the strain in one direction, thus the desirable figure of merit is d_{ZZ} / d_{ZZ}. It may be the case the force that it is desired the force actuator applies to the structure is maximized. In this case the figure of merit is e_{ZZ}. Above, only the 1-

dimenstional case was considered. If the 2-dimensional case of an actuator bonded to a plate was considered, Equation 3.5 will be complicated with off axis stiffness and piezoelectric terms due to the fact that S_Z and S_X must be equal in both the plate and the actuator. Given that numerous applications exist for actuators it is hard to define what set of material property are should be the figure of merit to determine the "best" material property.

In general, it can be said that for many situations where it is desired for the actuation strain to be maximized, the "best" actuator to use should have a large shorted Young's modulus and have a large d and e constants, and a large allowable electric field, however the trade off between the three is dependent on the application.

The conclusions reached for a piezoelectric material bonded to a beam also hold true for an AFC or a tmAFC. The constitutive relations for an AFC/tmAFC are given in Appendix I. If the shorted extensional stiffness of the AFC/tmAFC, Y_{ZZ}^{V}, is greater than the extensional stiffness of the structure, the figure of merit to maximize is the amount of stress free strain, Γ_{ZZ}, the actuator can deliver (Equation B.62). If the extensional stiffness of the AFC/tmAFC is less than the extensional stiffness of the structure, the figure of merit to maximize is the amount of stress the actuator can deliver in a strain free condition, Ψ_{ZZ} (Equation B.65). For all cases, it is desirable to maximize the voltage that can be applied to the actuator.

For AFCs and tmAFCs the figures of merit that will be analyzed are the shorted stiffness, Y_{ZZ}^{V}, the amount of stress free strain, Γ_{ZZ}, the actuator can deliver, the amount of stress the actuator can deliver in a strain free condition, Ψ_{ZZ}, and the maximum matrix electric field.

3.3 Analysis of an Interdigitated Block

Due to its geometry, piezoelectric coupling, and anisotropic material properties, analysis of an AFC/tmAFC is very difficult to do using closed form solutions. Analysis of the interdigitated block, as shown in Figure 1.5, is much easier to do and can provide some insight to the behavior of an AFC/tmAFC. First, the electric field and electric potential for an isotropic non-piezoelectric interdigitated block is analyzed. Then the effect of a low dielectric material between the electrode and the high dielectric block is analyzed.

3.3.1 The Electric Field and Electric Potential of an Interdigitated Block

The average electric field due to an applied voltage in an AFC/tmAFC is illustrated as being straight Figure 2.4. In actuality, between the two electrode finger pairs, the electric field curves, however this curvature is difficult to illustrate for a tmAFC. To get a feeling of

the path of the electric field in a tmAFC consider an interdigitated block as shown in Figure 1.5. Assume that the block is comprised of a perfectly insulating material that is not necessarily piezoelectric. If the block is very long with many electrode fingers in Z direction, and very wide in the X direction, then the electric field in the center of the block can be modeled as a 2-d field in the Y and Z directions, as shown in the callout of Figure 1.5.

Consider a block comprised of a non-pizoelectric, isotropic dielectric material with infinite resistivity and perfectly conducting electrodes. If a voltage is applied across the electrodes in a manner shown in Figure 1.5, then the electrical response of the block can be analyzed using electrostatic finite elements as shown in Figure 3.2.

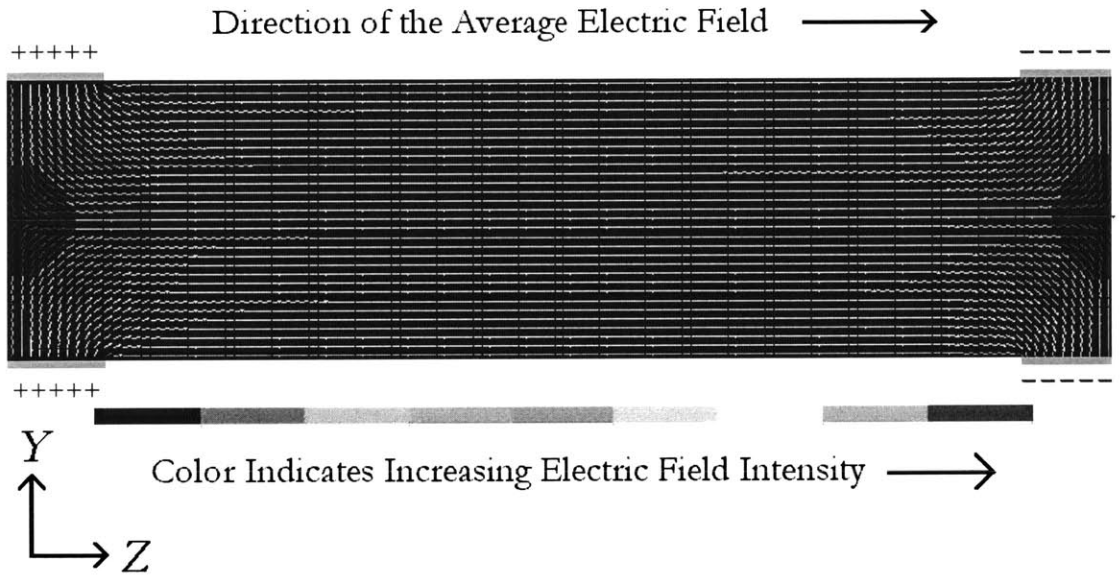

Figure 3.2 Illustration of the Electric Field of an Interdigitated Block

In Figure 3.2, the block has a height to length ratio of 23:90 and an electrode length to height ratio of 15:46. These are the same ratios for a single fiber in the active area of a PiezoFlex AFC as listed in Table 2.2. In Figure 3.2, the outer surfaces in the Y direction of the block were assumed charge free, except at the electrodes. The electric displacement across a surface of discontinuity is given by:

$$\hat{n} \bullet \left(\underline{D}_2 - \underline{D}_1 \right) = \sigma_f \tag{3.13}$$

Where $\underline{D}$ is the electric displacement vector, σ_f is the free change per unit area on the surface of discontinuity, and the *1* and *2* refer to side *1* and side *2* of the discontinuity respectively. $\hat{n}$ is the unit normal vector of the surface pointing from side *1* to side *2*. Because it is assumed that no fringing fields exist outside the block, ($\underline{D}_2$ = 0) and the outer surface are charge free (σ_f = 0) the electric displacement perpendicular to the Y surfaces equals zero.

For an isotropic dielectric material, the relationship between the electric displacement, and the electric field vector, $\underline{E}$, is given by:

$$\begin{aligned} \underline{D} &= \underline{\underline{\varepsilon}}\,\underline{E} \\ \underline{D} &= K\,\varepsilon_0\,\underline{\underline{I}}\,\underline{E} \end{aligned} \tag{3.14}$$

Where $\underline{\underline{\varepsilon}}$ is the permittivity matrix, K is the relative dielectric, and $\underline{\underline{I}}$ is the identity matrix. Because it was assumed that the Y surfaces are charge free, the electric displacement, and therefore the electric field, is perpendicular to the Y surfaces as illustrated in Figure 3.2.

When a voltage is applied to the block, free charge builds up on the electrodes supplying an electric field to the interior of the block. The electric field vector is given by:

$$\underline{E} = -\nabla\varphi \tag{3.15}$$

Where φ is the electric potential within the body. The electric field vector is in the direction that a theoretical positive charge would move in. The electric potential must equal the applied voltage at the electrodes. The electric potential is plotted for the interdigitated block as shown in Figure 3.3.

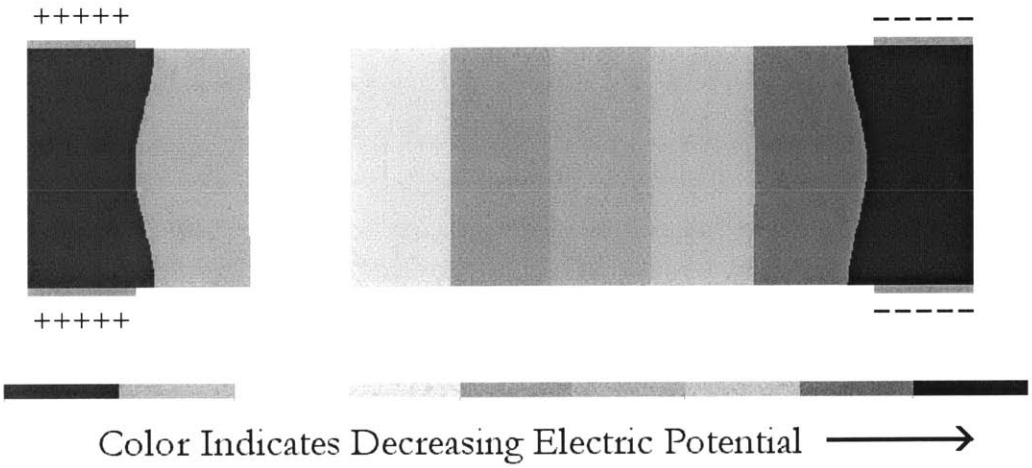

Figure 3.3 Electric Potential of an Interdigitated Block

As can be seen in Figure 3.3, under the electrodes the potential is nearly constant. Between the electrodes the electric potential is linear in the Z direction, and therefore the electric field is constant in the Z direction. This is due to the geometry of the interdigitated block and the electrodes which is the same as an AFC. The geometry of an AFC is chosen in Reference 34 to maintain a straight electric field in the Z direction between the electrodes while maintaining acceptable field levels beneath the electrodes. Because free charge exists on the electrodes, the electric displacement, and hence the electric field, is perpendicular to the electrodes due to Equation 3.13, as is illustrated in Figure 3.2. At the electrodes:

$$\hat{n} \bullet \underline{D} = \sigma_f \tag{3.16}$$

Where $\hat{n}$ is the unit vector normal to the electrodes pointing into the block.

If one follows an electric field line in the block, the electric field line starts out perpendicular to the positive electrode (in the Y direction), curves toward the Z direction beneath the electrode, becomes nearly constant between the electrodes, curves back in the Y direction and is perpendicular to the negative electrode. The electric field is highest at the edge of the electrode. This is because at corners of electrodes, the free charge per unit area is infinite and thus the electric field is infinite in an isotropic dielectric material. This is analogous to an infinitely sharp crack or a point force causing an infinite stress in a structural member. An electrode that is infinity thin or has an infinity sharp corner can cause the electric field to be infinite, however in reality neither case can truly exist. An infinite free charge per unit are is not the same as saying that the charge is infinite, if the free charge per unit area is integrated over the entire electrode it is found that the charge is finite.

The infinite electric field causes a problem when analyzing the interdigitated block using the finite element method, because as more elements are added to a uniform mesh the electric field becomes larger and larger, but only in the elements at the corner of the electrode. Because the elements becomes smaller and smaller, the capacitance approaches a finite value. Thus, the capacitance and not the electric field should not be used for a convergence criteria.

3.3.2 Effect of ξ on an Interdigitated Block

Analysis of an AFC/tmAFC to determine the effect of the distance that the electrode is from a fiber is presented in Section 3.7. Analysis of an interdigitated block can provide some insight to the effect that ξ has on the internal electric field of an AFC/tmAFC.

Consider the interdigitated block and the callout shown in Figure 1.5. Using the perfectly conducting electrodes, we wish to deliver as large as possible electric field in the z direction to a layer of high dielectric material with zero conductivity. Assume that the interdigitated block is infinitely wide in the x direction. For this section, let us assume that on the outer surfaces of the high dielectric material there is a thin layer of polymer with zero conductivity.

The electrodes of the interdigitated block are E_L long, with the spacing between electrodes being ℓ long. The thickness of the high dielectric material is $2\ R$ and the total interdigitated block h_A thick. If the block is very long with many electrode fingers in Z direction, and very wide in the X direction, then the electric field in the center of the block can be modeled as a 2-d rectangle in the Y and Z directions, as shown in the following Figure:

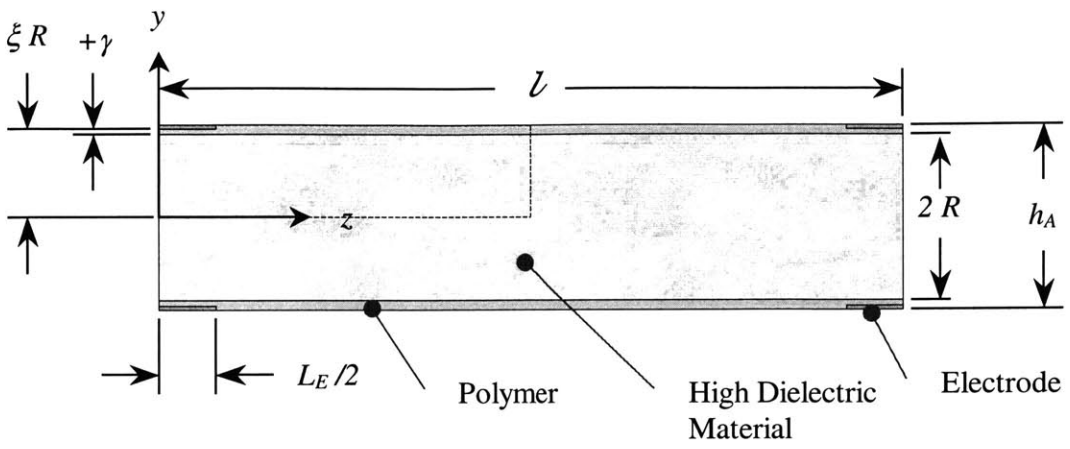

Figure 3.4 Geometry of an Interdigitated Rectangle with a Polymer Layer on the Outside

The interdigitated rectangle shown in Figure 3.4 is a single representative volume of the interdigitated block shown in Figure 1.5, and therefore there exists an infinite number of interdigitated rectangles extending in either direction of z, in Figure 3.4. γ is defined as the distance from the outer surface of the high dielectric material to the inner surface of the electrode. As with the AFC/tmAFC defined in Section 2.2, γ can be positive or negative as will be discussed below. The interdigitated rectangle shown in Figure 3.4 is the same a single fiber in the tmAFC shown in Figure 2.5 if the round fiber in the tmAFC is replaced with a rectangular fiber w wide, and the layers of polymer above and below the electrode fingers are removed. Therefore, the same symbols used for the tmAFC fiber in Figure 2.5 are the same symbols used in Figure 3.4. The interdigitated block and rectangle is symmetric with respect to geometry and materials about the x-z plane. The interdigitated rectangle is also symmetric with respect to geometry and materials about and the x-y plane at $z = l/2$.

We will consider four cases for the electrodes of the rectangle, as shown in Figure 3.5. First is case where a gap filled with polymer exists between the electrode and the high dielectric material. This is the case where the gap spacing, γ, is positive. The second case is where γ is equal to zero. For this case the electrodes touches the high dielectric material. This is the case where γ is equal to zero. In the case where γ is negative, some of the high dielectric material is removed so that the electrodes extend into the high dielectric material. The fourth case is where γ is equal to $-R$. For this case all the material beneath the electrodes are removed and the electrodes completely cover the ends of the polymer and the high dielectric material. Because the interdigitated rectangle shown in Figure 3.4 is similar to the single fiber in the tmAFC shown in Figure 2.5, Equation 2.3 can be used for both the interdigitated rectangle and the single fiber.

$$\xi = \frac{R+\gamma}{R} = 1+\frac{\gamma}{R} \qquad (\xi \geq 0\%) \tag{3.17}$$

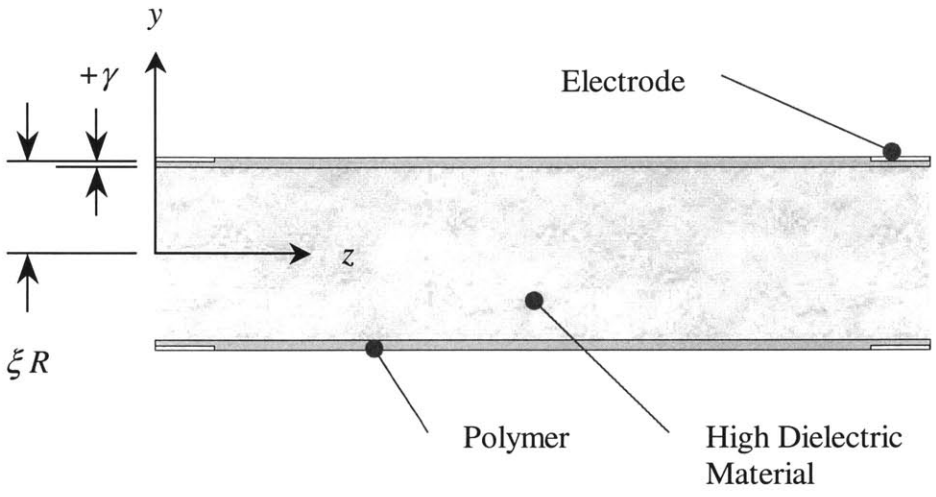

Electrode does not touch high dielectric material, $\gamma > 0$, $\xi > 100\%$

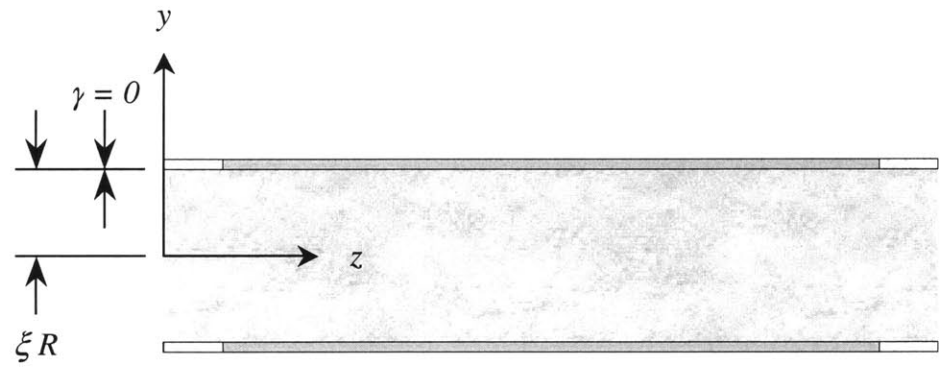

Electrode barely touches high dielectric material, $\gamma = 0$, $\xi = 100\%$

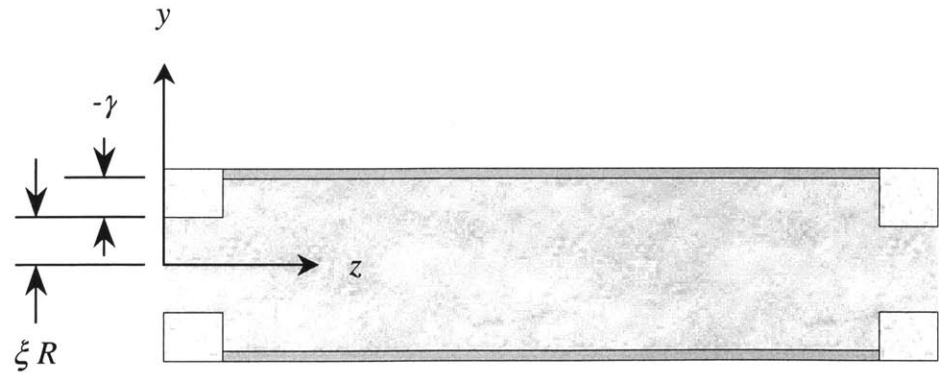

Electrodes pushed into high dielectric material, $\gamma < 0$, $\xi < 100\%$

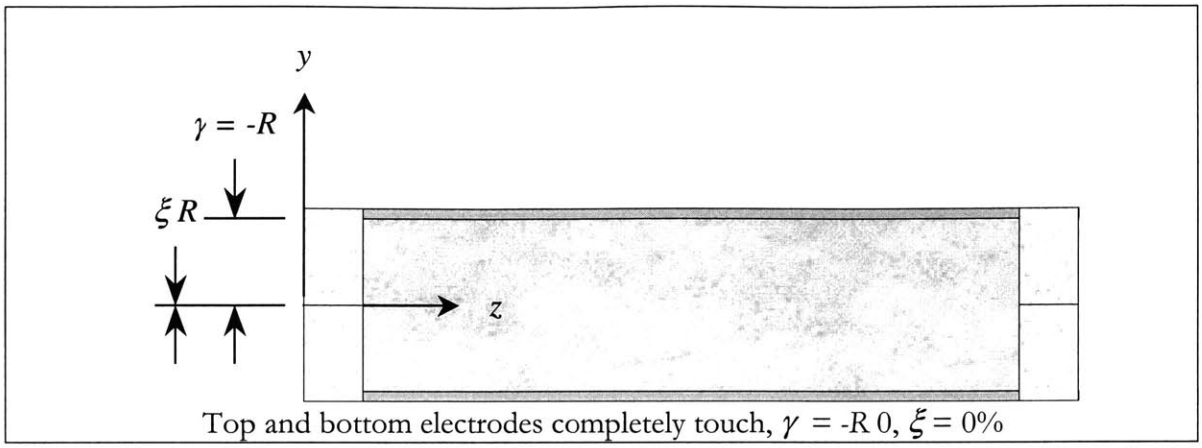

Figure 3.5 Illustration of ξ and γ in an Interdigitated Rectangle

It is assumed that in all four cases the electrodes are flush with the outside of polymer. Assume that the initially the interdigitated rectangle is completely charge free. A total DC voltage drop of 2 V_0 is then applied to the rectangle, as shown in Figure 3.6.

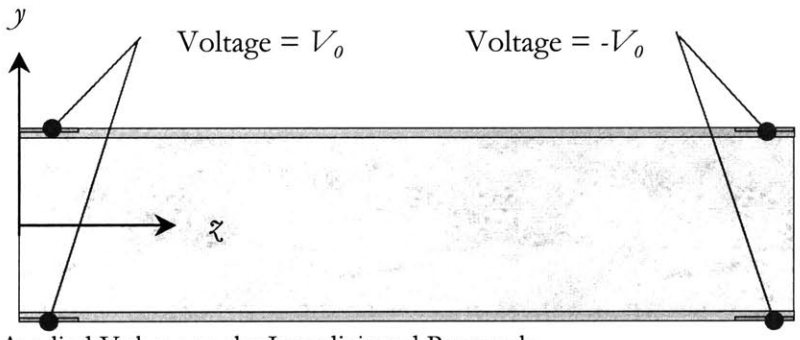

Figure 3.6 Applied Voltage to the Interdigitated Rectangle

Because interdigitated rectangle is infinitely wide in the x direction, it is assumed that no electric fields exist in the x direction and thus the electric potential is independent of x. Due to geometric and material symmetry and the values of the applied voltage, across the x-z plane the electric potential is symmetric, and therefore the electric field at y =0 is only in the z direction. About the x-y plane at z = l/ 2, the electric potential is antisymmetric. Therefore the electric potential is zero at z = l/ 2 and the electric field at this location is only in the z direction. If there is no fringing of the electric fields and the surfaces are assumed to be charge free, the electric displacement is perpendicular to the outer edges in the polymer at $y = \pm h_A / 2$. Because there are infinite rectangles extending in either direction of z, then the electric field in z direction is zero at the outer surfaces (z = 0, l/ 2). As discussed in Section 3.3.1, the electric displacement is perpendicular to the electrodes. Due to symmetry, one can solve the electric potential in a "¼th model" of the interdigitated

rectangle shown in Figure 3.4 and apply the solution to the entire rectangle. A ¼th model of the interdigitated rectangle is shown in the following Figure:

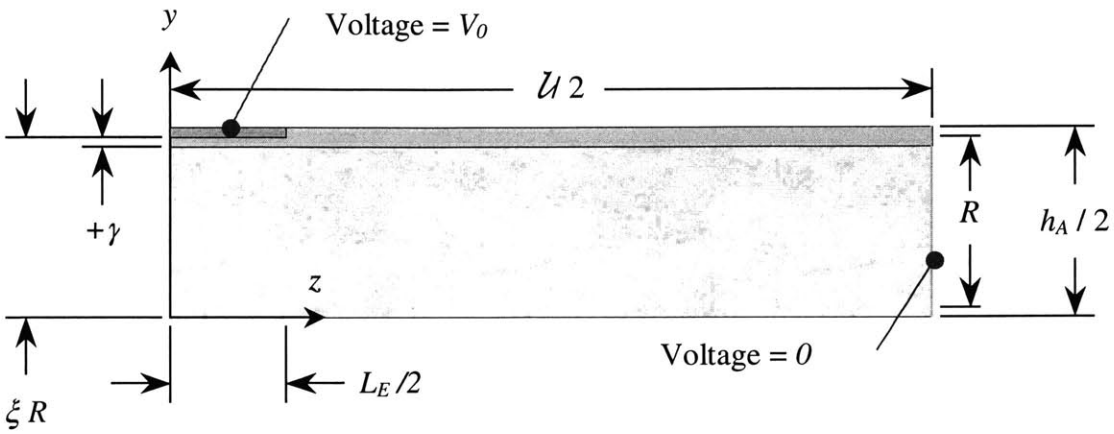

Figure 3.7 ¼th Model of Interdigitated Rectangle

The ¼th model of the interdigitated rectangle is the portion of the interdigitated rectangle shown in Figure 3.4 surrounded by the dotted line. In the ¼th model, a voltage equal to zero is applied across $z = \mathcal{U}/2$. It should be noted that the capacitance of the rectangle shown in Figure 3.4 is the same as the ¼th model.

Using Equation 3.13, we can determine the electric displacement in the y direction at the interface between the polymer and the high dielectric material ($y = \pm R$):

$$\hat{j} \bullet \left[\underline{D}_P \left(y = \pm R, z \right) - \underline{D}_D \left(y = \pm R, z \right) \right] = \sigma_f \left(y = \pm R, z \right) \tag{3.18}$$

Where $\underline{D}_P$ is the electric displacement in the polymer, $\underline{D}_D$ is the electric displacement in the high dielectric material, and $\sigma_f(y = 0, z)$ is the free charge at the interface. If the interdigitated rectangle initially was charge free, and both the polymer and the high dielectric material have zero conductivity then free charge cannot migrate through the rectangle, and thus σ_f must be zero. Therefore, Equation 3.18 can be written as:

$$\underline{D}_P \bullet \hat{j} = \underline{D}_D \bullet \hat{j} \qquad y = \pm R \tag{3.19}$$

Let us assume, that polymer and the high dielectric material is non-piezoelectric and is electrically isotropic. Therefore, using Equation 3.14, Equation 3.19 can be written as:

$$K_P \left(E_P \right)_y = K_D \left(E_D \right)_y \qquad y = \pm R \tag{3.20}$$

Where E is the electric field and the y subscript indicates that the electric field in the y direction. It should be noted that throughout the following discussion it is assumed that $K_P < K_D$. Solving for the electric field in the high dielectric material:

$$(E_D)_y = \frac{K_P}{K_D}(E_P)_y \qquad y = \pm R \tag{3.21}$$

Thus, if the dielectric of the high dielectric material is much greater than that of the polymer, then the electric field in the y direction in the high dielectric material is much less than that of the polymer at the interface. Equation 3.21 will have important consequences for the interdigitated rectangle and AFCs/tmAFCs.

Using the finite element program ANSYS[88], the electric potential of the ¼th model can be solved for. The model was solved for using the geometrical properties given in Table 3.1, which are the same properties for the PiezoFlex AFC in Table 2.2.

Table 3.1 Interdigitated Rectangle Geometrical Parameters Used for the FEM Model

Parameter	Value	Reference
ℓ	1.143 mm (45 mil)	Table 2.2
L_F	191 μm (7.5 mil)	Table 2.2
b_A	292 μm (11.5 mil)	Table 2.2
γ	Variable	
R	135 μm (5.3 mil)	Table 2.2

The distance between the electrode and the fiber was varied to determine the effect of the matrix gap, γ, on the electric potential of the interdigitated rectangle. The relative permittivity for the two materials was chosen to be:

Table 3.2 Interdigitated Rectangle Geometrical Parameters Used for the FEM Model

Parameter	Value	Reference
K_P	3.6	Average K for a polymer (Section 2.3.1)
K_D	1700	K_{33}^T for PZT-5A (Table 2.5)

It should be noted the K chosen for the high dielectric material was that of K_{33}^T for PZT-5A. However, K_{31}^T could have been chosen, (K_{31}^T=1730), making only a small difference in the solution of the electric potential.

The electric potential was solved for using 2-d eight node PLANE121 electrostatic elements with voltage degrees of freedom. 22,496 elements were using in rectangular mesh for a total number of nodes 68,233. This large number of nodes was used to guarantee convergence of the charge per unit width at the $x = \ell/2$ end to within 2 decimal places, the convergence criteria, as shown in Figure 3.8.

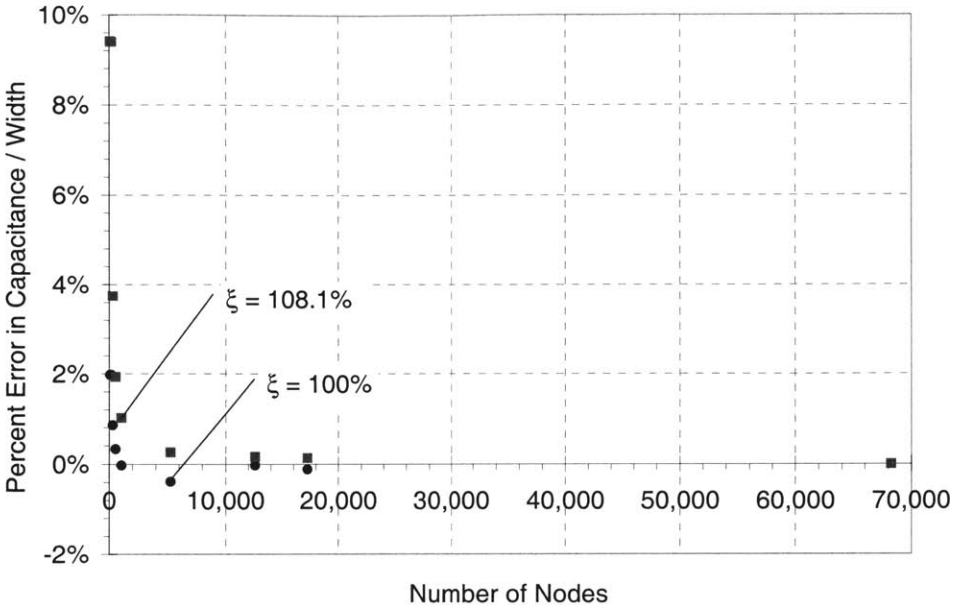

Figure 3.8 Convergence of Capacitance of FEM for the Interdigitated Rectangle

In Figure 3.8 the percent error in the capacitance per unit width is determined from:

$$\text{Percent Error in C/W} = \frac{\text{C/W}\left(n \text{ Nodes}\right)\text{-C/W}\left(68,233 \text{ Nodes}\right)}{\text{C/W}\left(68,233 \text{ Nodes}\right)} \tag{3.22}$$

When 68,233 nodes are used to analyze the interdigitated rectangle, the C/W for $\xi = 100\%$ and 108.1% is 269 and 3,746 pF respectively. A picture of the mesh has not been included in this work because the mesh does not print well due to the small size of the elements.

The electric potential inside the ¼th model is shown in Figure 3.9.

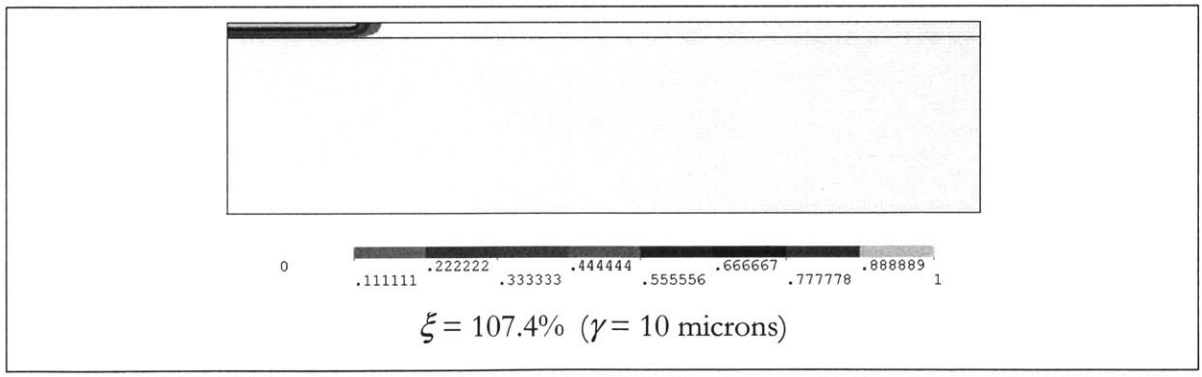

$\xi = 107.4\%$ ($\gamma = 10$ microns)

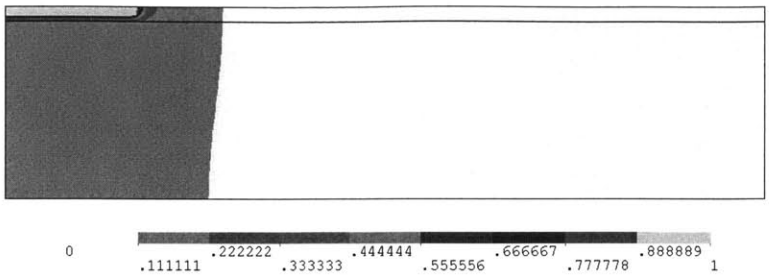

ξ = 103.7% (γ = 5 microns)

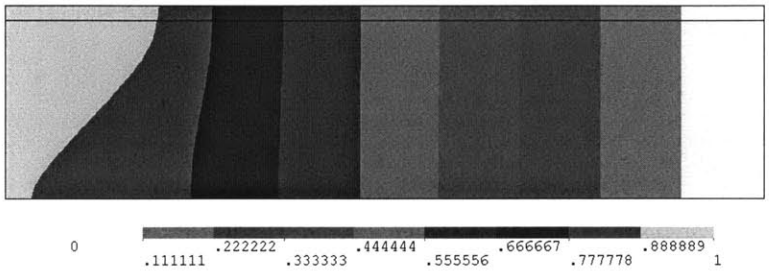

ξ = 100% (γ = 0 microns)

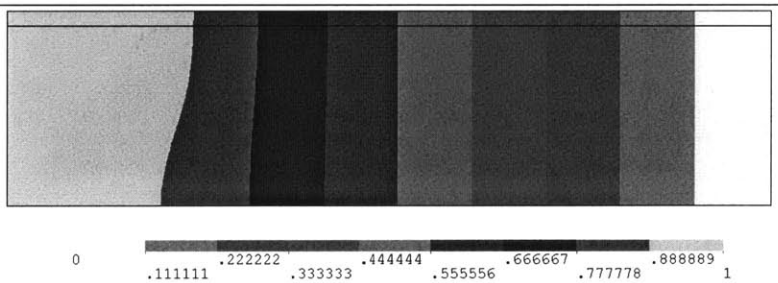

ξ = 66.7% (γ = -45 microns)

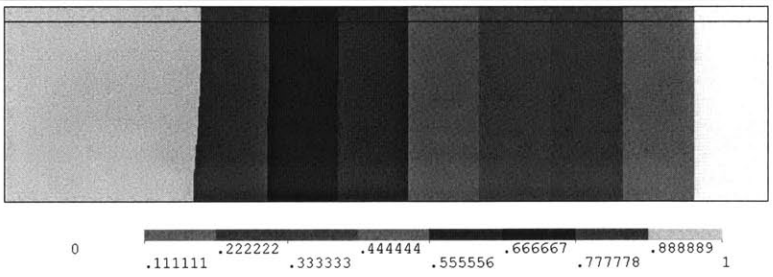

ξ = 33.3% (γ = -90 microns)

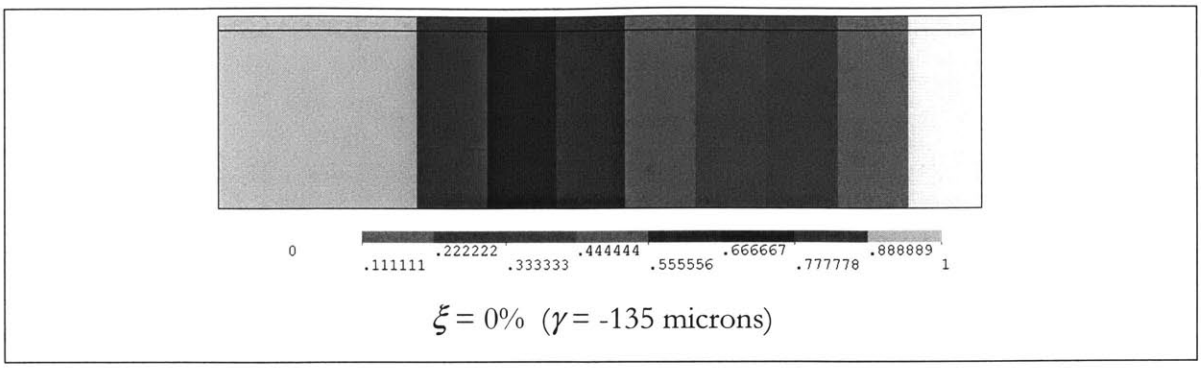

Figure 3.9 Electric Potential Inside an Interdigitated Rectangle with Various Electrode Spacings

As can be seen in Figure 3.9, the electric field (Equation 3.15) in the z direction in the high dielectric material increases as ξ decreases. When ξ >100%, the electrode is not touching the high dielectric material. The closest distance between the electrode surface and the interface between the polymer and the high dielectric material will be henceforth referred to as the "polymer gap". It should be noted that the polymer gap only exists for ξ > 100 %. Due to Equation 3.21, the electric field in the polymer gap is very large, causing a large potential drop in the polymer gap. If one follows a field line from the electrode, though the polymer gap, into the high dielectric material, and into the $z = L/2$ end, the total potential drop across the polymer gap and the high dielectric material must be equal to V_0. If the potential drop in the polymer gap is very high, the potential drop for the high dielectric material is drastically reduced. Due to the small voltage drop in the high dielectric material, and because of the large size of L compared to polymer gap, the electric field is in the high dielectric material will be very small. As the electrode comes closer to the high dielectric material, the potential drop in the polymer gap becomes less and thus there is a greater potential drop across the high dielectric material, and therefore the electric field in the high dielectric material increases. When the electrode touches the high dielectric material, ξ = 100%, and all the electric field lines at the electrode surface in the polymer tend to stay in polymer all the electric field lines at the electrode surface in the high dielectric material tend to stay in the high dielectric material. Now the entire potential drop occurs in both the polymer and high dielectric material, and thus a large electric field is delivered to the high dielectric material. As ξ decreases below 100% the electric potential close to the electrode tends to straighten out in the z direction due to the presence of the electrode. At the $z = L/2$ end, the electric field is linear with z. When ξ equals $-R$ the average electric field in the z direction in the high dielectric material is maximized due to the fact that the electric potential is linear with z between the electrode $z = L/2$, and there is no electric field in the y direction. It should be noted that once the electrode touches the high dielectric material the average electric field in the z direction in the high dielectric material is almost equal for all

cases where the is no polymer gap. When there is a polymer gap then the electric field in the high dielectric material is very small, and decreases as ξ increases. This is seen in the plot of capacitance per unit width for the ¼th model when plotted against ξ.

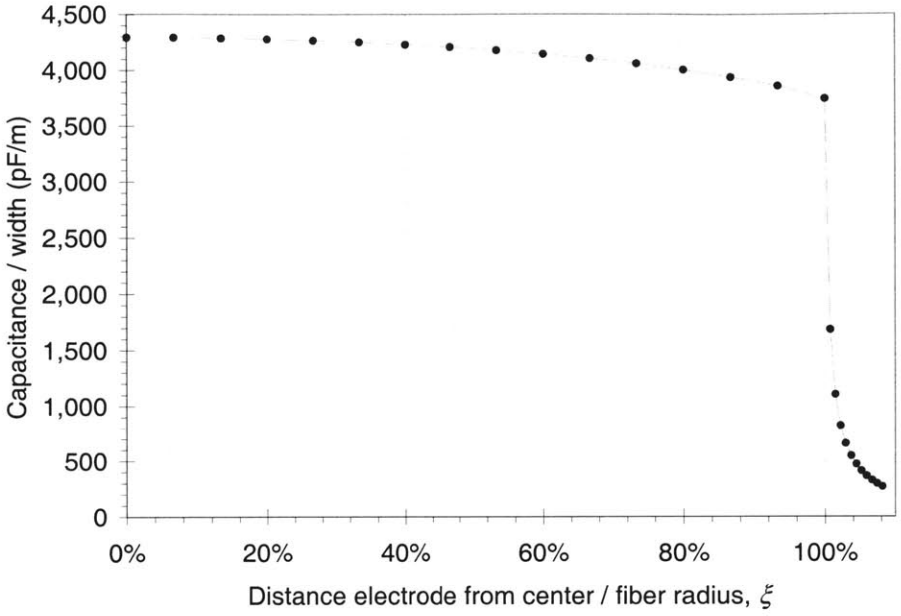

Figure 3.10 Capacitance / width verses ξ for an Interdigitated Rectangle

The capacitance per unit width was determined by dividing the total charge on the $z = l/2$, and electrode by the applied voltage, 1 V. As mentioned previously, the capacitance of the rectangle shown in Figure 3.4 is the same as the ¼th model.

For ξ = 0%, due to the path of the electric field, the total capacitance can be modeled as two capacitors in parallel, one due to the polymer and one due to the high dielectric material, as shown in the following figure:

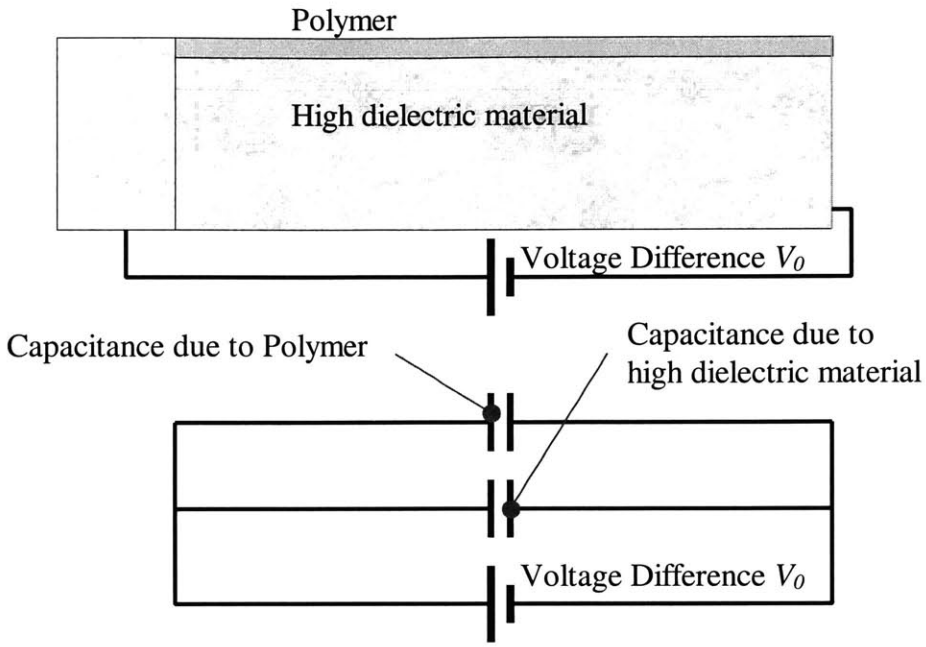

Figure 3.11 Capacitance Model for $\xi = 0\%$ for the Interdigitated Rectangle

For a capacitor electroded on the ends with a linear potential drop, the capacitance equals the permittivity times the area divided by the length. For two capacitors in parallel, the total capacitance is given by the sum of the capacitors. Therefore, the capacitance per width for interdigitated rectangle for $\xi = 0\%$ is given by:

$$C/W = \frac{\varepsilon_0}{\mathcal{L} - L_E}\left((K_D - K_P)R + K_P \frac{h_A}{2} \right) \qquad \xi = 0\% \tag{3.23}$$

Because K_D is much greater than K_P, and R is about equal to $h_A/2$, Equation 3.23 can be written as:

$$C/W \cong \frac{\varepsilon_0}{\mathcal{L} - L_E} K_D R \qquad \xi = 0\% \tag{3.24}$$

Using Equations 3.23 and 3.24 the capacitance per width fro the interdigitated rectangle is 4266.7 and 4267.4 pF/m respectively. The finite element solution using 68,223 nodes is C/W = 4293 pF/m, a percent difference of 0.6% for both cases. For all values of $\xi \leq 100\%$, the capacitance per width is about equal. This is due to the fact that the average electric field in the x direction for $\xi \leq 100\%$ is nearly independent of ξ.

As can be seen in Figure 3.10, the capacitance for $\xi > 100\%$ is very small compared to the capacitance for $\xi \leq 100\%$. This is because for $\xi > 100\%$, most of the potential drop is lost in the low dielectric polymer gap, and thus leaving little potential to generate charge on the surface of the electrode. Figure 3.12 gives a capacitor model for the interdigitared rectangle for $\xi > 100\%$.

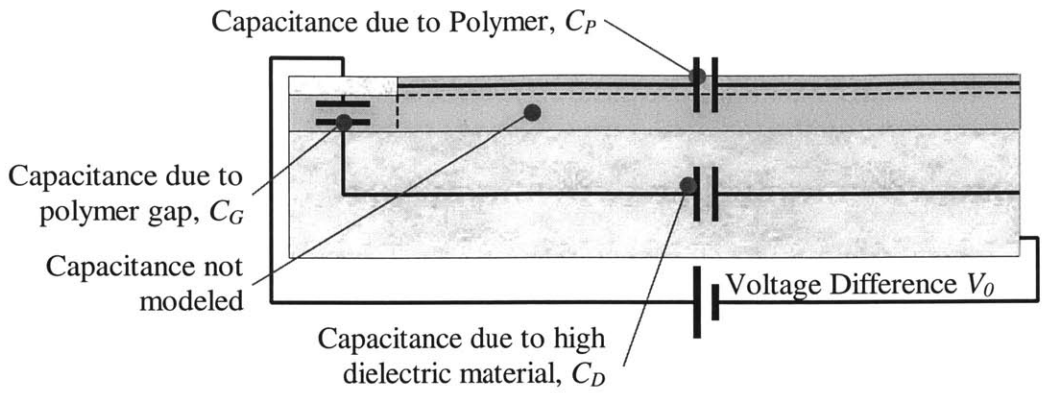

Figure 3.12 Capacitance Model for $\xi > 100\%$ for the Interdigitated Rectangle

Where in Figure 3.12 C_P, C_G, and C_D is the capacitance due to the polymer, the polymer gap, and the high dielectric material respectively. It should be noted that in Figure 3.12 there is a capacitance is not modeled due to the non-uniformity of the electric field in this area. The capacitance in the polymer and the polymer gap can be given by:

$$C_P = \frac{\varepsilon_0 K_P W}{\ell - L_E}(h_A - 2R - 2\gamma) \qquad \xi > 100\% \qquad (3.25)$$

$$C_G = \frac{\varepsilon_0 K_P L_E W}{2\gamma}$$

The capacitance in the high dielectric region is not known because the electric field in this region is not uniform. However, it is known that the C_D is finite and proportional to K_D times W.

$$C_D = \varepsilon_0 K_D W \widetilde{C} \qquad (3.26)$$

Where $\widetilde{C}$ is an unknown constant that is unitless. The capacitance per unit width for $\xi > 100\%$ is given by:

$$C/W = C_P/W + \frac{(C_G/W)(C_D/W)}{(C_G/W)+(C_D/W)} \qquad \xi > 100\% \qquad (3.27)$$

Where capacitors in series add like springs in parallel. Inserting Equation 3.25 into Equation 3.27 yields:

$$C/W = \frac{\varepsilon_0 K_P}{\ell - L_E}(h_A - 2R - 2\gamma) + \frac{\varepsilon_0 K_P L_E (C_D/W)}{\varepsilon_0 K_P L_E + 2\gamma (C_D/W)} \qquad \xi > 100\% \qquad (3.28)$$

In order to determine C_D consider the case where the electrode touches the fiber, $\gamma = 0$.

$$C/W(\gamma = 0) = \frac{\varepsilon_0 K_P}{\ell - L_E}(h_A - 2R) + C_D/W \qquad (3.29)$$

Solving for C_D/W yields:

$$C_D/W = C(\gamma = 0)/W - \frac{\varepsilon_0 K_P}{\ell - L_E}(h_A - 2R) \tag{3.30}$$

Thus, if the capacitance per unit width for $\gamma = 0$ is known, then the capacitance per unit width in the high dielectric area can be estimated. Using the FEM results presented in Figure 3.10 and the result that the capacitance per unit width for $\gamma = 0$ is 3,746 pF/m, the capacitance per unit width for the interdigitated rectangle for $\xi > 100\%$ (Equation 3.28) can be plotted versus ξ.

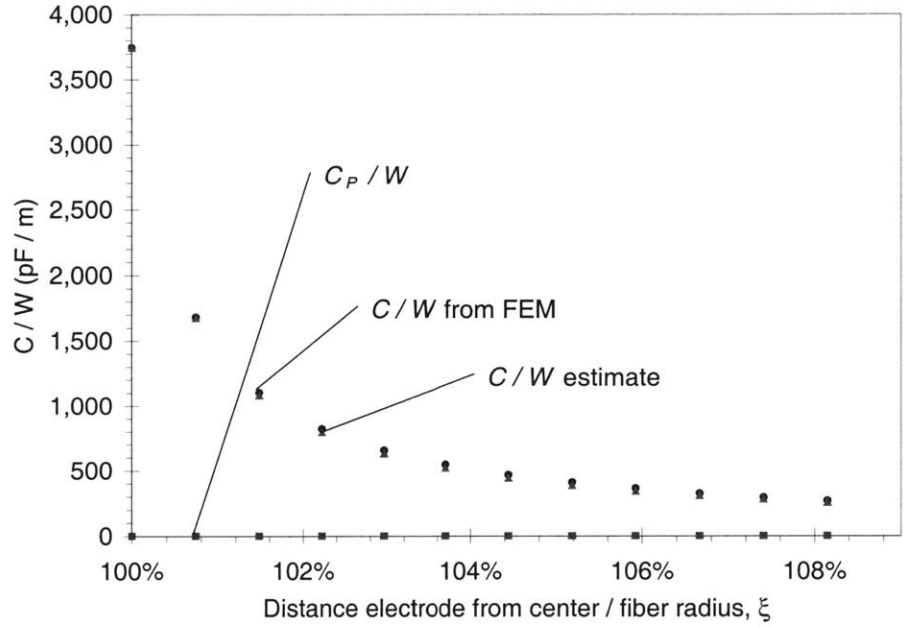

Figure 3.13 Capacitance per Unit Width plotted for ξ for the Interdigitated Rectangle for $\xi >$ 100%

As can be seen in Figure 3.13, Equation 3.28 provides a very good estimate of the capacitance of the interdigitated rectangle for $\xi > 100\%$. The percent difference between the finite element model and Equation 3.28 ranges between 0% (at $\xi = 100\%$) and 5.39%. In Figure 3.13 the capacitance per unit width is plotted versus ξ for the polymer. As can be seen C_P / W is very small compared to C / W. Therefore, Equation 3.28 can be written as:

$$C/W \cong \frac{\varepsilon_0 K_P L_E (C_D/W)}{\varepsilon_0 K_P L_E + 2\gamma (C_D/W)} \qquad \xi > 100\% \tag{3.31}$$

The percent error in Equation 3.31 and the finite element model ranges between 0.02% and 5.45%. Equation 3.31 can be rewritten as:

$$C/W \cong \varepsilon_0 \frac{K_P K_D L_E \widetilde{C}}{K_P L_E + 2\gamma K_D \widetilde{C}}$$

$$\frac{1}{C/W} \cong \frac{1}{\varepsilon_0 K_D}\left[\frac{1}{\widetilde{C}} + \frac{K_D}{K_P}\frac{2\gamma}{L_E}\right] \qquad \xi > 100\% \qquad (3.32)$$

Therefore, if 1 / capacitance per unit width is plotted against ξ for the finite element results should be a straight line:

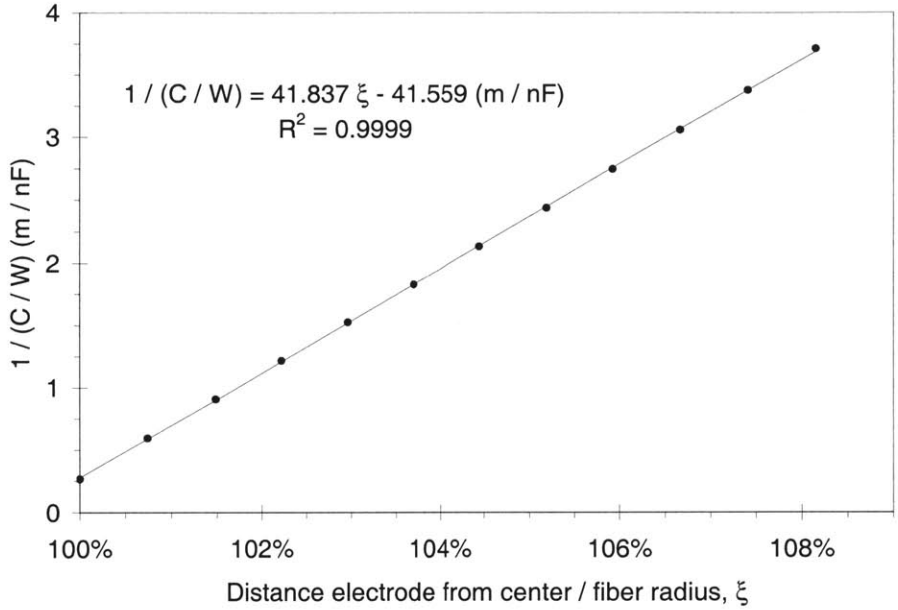

Figure 3.14 1 / Capacitance per unit Width versus ξ for the Finite Element Results of the Interdigitated Rectangle

As can be seen in Figure 3.14, when 1 / capacitance per unit width is plotted against ξ for the finite element results a straight line is seen with R^2 = 0.9999, thus validating the assumptions that went into Equation 3.31.

It should be noted that the capacitive model of Figure 3.12 is very similar to the assumptions made in the uniform fields model to determine the actuation of an AFC (Reference 34 pages 84-96). The uniform fields model made an assumption that a layer of polymer existed between the electrode and the fiber (ξ > 100%) thus reducing the actuation of the AFC and this layer could be modeled as a capacitor. As will be seen in Section 3.7 this assumption is approximately true.

The ratio of the permittivity in the polymer to the high dielectric material, K_P/K_D, is very important to the potential drop in the high dielectric material for ξ > 100%. As K_P/K_D increases, then the potential drop in the polymer gap decreases, and thus the average electric field in the z direction in the high dielectric material increases. Thus if ξ > 100%, to

maximize the average electric field in the ζ direction in the high dielectric material one should attempt to find a polymer with as large a K_P as possible. For $\xi \leq 100\%$ the average electric field in the ζ direction in the high dielectric material is nearly independent of the ratio K_P/K_D. This conclusion holds true for a true for an AFC/tmAFC where the high dielectric material is the piezoelectric fiber. Further discussion of the fields inside the interdigitated block and an AFC/tmAFC are presented in Section 3.7.

3.4 Reduction of the Response of the Active Area of an AFC/tmAFC to a Single Fiber

As mentioned in Section 3.3, the electric field for a single fiber in an AFC/tmAFC is similar to that of an interdigitated block. However, the AFC/tmAFC is comprised of several materials, and rectangular and cylindrical shapes, making the AFC/tmAFC very difficult to analyze AFC/tmAFC using closed form solutions, and thus approximate solutions and finite element solutions must be relied upon. Most solutions will involve the single fiber Figure 2.5 because as discussed in Appendix I. The results of a single fiber can be used to determine the results for an entire AFC/tmAFC if some assumptions are employed.

1. The electrodes are assumed to be perfectly conducting

2. All fields are applied quasi-statically, as defined in Section II.2

3. The frequencies of the applied field are small such that magnetic forces can be ignored

4. The fibers are straight and evenly spaced in the X direction with spacing w

5. The material and geometry of the AFC/tmAFC is symmetric about the X-Z plane

6. All fibers are within the active area

7. No electric fields occur outside the AFC/tmAFC

8. There are a large number of fibers and electrode finger pairs

9. No electric field fringing occurs outside the active area

10. All strains and stresses are applied uniformly to the active area

In Assumption 1, the conductance of the electrode is assumed to be infinite. This is another way of stating that the impedance of the fibers is much greater than the impedance of the electrode, which is typically true. In Assumption 2, it is assumed that all fields are applied quasi-statically. This is to avoid electrical and mechanical resonance's as described in Section II.2. Typically, AFCs/tmAFCs are operated in ranges below 1 kHz to avoid the generation of heat which can damage the actuator. As seen in Appendix IV, the electrical resonance's are typically above 10 kHz. Assumption 3 is a typical assumption made for non-magnetic materials in which the applied frequencies are low. Assumptions 4, 5, and 6 are the goals for correctly manufactured AFCs/tmAFCs. Assumption 7 states that no electric field exists outside the AFC/tmAFC. If electric fields are present then it is the goal that they are small such that actuation of the AFC/tmAFC does not cause electrical damage to the host structure that the AFC/tmAFC is embedded into. Assumption 8 states that there are a large number of fibers and electrode finger pairs. If there are a large number of electrode fingers and fibers effects due to the fibers being close to the edges of the active area will be minimized. In addition, single fibers can be modeled as if they are surrounded by an infinite number of fibers in the x and z directions, which is true for the fibers close to the center of the AFC/tmAFC. Assumption 9 states that no electric field fringing occurs outside the active area. The electrodes were designed such that electric fields between the electrode fingers and the rails would be small compared to the fields between the fingers (Reference 34). Because of Assumption 8, any effects of field fringing would be minimized. Assumption 10, as discussed in Appendix I, is made to reduce the response of the active area to the response of a single fiber. In general, the end user of the AFC/tmAFC is interested in only the global response of the AFC/tmAFC, and not how strain varies throughout the composite. AFCs/tmAFCs also are used in cases where forces and strains are applied across composite in general, and not point-wise.

If electrodes of the AFC/tmAFC are perfectly conducting, a voltage drop placed across the electrode pads, the magnitude of the voltage drop is the same across each electrode fingers. In Figure 2.4 the average electric field for an AFC/tmAFC is shown with field fringing. However due to Assumption 8, field fringing is assumed to be zero. In Figure 3.15 the average electric field for an AFC/tmAFC is shown without field fringing, where the arrows in the active area give the average electric field. As can be seen in Figure 3.15, when a voltage is applied to the AFC/tmAFC, the average electric field is in either the positive or negative Z direction, as shown in Figure 2.1.

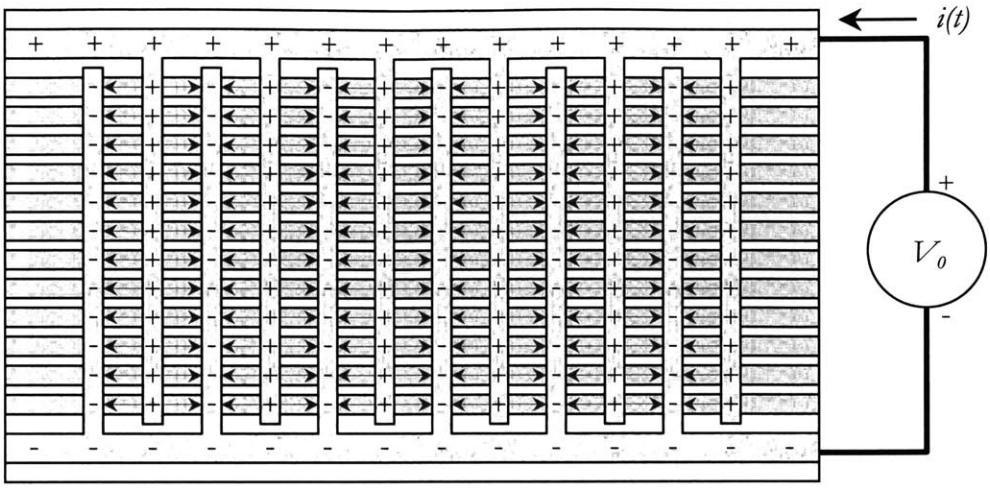

Figure 3.15 Illustration of the Electric Field in an AFC/tmAFC Without Fringing

In a conductive body, the electrons are not tightly bound to the nucleus of the atoms, and the application of an electric field causes movement of the electrons resulting in a conduction current. In a dielectric body, the electrons are very tightly bound to the nucleus and the application of an electric field causes the electrons to slightly displaces from the positive nucleus. This displacement is known as electronic polarization and is illustrated below.

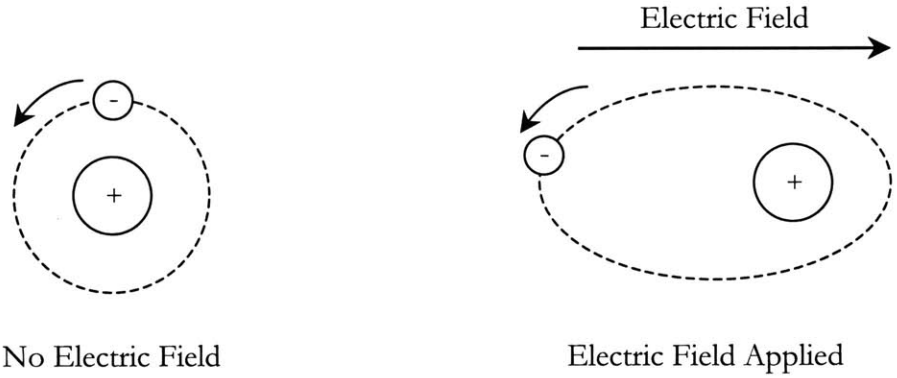

Figure 3.16 Illustration of Electronic Polarization

Other types of polarization are known as ionic and orientational polarization in which the bonds between ions stretch and rotate under the application of an electric field. When the electric field is removed, changes and ions return to their original positions. The positive direction of the polarization vector is defined as being from the negative polarizing charge to the positive polarizing charge.

During the poling process, a large electric field is applied under high temperatures, aligning the polarized domains with the electric field. After removal of the electric field and temperature, some of the polarized domains return to their pre poling state. Some of the

polarizations of the domains remain aligned with the poling field yielding a "remnant polarization". Prior to poling, the piezoelectric material is isotropic, but becomes anisotropic due to the remnant polarization. Figure 3.17 shows the effect of poling on a piezoelectric interdigitated block.

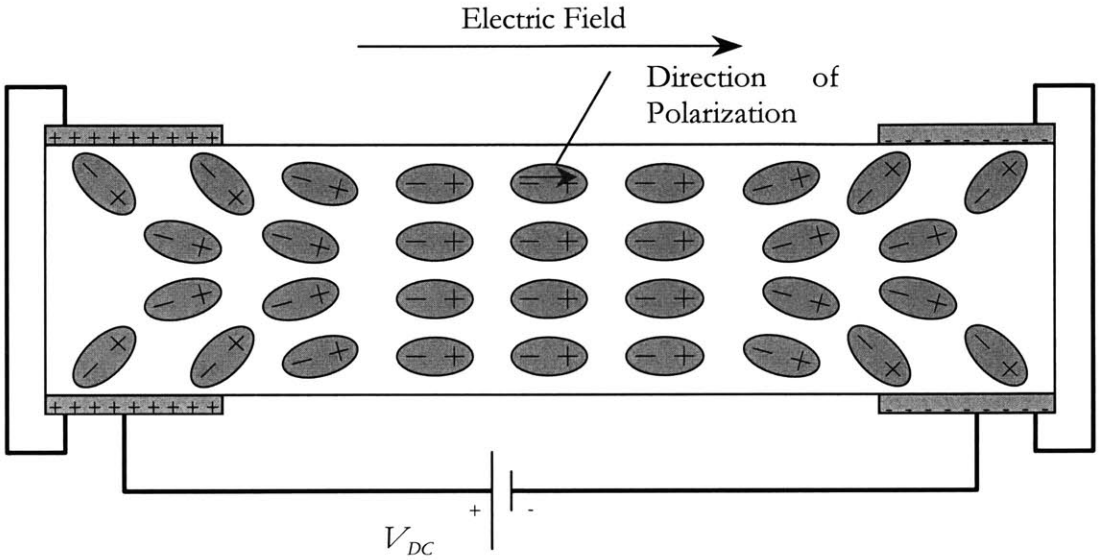

Application of a DC voltage during poling aligns domains with the poling field

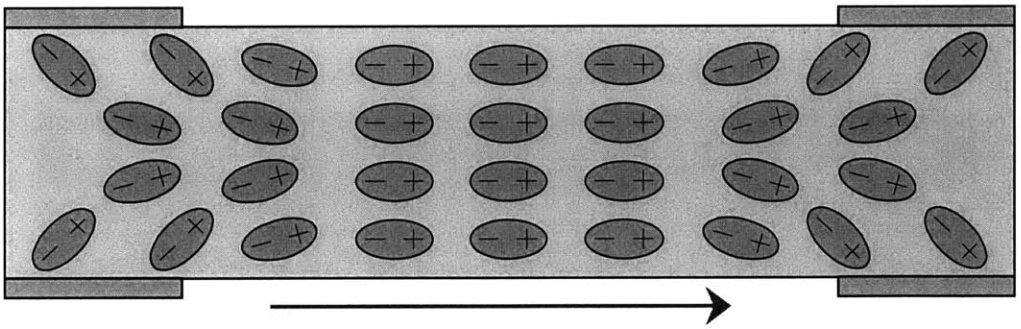

Average Direction of Remnant Polarization

Removal of the poling field does not completely realign domains

Figure 3.17 Illustration of the Polarization Direction During Poling for an Interdigitated Block

The "*3*" direction in the curvilinear path of following the remnant polarization vectors the direction. In the case of the interdigitated block, the "*3*" direction starts out perpendicular to the positive electrode (in the *Y* direction), curves toward the *Z* direction beneath the electrode, becomes nearly constant between the electrodes, curves back in the *Y* direction and is perpendicular to the negative electrode, as can be seen in Figure 3.17. This yields an average remnant polarization in the *Z* direction as shown above, and thus it can be said that the "*3*" direction is on average in the *Z* direction. After polarization, the

piezoelectric block can be actuated. When a driving voltage source is connected to the piezoelectric block a electric field is introduced into the block following the path of the "*3*" direction. If the high side of the driving voltage source is connected to the electrode that was connected to the high side of the poling voltage source, the electric field is in the positive "*3*" direction. If the low side of the driving voltage source is connected to the electrode that was connected to the high side of the poling voltage source, the electric field is in the negative "*3*" direction. If the electrodes are the only source of applied electric fields, the electric field in the block is always in the positive or negative "*3*" direction.

After an AFC/tmAFC is manufactured the fibers are not poled, and need to be poled in order for actuation to occur. Between the electrode fingers, the poling direction is similar to the poling direction of the interdigitated block as shown in Figure 3.17. However due to the interdigitated fingers, the average polarization direction alternates in the positive and negative *Z* directions as shown in Figure 3.15. Thus, like a piezoelectric stack, the average remnant polarization direction of an AFC/tmAFC alternates between the electrode fingers. Like the interdigitated block, when a driving voltage source is connected to the AFC/tmAFC, an electric field is introduced into the AFC/tmAFC following the path of the "*3*" direction. If the high side of the driving voltage source is connected to the electrode pad that was connected to the high side of the poling voltage source, the electric field is in the positive "*3*" direction. If the low side of the driving voltage source is connected to the electrode pad that was connected to the high side of the poling voltage source, the electric field is in the negative "*3*" direction. If the electrodes are the only source of applied electric fields, the electric field in the AFC/tmAFC is always in the positive or negative "*3*" direction for all the electrode finger pairs. This is further discussed in Appendix I.

In the center of the electrodes due to the proximity of two negative polarization charges, large stresses build up and cracking can occur in the piezoelectric material as shown below:

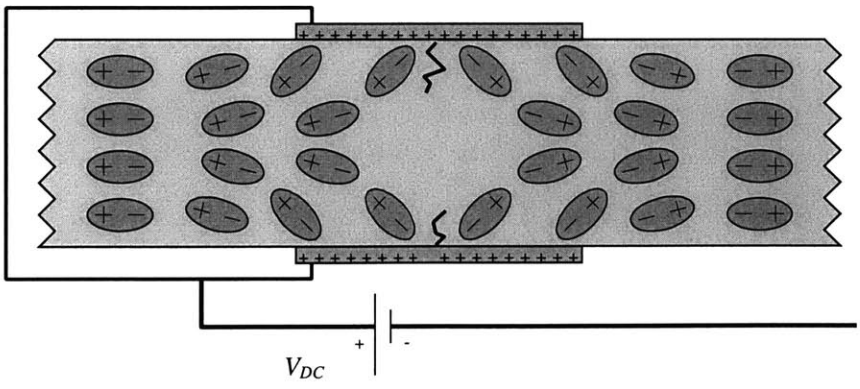

Figure 3.18 Cracking due to Polarization beneath the Electrode in an AFC/tmAFC

Like the interdigitated block, the electric field in an AFC/tmAFC is highest at the corners of the electrode. If the corners of the electrode are infinitely sharp then the electric field is infinite. In reality, the corners of the electrode are not infinity sharp and thus the electric field at the corners is large, but finite. This large electric field yields electrical damage in the AFC, and was seen in electrical fatigue tests of AFCs in Reference 58 (pages 101-110).

If there is no fringing of the electric fields, and due to symmetry of the materials in the AFC/tmAFC, a voltage drop placed across any fiber is the same as any other fiber. This voltage drop creates an electric field whose average direction although alternates in the Z direction, is always in either the positive *3* direction or the negative *3* direction in every fiber. Because it is assumed that any stress or stain applied to the active area of the AFC/tmAFC is uniformly applied, the applied stress and strain in any single fiber is the same as in any other fiber. Therefore because the applied stress and strain, electric field and electric potential is the same in every fiber, the response of every fiber is the same, and therefore as described in Appendix I, the response of the active area of an AFC/tmAFC can be reduced to the response of a single fiber.

Consider the single fiber of an AFC/tmAFC in the active area as shown in Figure 2.5. Assume that this fiber is one of many fibers in the active area of an AFC/tmAFC. Assume that the fiber has a applied voltage of $V(t)$ on the $z = 0$ electrode and an applied voltage of $-V(t)$ on the $z = \mathcal{L}$ electrodes, for a total voltage drop of $2\ V(t)$. Assume that stresses and strain supplied to the single fiber are uniform over the entire fiber. Due to geometric and material symmetry and the values of the applied voltage, across the x-z plane the electric potential is symmetric, and therefore the electric field at $y = 0$ is only in the z direction. About the x-y plane at $z = \mathcal{L}/2$, the electric potential is anti-symmetric. Therefore the electric potential is zero at $z = \mathcal{L}/2$ and the electric field at this location is only in the z direction. If there is no fringing of the electric fields, the electric displacement is perpendicular to the outer edges in the matrix at $y = \pm h/2$. Because there are infinite fibers extending in either direction of z, then the electric field in z direction is zero at the outer surfaces ($z = 0,\ \mathcal{L}/2$). Because there are infinite fibers extending in either direction of x, then the electric field in x direction is zero at the outer surfaces ($x = -\mathcal{W}/2,\ \mathcal{W}/2$). For reasons discussed in Section 3.3, the electric displacement is perpendicular to the electrodes. As mentioned in Appendix I, when the fiber is actuated using an applied voltage, the volume of the fiber does not shear, and thus the displacement in the z direction at $z = 0$ must be independent of x and y. Similar arguments can be used to prove:

$$\begin{aligned} u(\mathcal{W}/2, y, z) &= u(x = \mathcal{W}/2) \\ u(-\mathcal{W}/2, y, z) &= u(x = -\mathcal{W}/2) \\ w(x, y, 0) &= w(z = 0) \\ w(x, y, \mathcal{L}) &= w(z = \mathcal{L}) \end{aligned} \qquad (\underline{T})_F = 0 \qquad (3.33)$$

Consider the case of single fiber shown in Figure 2.5 where the stress boundary conditions are assumed symmetric (for example stress free on the x and y boundaries with an applied stress, T_0, on the z boundary). The displacement boundary conditions are also assumed to be anti symmetric (for example no displacements on the y and z boundaries with a displacement $\pm u$ on the edges $x = \mp W/2$). For this case, the x, y, and z displacements are anti-symmetric about the y-z, x-z, and x-y planes respectively. The problem of modeling the displacements, strain, stress, electric potential, electric field, and electric displacement can be then reduced to a "1/8th model" of the single fiber shown in Figure 2.5.

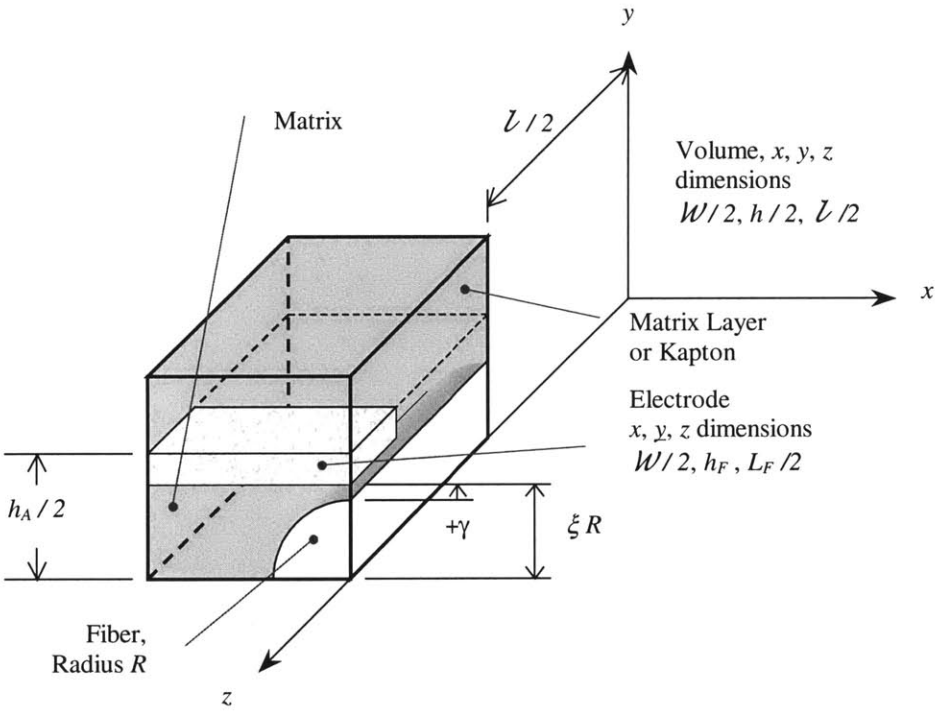

Figure 3.19 1/8th Model of a Single Fiber of an AFC/tmAFC

Due to the anti-symmetry of the displacements and electric potential, u, v, w, and φ is zero on the $x = 0$, $y = 0$, $z = l/2$, and $z = l/2$ faces respectively. At the electrode a potential equal to $-V(t)$ is applied yielding an electric field in the z direction. This 1/8th model will be used extensively in Section 3.8.

3.5 Rule Mixtures Analysis of an AFC/tmAFC

In Appendix III, the rule of mixtures for active materials is derived. Using the rule of mixtures one can estimate the effect of the matrix Young's modulus on the open and short circuited Young's modulus of an AFC/tmAFC. The effect of the matrix Young's modulus on the stress free strain per unit volt of an mpAFC is also analyzed.

3.5.1 Effect of Matrix Young's Modulus on the Short Circuited Young's Modulus of an AFC/tmAFC

Using Equation C.30 and the geometry in Figure 2.5, the Young's modulus in the Z direction under a shorted circuited condition for the active area of a PiezoFlex AFC can be determined, $\left(Y_{ZZ}^{V}\right)_{A}$.

$$\left(Y_{ZZ}^{V}\right)_{A} = \frac{\sum_{i=1}^{N} A_i \left(Y_{33}^{E}\right)_i}{\sum_{i=1}^{N} A_i} \tag{3.34}$$

Where

$$\begin{aligned} \left(Y_{33}^{E}\right)_1 &= E_M & A_1 &= W h_A - \pi R^2 \\ \left(Y_{33}^{E}\right)_2 &= E_K & A_2 &= W\left(h - h_A\right) \\ \left(Y_{33}^{E}\right)_3 &= Y_{33}^{E} & A_3 &= \pi R^2 \end{aligned} \tag{3.35}$$

Where the 1, 2, and 3 subscripts represent the matrix, Kapton, and the fibers, the M subscript indicates the matrix, the K subscript indicates the Kapton, E is the Young's modulus, and Y_{33}^{E} is the Young's modulus of the fiber. Equation 3.34 can be written as:

$$\left(Y_{ZZ}^{V}\right)_{A} = \frac{E_M\left(W h_A - \pi R^2\right) + E_K\left(W\left(h - h_A\right)\right) + Y_{33}^{E}\left(\pi R^2\right)}{W h} \tag{3.36}$$

Using the geometry and material properties for the PiezoFlex AFC in Table 2.2 and the fiber properties in Table 2.5, the average Young's modulus in the Z direction under a shorted condition in the active area of a PiezoFlex AFC can be plotted versus the matrix Young's modulus, E_M:

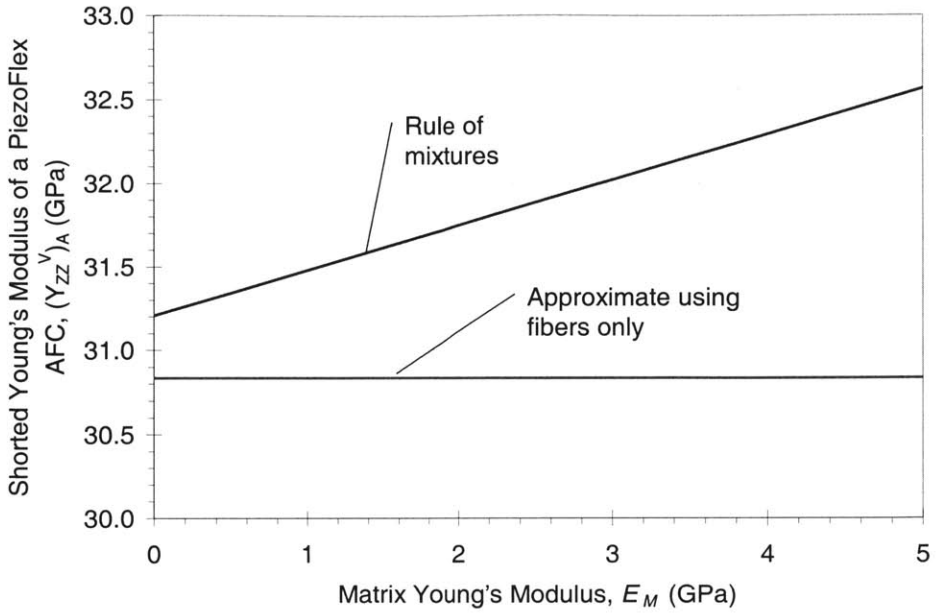

Figure 3.20 Young's Modulus in the *ZZ* Direction under a Shorted Condition in the Active Area of a PiezoFlex AFC versus Matrix Young's Modulus

As can be seen from Figure 3.20, there is only a slight change in the shorted AFC stiffness as the matrix stiffness is changed. This is because the fibers have a dramatically higher shorted stiffness than any other material in the AFC. Using Equation 3.36 and assuming that the matrix and Kapton have infinite compliance (i.e. the fiber is the only material in the AFC), we see that:

$$\left(Y_{ZZ}^V\right)_A \cong \frac{Y_{33}^E\left(\pi R^2\right)}{W h} \tag{3.37}$$

Using Equation 3.36, for the case of the active area of a PiezoFlex AFC, $Y_{ZZ}^V = 32.0\,\text{GPa}$, using a matrix Young's modulus of 2.9 GPa. Using Equation 3.37 the short circuited PiezoFlex AFC Young's modulus can be estimated, $Y_{ZZ}^V \cong 30.8\,\text{GPa}$, using a matrix Young's modulus of 2.9 GPa, yielding a percent difference of 3.6 %. Ignoring all the other materials in the AFC, Y_{ZZ}^V using the fibers only has a percentage difference of 1.2 % to 5.3 % from the Y_{ZZ}^V given in Figure 3.20, and therefore it can be assumed that the matrix stiffness has only a minimal effect on the shorted Young's modulus of the AFC.

3.5.2 Effect of Matrix Young's Modulus on the Open Circuited Young's Modulus of an AFC/tmAFC

Using Equation C.36 and the geometry in Figure 2.5, the Young's modulus in the Z direction under an open circuited condition for the active area of a PiezoFlex AFC can be determined, $\left(Y_{ZZ}^{i}\right)_{A}$.

$$\left(Y_{ZZ}^{i}\right)_{A} = \left(Y_{ZZ}^{V}\right)_{A} + \frac{\left[\sum_{i=1}^{N} A_i \left(d_{33}\right)_i \left(Y_{33}^{E}\right)_i\right]^2}{\left[\sum_{i=1}^{N} A_i\right]\left[\sum_{i=1}^{N} A_i \left(\varepsilon_{33}^{T}\right)_i \left(1-\left(k_{33}^{2}\right)_i\right)\right]} \tag{3.38}$$

$$\begin{aligned} \left(\varepsilon_{33}^{T}\right)_1 &= \varepsilon_M \quad \left(d_{33}\right)_1 = 0 \quad \left(k_{33}\right)_1 = 0 \\ \left(\varepsilon_{33}^{T}\right)_2 &= \varepsilon_K \quad \left(d_{33}\right)_2 = 0 \quad \left(k_{33}\right)_2 = 0 \\ \left(\varepsilon_{33}^{T}\right)_3 &= \varepsilon_{33}^{T} \quad \left(d_{33}\right)_3 = d_{33} \quad \left(k_{33}\right)_3 = k_{33} \end{aligned} \tag{3.39}$$

Where ε is the shorted permittivity, d is the "strain" piezoelectric coefficient, and k is the coupling coefficient. Equation 3.38 can be written as:

$$\left(Y_{ZZ}^{i}\right)_{A} = \left(Y_{ZZ}^{V}\right)_{A} + \frac{\left[\pi R^2 d_{33} Y_{33}^{E}\right]^2}{\mathcal{W} h\left[\varepsilon_M \left(\mathcal{W} h_A - \pi R^2\right) + \varepsilon_K \left(\mathcal{W}\left(h - h_A\right)\right) + \varepsilon_{33}^{T}\left(\pi R^2\right)\left(1-k_{33}^{2}\right)\right]} \tag{3.40}$$

Using the geometry and material properties for the PiezoFlex AFC in Table 2.2 and the fiber properties in Table 2.5, the average Young's modulus in the Z direction under an open circuit condition in the active area of a PiezoFlex AFC can be plotted versus the matrix Young's modulus, E_M:

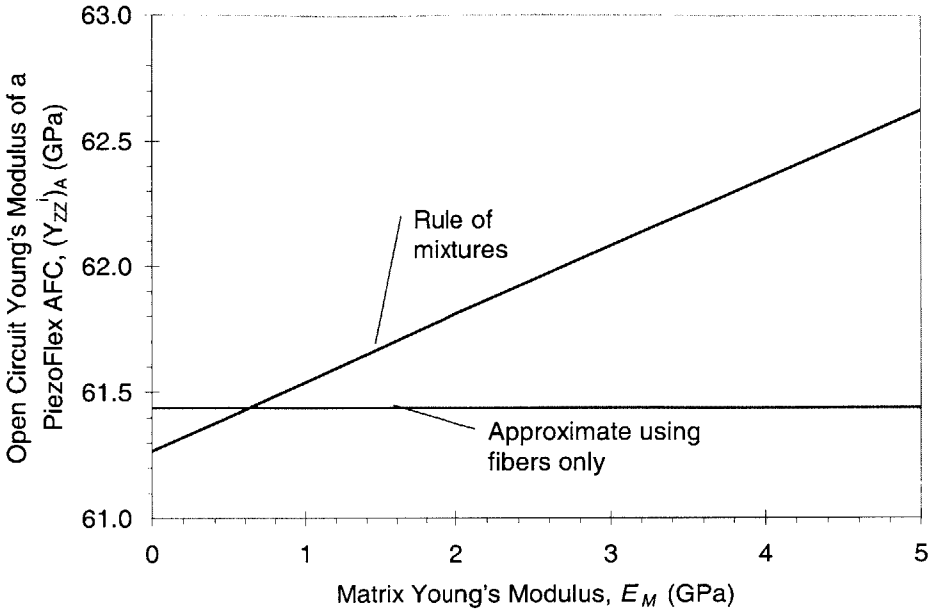

Figure 3.21 Young's Modulus in the ZZ Direction under an Open Circuit Condition in the Active Area of a PiezoFlex AFC versus Matrix Young's Modulus

As can be seen from Figure 3.21, there is only a slight change in the open circuit AFC stiffness as the matrix stiffness is changed. This is because the fibers have a dramatically higher open circuit stiffness than any other material in the AFC. Using Equations 3.36 and 3.38 and assuming that the matrix and Kapton have infinite compliance and infinite impermittivity, we see that:

$$\left(Y_{ZZ}^{V}\right)_A \cong \frac{Y_{33}^{D}\left(\pi R^2\right)}{W h} \tag{3.41}$$

Using Equations 3.36 and 3.38, for the case of the active area of a PiezoFlex AFC, $Y_{ZZ}^{i} = 62.1\,\text{GPa}$, using a matrix Young's modulus of 2.9 GPa. Using Equation 3.41 the short circuited PiezoFlex AFC Young's modulus can be estimated, $Y_{ZZ}^{i} \cong 61.4\,\text{GPa}$, yielding a percent difference of 1.0 %. Ignoring all the other materials in the AFC, Y_{ZZ}^{i} using the fibers only has a percentage difference of -0.3 % to 1.9 % from the Y_{ZZ}^{i} given in Figure 3.21, and therefore it can be assumed that the matrix stiffness has only a minimal effect on the open circuit Young's modulus of the AFC. This percent difference is less than the percent difference for the short circuit Young's modulus. This is because the open circuit stiffness of the fiber is higher than the short circuit stiffness.

3.5.3 Effect of Matrix Young's Modulus on the *ZZ* Strain per unit Volt under Stress Free Conditions for a mpAFC

Using Equation C.36 and the geometry in Figure 2.5, the *ZZ* strain per unit volt under stress free conditions for a PiezoFlex AFC can be determined.

$$S_3(t) = \frac{\sum_{i=1}^{N} A_i \left(d_{33} Y_{33}^E\right)_i}{\sum_{i=1}^{N} A_i \left(Y_{33}^E\right)_i} E_3(t) \tag{3.42}$$

Where in Equation 3.42, E_3 is the electric field in the *3* direction. As seen in Figure 3.9, the electric field in an interdigitated block is dependant on the parameter ξ, and the electric field in an AFC will be shown to be dependant on the parameter ξ in Section 3.7. In Figure 3.9. when ξ = 0% the electric field for the interdigitated block is uniform in the z direction between $z = L_E / 2$ and $z = l / 2$. For the mpAFC (ξ = 0%) it can be assumed that the electric field and *3* direction is uniform in the z direction between $z = L_E / 2$ and $z = l / 2$. The electric field in the z direction is therefore given by:

$$E_3(t) = \frac{V(t)}{l - L_F} \tag{3.43}$$

Thus using Equation 3.42 and 3.43, the *33* strain between the electrodes can be determined.

$$S_{33}(t) = \frac{V(t)}{l - L_F} \frac{\sum_{i=1}^{N} A_i \left(d_{33} Y_{33}^E\right)_i}{\sum_{i=1}^{N} A_i \left(Y_{33}^E\right)_i} \tag{3.44}$$

The strain in Equation 3.44 is the strain between the electrodes in Figure 2.5. The zz strain for a single fiber in the active area is the displacement divided by the center-to-center length between the electrodes. The relationship between the zz strain for a single fiber in the active area, S, and the strain between the electrodes is given by:

$$S_{zz}(t) = \frac{l - L_F}{l} S_{33}(t) \tag{3.45}$$

Inserting Equations 3.35, 3.39 and 3.44 into Equation 3.45 yields:

$$\left(\Gamma_{ZZ}\right)_A = \frac{S_{ZZ}(t)}{V(t)} = \frac{\pi R^2}{l} \frac{d_{33} Y_{33}^E}{E_M \left(W h_A - \pi R^2\right) + E_K \left(W (h - h_A)\right) + Y_{33}^E \left(\pi R^2\right)} \tag{3.46}$$

Using the geometry and material properties for the PiezoFlex AFC in Table 2.2 and the fiber properties in Table 2.5, the strain per unit volt under stress free conditions for a mpAFC can be plotted versus the matrix Young's modulus, E_M:

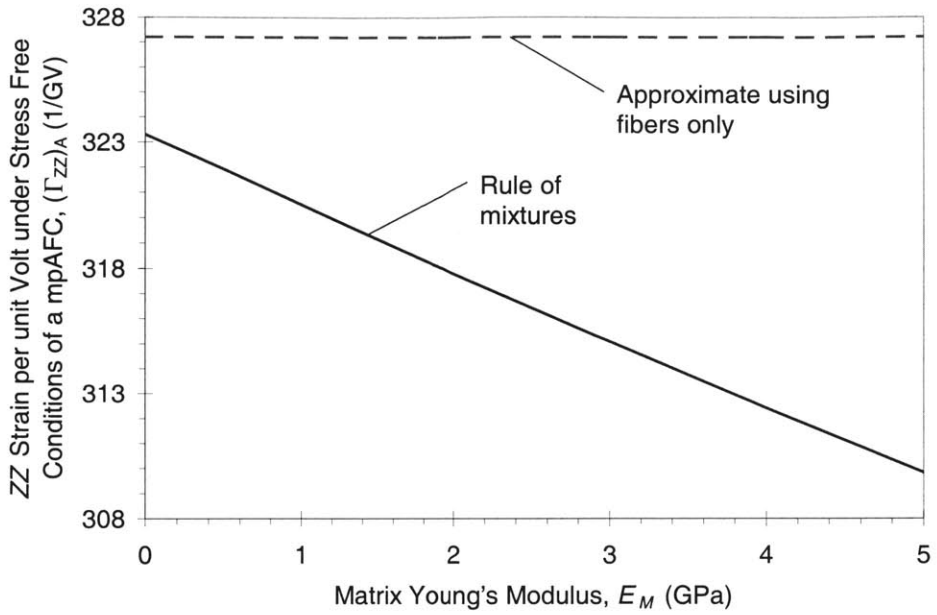

Figure 3.22 *ZZ* Strain per unit Volt under Stress Free Conditions of an mpAFC versus Matrix Young's Modulus

As can be seen from Figure 3.21, the stiffness due to the Kapton and the matrix reduces the *ZZ* strain per unit volt under stress free conditions. This is because the extension of the fibers is fought by the stiffness of the matrix and the Kapton. It can also be seen that there is a slight change in the *ZZ* strain per unit volt under stress free conditions of an mpAFC as the matrix stiffness is changed. This is because the fibers have a dramatically higher short circuit stiffness than any other material in the AFC.

Using Equations 3.46 and assuming that the matrix and Kapton have infinite compliance, we see that:

$$\Gamma_{ZZ} \cong \frac{d_{33}}{\mathcal{L}} \tag{3.47}$$

Using Equations 3.46 for the case of the active area of an mpAFC, $(\Gamma_{ZZ})_A$ = 315.3 1/GV, using a matrix Young's modulus of 2.9 GPa. Using Equation 3.47, the *ZZ* strain per unit volt under stress free conditions of an mpAFC can be estimated, $(\Gamma_{ZZ})_A$ 327.2 1/GV, yielding a percent difference of 3.8 %. The percent difference between Equations 3.46 and 3.47 for a matrix Young's modulus of 0 GPa to 5 GPa has a percentage difference of 1.2 % to 5.6 % respectively, and therefore it can be assumed that the matrix stiffness has only a minimal effect on the *ZZ* strain per unit volt under stress free conditions.

3.6 Approximation of the Longitudinal Stress Output of an AFC/tmAFC

When an AFC or a tmAFC is going to be used as an actuator for a system, it is desirable to maximize the maximum force that the AFC or the tmAFC can apply to the system. Equation 1.4, for a Hexagonal Crystal – Class 6 mm poled ferroelectric with the polarization direction in the *3* direction, can be written as:

$$\begin{Bmatrix} D_1 \\ D_2 \\ D_3 \\ \hline T_1 \\ T_2 \\ T_3 \\ T_4 \\ T_5 \\ T_6 \end{Bmatrix} = \left[\begin{array}{ccc:ccccccc} \varepsilon_{11}^S & 0 & 0 & 0 & 0 & 0 & 0 & e_{15} & 0 \\ 0 & \varepsilon_{11}^S & 0 & 0 & 0 & 0 & e_{15} & 0 & 0 \\ 0 & 0 & \varepsilon_{33}^S & e_{31} & e_{31} & e_{33} & 0 & 0 & 0 \\ \hdashline 0 & 0 & e_{31} & c_{11}^E & c_{12}^E & c_{13}^E & 0 & 0 & 0 \\ 0 & 0 & e_{31} & c_{12}^E & c_{11}^E & c_{13}^E & 0 & 0 & 0 \\ 0 & 0 & e_{33} & c_{13}^E & c_{13}^E & c_{33}^E & 0 & 0 & 0 \\ 0 & e_{15} & 0 & 0 & 0 & 0 & c_{44}^E & 0 & 0 \\ e_{15} & 0 & 0 & 0 & 0 & 0 & 0 & c_{44}^E & 0 \\ 0 & 0 & 0 & 0 & 0 & 0 & 0 & 0 & c_{66}^E \end{array}\right] \begin{Bmatrix} E_1 \\ E_2 \\ E_3 \\ \hline S_1 \\ S_2 \\ S_3 \\ S_4 \\ S_5 \\ S_6 \end{Bmatrix} \tag{3.48}$$

Where c_{ij}^E is a component of the stiffness, ε_{ij}^S is a component of the dielectric, and e_{ij} is a piezoelectric "stress" component. The *S* superscript indicates measured at constant strain, while the *E* superscript indicates measured at constant electric field. Comparing Equation 3.48 and Equation 1.2, one can solve for e_{33} as:

$$e_{33} = -\left.\frac{T_3}{E_3}\right|_{S=0} = \frac{d_{33}\left(s_{11}^E + s_{12}^E\right) - 2\,d_{31}\,s_{13}^E}{\left(s_{11}^E + s_{12}^E\right)s_{33}^E - 2\left(s_{13}^E\right)^2} \tag{3.49}$$

For an actuator applying force in the *3* direction it is desirable for e_{33} to be maximized. As mentioned in Section 1.2.1, *3-3* actuation is roughly 2 to 2.5 times greater than *3-1* actuation for a PZT material. From Table 2.5 it can be seen that s_{13}^E is -2.3 and -2.6 times smaller than s_{11}^E and s_{33}^E respectively. Therefore, we can write Equation 3.49 as approximately:

$$\begin{aligned} T_3 &= -e_{33}\,E_3\big|_{S=0} \\ e_{33} &\cong \frac{d_{33}}{s_{33}^E} = d_{33}\,Y_{33}^E \end{aligned} \tag{3.50}$$

From Table 2.5, e_{33} = 15.8 C / m^2 and from Equation 3.50 $e_{33} \cong$ 19.9 C / m^2. The assumptions used in Equation 3.50 can be assumed to hold true for the active area of an AFCs/tmAFCs because the actuation in the *Z* direction is greater than that in any other direction, and the stiffness in the *Z* direction is greater than any other direction. Using the constitutive relations derived in Appendix I:

$$(T_3)_A = -(\psi_{ZZ})_A V\big|_{S=0}$$
$$(\psi_{ZZ})_A \cong (\Gamma_{ZZ})_A \left(Y_{ZZ}^V\right)_A \tag{3.51}$$

Equation 3.51 can be derived from Equation B.57 by setting Γ_{XX}, Γ_{YY}, s_{XY}^V, s_{XZ}^V, and s_{YZ}^V to zero.

3.7 Capacitance Model of an AFC/tmAFC for $\xi > 100\%$

In Section 3.3.2, the capacitance of an interdigitated block with $\xi > 100\%$ is modeled using lumped capacitors. This model is very similar to the uniform fields model used to determine the actuation of an AFC (Reference 34 pages 84-96). The uniform fields model made an assumption that a layer of polymer existed between the electrode and the fiber ($\xi >$ 100%) thus reducing the actuation of the AFC and this layer could be modeled as a capacitor. This section derives a simple capacitance model for the AFC/tmAFC to determine the necessary electrical parameters that need to be maximized when attempting to maximize the strain output of the AFC/tmAFC.

Consider a $1/8^{th}$ model of a single fiber the active area of an AFC/tmAFC as shown in Figure 3.19. Assume that no stresses or displacements are placed on the external surfaces of the fiber, and that the a sinusoidal voltage, $V(t)$, with radial frequency, ω, is applied to the fiber. As discussed in Sections 3.4 and 3.3.2, the single AFC/tmAFC fiber under stress free actuation can be reduced to a $1/8^{th}$ model with an applied voltage of $V(t)$ on the electrode, and the location $z = L/2$ shorted. A 2-dimensional illustration of the$1/8^{th}$ model is shown figure:

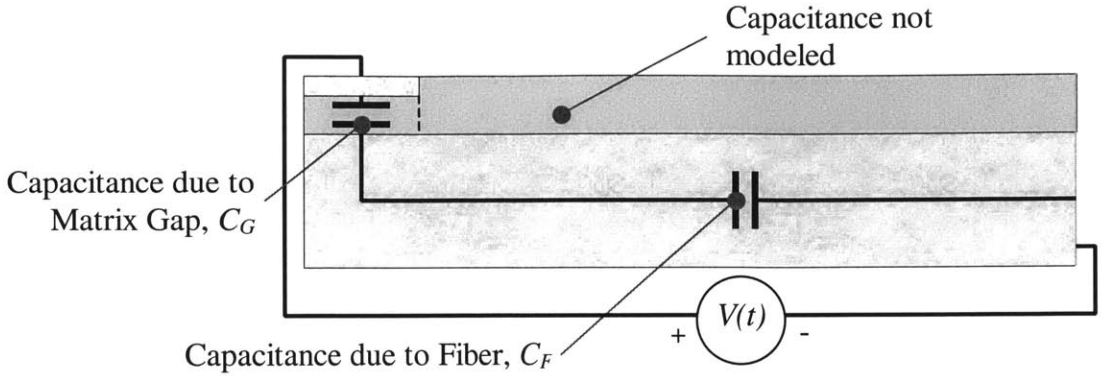

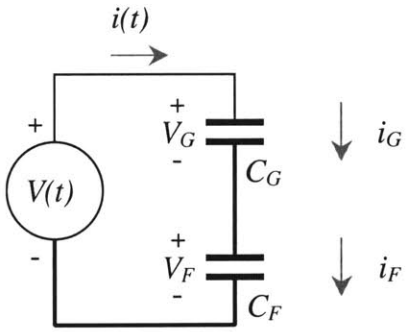

Figure 3.23 Capacitance Model of and AFC/tmAFC with $\xi > 100\%$

In Figure 3.23, the fiber and the matrix gap are modeled using lumped capacitors C_F and C_G respectively. The matrix gap is defined as the matrix region between the underside of the electrode and the fiber. V_G, V_F refer to the voltage drop across the matrix gap and fiber respectively, *i(t)* and i_G, i_F is the current though the voltage source, the matrix gap, and the fiber respectively. The capacitance of the polymer to the right of the electrode is not modeled because it is small compared to that of the fibers, as seen for the interdigitated block in Section 3.3.2. The for an applied sinusoidal voltage, *V(t)*, the electrical response in the matrix gap and fiber are sinusoidal:

$$\begin{aligned} V(t) &= \overline{V}\, e^{j\omega t} \quad V_G = \overline{V}_G\, e^{j\omega t} \quad V_F = \overline{V}_F\, e^{j\omega t} \\ i(t) &= \bar{i}\, e^{j\omega t} \quad i_G = \bar{i}_G\, e^{j\omega t} \quad i_F = \bar{i}_F\, e^{j\omega t} \end{aligned} \tag{3.52}$$

Where the over bar in Equation 3.52 indicates the amplitude. From Kirckoff's voltage and current laws:

$$\overline{V}(t) = \overline{V}_G + \overline{V}_F \tag{3.53}$$

$$\bar{i}(t) = \bar{i}_G = \bar{i}_F \tag{3.54}$$

For a sinusoidal input, the admittance, Y, for a capacitor is given by:

$$\begin{aligned} i(t) &= Y V(t) \\ Y &= j\omega C \end{aligned} \tag{3.55}$$

Where C is the capacitance. Thus, Equation 3.55 can be written as:

$$\begin{aligned} \bar{i}_G &= j\omega C_G V_G \\ \bar{i}_F &= j\omega C_F V_F \end{aligned} \tag{3.56}$$

Using Equations 3.54:and 3.56 solving for the magnitude of the voltage drop across the matrix gap yields:

$$\overline{V}_G = \frac{C_F}{C_G}\overline{V}_F \tag{3.57}$$

It should be noted that the ratio C_F / C_G is always greater than or equal to zero. From Equation 1.2, in order to maximize the amplitude of the strain in zz direction of the AFC/tmAFC, $\overline{S}_{zz}$, per applied volt, one should maximize the amplitude of the average electric field in the *3* direction the fiber, $\left(\overline{E}_3\right)_F$, for a given applied voltage.

$$\frac{\overline{S}_{zz}}{\overline{V}} \propto \frac{\left(\overline{E}_3\right)_F}{\overline{V}} \tag{3.58}$$

The amplitude of the electric field in the fiber is proportional to the amplitude of the voltage drop across the fiber:

$$\frac{\overline{S}_{zz}}{\overline{V}} \propto \frac{\overline{V}_F}{\overline{V}} \tag{3.59}$$

Therefore, maximizing the amplitude of the strain in zz direction of the AFC/tmAFC per applied volt is accomplished by maximizing the voltage drop across the fiber per applied volt.

Inserting Equation 3.57 into Equation 3.53 yields:

$$\frac{\overline{V}_F}{\overline{V}} = \frac{C_G/C_F}{1+C_G/C_F} \tag{3.60}$$

Plotting Equation 3.60 yields:

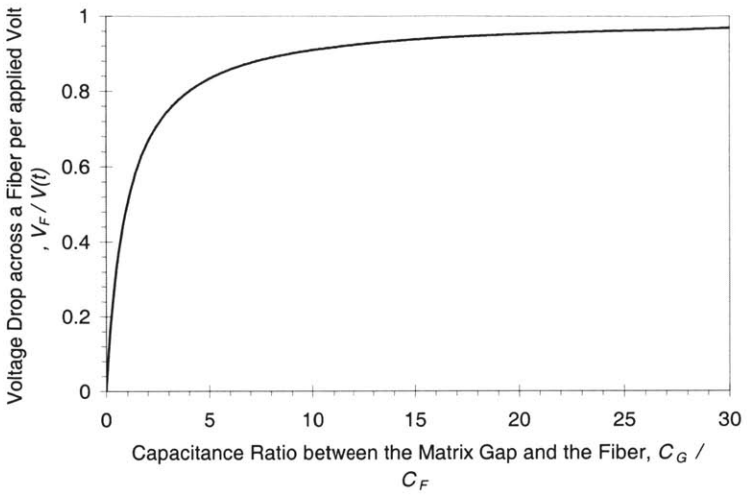

Figure 3.24 Voltage Drop across a Fiber per applied Volt versus the Capacitance Ratio between the Matrix Gap and the Fiber

As can be seen from Figure 3.24, $\overline{V}_F/\overline{V}$ in Equation 3.60 is zero when C_G / C_F is zero and asymptomatically approaches 1 as C_G / C_F approaches infinity. Thus to maximize the actuation per applied volt of the AFC/tmAFC one should maximize C_G / C_F.

The capacitance in the matrix gap is unknown and cannot be estimated easily because the thickness of the matrix gap in the y direction is a function of x. As mentioned in Section 3.4, the electric field is not uniform in direction and thus the capacitance cannot be estimated easily. Because the matrix is electrically isotropic, it is known that the capacitance of the matrix gap is proportional to the dielectric constant of the matrix gap, K_M:

$$C_G = \varepsilon_0 K_M \widetilde{C}_G \tag{3.61}$$

Where $\widetilde{C}_G$ is an unknown constant dependant on the geometry of the matrix gap with units of length. The capacitance of the fiber is harder to estimate because the capacitance of the fiber is dependant on stresses and the electric fields in the fiber, and is thus dependant on $\underline{\underline{s}}^E$, $\underline{d}$, and $\underline{\underline{\varepsilon}}^T$ of the fiber. If it is assumed that the stresses in the fiber are approximately equal to zero during actuation, then the capacitance can be written as:

$$C_F \cong \varepsilon_0 K_{33}^T \widetilde{C}_F \tag{3.62}$$

Where K_{33}^T is the *33* dielectric under stress free conditions, and $\widetilde{C}_F$ is an unknown constant dependant on geometry with units of length. $\widetilde{C}_F$ should not be dependant on the ratio of K_{33}^T to K_{31}^T, as is typical with solutions with anisotropic dielectric matrices, because the electric field always follows the *3* direction in the fiber. Thus using Equations 3.61 and 3.62, Equation 3.60 is given by:

$$\frac{\overline{S}_{zz}}{\overline{V}} \propto \frac{\left(K_M/K_{33}^T\right)\left(\widetilde{C}_G/\widetilde{C}_F\right)}{1+\left(K_M/K_{33}^T\right)\left(\widetilde{C}_G/\widetilde{C}_F\right)} \qquad \xi > 100\,\% \tag{3.63}$$

Thus to receive the maximum strain per applied volt for an AFC/tmAFC with ξ > 100 %, one should either find a matrix material with as large a dielectric constant as possible (maximize K_M/K_{33}^T) or change the geometry to maximize $\widetilde{C}_G/\widetilde{C}_F$ (such as decreasing γ). It should be noted that the ratio K_M/K_{33}^T is always greater than zero. By maximizing the electric field in the fiber, the voltage drop across the matrix gap (Equation 3.57) is minimized, and therefore the potential for dielectric breakdown in the matrix gap decreased.

Since the two capacitors are in parallel, the stress free capacitance of the AFC/tmAFC, C^T, for ξ > 100 %, can be estimated by:

$$C^T \cong C_F \frac{C_G/C_F}{C_G/C_F+1} \tag{3.64}$$

Therefore, using Equations 3.61, 3.62, and 3.64:

$$C^T \cong \varepsilon_0 K_{33}^T \widetilde{C}_F \frac{\left(K_M/K_{33}^T\right)\left(\widetilde{C}_G/\widetilde{C}_F\right)}{1+\left(K_M/K_{33}^T\right)\left(\widetilde{C}_G/\widetilde{C}_F\right)} \qquad \xi > 100\,\% \tag{3.65}$$

Thus, increasing K_M/K_{33}^T increases the stress free capacitance of the AFC/tmAFC to a maximum of C_F. Changing the geometry to increase $\widetilde{C}_G/\widetilde{C}_F$ increases the stress free capacitance of the AFC/tmAFC to a maximum of C_F also. Using Equations 3.63 and 3.65, one can show that AFCs/tmAFCs with a high capacitance have a high strain amplitude per applied volt:

$$C^T \propto \overline{S}_{ZZ} \qquad \xi > 100\,\% \tag{3.66}$$

Inverting Equation 3.65 yields:

$$\frac{1}{C^T} \cong \frac{1}{\varepsilon_0}\left[\frac{1}{K_M \widetilde{C}_G}+\frac{1}{K_{33}^T \widetilde{C}_F}\right] \qquad \xi > 100\,\% \tag{3.67}$$

A key assumption in the uniform fields model is that $\widetilde{C}_G$ is inversely proportional to $c + \gamma$ where c is a constant greater than zero which is dependant on the fiber geometry (square, circular, ect.):

$$\widetilde{C}_G \cong \frac{\widetilde{A}_G}{c+\gamma} \tag{3.68}$$

Where $\widetilde{A}_G$ is the effective area of the capacitance of the matrix gap (capacitance for a rectangular capacitor = Permittivity times Area / Length). Inserting Equation 3.68 into Equation 3.67 yields:

$$\frac{1}{C^T} \cong \frac{1}{\varepsilon_0 K_M \widetilde{A}_G}\gamma + \left[\frac{c}{\varepsilon_0 K_M \widetilde{A}_G} + \frac{1}{\varepsilon_0 K_{33}^T \widetilde{C}_F}\right] \qquad \xi > 100\% \qquad (3.69)$$

Using the assumption in the uniform fields model that the capacitance of the matrix gap is inversely proportional to $c + \gamma$, the inverse of the capacitance is linear with respect to γ for $\xi > 100\%$. This assumption will be tested in Section 3.8.4

In Reference [89], the 2 capacitor model of an AFC/tmAFC with $\xi > 100$ % was extended to include electrical conduction. In this case, free charge from the electrode could migrate from through the AFC/tmAFC, building up on interfaces between different materials, such as the fiber and the matrix. This charge buildup in the AFC/tmAFC would change the electric fields and electric potential within the fiber. The free charge migration was not instantaneous, but occurred with time constants on the order of hundreds of seconds. Thus, the model was useful in predicting the electric fields in an AFC/tmAFC when a voltage is applied for a long time, such as poling, or when a DC voltage is applied to the AFC/tmAFC. For sinusoidal actuation of the AFC/tmAFC using driving frequencies greater than 0.1 Hz, no charge migration would occur and the model reduced to the two capacitor model.

3.8 Finite Element Modeling of the Active Area of PiezoFlex AFCs

In order to determine the effect of the Young's Modulus, Poisson's ratio, and dielectric of the matrix on the actuation properties of PiezoFlex AFCs, a finite element model of the active area was constructed using ANSYS. A FEM model of the $1/8^{th}$ single fiber (Figure 3.19) is shown in Figure 3.25.

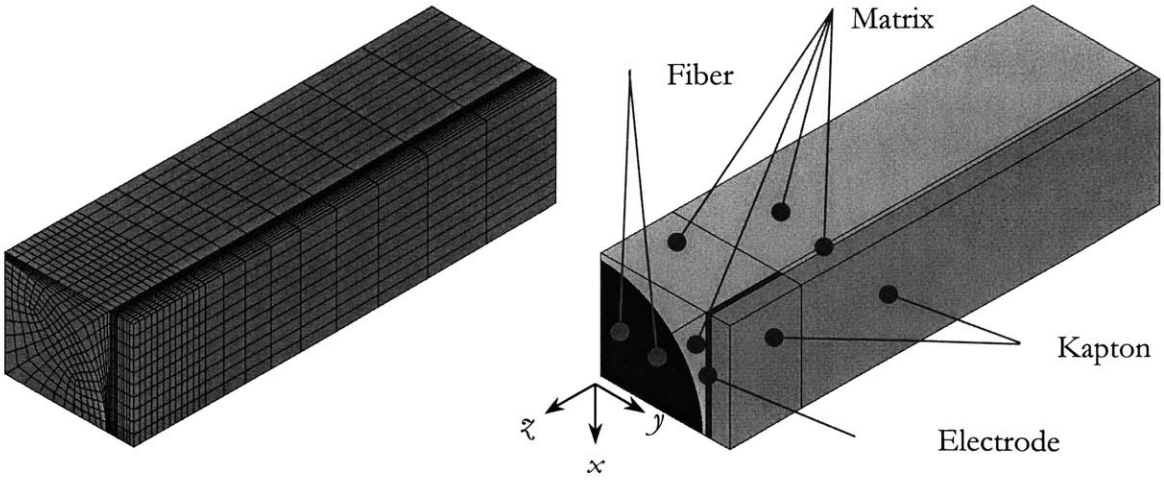

Figure 3.25 One-Eighth FEM Model of a Single fiber of a PiezoFlex AFC with $\xi > 0$, 8400 Elements and 9680 Nodes

It should be noted that Figure 3.25 is rotated 90° about the z-axis compared to Figure 2.5 and Figure 3.19. The volume of the AFC modeled in Figure 3.25 represents the volume in Figure 3.19, which is the same as the volume in Figure 2.5 bounded by $x = -W/2$, $x = 0$, $y = 0$, $y = h/2$, $z = L/2$, and $z = L$. This FEM model was constructed using the geometry shown in Table 3.3 with the parameters illustrated in Figure 2.5:

Table 3.3 PiezoFlex AFC Geometrical Properties Used for the FEM Model

Parameter	**Value**	**Reference**
L	1.143 mm (45 mil)	Table 2.2
L_F	191 μm (7.5 mil)	Table 2.2
W	288 μm (11.3 mil)	Table 2.2 and Equation 2.5
h	343 μm (13.5 mil)	Table 2.2
h_A	292 μm (11.5 mil)	Table 2.2
γ	Variable	
R	135 μm (5.3 mil)	Table 2.2

The distance between the electrode and the fiber was varied to determine the effect of the matrix gap, γ, on the actuation of the AFC. The geometry was meshed using piezoelectric 8 node SOLID5 3-d coupled field brick elements with displacement and voltage degrees of freedom using a static model. x-y cross sections of the mesh was uniform with elements of varying length along the length of the fiber with most elements being concentrated between the electrode and the interface between the fiber and the matrix.

It was assumed that the fiber was uniformly poled in z direction along the entire length of the fiber because a poling direction must be specified in ANSYS. Material properties for the Kapton layer and the PZT-5A fibers are given in Table 2.2 and Table 2.5 respectably. The baseline material properties and ranges for the matrix are given in Table 2.4, however the material properties were varied in the finite element model to determine the effect of the matrix material on the AFC. The electrode was assumed to have the same material properties as the matrix.

The electrode fingers were modeled by applying the driving voltage over a volume of nodes only in the matrix. This volume of nodes in the matrix was bounded by $x = -W/2$, $x = 0$, $y = R + \gamma$, $y = +h_A/2$, $z = L - L_F$, $z = L$. The distance between the fiber and the electrode, γ, was varied.

3.8.1 Finite Element Modeling of the Actuation of a PiezoFlex AFC under Stress Free Conditions

Consider the case where the AFC is stress free and a voltage is applied to the electrodes to induce strain. On the outer surfaces of Figure 2.5, the stresses are equal to zero. The AFC was subjected to a driving voltage of 2000 V between the fingers. This was accomplished by applying a voltage of 1000 V at the finger and grounding the interface at $z = L/2$.

At the areas $x = 0$, $y = 0$ and $z = 0$ the nodal displacements in the x, y, and z directions respectively were set to zero. Nodal displacements in the z direction at the area $z = L$ were forced to move together as well as displacements in the x direction at $x = -W/2$. At $y = h/2$ a pressure and a surface charge equal to zero was applied. At $x = -W/2$ a free surface charge equal to zero was applied. The free surface charge is given by Equation 3.13. These areas of no free surface charge are applied to materials with electrically isotropic constitutive relations, therefore on these areas the electric displacement and the electric field perpendicular to the area is zero.

For this case the actuation strain in the xx and zz directions is given by:

$$S_{xx}(x,y,z) = \frac{2u(-W/2,y,z)}{W} \tag{3.70}$$

$$S_{zz}(x,y,z) = \frac{2w(x,y,L)}{L} \tag{3.71}$$

Where u and w is the displacements in the x and z directions respectively. The strain per unit volt, Γ, for the single fiber and the active area can then be determined from Equation B.75 by setting $T = 0$:

$$(\Gamma_{xx})_F = (\Gamma_{XX})_A = -\frac{S_{xx}}{2V} \tag{3.72}$$

$$(\Gamma_{zz})_F = (\Gamma_{ZZ})_A = -\frac{S_{zz}}{2V} \tag{3.73}$$

Where V is the applied voltage at one of the electrode fingers (1000 V). The factor of 2 is present in Equations 3.72 and 3.73 because only 1000 V was applied to the $1/8^{th}$ finite element model. This voltage is doubled when applied across the entire fiber shown in Figure 2.5. The minus sign appears in Equations 3.72 and 3.73 because the electric field produced by the applied voltage is in the $-z$ direction, while the remnant polarization is in the $+z$ direction. Thus, the voltage being applied is in the "negative voltage direction", as defined in Section II.3. This problem could have been fixed by reversing the voltage (technically the AFC would be running with a DC offset), reversing the poling direction in the finite element

model (the help for this command was unclear), or by multiplying the values by –1. The multiplication was the chosen solution.

The effect of the closest distance the electrode is from the center of the AFC divided by the fiber radius, ξ, on the stress free actuation of the AFC active area in the X and Z directions, is shown in Figure 3.26.

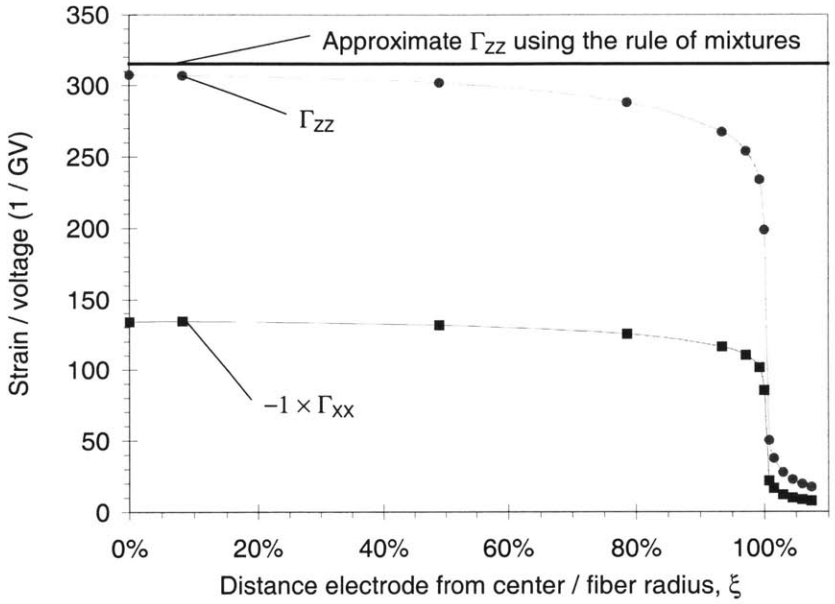

Figure 3.26 Stress Free Actuation of the Active Area of a CP PiezoFlex AFC as a Function of ξ

In Figure 3.26 it can be see that $(\Gamma_{ZZ})_A$ increases dramatically as the fiber touches the electrode and quickly increases to a steady state of 307 4 (1 / GV), the value for a mpAFC. For the active area of a PiezoFlex AFC $(\Gamma_{XX})_A$ / $(\Gamma_{ZZ})_A$ = -0.43 for all values of ξ. Using the data in Table 2.5, for PZT-5A d_{31} / d_{33} = -0.46 which is very close to the value of $(\Gamma_{XX})_A$ / $(\Gamma_{ZZ})_A$, and therefore the geometry of the AFC does not reduce the actuation strain ratio of the fibers dramatically.

$$\frac{(\Gamma_{XX})_A}{(\Gamma_{ZZ})_A} = -0.43 \cong \frac{d_{31}}{d_{33}} \tag{3.74}$$

As can be seen from Figure 3.26, if there is a layer of matrix between the fiber and the electrode (ξ > 100 %) the actuation is very low compared to the Γ_{ZZ} for the mpAFC. In Figure 3.27 the potential is plotted for a PiezoFlex AFC with ξ equal to 105%, 100%, 79% and 0%.

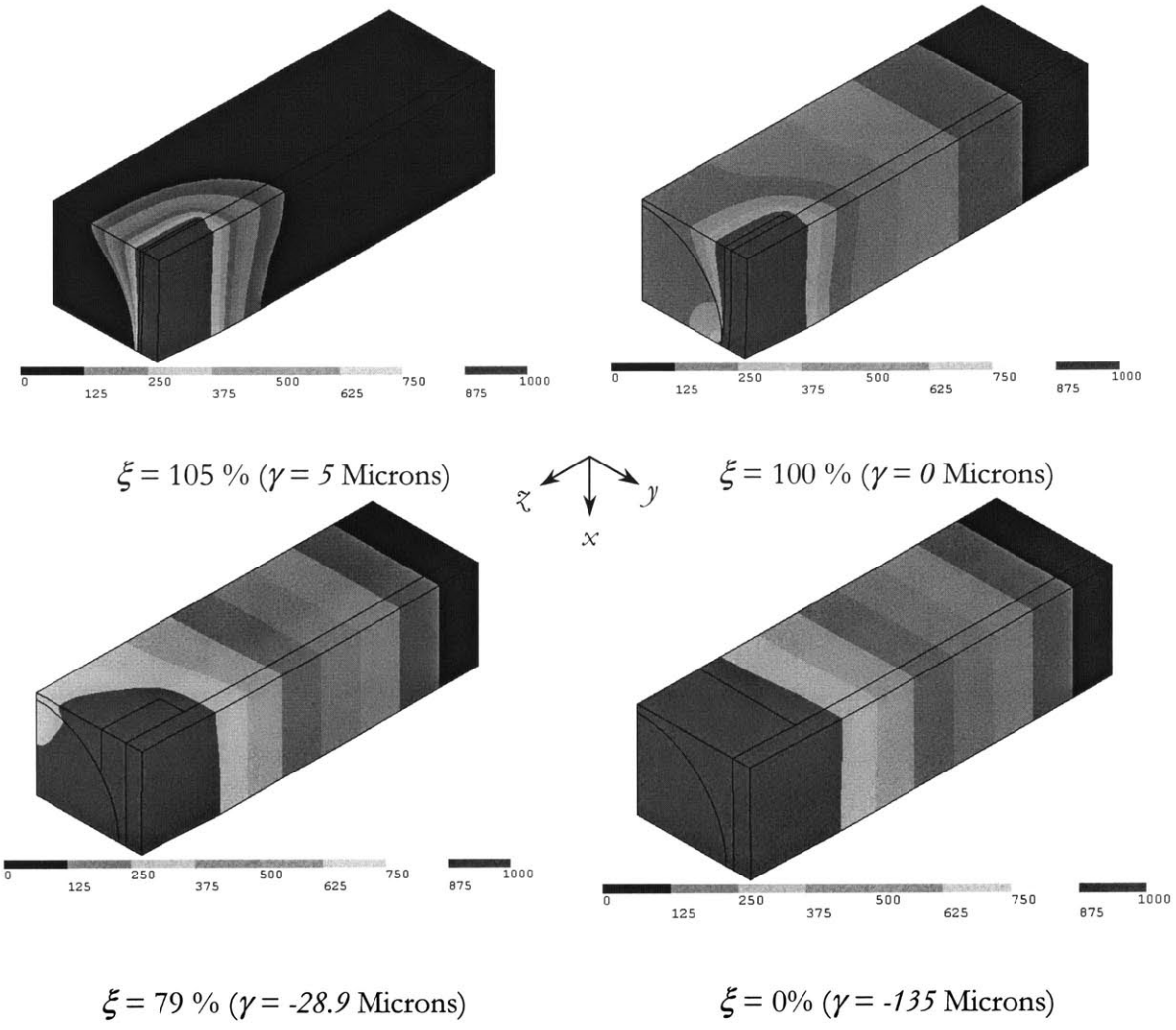

Figure 3.27 Electric Potential in the Active Area for a PiezoFlex AFC for ξ =0%, 79%, 100%, and 105%

Comparing the four plots, as ξ decreases, the potential lines straighten between the fingers and the electric field becomes stronger in the z direction. Because the electric field is stronger in between the fingers as ξ decreases, from Equation 1.2, the actuation will increase, as seen in Figure 3.26. This behavior of the straightening of the potential lines between the electrodes was seen in the interdigitated rectangle in Figure 3.9.

The electric potential for ξ = 105 % (γ = *5* Microns) is shown in Figure 3.28.

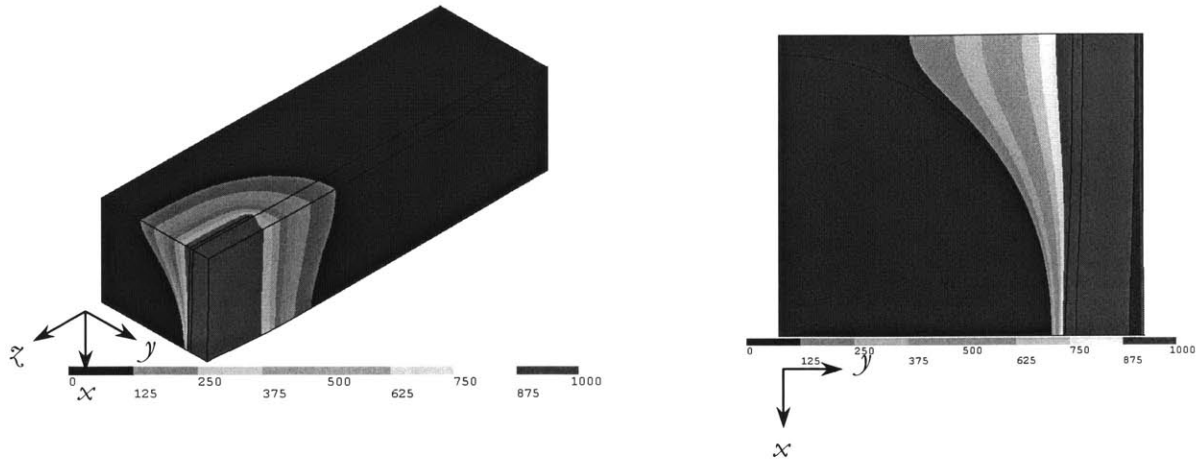

Figure 3.28 Electric Potential in the Active Area in a PiezoFlex AFC for ξ = 105 % (γ = 5 Microns)

As can be seen in Figure 3.28, a large potential drop occurs between the electrodes and the fiber in the matrix gap. This potential drop was seen for values of ξ greater than 100 % in the interdigitated block in Figure 3.9. For the interdigitated block, the dielectric mismatch between the polymer gap and the high dialectic material caused a large voltage drop, and thus a high electric field, in the polymer gap (Equation 3.21). The electric field in the polymer gap is greater that the electric field in the fiber, and as mentioned in Section 3.4, is a potential location for dielectric breakdowns. As can be seen in Figure 3.28 the voltage drop between the electrode and the fiber is approximately 889 V (1000 V – 111.111 V) over a distance of 5 microns. Therefore, the electric field between the fiber and the electrode is approximately 178 kV/mm, which is over 100 times greater than the nominal electric field in the fibers (2000 V / 1.143 mm = 1.75 kV/mm), the applied voltage divided by the center-to-center electrode spacing of the electrode fingers. For values of ξ greater than 100 % the electric field in the matrix gap between the fiber and the matrix can be very large compared to the nominal electric field in the fibers, and has the potential to cause dielectric breakdowns, as mentioned in Section 3.7.

As mentioned previously, when ξ < 100 %, $(\Gamma_{ZZ})_A$ is nearly independent of ξ. In Figure 3.26, the approximate $(\Gamma_{ZZ})_A$ for an mpAFC is plotted (Equation 3.46). As can be seen in Figure 3.26, Equation 3.46 does a very good job approximating the strain per unit volt under stress free conditions in the fiber direction for an mpAFC with a percent error of about 2.5%. Thus for ξ < 100 %, $(\Gamma_{ZZ})_A$ can be approximately written as:

$$(\Gamma_{zz})_A \cong \frac{\pi R^2}{\mathcal{V}} \frac{d_{33} Y_{33}^E}{E_M \left(\mathcal{W} h_A - \pi R^2\right) + E_K \left(\mathcal{W}\left(h - h_A\right)\right) + Y_{33}^E \left(\pi R^2\right)} \qquad \xi < 100\% \quad (3.75)$$

From the above discussion it would seem that in order to have the "best" AFC it would be most desirable to manufacture mpAFCs because they have the highest Γ_{zz}. However, AFCs with electrodes that barely touch the fiber (ξ = 100%) have only 35% less actuation than do mpAFCs as shown in Figure 3.29:

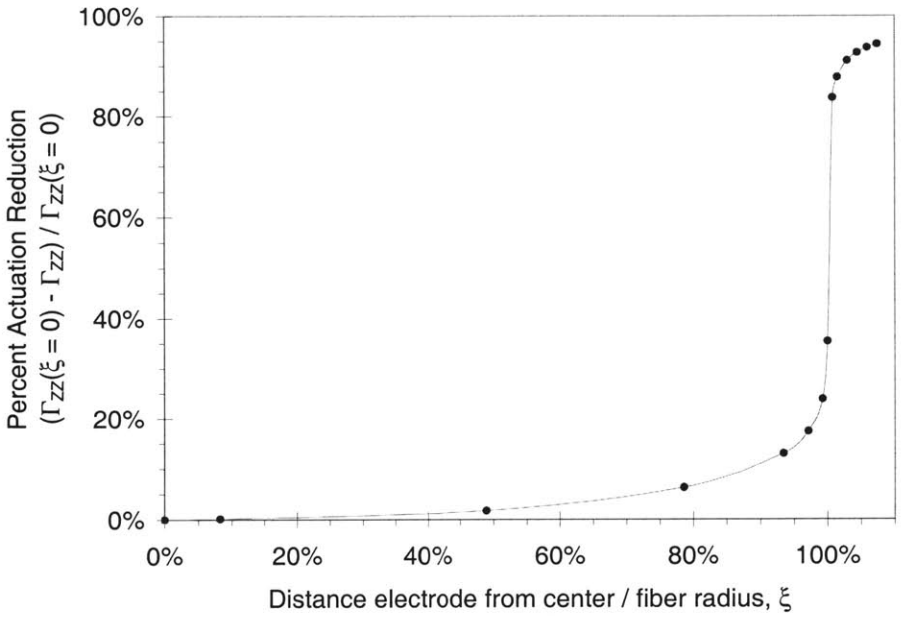

Figure 3.29 Reduction in Actuation (Compared to mpAFCs) versus ξ

As can be seen in Figure 3.29, AFCs with ξ greater than 100 % barely actuate compared to mpAFCs, however once the electrode barely touches the fiber the actuation reduction decreases dramatically. At ξ about equal to 72 % the actuation is 95 % of the mpAFCs. As will be discussed in Chapter 4, as ξ is decreased more and more, the angle that the electrode must conform to between fibers becomes sharper and sharper, increasing the chance that the electrode will break and thus making manufacturing increasingly difficult. When choosing the manufacturing techniques there is a trade off between the ease of manufacturing and decreasing ξ. This tradeoff was illustrated in the unconventional and difficult manufacturing techniques of Reference 53 to manufacture AFCs with ξ = 0 %. The "best" AFC is one that can be manufactured easily and provide the level of actuation desired. Therefore, a simple manufacturing technique that produces an AFCs with ξ less than 100% is highly desirable.

As seen in Figure 3.29, for ξ = 100% and 100.7%, the actuation is reduced 35.4 % and 83.7% percent respectively compared to an mpAFC. This corresponds with a 0 μm and a 1 μm (0 mil and 0.039 mil) gap between the electrode and the fiber. Thus as can be seen from Figure 3.29, even the smallest gap between the electrode and the fiber dramatically reduces the actuation of the AFC.

In order to guarantee convergence for the finite element results of Figure 3.26, the number of nodes was increased until the change in Γ_{ZZ} would be less than 2 % if the number of nodes were doubled. The number of nodes used was between 13,200 and 29,438 for a run time of about 15 minutes to several hours. For γ = *-1, 0,* and *1* microns, the solution for Γ_{ZZ} converged more slowly due to the sharp angle of the interface of the matrix between the electrode and the fiber. In order to prevent the processing capabilities of the computer from being exceeded, a less strict convergence criteria was selected for the three values of γ. For γ = *-1, 0,* and *1* microns the number of nodes was increased until the change in Γ_{ZZ} would be less than 5 % if the number of nodes was doubled. Convergence of $(\Gamma_{ZZ})_A$ and C_F^T (the stress free capacitance of a single fiber presented in Section 3.8.4) for ξ = 0% (γ = -135 microns) and ξ = 100% (γ = 0 microns) is plotted in Figure 3.30

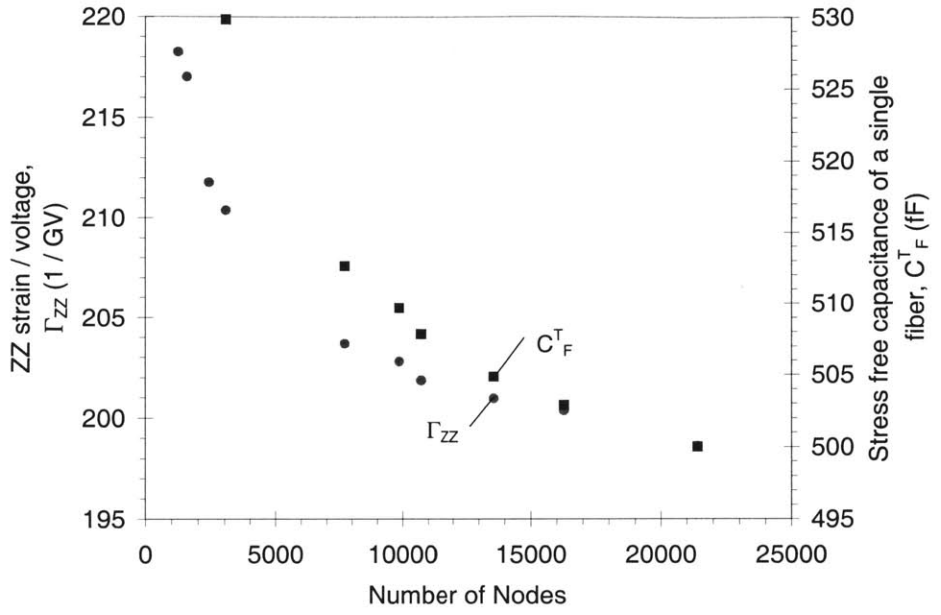

Electrode barely touches fiber, $\xi = 100$ % ($\gamma = 0$ microns)

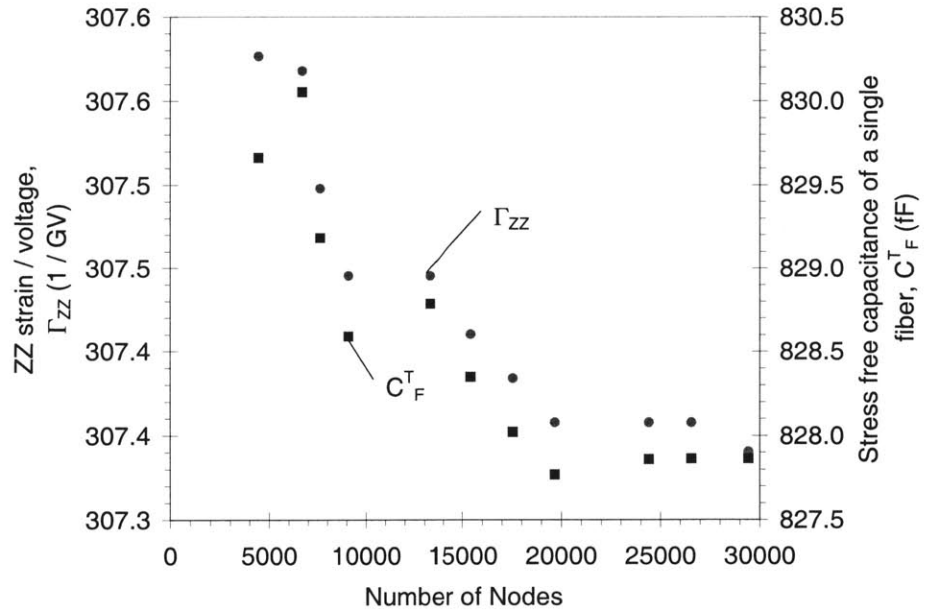

mpAFC, $\xi = 0$ % ($\gamma = -135$ microns)

Figure 3.30 *ZZ* Strain per unit Volt and Capacitance under Stress Free Conditions versus the Number of Nodes used in the Finite Element Model

In Figure 3.30 we can see that for $\xi = 0\%$, $(\Gamma_{ZZ})_A$ and C_F^T converged very rapidly. This is because the geometry is regular and the electric field is nearly constant between the electodes, as seen in Figure 3.27. For $\xi = 100\%$, $(\Gamma_{ZZ})_A$ and C_F^T converged much more

slowly. This is because the sharp angle between the electrode and the fiber causes the electric field to bend and twist and thus the field lines are non-uniform, as seen in Figure 3.27. These two cases represent the fastest converging and slowest converging cases for the finite element model. When plotting the results throughout this section, 29438 and 21411 nodes were used for ξ = 0% and ξ = 100% respectively. Although more nodes were used for ξ = 0%, the run time for the finite element analysis was approximately the same for the two cases.

In order to determine the effect the matrix material properties have on the actuation of a PiezoFlex AFC the matrix material properties were varied and the resulting actuation was calculated, as seen in Table 3.4. In Table 3.4, the values for ξ are not at discrete intervals because γ was used in the finite element model and ξ was calculated after, and a programming error made some values of γ be non-round (the error did not effect the results, just the value of γ). In addition, more cases of γ were analyzed in areas where the output was changing dramatically to reduce the number of runs.

Table 3.4 Effect of Matrix Material Properties on the *ZZ* Strain per Unit Volt in the Active Area for a PiezoFlex AFC (in 1 / GV)

ξ	γ (μm)	**CP AFC**	ν_M = 0.3	ν_M = 0.4	E_M = 1.9 *GPa*	E_M = 3.9 *GPa*	K_M = 2.5	K_M = 4.7
107.4%	10	17.3	17.3	17.3	17.4	17.1	12.5	21.9
105.9%	8	19.5	19.5	19.5	19.6	19.3	14.0	24.6
104.4%	6	22.5	22.5	22.5	22.7	22.3	16.3	28.5
103.0%	4	27.5	27.5	27.5	27.7	27.2	19.9	34.6
101.5%	2	37.6	37.6	37.6	37.9	37.2	27.5	46.9
100.7%	1	50.0	50.0	50.0	50.5	49.5	37.1	61.6
100.0%	0	199	199	199	202	195	196	202
99.3%	-1	234	234	234	236	232	233	234
97.1%	-3.9	254	254	254	256	252	254	254
93.4%	-8.9	267	267	267	270	265	267	267
78.6%	-28.9	288	288	288	291	286	288	288
49.0%	-68.9	302	305	302	305	299	302	302
8.2%	-123.9	307	307	307	310	304	307	307
0.0%	-135	307	307	307	310	305	307	307

Where in Table 3.4, ν_M is the matrix Poisson's ration, E_M is the matrix Young's modulus, and K_M is the relative dielectric of the matrix. Using the data in Table 3.4, the percent change in $(\Gamma_{ZZ})_A$ per percent change in a matrix material property was calculated:

$$\frac{\text{Percent change in } (\Gamma_{ZZ})_A}{\text{Percent change in a matrix material property}} = \frac{\partial (\Gamma_{ZZ})_A}{\partial X} \frac{X}{(\Gamma_{ZZ})_A} \tag{3.76}$$

Where X is the material property in question. Because the data is in discrete points, the derivative in Equation 3.76 is calculated by using the finite difference equation:

$$\frac{\partial \left(\Gamma_{ZZ}(\xi, X)\right)_A}{\partial X} = \frac{\left(\Gamma_{ZZ}(\xi, X+h)\right)_A - \left(\Gamma_{ZZ}(\xi, X-h)\right)_A}{2h} \tag{3.77}$$

Where $2\ h$ is the difference between the maximum and minimum material property. For example, when calculating the material property for ν_M, $X = 0.35$, and $h = 0.05$.

$$\frac{\partial \left(\Gamma_{ZZ}(\xi, 0.35)\right)_A}{\partial \nu_M} = \frac{\left(\Gamma_{ZZ}(\xi, 0.4)\right)_A - \left(\Gamma_{ZZ}(\xi, 0.3)\right)_A}{2 \times 0.05} \tag{3.78}$$

The percent change in $(\Gamma_{ZZ})_A$ per percent change in a matrix material property versus ξ is plotted in Figure 3.31.

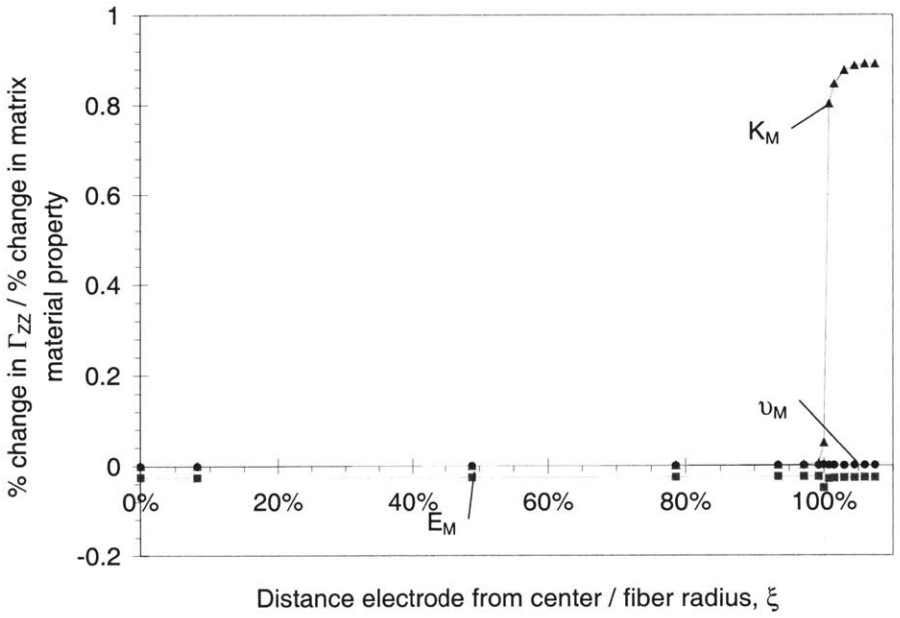

Figure 3.31 Percent Change in the *ZZ* Strain per unit Volt per Percent Change in a Matrix Material Property versus ξ for a PiezoFlex AFC

The material data in Table 2.4 for the average value and the range of matrix material properties for a PiezoFlex AFC was used to determine how much to vary the material properties for the finite element model. A typical engineering polymer has a Poisson's ratio from about 0.3 to 0.4. From Table 3.4 and Figure 3.31 it can be seen that the Poisson's ratio of the matrix has very little effect on the actuation properties of the AFC. As expected from Section 3.5.3, if the stiffness of the matrix is increased or decreased by 1 GPa the actuation is

reduced or increased respectively as seen in Table 3.4. From Figure 3.31 is can be seen that the percent change in $(\Gamma_{ZZ})_A$ per percent change in E_M is negative because a higher matrix stiffness reduces $(\Gamma_{ZZ})_A$. The percent change in $(\Gamma_{ZZ})_A$ per percent change in E_M is nearly independent of ξ. This is because the voltage supplied to the fiber is independent of E_M, however the actuation $(\Gamma_{ZZ})_A$ is inversely proportional to E_M, as shown in Equation C.41. If this data is extrapolated using a straight line at γ = -135 microns, then the difference in $(\Gamma_{ZZ})_A$ is approximately 14 1/GV at E_M = *1* GPa and E_M = *5* GPa (the approximate range in Young's modulus of unfilled engineering polymers). This is a very small percentage of the actuation of the mpAFC (14 / 307 = 4.5%), and thus we can say for an unfilled engineering polymer that the actuation does not depend greatly on the Young's modulus of the matrix.

As mentioned in Section 2.3.1, the average relative dielectric of a polymer is 3.6 with a standard deviation of 1.1. For positive values of γ, changing the relative dielectric of the matrix by one standard deviation has a very large effect on the actuation of the AFC. For γ = 10 microns the change in actuation is about 25 %. This is because normal to the fiber matrix interface the electric displacement must be equal and that dielectric mismatch between the fiber and the matrix causes a large voltage drop in the gap between the fiber and the electrode. This voltage drop can be approximated by assuming that the gap acts as a capacitor with a low capacitance in series with the high capacitance fiber, as was done in Section 3.7. Thus, increasing the dielectric of the matrix increases the electric field in the fiber (Equation 3.21) and yields a higher output strain (Equation 3.63). For γ less than zero, the matrix dielectric has little effect on the actuation of the AFC, because the electrode is directly touching the fiber and therefore majority of the field in the fiber is given by the voltage divided by the length of the fiber. Thus it can be said that changing the matrix dielectric for γ greater than zero has a very large effect on the AFC, but almost no effect for γ less than zero.

3.8.2 Finite Element Modeling of the Shorted Stiffness of a PiezoFlex AFC

A finite element analysis was performed to determine the shorted stiffness in the active area for a PiezoFlex AFC. The model was similar to the actuation model, Section 3.8.1, except that all the voltage degrees of freedom set to zero, and a 1 MPa compressive stress was applied over the area at $z = \ell$:

$$T_{zz}(x, y, \ell) = -1 \text{ MPa} \tag{3.79}$$

The shorted *ZZ* Young's modulus, $\left(Y_{ZZ}^{V}\right)_A$ and the shorted *ZX* Poisson's ratio $\left(\sigma_{ZX}^{V}\right)_A$ were determined using:

$$\left(Y_{ZZ}^{V}\right)_{A} = \frac{T_{zz}}{S_{zz}} \tag{3.80}$$

$$\left(\sigma_{ZX}^{V}\right)_{A} = -\frac{S_{xx}}{S_{zz}} \tag{3.81}$$

The strains in the AFC were determined using Equations 3.70 and 3.71. The Shorted *ZZ* Young's modulus, $\left(Y_{ZZ}^{V}\right)_{A}$ and the shorted *ZX* Poisson's ratio $\left(\sigma_{ZX}^{V}\right)_{A}$ versus ξ for a PiezoFlex AFC, (Equations 3.80 and 3.81) are plotted versus ξ for a PiezoFlex AFC in Figure 3.32.

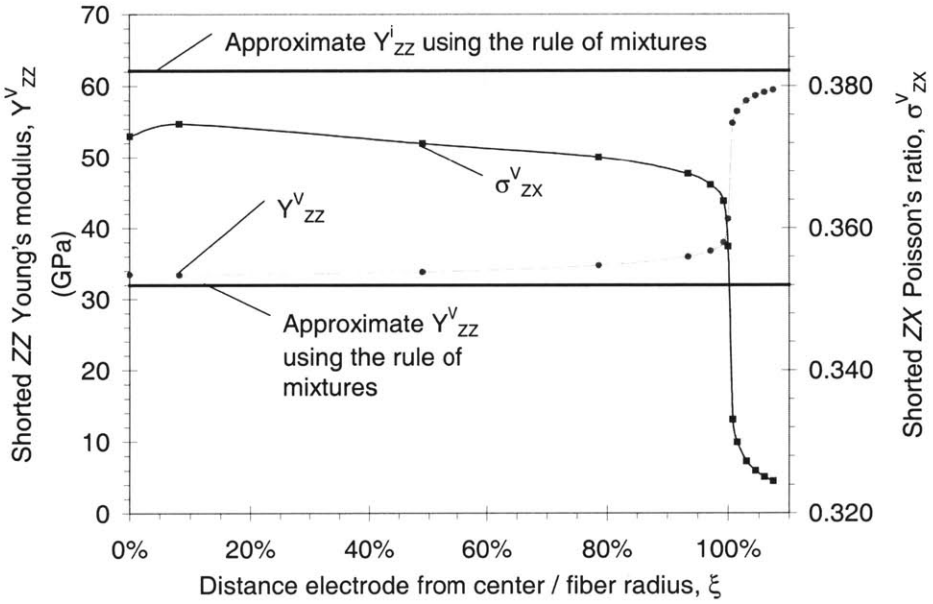

Figure 3.32 Shorted *ZZ* Young's Modulus and the Shorted *ZX* Poisson's Ratio versus ξ for a PiezoFlex AFC

In Figure 3.32 the approximate short circuit and open circuit Young's modulus (Equations 3.36 and 3.40 respectively) is plotted for a PiezoFlex AFC. As can be seen in Figure 3.32 the approximate short circuit Young's modulus best predicts the Young's modulus for values of ξ close to 0 % (for an mpAFC). For this case, the electrode partially touches the fiber and shorting the voltage of the AFCs forces the electric field in the fiber to be zero. For the case where ξ is greater than 100 %, the electrode does not touch the fiber. When a force is applied to AFC chare is generated at the fiber surface. If the electrode touches the fiber this charge would be nullified when the electrodes are shorted. However, if a layer of matrix exists the charge on the fiber surface cannot dissipate if the electrodes are shorted, because of the assumption of zero conductivity. Therefore, the fibers act as if they are open circuited and the AFC's short-circuited stiffness appears to be that of the zero current stiffness, $\left(Y_{ZZ}^{i}\right)_{A}$ (Equation 3.40).

In order to determine the effect the matrix material properties have on the shorted stiffness of a PiezoFlex AFC, the matrix material properties were varied and the resulting stiffness was calculated, as seen in Table 3.5.

Table 3.5 Effect of Matrix Material Properties on the Shorted Young's Modulus in the Active Area for a PiezoFlex AFC (in GPa)

ξ	γ (μm)	**CP AFC**	ν_M = 0.3	ν_M = 0.4	E_M = 1.9 *GPa*	E_M = 3.9 *GPa*	K_M = 2.5	K_M = 4.7
107.4%	10	59.4	59.4	59.4	58.9	60.0	60.2	58.7
105.9%	8	59.1	59.1	59.1	58.6	59.7	59.9	58.3
104.4%	6	58.6	58.6	58.6	58.1	59.2	59.6	57.7
103.0%	4	57.9	57.9	57.9	57.4	58.5	59.0	56.9
101.5%	2	56.4	56.4	56.4	55.9	57.0	57.9	55.2
100.7%	1	54.8	54.8	54.8	54.2	55.3	56.5	53.3
100.0%	0	41.3	41.3	41.3	40.7	41.9	41.5	41.1
99.3%	-1	38.0	38.0	38.0	37.7	38.3	38.0	38.0
97.1%	-3.9	36.8	36.8	36.8	36.5	37.1	36.8	36.8
93.4%	-8.9	36.0	36.0	36.0	35.7	36.2	36.0	36.0
78.6%	-28.9	34.7	34.7	34.7	34.4	35.0	34.7	34.7
49.0%	-68.9	33.8	33.8	33.8	33.5	34.1	33.8	33.8
8.2%	-123.9	33.4	33.4	33.4	33.1	33.7	33.4	33.4
0.0%	-135	33.4	33.4	33.4	33.2	33.7	33.4	33.4

Were in Table 3.5, ν_M is the matrix Poisson's ration, E_M is the matrix Young's modulus, and K_M is the relative dielectric of the matrix. Using the data in Table 3.5 and Equation 3.77, the percent change in $\left(Y_{ZZ}^{V}\right)_A$ per percent change in a matrix material property was calculated:

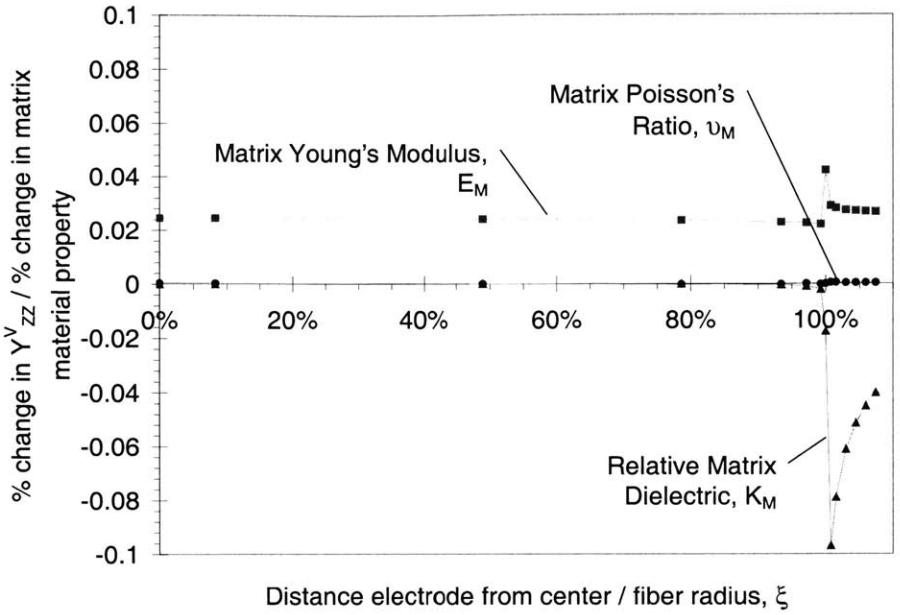

Figure 3.33 Percent Change in Shorted Young's Modulus per Percent Change in a Matrix Material Property versus ξ for a PiezoFlex AFC

The material data in Table 2.4 for the average value and the range of matrix material properties for a PiezoFlex AFC was used to determine how much to vary the material properties for the finite element model. As can be seen in Table 3.5, changing the Poisson's ratio in the range of 0.3 to 0.4 has no discernable effect on the shorted stiffness of the active area of a PiezoFlex AFC. This is due to the fact that the fiber stiffness dominates the stiffness properties of the AFC as was discussed in Sections 3.5.1 and 3.5.2. Increasing the stiffness of the matrix by 1 GPa always increases the shorted stiffness of the active area, as was seen in Table 3.5. For ξ < 100 % the percent change in the shorted stiffness per percent change in matrix stiffness is approximately the same for the mpAFC, 0.025. This is because the shorted stiffness of an mpAFC is linear with the matrix stiffness (Equation 3.36), as should be an AFC. For ξ > 100 %, the active area of the AFC behaves as if it is open circuited. For an mpAFC the open circuit stiffness is the sum of the short circuit stiffness and an additional term which is comprised of $d_{33} \times Y_{33}^E$ and K for each material (Equation 3.40). From Figure 3.33, it can be seen that the shorted stiffness is a complex function of the matrix Young's modulus for ξ > 100 %.

As mentioned in Section 2.3.1, the average relative dielectric of a polymer is 3.6 with a standard deviation of 1.1. For γ less than zero, the matrix dielectric has little effect on the actuation of the AFC, because the electrode is directly touching the fiber and therefore the fiber acts as if it is completely shorted. For positive values of γ, changing the relative dielectric of the matrix by one standard deviation has a very large effect on the shorted

stiffness of the AFC. As mentioned previously, for an mpAFC the open circuit stiffness is a function of d, Y, and K for each material. For positive values of γ, increasing the matrix dielectric decreases the fiber stiffness. Thus it can be said that changing the matrix dielectric for γ greater than zero has a very large effect on the AFC, but almost no effect for γ less than zero. It should be noted that the percent change in short stiffness per percent change in a matrix material property for the matrix relative dielectric is smaller for the shorted stiffness case, Figure 3.33, than is the stress free actuation case, Figure 3.31.

3.8.3 Finite Element Modeling of the Stress per Unit Volt under Strain Free Conditions of a PiezoFlex AFC

A finite element analysis was performed to determine the stress per unit volt under strain free conditions in the active area for a PiezoFlex AFC. At the areas $x = 0, y = 0$ and $z = L/2$ the nodal displacements in the x, y, and z directions respectively were set to zero. In order to apply strain free conditions, all nodal displacements at $x = -W/2, y = h/2$, and $z = L$ were set to zero. The AFC was subjected to a driving voltage of 2000 V between the fingers by applying a voltage of 1000 V at the finger and grounding the interface at $z = L/2$. T_{xx}, T_{yy}, T_{zz} the stress in the xx, yy, and zz directions respectively, is given by:

$$T_{xx}(x,y,z) = \frac{4\sum F_x(-W/2,y,z)}{hL} \tag{3.82}$$

$$T_{yy}(x,y,z) = \frac{4\sum F_y(x,h/2,z)}{WL} \tag{3.83}$$

$$T_{zz}(x,y,z) = \frac{4\sum F_z(x,y,L)}{hW} \tag{3.84}$$

Where F_x, F_y, and F_z is the nodal force x, y, and z directions respectively which is summed over the entire area. The factor of 4 is present in Equations 3.82 - 3.84 because a $1/8^{th}$ finite element model of a single fiber is analyzed instead of the entire single fiber. The stress per unit volt, Ψ, for the single fiber and the active area can then be determined from Equation B.78 by setting $S = 0$:

$$(\psi_{xx})_F = (\psi_{XX})_A = -\frac{T_{xx}}{2V} \tag{3.85}$$

$$(\psi_{yy})_F = (\psi_{YY})_A = -\frac{T_{yy}}{2V} \tag{3.86}$$

$$(\psi_{zz})_F = (\psi_{ZZ})_A = -\frac{T_{zz}}{2V} \tag{3.87}$$

Where V is the applied voltage at one of the electrode fingers (1000 V). The factor of 2 is present in Equations 3.85 and 3.87 because only 1000 V was applied to the $1/8^{th}$ finite element model. This voltage is doubled when applied across the entire fiber shown in Figure 2.5.

The effect of the closest distance the electrode is from the center of the AFC divided by the fiber radius, ξ, on the stress per unit volt under a strain free conditions for the active area of a PiezoFlex AFC, is shown in Figure 3.34.

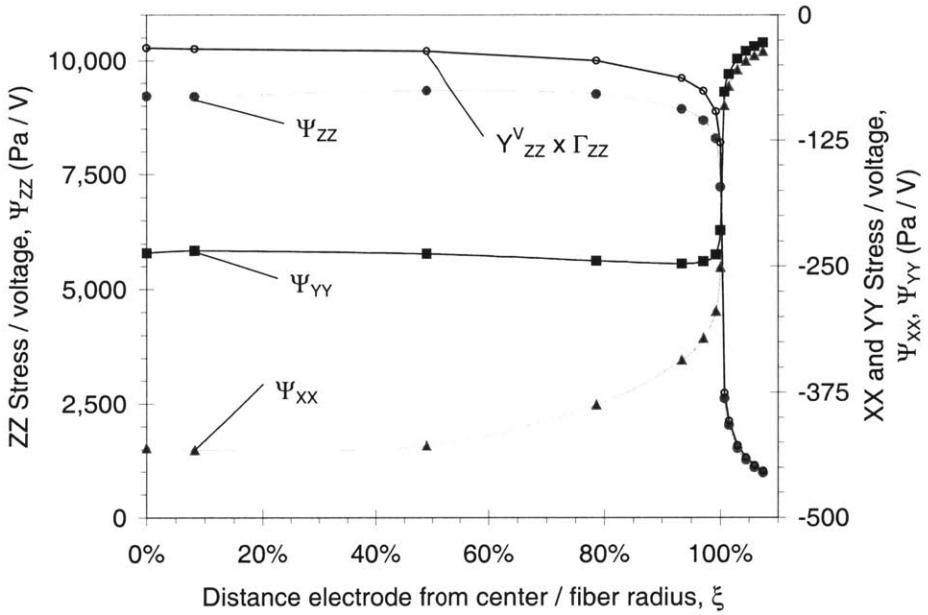

Figure 3.34 Stress per Unit Volt under a Strain Free Condition for the Active Area of a CP PiezoFlex AFC as a Function of ξ

In Figure 3.34 it can be see that $(\Psi_{ZZ})_A$ increases dramatically as the fiber touches the electrode and quickly increases to a steady state of 9,218 (Pa / V), the value for a mpAFC. For the active area of a PiezoFlex AFC, $(\Psi_{XX})_A$ / $(\Psi_{ZZ})_A$ ranges between –0.05 and –0.04. For the active area of a PiezoFlex AFC, $(\Psi_{YY})_A$ / $(\Psi_{ZZ})_A$ is about equal to –0.03. In Figure 3.34, the percent error between $(\Psi_{ZZ})_A$ and the approximation for $(\Psi_{ZZ})_A$ (Equation 3.51) yields a percent error between -4.7% and –13.5%, where the percent error is calculated from:

$$\text{Percent Error} = \frac{(\psi_{ZZ})_A - \Gamma_{ZZ} Y^V_{ZZ}}{(\psi_{ZZ})_A} \tag{3.88}$$

The average percent error is –8.6%. This average percent error was calculated by determining the area beneath the lines plotted in Figure 3.34 using the trapezoidal rule. These areas were substituting into Equation 3.88 in place of the values to determine the average percent error. Given the crudeness of the approximation when calculating $(\Psi_{ZZ})_A$

(all off axis terms are equal to zero), Equation 3.51 yields a good approximation to $(\Psi_{ZZ})_A$. It should be noted that in Figure 3.34, $(\Psi_{YY})_A$ and more obviously $(\Psi_{XX})_A$ appears to have a slightly different functional form when plotted against ξ than does $(\Psi_{ZZ})_A$ This may be due to the fact that $(\Psi_{ZZ})_A$ was used for the convergence criteria, and not $(\Psi_{XX})_A$ or $(\Psi_{YY})_A$. More likely this is due to the fact that $(\Psi_{ZZ})_A$ is mostly dependant on fiber properties and $(\Psi_{XX})_A$ and $(\Psi_{YY})_A$ are more dependant on matrix properties.

In order to determine the effect the matrix material properties have on the stress per unit volt under strain free conditions for the active area for a PiezoFlex AFC, the matrix material properties were varied and the resulting $(\Psi_{ZZ})_A$ was calculated, as seen in Table 3.6.

Table 3.6 Effect of Matrix Material Properties on the Stress per unit Volt under Strain Free Conditions for the Active Area for a PiezoFlex AFC (in Pa / V)

ξ	γ (μm)	**CP AFC**	ν_M = 0.3	ν_M = 0.4	E_M = 1.9 *GPa*	E_M = 3.9 *GPa*	K_M = 2.5	K_M = 4.7
107.4%	10	979	980	979	1010	957	716	1230
105.9%	8	1100	1100	1100	1130	1070	803	1370
104.4%	6	1260	1260	1260	1300	1240	926	1570
103.0%	4	1520	1520	1520	1570	1490	1120	1880
101.5%	2	2030	2030	2030	2090	1990	1520	2470
100.7%	1	2620	2620	2620	2690	2570	2000	3130
100.0%	0	7220	7230	7210	7470	7050	7140	7290
99.3%	-1	8280	8280	8270	8420	8180	8270	8290
97.1%	-3.9	8680	8680	8670	8830	8560	8680	8680
93.4%	-8.9	8930	8930	8920	9090	8800	8930	8930
78.6%	-28.9	9260	9250	9250	9450	9100	9260	9260
49.0%	-68.9	9340	9330	9340	9580	9150	9340	9340
8.2%	-123.9	9210	9219	9220	9490	8970	9210	9210
0.0%	-135	9220	9200	9230	9500	8990	9220	9220

Were in Table 3.6, ν_M is the matrix Poisson's ration, E_M is the matrix Young's modulus, and K_M is the relative dielectric of the matrix. Using the data in Table 3.6 and Equation 3.77, the percent change in $(\Psi_{ZZ})_A$ per percent change in a matrix material property was calculated:

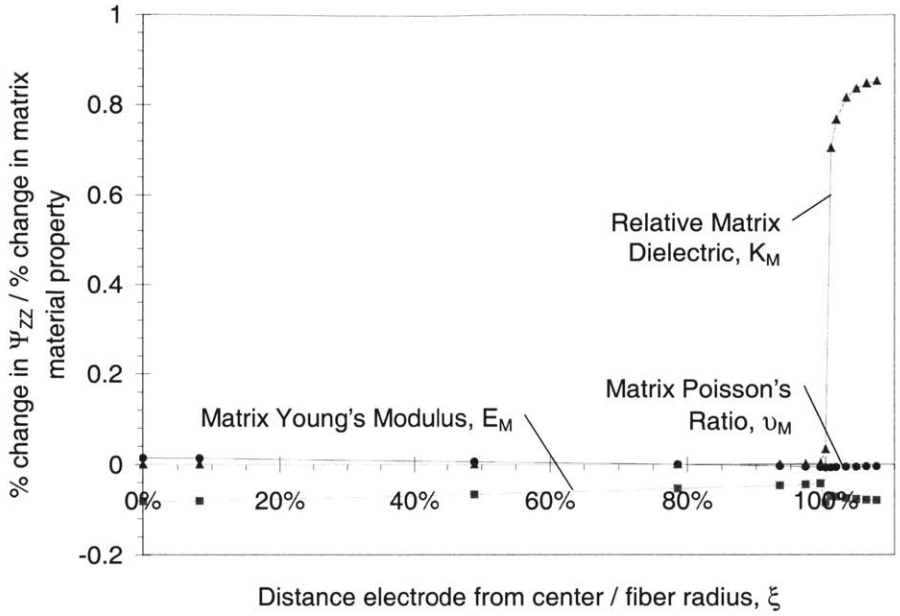

Figure 3.35 Percent Change in Stress per unit Volt under Strain Free Conditions per Percent Change in a Matrix Material Property versus ξ

The material data in Table 2.4 for the average value and the range of matrix material properties for a PiezoFlex AFC was used to determine how much to vary the material properties for the finite element model. As can be seen in Table 3.6, changing the Poisson's ratio in the range of 0.3 to 0.4 has only a small effect on the stress per unit volt under strain free conditions. This is because the fiber stiffness dominates the stress output in the *ZZ* direction. Increasing the stiffness of the matrix by 1 GPa always decreases the stress per unit volt under strain free conditions, as seen in Figure 3.35. For γ less than zero, the matrix dielectric has little effect on the stress per unit volt under strain free conditions, because the electrode is directly touching the fiber and therefore the fiber acts as if the entire voltage drop is across it. For positive values of γ, changing the relative dielectric of the matrix by one standard deviation has a very large effect on the stress per unit volt under strain free conditions. This is most likely because changing K_M has a large effect on $(\Gamma_{ZZ})_A$, as mentioned in Section 3.8.1, and from Equation 3.51, $(\psi_{ZZ})_A \cong (\Gamma_{ZZ})_A (Y^V_{ZZ})_A$.

3.8.4 Finite Element Modeling of the Stress Free and Strain Free Capacitance of a Single Fiber of a PiezoFlex AFC and Determination of the Electro-Mechanical Efficiency

A finite element analysis was performed to determine the stress free capacitance, C_F^T, and the strain free capacitance, C_F^S, of a single fiber.

Using the finite element model in Section 3.8.1, the stress free capacitance for a single fiber could be determined.

$$C_F^T = -2\frac{\sum q\left(x, y, \ell/2\right)}{V} \tag{3.89}$$

Where q is the charge which is summed over the entire area at $z = \ell/2$. In Equation 3.89, the minus sign appears because the capacitance is a positive quantity and at $z = \ell/2$ the model is grounded and thus the charge is negative for $V = 1000$, and therefore the negative sign used. The factor of 2 in the beginning of Equation 3.89 is due to the fact that the finite element model is a $1/8^{th}$ model of Figure 2.5. The capacitance of the fiber in Figure 2.5 is two times that of the $1/8^{th}$ model (four capacitors in parallel are in series with four capacitors in parallel).

Using the finite element model in Section 3.8.3, the strain free capacitance for a single fiber could also be determined. This capacitance was calculated in the same manner as Equation 3.89.

$$C_F^S = -2\frac{\sum q\left(x, y, \ell/2\right)}{V} \tag{3.90}$$

The effect of the closest distance the electrode is from the center of the AFC divided by the fiber radius, ξ, on the capacitance for a single fiber of a PiezoFlex AFC, is shown in Figure 3.36.

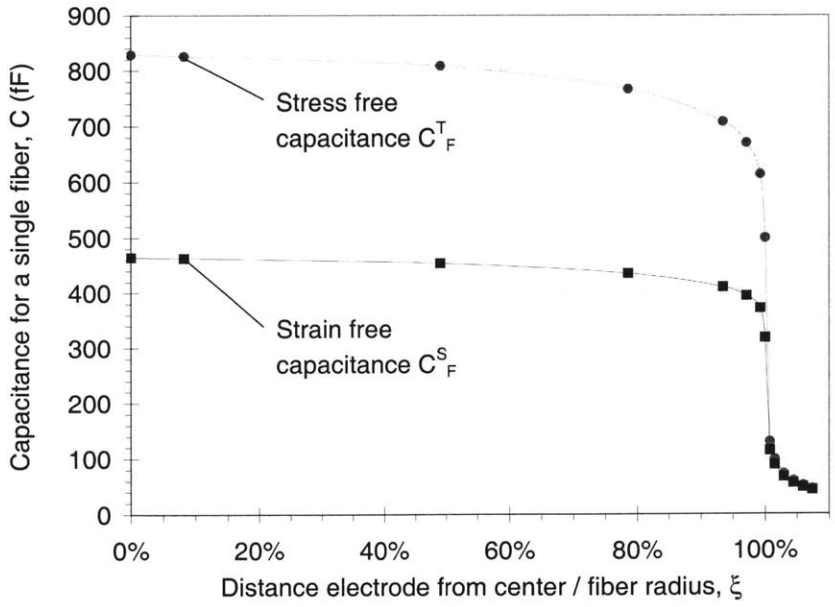

Figure 3.36 Stress Free and Strain Free Capacitance for a Single Fiber of a CP PiezoFlex AFC as a Function of ξ

As can be seen in Figure 3.36, the capacitance for $\xi > 100\%$ is very low, however when the electrode touches the fiber, the capacitance is almost the capacitance for the mpAFC. From Equation B.94, Subtracting the strain free capacitance from the stress free capacitance yields $(\underline{\Psi}\bullet\underline{\Phi})_F$.

In Section 3.7, it was determined that for an AFC with $\xi > 100\%$, the ZZ actuation strain is proportional to the stress free capacitance (Equation 3.66). Plotting the stress free capacitance versus the ZZ stain per unit volt under stress free conditions yields:

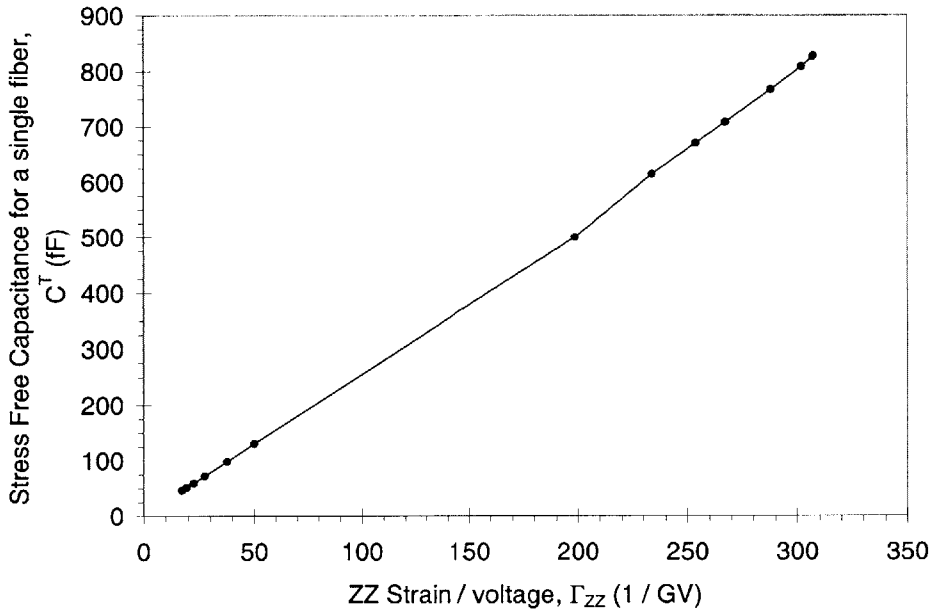

Figure 3.37 Stress Free Capacitance versus the ZZ Stain per unit Volt under Stress Free Conditions of a PiezoFlex AFC

In Figure 3.37, several things are apparent. First, the capacitance is nearly linear with strain thus justifying Equation 3.66. It appears hat this line is composed of two lines, one for $\xi > 0$ and $\xi < 0$, each with different slopes. It appears that the point for $\xi = 0$ is slightly off. This may be due to the difficulty achieving convergence for this point, as mentioned in 3.8.1.

As discussed in Section 3.7, using the assumption in the uniform fields model that the capacitance of the matrix gap is inversely proportional to $c + \gamma$, the inverse of the capacitance should be linear with respect to γ for $\xi > 100\%$. In Figure 3.38 the capacitance for a single fiber under stress free conditions and strain free conditions is plotted versus γ.

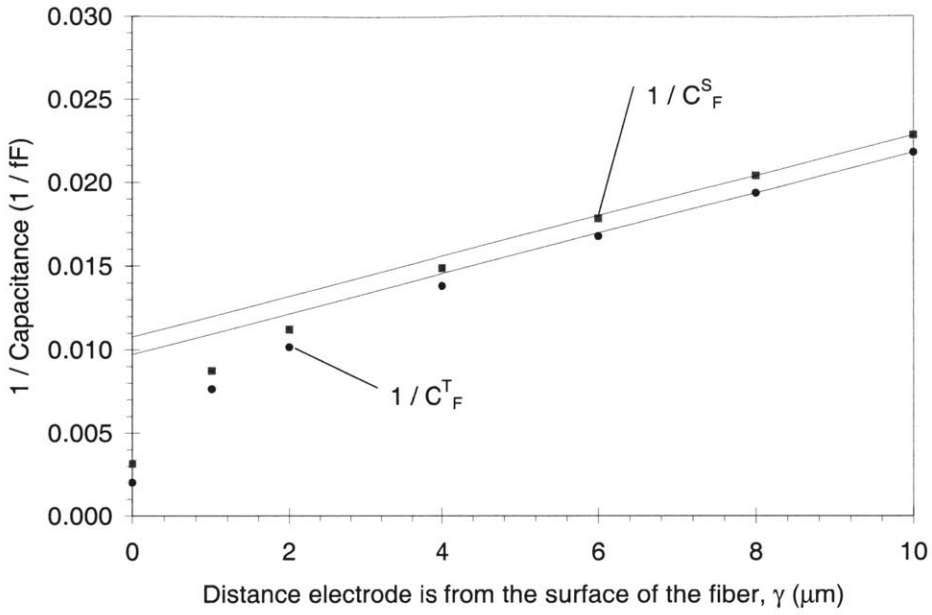

Figure 3.38 1 / Capacitance for a Single Fiber versus the Distance the Electrode is from the Surface of the Fiber, γ, for a PiezoFlex AFC

The two solid lines in Figure 3.38 are lines fitted to the points at $\gamma = 8$ and 10 μm. As can be seen in Figure 3.38, the capacitance for a single fiber under stress free conditions and strain free conditions is approximately linear with respect to γ for larger values of γ greater than 2 μm thus justifying Equation 3.68. However, as γ approaches zero, Equation 3.69 appears to hold less and less. At $\gamma = 6$, 2, and 0 μm the percent error between $1/C_F^T$ and the fitted lines is –1.2%, -19.7%, -386% respectively. At $\gamma = 6$, 2, and 0 μm the percent error between $1/C_F^S$ and the fitted lines is –1.1%, -17.7%, -233% respectively. The percent error equals 1 - value for the fitted line / $1/C_F^T$.

The slope for the stress free capacitance and the strain free capacitance lines is equal (0.0012 1 /(fF μm). Taking the derivative of Equation 3.69 with respect to γ, and assuming $\widetilde{A}_G$ is independent of γ yields:

$$\frac{d}{d\gamma}\left(\frac{1}{C^T}\right) \cong \frac{1}{\varepsilon_0 K_M \widetilde{A}_G} \qquad \xi > 100\% \qquad (3.91)$$

Equation 3.91 is independent of γ and the properties of the fibers, which may account for the reason that the slope of the inverse of the capacitance for large values of γ, is independent on the stress state or the strain state of the fibers. For large values of γ, the matrix gap capacitance dominates the capacitance of the AFC/tmAFC.

Consider the following conversion of energy from an electrical source to mechanical work. Originally, a single fiber in an AFC/tmAFC that is stress free has a voltage source with strength V_0 applied to it. After the AFC/tmAFC expands quasistatically, the strain in the fiber is given by Equation B.75. The fiber of the AFC/tmAFC is now blocked, and then the voltage source is quasistatically removed. When the voltage is zero the mechanical block is removed and in its place a finite mechanical stress is applied. This is the same mechanical work cycle used to define the coupling coefficient, $\left(k_{33}^{l}\right)^2$, in Reference 23 (page 38). For $\left(k_{33}^{l}\right)^2$, the electric field was applied in the *3* direction, the displacement was blocked in the *3* direction, and the mechanical stress was applied in the *3* direction. For the case of the AFC/tmAFC, the coupling coefficient k_{iZ}^2 is defined as:

$$k_{iZ}^2 = \frac{C_F^T - C_F^S}{C_F^T} \tag{3.92}$$

Equation 3.92 is of a similar form and uses a similar derivation to the invariant coupling coefficient k_{i3}^2 (Equation 2.9). The effect of the closest distance the electrode is from the center of the AFC divided by the fiber radius, ξ, on the coupling coefficient k_{iZ}^2 for a single fiber of a PiezoFlex AFC, is shown in Figure 3.39.

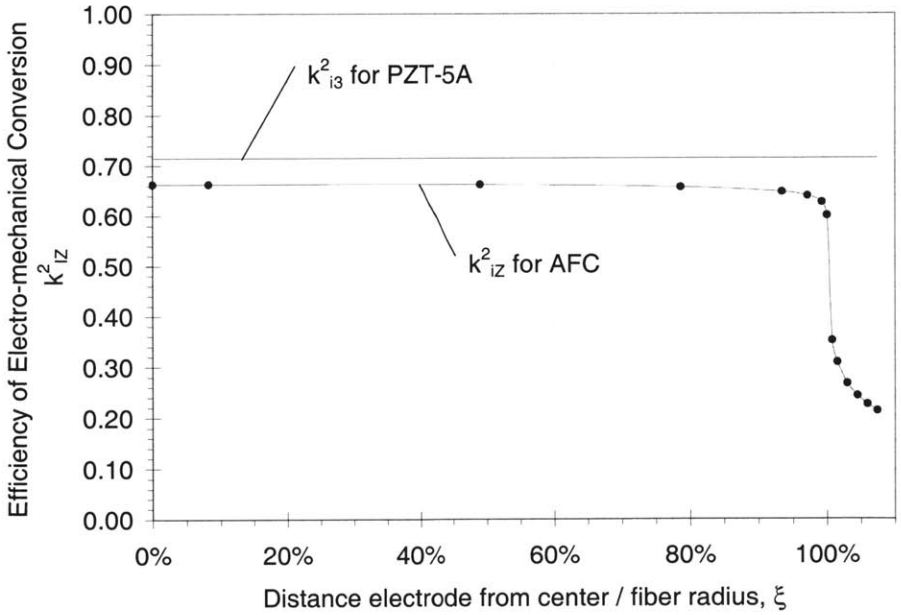

Figure 3.39 Efficiency of Electromechanical Conversion for a single fiber of a CP PiezoFlex AFC as a Function of ξ

As can be seen in Figure 3.39, for $\xi > 100$ % the efficiency of electromechanical conversion is very low, however when the electrode touches the fiber ($\xi < 100$ %) the efficiency of

electromechanical conversion is nearly constant. The efficiency of electromechanical conversion for the mpAFC is 0.663, which is 7.3% smaller than k_{i3}^2 for PZT-5A. This difference can be attributed to the fact that the field lines in the AFC are not straight, and the AFC must actuate against the matrix and the Kapton.

In order to determine the effect the matrix material properties have on the efficiency of electromechanical conversion for a single fiber, the matrix material properties were varied and the resulting k_{i3}^2 was calculated, as seen in Table 3.7.

Table 3.7 Effect of Matrix Material Properties on the Efficiency of Electromechanical Conversion for a single fiber of a CP PiezoFlex AFC

ξ	γ (μm)	**CP AFC**	ν_M = 0.3	ν_M = 0.4	E_M = 1.9 *GPa*	E_M = 3.9 *GPa*	K_M = 2.5	K_M = 4.7
107.4%	10	0.213	0.213	0.213	0.213	0.213	0.182	0.239
105.9%	8	0.226	0.226	0.226	0.226	0.225	0.193	0.253
104.4%	6	0.243	0.242	0.243	0.243	0.242	0.208	0.271
103.0%	4	0.267	0.267	0.267	0.267	0.266	0.229	0.297
101.5%	2	0.309	0.309	0.309	0.310	0.309	0.268	0.341
100.7%	1	0.352	0.352	0.353	0.353	0.352	0.308	0.385
100.0%	0	0.601	0.600	0.601	0.602	0.598	0.598	0.603
99.3%	-1	0.627	0.627	0.628	0.628	0.626	0.627	0.628
97.1%	-3.9	0.640	0.640	0.640	0.641	0.639	0.640	0.640
93.4%	-8.9	0.648	0.647	0.648	0.648	0.647	0.648	0.648
78.6%	-28.9	0.657	0.657	0.658	0.658	0.657	0.658	0.657
49.0%	-68.9	0.662	0.662	0.663	0.663	0.662	0.662	0.662
8.2%	-123.9	0.663	0.663	0.663	0.663	0.662	0.663	0.663
0.0%	-135	0.663	0.662	0.663	0.663	0.662	0.663	0.663

Were in Table 3.7, ν_M is the matrix Poisson's ration, E_M is the matrix Young's modulus, and K_M is the relative dielectric of the matrix. Using the data in Table 3.7 and Equation 3.77, the percent change in k_{i3}^2 per percent change in a matrix material property was calculated:

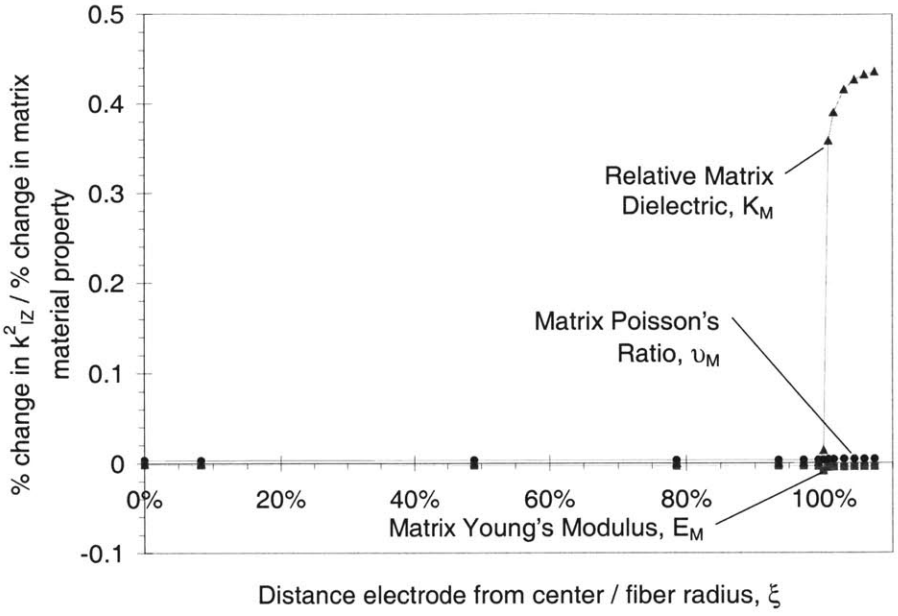

Figure 3.40 Percent Change in the Efficiency of Electromechanical Conversion per Percent Change in a Matrix Material Property versus ξ for a single fiber of a CP PiezoFlex AFC

The material data in Table 2.4 for the average value and the range of matrix material properties for a PiezoFlex AFC was used to determine how much to vary the material properties for the finite element model. As seen in Figure 3.40, increasing the matrix Poisson's ratio a positive amount increases the efficiency of electromechanical conversion a small amount. Increasing the matrix stiffness decreases the efficiency of electromechanical conversion because the AFC must work against the greater stiffness. Increasing the relative dielectric of the matrix dramatically increases the efficiency of electromechanical conversion for $\xi \geq 100$ %, however for $\xi < 100$ % increasing the relative dielectric of the matrix slightly decreases the efficiency of electromechanical conversion.

3.8.5 Finite Element Modeling of the Actuation of tmAFC 20 under Stress Free Conditions

A finite element analysis was performed to determine the *XX* and *ZZ* strain per unit volt under stress free conditions for the active area of tmAFC 20, $(\Gamma_{XX})_A$ and $(\Gamma_{ZZ})_A$, and the capacitance under stress free conditions for a single fiber, C_F^T. This finite element analysis was performed to determine if there was a large percent difference between the actuation properties of AFCs and tmAFC.

This finite element model was the same as the finite element model used in Section 3.8.1 with the following differences in geometry and matrix materials.

Table 3.8 Differences in Geometry and Matrix Materials between a CP PiezoFlex AFC and tmAFC 20.

Property	PiezoFlex AFC	AFC Reference	tmAFC 20	tmAFC Reference	Percent Difference
Thickness, h	343 μm	Table 2.2	370 μm	Table 5.8	-7.9%
Line Fraction, LF	93.8 %	Table 2.2	94.8 %	Table 5.8	-1.1 %
Height of the Active Area, h_A	292 μm	Table 2.2 ($h - 2\ h_K$)	321 μm	Assumed see below	-9.9 %
Matrix Young's Modulus, E_M	2.9 GPa	Table 2.4	3.2 GPa	Table 4.4	-10 %
Matrix Poisson's Ratio, ν_M	0.35	Table 2.4	0.38	Table 4.4	-8.5%
Relative Matrix Dielectric, K_M	3.6	Table 2.4	3.15	Table 4.4	13 %

In Table 3.8, it can be seen that the percent difference between the properties of the AFC and the tmAFC are approximately 10%. The percent difference for Table 3.8 equals 1 – tmAFC values / AFC value. The height of the active area of tmAFC 20 was determined by assuming that the electrode touches and conforms the fiber, but was not compressed through the thickness during manufacturing (as seen in Figure 4.27). Therefore, the height of the active area is assumed to be the diameter of the fiber (270 μm) + 2 times the thickness of the electrode (25.4 μm).

The effect of the closest distance the electrode is from the center of the AFC divided by the fiber radius, ξ, on the actuation and capacitance of tmAFC 20 and PiezoFlex AFC under stress free conditions, is shown in Figure 3.41.

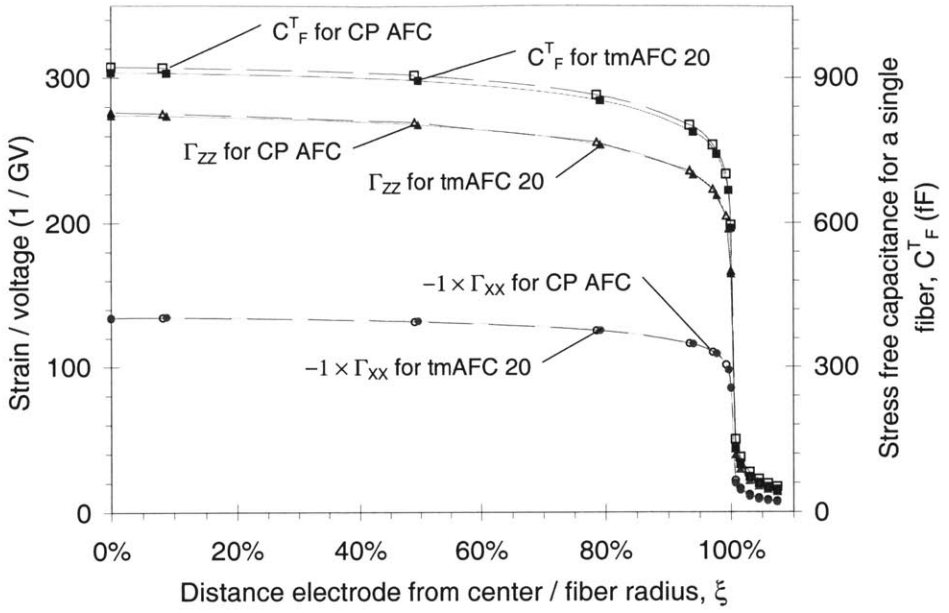

Figure 3.41 Actuation and Capacitance of tmAFC 20 and a CP PiezoFlex AFC under Stress Free Conditions as a Function of ξ

As can be seen in Figure 3.41, there is very little difference between the properties of tmAFC 20 and a CP PiezoFlex AFC under stress free conditions, despite the differences listed in Table 3.8. The percent difference between, $(\Gamma_{XX})_A$, $(\Gamma_{ZZ})_A$, and C_F^T is –0.27 %, 1.28 %, and 0.66 % respectively, where the percent difference is calculated from:

$$\text{Percent Difference in x} = 1 - \left(\left[\int_0^{107.4\%} x \, d\xi \right]_{tmAFC} \Big/ \left[\int_0^{107.4\%} x \, d\xi \right]_{AFC} \right) \tag{3.93}$$

Where x is the material property in question. Due to the small percent differences between the properties of tmAFC 20 and a CP PiezoFlex AFC under stress free conditions, it can be assumed that the conclusions reached for CP PiezoFlex AFC hold for tmAFCs.

3.8.6 Comparison between the Finite Element Model for a PiezoFlex AFC and AFC Material Data

The comparison between the finite element model and material data is difficult because the material properties for the fiber and the matrix are unknown and needed to be estimated. Finite element modeling requires the geometry and material properties to be known before FEM analysis can be done. The geometry of the actuators modeled using FEM was chosen based upon test articles used in Reference 58.

In Reference 58 the free strain actuation of an AFC was measured. Using the low field d_{ZZ} data for the AFC presented in Section 5.4.2, $(d_{ZZ})_{AFC}$ = 196 pm/V for the AFC

(active area and passive area). Using Equation C.41, the finite element data in Table 3.4, the geometry in the Reference 58 (page 51), and the Kapton and matrix properties presented in Table 2.2 and Table 2.4, ξ for the active area could be determined. Expanding Equation C.41 yields:

$$(\Gamma_{ZZ})_{AFC} = \frac{A_A (\Gamma_{ZZ})_A (Y^V_{ZZ})_A}{A_A (Y^V_{ZZ})_A + A_M E_M + A_K E_K} \tag{3.94}$$

Where *AFC*, *A*, *M*, and *K* subscripts indicate the parameter is for the entire AFC, active area, matrix, and Kapton respectively. Dividing d_{ZZ} by the center-to-center finger spacing, l in Table 2.2, yields:

$$(\Gamma_{ZZ})_{AFC} = \frac{(d_{ZZ})_{AFC}}{l} = 171 \quad nm/mV \tag{3.95}$$

Using Equation 3.94, $(\Gamma_{ZZ})_{AFC}$ was calculated for the discrete finite element data in Table 3.4. Using the $(\Gamma_{ZZ})_{AFC}$ data points above and below the value of $(\Gamma_{ZZ})_{AFC}$ in Equation 3.95, straight line was fitted to the data With this line ξ for the active area could be determined. For the AFC data in Reference 58, ξ = 100.1 %. To estimate the error, ξ was determined using the data in Figure 3.43. As will be described in Section 3.8.7, in order to determine the effect that assuming a poling direction has on the output of the AFC, finite element analyses were performed assuming that the fibers beneath the electrode was not piezoelectric. Using this data, ξ = 99.4 %. Thus the finite element analysis predicts for a PiezoFlex AFC $\xi >$ 99.4 and $\xi <$ 100.1 %.

At the time that the finite element analysis was started, Mr. Wickramasinghe (Author of Reference 58) had plans to measure the stress free actuation and the shorted Young's modulus. This data was going to be used to compare to the finite element analysis presented in Section 3.8.2. Due to testing difficulties, the open circuit Young's modulus of an AFC with e-glass plies on the outside was measured instead. The stiffness contribution of the e-glass plies was subtracted from the AFC using the rule of mixtures (Appendix III). This yielded an open circuit modulus for the entire AFC (active and passive area) of $Y^i_{ZZ} = 39.9\,GPa$ (Reference 58 page 64), which differs greatly than the open circuit modulus of a single fiber of an mpAFC, $Y^i_{ZZ} = 62.1$ GPa (Section 3.5.2).

Mr. Wickramasinghe's stated that the extracted initial modulus data agreed to within 2.7% of his rule of mixtures calculations. In his calculations, he used an open circuit Young's modulus for PZT-5A of $Y^D_{33} = 71\,GPa$ (Reference 58 page 64). He also states that the short circuit Young's modulus for PZT-5A is $Y^E_{33} = 62\,GPa$. Using these two values, k_{33}, can be calculated:

$$Y_{33}^{E} = Y_{33}^{D}\left(1 - k_{33}^{2}\right) \tag{3.96}$$

Using Equation 3.96, k_{33} = 0.36 for Mr. Wickramasinghe's data. In Table 2.6, material data from four manufactures of Navy type II material is presented. The Young's modulus and k_{33} data for Mr. Wickramasinghe's Young's modulus' appears to be very different when compared to the Navy type II data seen in Table 2.6. For example, Mr. Wickramasinghe's Y_{33}^{D} differs from the average Y_{33}^{D} data in Table 2.6 by 35 %. It is the authors opinion that Mr. Wickramasinghe's Young's modulus data, used in the rule of mixtures, is in error. Based upon the error in Y_{33}^{D}, the fact that the measured Young's modulus data agrees Mr. Wickramasinghe's rule of mixtures calculations using this wrong Y_{33}^{D}, and the fact that in Section 3.5.2 it was seen that the fiber properties dominate the open circuit stiffness data, it is felt that when the open circuit AFC was tested it was not truly open circuited. Therefore, it was felt that this data was not good data to replicate using a finite element modeling, and thus was not compared to.

Mr. Pizzochero at Continuum Photonics was contacted regarding material properties for PiezoFlex AFCs. He stated that "I would consider Viresh's data as quite accurate in general, particularly since there was emphasis to characterize performance in the Boeing application."[90] He also noted that "The properties listed on the" PiezoFlex by Continuum Rev 1.0-AP 8/00 (Reference 42) "sheet are on average the most accurate. As you know, there is some property variation, mostly due to fiber quality." In Reference 42, the short circuit Young's modulus of the AFC (active area and passive area) is given by $\left(Y_{ZZ}^{V}\right)_{AFC}$ = 25.6. Using Equation C.30, the Kapton and matrix properties presented in Table 2.2 and Table 2.4, the geometry in the Reference 58 (page 51), and the active width of 48 mm (Reference 90), $\left(Y_{ZZ}^{V}\right)_{AFC}$ could be determined using the following Equation

$$\left(Y_{ZZ}^{V}\right)_{AFC} = \frac{1}{hW}\left[A_A\left(Y_{ZZ}^{V}\right)_{A} + A_M\, E_M + A_K\, E_K\right] \tag{3.97}$$

In Equation 3.97, the finite element data in Table 3.5 was used for the shorted stiffness of the active area. Using this data, it can be seen that $\left(Y_{ZZ}^{V}\right)_{AFC}$ using the finite element data is 29.5 GPa, 36.4 GPa, and 52.2 GPa for ξ = 0 %, 100 %, and 107.4 % respectively, which is greater than the measured data, $\left(Y_{ZZ}^{V}\right)_{AFC}$ = 25.6 GPa. Therefore, the finite element model does not agree with the measured data. It should be noted that in Reference 42 the AFC data was measured for a smaller fiber diameter, 250 microns, smaller line fraction, 85-90%, and a smaller thickness, 330 microns, than compared to the data in used in the finite element model (Table 2.2). The data in Table 2.2 was taken from the AFC data in Reference 58. These geometric differences may account for the differences in the Young's modulus.

In Reference 42, $(d_{33})_{AFC}$ is reported to be 150 pm/V, yielding $(\Gamma_{ZZ})_{AFC}$ = 131 nm/m V. Using the Equation 3.94 and the data in the above paragraph it was determined that ξ = 100.3 % for these AFCs. Because of the geometric differences between the data in Table 2.2 and Reference 58, and the inability for the finite element model to predict the shorted stiffness of the AFC, it is felt that analysis for the data in Reference 58 is more valid. Therefore, the finite element analysis predicts for a PiezoFlex AFC $\xi > 99.4$ and $\xi < 100.1$ %.

3.8.7 Finite Element Modeling Conclusions and Discussion

Using finite element modeling $(\Gamma_{XX})_A$, $(\Gamma_{ZZ})_A$, $(\psi_{XX})_A$, $(\psi_{YY})_A$, $(\psi_{ZZ})_A$, $\left(Y^V_{ZZ}\right)_A$, $\left(\sigma^V_{ZX}\right)_A$, C_F^T, C_F^S, and k_{iZ}^2 was calculated as a function of ξ and the matrix material properties ν_M, E_M, and K_M. As mentioned in Section 3.2, in order to maximize the 1-dimensional actuation of the AFC, AFCs with $(\Gamma_{ZZ})_A$, $(\psi_{ZZ})_A$, and $\left(Y^V_{ZZ}\right)_A$ should be maximized. In general, ν_M has little effect on the ZZ actuation properties. Increasing E_M always has slightly negative effect on $(\Gamma_{ZZ})_A$, $(\psi_{ZZ})_A$, and $\left(Y^V_{ZZ}\right)_A$. Increasing K_M always has a large positive effect on the ZZ actuation properties for $\xi > 100$ %, however has almost no effect for $\xi < 100$ %. It should also be noted that decreasing ξ to increase the strain per volt, $(\Gamma_{ZZ})_A$, increases the stress per volt, $(\psi_{ZZ})_A$, as well, however it has the effect of lowering the stress free stiffness of the AFC. Decreasing ξ to increase the strain per volt increases the stress free capacitance of a single fiber also, thus increasing the power requirements to achieve the maximum strain. Thus depending on the application, it is not obvious that for the "best" AFC is an mpAFC.

It should be noted that although the analysis was performed on an AFC, the results determined for an AFC remain true for a tmAFC, as seen in Section 3.8.5. This is because any tmAFC will have a similar geometry and similar matrix properties to a PiezoFlex AFC. The effect of material properties and ξ should produce similar results on a tmAFC. An AFC was chosen to be analyzed instead of a tmAFC because as will be discussed in Chapter 4, various thicknesses of polymer were used for manufacturing, and thus there did not exist a uniform geometry that could be analyzed for a tmAFC.

Most material properties appeared to follow a step function pattern with an offset when plotted versus ξ. In order to test the theory that each of the material properties follows the same pattern when plotted against ξ the material properties were rescaled using a parameter, c, so that at ξ = 0 %, c = 0 %, and at $\xi = \infty$ %, c = 100 %. Since no data exists for $\xi = \infty$ %, data for ξ = 107.4 % was used. Therefore, c can be defined as:

$$c = \frac{f(\xi) - f(\xi = 0)}{f(\xi = \infty) - f(\xi = 0)} \cong \frac{f(\xi) - f(\xi = 0)}{f(\xi = 107.4\,\%) - f(\xi = 0)} \tag{3.98}$$

Where f is the parameter that we are considering. Plotting c versus ξ yields.

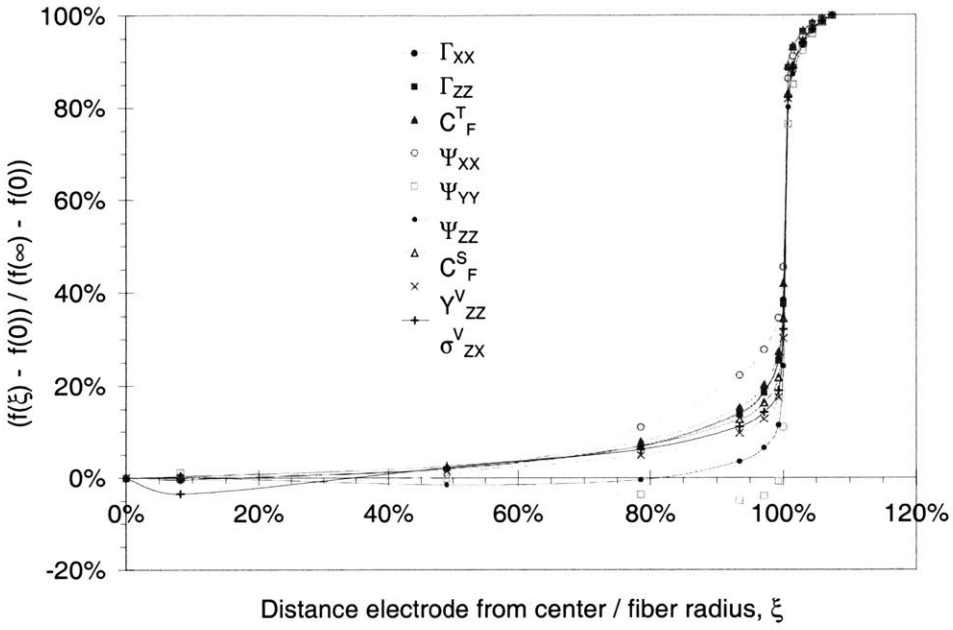

Figure 3.42 Rescaled AFC material property, c, versus ξ

As can be seen in Figure 3.42, all material properties when plotted versus ξ have the same pattern for all the material properties considered. This statement is true except close to ξ = 100 %, where a geometric discontinuity occurs, that is for ξ > 100 % there is matrix gap, and for ξ < 100 % the electrode touches the fiber.

It should be noted that all the material properties used in the finite element model were low field properties, and will change as a function of electric field, and frequency. Because ANSYS requires the poling direction be specified for the piezoelectric elements, it was assumed the fiber was uniformly poled in the z direction, which is a good assumption over most of the fiber, but in actuality is not the case. Under the electrode, the fiber should be poled nearly perpendicular to its surface, and then curve toward the z direction, as discussed in Section 3.4. Thus, the calculated values of the effective material properties will differ slightly from the actual values. In order to determine the effect that the assumption that the fiber was uniformly poled in the z direction, $(\Gamma_{ZZ})_A$, C_F^T, and Y_{ZZ}^V were recalculated assuming that the area in the fiber under the electrode is not piezoelectric, that is e = 0, however all other material properties for the fibers are used. Plotting the strain per unit volt and stress free capacitance versus ξ for a single fiber of a CP PiezoFlex AFC for the volume under the electrode being piezoelectric and non-piezoelectric yields:

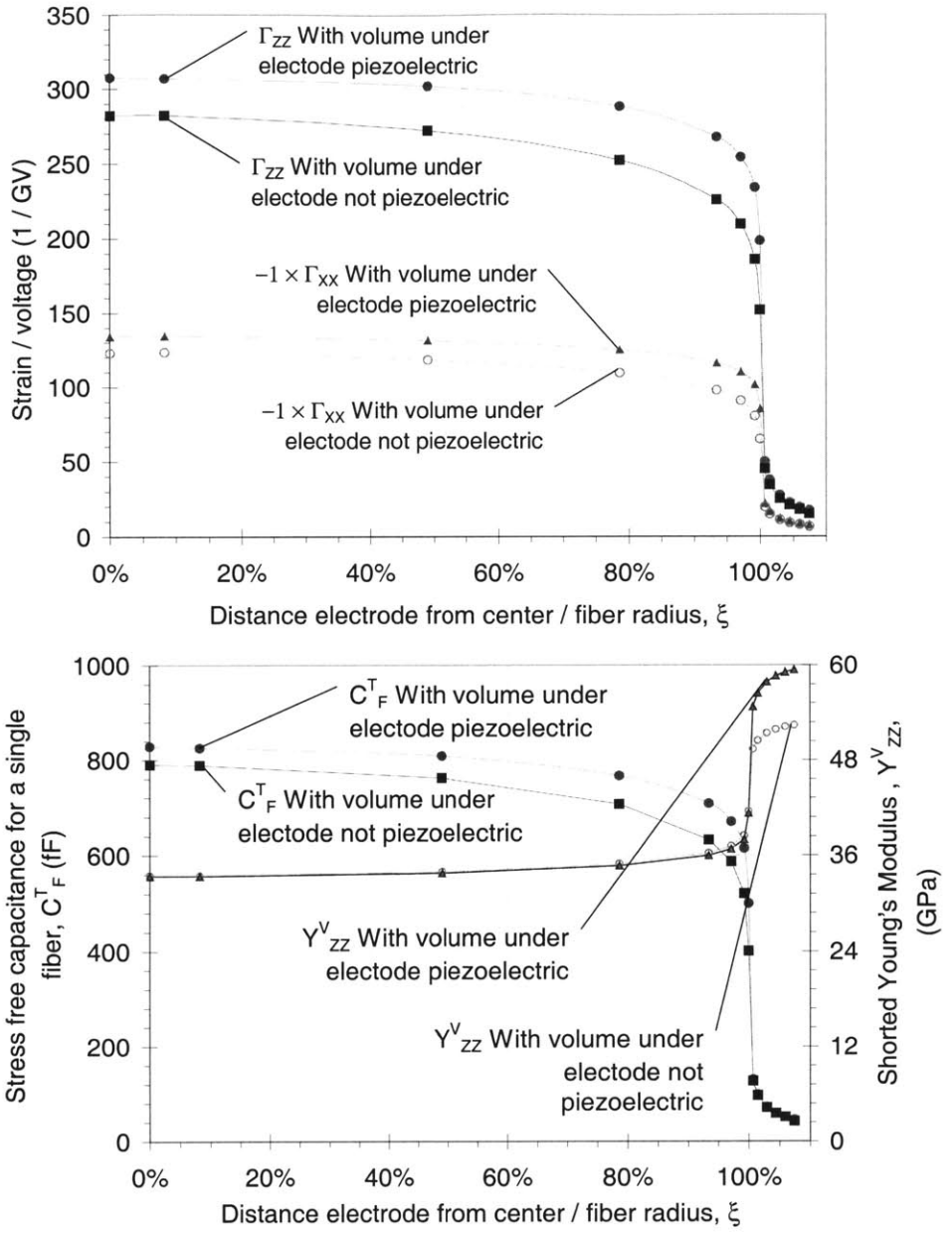

Figure 3.43 Strain per Unit Volt, Stress Free Capacitance, and Young's Modulus under Shorted Conditions versus ξ for a single fiber of a CP PiezoFlex AFC for the Volume under the Electrode Being Piezoelectric and Non-Piezoelectric

As can be seen in Figure 3.43, if the volume under the electrodes is not piezoelectric then the stress free actuation and the stress free capacitance is reduced. The percent difference varies between –12% at ξ = 107.4 %, to a maximum of –23% at ξ = 100 %, and decreases to -8% at ξ = 0 % for the stress free actuation. The percent difference for the stress free capacitance varies between –8% at ξ = 107.4 %, to a maximum of –20% at ξ = 100 %, and decreases to -5% at ξ = 0 %. For the shorted Young's modulus, the percent difference

varies between a maximum of –12% at ξ = 107.4 %, decreases to 1% at ξ = 100 %, and is a minimum of 0% at ξ = 0 %. The percent difference is calculated by:

$$\text{Percent Difference in } f = \frac{f(\text{not poled}) - f(\text{poled})}{f(\text{poled})} \tag{3.99}$$

Where f is the variable being considered. The average percent difference between $(\Gamma_{ZZ})_A$ with the fiber volume under the electrodes poled and not poled is –11 %. The average percent difference between for C_F^T and Y_{ZZ}^V in the same case is –7 % and –1 % respectively. This average percent difference was calculated by determining the area beneath the lines plotted in Figure 3.43, and substituting the area into Equation 3.99 in place of f. The area was calculated by the trapezoidal rule. The length of one of the electrodes divided by the center to center spacing between the electrode fingers is 0.16. Thus, it is not surprising that the percent difference is on that order.

The finite element model the material properties for the fibers is constant for all values of ξ. In order to achieve this the electric field in the fiber must be constant for all values of ξ. In order to do this higher poling voltages must be applied for higher values of ξ because of the smaller voltage drop across the fiber, as discussed in Section 3.7. In practice when an AFC is manufactured, ξ is unknown, and thus a pre-agreed upon poling voltage is applied to the AFC. If ξ is very large then the voltage will be inadequate to completely pole the AFC, and thus the material properties of the fiber will be close to the unpoled values, as seen in Reference 70. Therefore when using this poling practice, $(\Gamma_{ZZ})_A$ $(\psi_{ZZ})_A$, C_F^T, and k_{iZ}^2 will be less at higher values of ξ the calculated using the finite element model, and Y_{ZZ}^A, will be greater at higher values of ξ.

4. tmAFC Manufacturing

4.1 Introduction

Active Fiber Composites are composite plies composed of piezoelectric fibers embedded in a thermoset matrix. An interdigitated electrode is adhered to each side to deliver an electric filed to the fibers. A high dielectric layer, such as Kapton, is adhered to the outside to prevent dielectric breakdown. A tmAFC similar in makeup to an AFC except is comprised of a thermoplastic matrix. Depending on the manufacturing method, some tmAFCs have Kapton to prevent dielectric breakdown, and some have a layer of thermoplastic to prevent dielectric breakdown.

A primary goal of this research is to manufacture tmAFCs with high levels of actuation. Before tmAFCs could be manufactured, the thermoplastic to be used for the tmAFC matrix had to be determined. This was done by formulating requirements for the matrix and doing material searches based upon those requirements. tmAFCs have been manufactured using three methods, which will be referred to as solvent casted tmAFCs, externally electroded tmAFCs, and internally electroded tmAFC. Each manufacturing method will be discussed as well as problems and solutions.

4.2 Minimum Requirements for a tmAFC Matrix

In order to determine what thermoplastic polymer to choose to manufacture tmAFC, the minimum requirements for a tmAFC matrix had to be determined. Using the analyses in Chapter 3 and the minimum requirements, the search for a thermoplastic matrix material to be used for the tmAFCs was narrowed considerably.

Several constraints exist on the thermoplastic matrix material for tmAFCs forcing the usage of certain classes of polymers. These constraints are given below:

1. The thermoplastic must have a low melt viscosity

2. The thermoplastic must have a high dielectric breakdown strength

3. The thermoplastic must have a high usage temperature

4. The thermoplastic must have a high dielectric

5. The thermoplastic must have a failure strain greater than that of the fibers

Constraint 1 states that the thermoplastic must have a low melt viscosity. This is due to the fact that when the matrix is melted it must flow into the pores of the fiber to allow it to adhere to the fiber. Unfortunately, most plastic manufactures do not provide melt viscosity data, however many manufactures will classify their polymer as low or high melt viscosity. Many experiments were done on different materials to determine if a thermoplastic material could adhere to the fibers as discussed in Section 4.4.

Constraint 2 states that the thermoplastic must have a high dielectric breakdown strength. During the poling process, the tmAFC is subjected to a constant DC field ranging from 2 to 4 kV. This field is applied over a length of $\mathcal{L}$= 1.14 mm (45 mil) giving an approximate electric field of 1.75 – 3.50 kV/mm. However due to the dielectric mismatch between the polymer under the electrode and the fiber, the field under the finger can be much greater than the field in the fibers, as was discussed in Section 3.3.2 (Equation 3.21). Most polymers have a dielectric breakdown strength in the vicinity of 20 kV/mm however PVC has a dielectric breakdown strength approaching 50 kV/mm[91]. Thin samples of polymer also display a higher dielectric breakdown strength compared to thicker samples because for a thinner polymer there exists less of a potential for a fatal flaw across its thickness. Material data for dielectric breakdown strength has much scatter in it due to the thickness used and the medium the specimen is tested in (air or oil) as will be seen in Table 4.4. Whether a polymer had an acceptable dielectric breakdown strength was determined by trial and error. None of the polymers used to manufacture tmAFCs in Chapter 4 appeared to have an unacceptable dielectric breakdown strength.

Constraint 3 states that the thermoplastic must have a high usage temperature. This is due to the fact that the tmAFC after being manufactured will be cured into a passive composite structure to be actuated. Many composite prepregs are cured at either 121 °C (250 °F) or 177 °C (350 °F). To increase the potential commercial market of the tmAFCs, it was decided that the usage temperature of the matrix should be at a minimum of 121 °C (250 °F) with a usage temperature of greater than 177 °C (350 °F) being more desirable. The usage temperature can roughly be defined as the temperature at which the polymer does not strain excessively under an applied stress. Polymer manufactures typically provide data on the Vicat softening temperature or the thermal deflection temperature. Both are a measure

of the plastics ability to deform a prescribed amount at an elevated temperature under a defined loading. Some manufactures provide information on the glass transition temperature. Below the glass transition temperature the polymer behaves in a solid or "glass-like" manner. Above the glass transition temperature the polymer becomes highly elastic. Polymers for manufacturing were selected such that the Vicat softening temperature, the thermal deflection temperature, and the glass transition temperature were above 121 °C (250 °F) when any of these material properties were known.

Constraint 4 states that the thermoplastic must have a high dielectric. Previous analysis for AFCs (Reference 34 pages 79-124) has shown that in order for the actuation of the AFC to be maximized the dielectric constant of the matrix must be maximized, as was shown in Table 3.4 for ξ greater than 100%. A search on the Internet described in Section 2.3.1 indicated that the average relative dielectric for a polymer is about 3.6 with a variance of $\sigma^2 = 1.2$. Most manufactures provide dielectric data at one frequency, however different manufactures provide dielectric data at different frequencies making comparisons between the polymers difficult. A matrix material with a low dielectric constant can still be used as long as ξ is less than or equal to 100%, as shown in Table 3.4. Because of the difficulty in comparing dielectric constants, the narrow possible range that the dielectric constants could be in, and the fact that if ξ is less than 100% the dielectric of the matrix doesn't significantly effect the actuation, the dielectric constant was not used as a criterion for determining the viability of a polymer as a tmAFC matrix material.

Constraint 5 states that thermoplastic must have a failure strain greater than that of the fibers. When a tensile load is applied to a tmAFC, the brittle fibers of tmAFC have a tendency to fail. It is desirable for the matrix to have a higher failure strain than the fibers to carry the load around broken fibers. The ultimate elongation strain of a polymer lies in a very broad range, typically between 1% in the case of brittle polymers to 1000% in the case of elastomers (Reference 91, page 81). PZT-5A can be assumed to fail at approximately the same strain value as PZT-5H, 1300 με (Reference 34). For all the candidate tmAFC matrix materials, the ultimate failure strain of a polymer was greater than that of PZT-5A and thus the ultimate failure strain proved not to be a driving factor in tmAFC matrix material selection.

Table 4.1 summarizes the minimum constraints for a tmAFC matrix material

Table 4.1 Minimum Constraints for a tmAFC Matrix Material

Constraint	Comments
The thermoplastic must have a low melt viscosity to allow the matrix to adhere to the fibers	Melt viscosity data not typically supplied by manufactures. Chose polymers whose melt viscosity was classified as low by the manufacturer. Acceptable materials determined by manufacturing trial and error.
The thermoplastic must have a high dielectric breakdown strength	Maximum electric field is unknown. Most polymers have a dielectric breakdown strength in the vicinity of 20 kV/mm. Acceptable materials determined by manufacturing trial and error, however of the materials tested none were deemed unacceptable.
The thermoplastic must have a usage temperature higher than the cure temperature of common prepregs, 121 °C (250 °F)	Forced the usage of materials with a Vicat softening temperature, thermal deflection temperature, and glass transition temperature greater than 121 °C (250 °F)
The thermoplastic must have a high dielectric to allow for greater actuation	Very narrow range of possible relative dielectric constants (2-6). Data that is comparable between manufactures not available. Low dielectric polymers could perform better than high dielectric polymers if ξ was decreased.
The thermoplastic must have a failure strain greater than that of the fibers to allow load transfer around broker fibers	The ultimate elongation strain of a polymer lies between 1% in the case of brittle polymers to 1000%. PZT-5A can be assumed to fail at approximately the same strain value as PZT-5H, 1300 με (Reference 34) which is smaller than most polymers considered.

Of the constraints listed in Table 4.1, only the first and the third constraint proved to affect the choice of polymers. As will be discussed in Section 4.4, polymer samples with a usage temperature of greater than 121 °C (250 °F) were obtained from various polymer manufactures. These samples were then tested to determine their ability to adhere to the fibers.

4.3 Solvent Casted PVDF tmAFC Manufacturing

tmAFCs were first developed by Patrick Trapa at the Active Materials and Structures Laboratory at the Massachusetts Institute of Technology[92]. Mr. Trapa stated work on tmAFCs in the summer of 1997 attempting to manufacture a tmAFC with a Polyvinylidene Fluoride (PVDF) matrix. Mr. Trapa made tmAFCs by solvent casting PVDF onto the fibers and hot pressing PVDF sheets with silver electrodes screen printed onto them. Many electrical breakdown problems occurred due to the quality of the electrodes and the solvent casted sheets.

For all the solvent casted tmAFCs, Kynar 2801-00[93] PVDF was used. Material properties of Kynar 2801-00 PVDF are given in Table 4.2.

Table 4.2 Material properties of Kynar 2801-00 PVDF[94]

Property	Value	Test Method
Tensile Modulus at 23 °C (73 °F)	550 MPa- 900 MPa	ASTM D638
Tensile Yield Elongation at 23 °C (73 °F)	10-20 %	ASTM D638
Tensile Break Elongation	200-400 %	ASTM D638
Melting Temperature	141 – 145 °C (285 – 293 °F)	ASTM D3418
Thermal Decomposition TGA 1% wt. lossin nitrogen	410 °C (770 °F)	-
Dielectric Constant at 100 Hz and 23 °C (73 °F)	9.4 - 10.6	ASTM D150
Dielectric Strength at 23 °C (73 °F)	51-59 kV/mm	ASTM D149
Specific Gravity at 23 °C (73 °F)	1.76 - 1.79	ASTM D792

A range of values for material properties are given in Table 4.2 because the data was taken from Reference 94 and the values for the 2800-2900 family of polymers. In addition, the material properties are dependant on the processing of the PVDF. For the solvent casted PVDF tmAFCs, Kynar 2801-00 was purchased in power form. In Section 4.2, it was stated that a polymer with a high dielectric constant was desirable to increase the actuation of tmAFC. In Section 2.3.1, a search was done on that showed that the average relative dielectric for a polymer is about 3.6 with a variance of $\sigma^2 = 1.2$. Kynar 2801-00 was chosen by Mr. Trapa due to its high relative dielectric compared to most polymers, and because it is piezoelectric and therefore should act as another actuator inside the tmAFC.

The author started working on tmAFCs in the spring of 1999, using Mr. Trapa's manufacturing process as a baseline to manufacture tmAFCs. First a film of PVDF plastic was solvent casted by mixing Kynar powder into a solution of Methyl Ethyl Ketone (MEK). This mixture was stirred using an ultrasonic stirrer to fully dissolve the powder. This mixture was pored onto a glass plate which has a piece of metal shaped like a picture frame adhered to one side using double stick tape. The solution is poured into the interior of the picture frame. The MEK is allowed to evaporate leaving a meniscus shaped film, which can be detached from the glass using a razor. The edges of the film are trimmed and the sheet is cut length wise to form two sheets that are slightly larger than the desired electrode area. The thickness of the sheets could be controlled by controlling the mass of the powder put into the solution. The piezoelectric fibers are then aligned and the ends are glued together

using 5 minute epoxy[95] to form a fiber mat to prevent the fibers from moving during manufacture. The mold is cleaned and 127 micron (5 mil.) Guaranteed Non-Porous Teflon[96] (GNPT) is taped to the mold. A 25 micron (1 mil.) thick piece of Kapton with either a copper or silver electrode pattern printed on one side is then placed onto the GNPT, electrode side facing up. Then a sheet of Kynar is placed on top of it. The fibers are placed on top next and are aligned so that they fit within the electrode pattern. Another sheet of Kynar is placed on next and then another electrode face down is placed on top. A second sheet of GNPT is placed onto the electrode and the top piece of the mold is put on as shown in Figure 4.1.

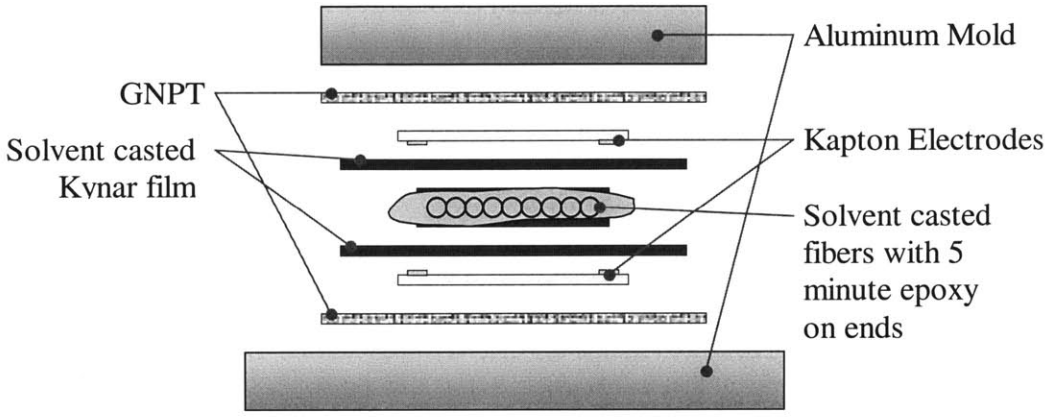

Figure 4.1 tmAFC Lay-up for Solvent Casting

The mold is then placed into the hot press[97] and a low vacuum, 686-737 mm of hg (27-29" of hg), is drawn. A picture of the hot press manufactured by Tetrahedron Associates, Inc is shown in Figure 4.2.

Figure 4.2 Hot Press Manufactured by Tetrahedron Associates, Inc

Although not shown Figure 4.1 to increase clarity, the top and the bottom plates of the mold are spaced apart by springs. These springs are used to slow down the rate at which force is applied in the hot press. It is also desirable for the mold to be open when a vacuum is being drawn to allow the air to flow out, and the springs help do this. The press is commanded to close and then the press is heated up to 218 °C (424 °F), which is above the melting temperature of Kynar. This temperature is held for 10 minutes to ensure that the mold is at a uniform temperature, and then the temperature is reduced with the force still being held, and when the platens of the press reaches 49 °C (120 °F) the force is released. The force is not released until the tmAFC is cooled from the maximum temperature because the plastic at the maximum temperature is still molten and severe warping will occur of the tmAFC while it is cooled down with no load on it. Excess plastic is then trimmed off the tmAFC and it is ready to test. A top view and cross section of a tmAFC is shown below:

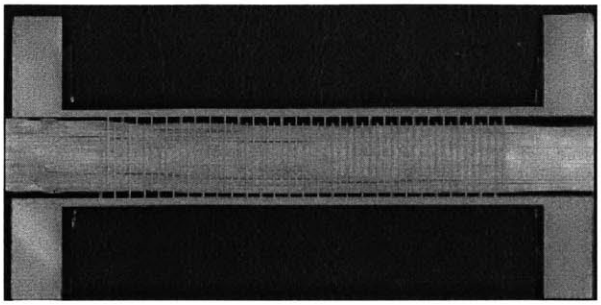

Figure 4.3 Solvent Casted Kynar tmAFC Top View

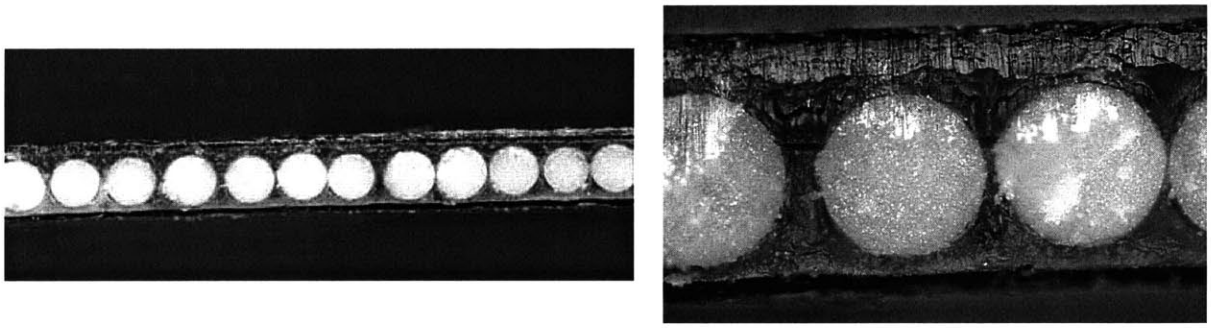

Figure 4.4 Solvent Casted Kynar tmAFC Cross Sections

Several problems exist with solvent casted tmAFCs. First, the film would contain lumps due to solvent and air bubbles being trapped within the film. This is because when the solvent was allowed to evaporate it would evaporate first on the side exposed to air forming an outer skin of plastic slowing the evaporation rate of the remaining solvent. Often time dirt present in the air would also be trapped within the plastic because the sheets were not manufactured under clean room conditions. Very often electrical breakdown would occur due to the inhomogeneity of the plastic when 4 kV was applied to the tmAFC to pole it. In order remove as much solvent as possible, the solution after being poured onto the glass, was placed within a vacuum chamber and a low vacuum 686-737 mm of hg (27-29" of hg) was drawn. This method did remove the trapped solvent and air, however as the air bubble floated to the surface of the film it would pop forming a crater in the surface of the film thus rendering it useless. In order to release the trapped solvent the film several attempts were made to dry the plastic by heating the film to an elevated temperature in a convection oven. Drying did not seem to increase the electrical breakdown voltage of the tmAFCs and was thus abandoned. Another problem with this manufacturing method is that the thickness of the plastic film is hard to control to within 25 microns (1 mil.). When the solution with the plastic is poured onto the glass plate with the picture frame, as mentioned previously the mixture has a tendency to form a meniscus shape with the center of the plastic being much thinner than the edges, thus giving a non-uniform thickness plastic film after drying. The films thickness was then measured using a micrometer with at least 9

measurements at various locations and a curve of plastic mass versus film thickness was constructed. Because of the meniscus shape of the plastic it was not possible to correlate the thickness of the sheets to the amount of plastic power placed in the mixture to within 25 microns (1 mil.). If too little plastic were used to make the mixture the film the film would contain holes near the center.

Another problem encountered in the manufacturing of solvent casted tmAFCs is that the plastic film would often delaminate from the fibers. This is due to the fact the melt viscosity of the Kynar was so high that the plastic could not flow into the pores of the fibers. In order to increase adhesion between the fibers and the matrix, a thin layer of Kynar was solvent casted onto the fibers, after the fibers were bonded together with epoxy at the ends. The solution of MEK and Kynar had a lower viscosity compared to the melt viscosity of the plastic and thus would flow into the pores of the fibers. The plastic film could then be melted onto the fibers without delamination. This solution, although prevented delamination, decreased actuation by increasing the distance between the fibers and the electrodes further (Figure 3.26). Solvents casting the fibers caused them to warp do to an uneven distribution of Kynar. To reduce the amount of warping fibers would be individually dipped in a solution with a very small amount, 1%-10%, of Kynar prior to bonding the fibers together with epoxy. Due to the problems with removing the solvent trapped within the matrix and the poor actuation, this manufacturing method was not pursued further.

4.4 Noryl Externally Electoded tmAFC Manufacturing

Manufacturing of externally electroded tmAFCs is very similar to the manufacturing methods for solvent cast tmAFCs. The first major difference between the two methods are that with externally electroded tmAFCs the plastic is bought in film form from a manufacturer instead of being solvent cast. Because the film is usually produced at very high pressures, any voids trapped within the film are likely to be smaller than voids in solvent cast films, thus increasing the films dielectric breakdown strength. The minimum thickness of the plastic film that could be used is given by:

$$t \geq \frac{(4-\pi)}{4} R \approx 0.22\, R = \begin{cases} 15\ \mu\text{m for 140 } \mu\text{m diameter fibers} \\ 29\ \mu\text{m for 270 } \mu\text{m diameter fibers} \end{cases} \quad (4.1)$$

Where t is the film thickness and R is the fiber radius. This minimum distance is determined from the amount of plastic film required to fill in a square area around half a fiber (two films are placed on either side of the fiber). This equation gives the minimum thickness required to fill in the fiber because it assumes that there are no gaps between fibers in the tmAFC, and it assumes that the metal electrode on the Kapton is infinitely thin and therefore plastic does not need to flow in between the electrode fingers to adhere to the Kapton. In practice however it was found that the plastic should be at least 25 microns (1 mil.) thicker than the

thickness given by the above equation. This allowed the plastic to flow between the electrode fingers, which are 25 microns (1 mil.) thick on the silver electrodes, and between the gaps between the fibers.

The second major difference between the two manufacturing methods is that with externally electroded tmAFCs no plastic is solvent casted onto the fibers prior to manufacturing. This removes the plastic layer that increases the distance between the fiber and the electrode. As mentioned previously tmAFCs manufactured with solvent cast Kynar were prone to delamination and thus a layer of Kynar was solvent casted directly onto the fibers to promote adhesion between the film and the fibers. In order to eliminate this layer a plastic with a low melt viscosity was chosen. Because this data is not readily available for most plastics, several manufacturers of plastic film were contacted. The manufactures sent samples of plastic film that their technical representatives thought would adhere to the fibers. The material properties of these samples also conformed to the minimum criteria for the plastic as specified in Section 4.2. 5.1 cm (2") long PZT-5A fiber mats were manufactured and sandwiched between 2.54 cm x 2.54 cm (1" x 1") samples of plastic that were cut from the film samples. These were heated and pressed in the hot press at temperatures above the melting temperature for each individual plastic. An attempt was then made to insert a razor blade between the plastic and the fibers to determine in a qualitative way the propensity of the fibers and matrix to delaminate. Most of the plastics tested delaminated except for Noryl EN265-701[98] (a modified polyphenylene oxide). A sample of film was donated by Westlake Plastics[99], and more was purchased from them. Material properties for Noryl EN265-701 is shown in Table 4.3.

Table 4.3 Material Properties for Noryl EN265-701[100]

Property	**Value**	**Test Method**
Tensile Strength, yield, Type I, 2.0 in/min	63.4 MPa (9200 psi)	ASTM D 638
Tensile Elongation, break, Type I, 2.0 in/min	25%	ASTM D 638
Unannealed Heat Deflection Temperature, 1.82 MPa (264 psi), 6.4 mm (0.250")	123 °C (254 °F)	ASTM D 648
Melt Range	227-254 °C (440-490 °F)	-
Dielectric Constant, 60 Hz	2.69	ASTM D 150
Dielectric Strength, in oil, 3.175 mm (125 mils)	19.7	ASTM D 149
Specific Gravity, solid	1.08	ASTM D 792

0.076 mm (3 mil.) thick Noryl film was used to manufacture most of the externally electroded tmAFCs, although some tmAFCs were manufactured using Kynar film. The lay-up process for the Noryl externally electroded tmAFCs was the same as the solvent casted tmAFCs except between the mold and the GNPT a 4.7 mm (3/16" in) piece of silicon rubber[101] sold by McMaster-Carr Supply Company was placed to provide a more even distribution of force than could be provided by flat surfaces of the mold, as shown in Figure 4.5.

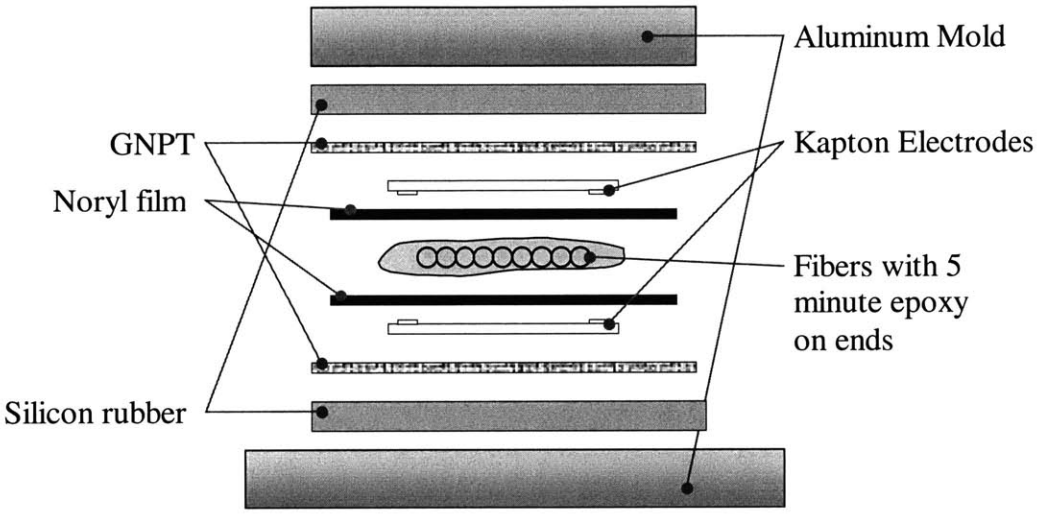

Figure 4.5 Externally Electoded tmAFC Lay-up

If the composite is pressed between two rigid blocks, as the blocks close the pressure is applied to first to the thickest parts of the composite, the area at the top and bottom of the fibers. This puts the fibers in a very high state of stress and potentially breaking the fibers, thus limiting the maximum amount of force that can be applied. If any fibers are crossed over the entire pressure is placed upon them, breaking them. The matrix in between the fibers receives very little pressure and voids can form between the fibers. The silicon rubber more evenly distributes the force allowing pressure to be applied to the spaces in between the fibers, thus consolidating the composites better. A top view of an externally electoded Noryl tmAFC with the Kapton removed is shown below:

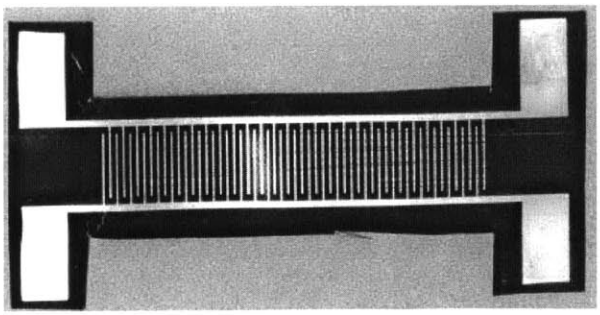

Figure 4.6 Externally Electroded Noryl tmAFC

Two problems occurred with externally electroded tmAFCs. Because plastic film can only be purchased in discrete thicknesses, the thickness of film that was bought was thicker that the thickness of film given in Equation 4.1. Because the externally electroded Noryl tmAFCs stated with thicker than desired plastic films, the electrodes were far away from the fibers ($\gamma > 0$) and thus actuation performance for these tmAFCs was poor. If the desired thickness of film could have been obtained, then the actuation performance would have been equal to AFCs manufactured by Continuum Photonics, however this would have involved buying an entire production run of film, which due to budgetary constraints was not possible. The second problem is that due to Kapton's smooth surface the plastic would not adhere very well to the Kapton electrode. Delaminations would form between the electrode fingers. These delaminated areas were locations for electrical breakdowns during poling.

While attempting to peel off a Kapton electrode from a Noryl tmAFC to qualitatively determine the strength of the bond between the electrode and the matrix, it was noticed that some of the silver electrode delaminated from the Kapton and remained embedded on the surface of the tmAFC. After several cures, it was determined using a temperature of 232 ^{o}C (450 ^{o}F) that the electrode could be transferred with some reproducibly. During manufacturing, plastic would flow into the pores of the silver electrode and after cooling would solidify. Because the strength of the bond between the silver and the matrix was stronger than that of the Kapton and the silver, the silver would transfer to the matrix when the Kapton is peeled off. In order to prevent dialectic breakdowns these tmAFCs would require a coating with a high dielectric breakdown strength to actuate.

4.5 Internally Electoded tmAFC Manufacturing

4.5.1 Noryl Inernally Electroded tmAFCs

Because of the problems encountered with the externally electroded tmAFC manufacturing methods with ξ being greater than 100 %, a new way was sought to reduce the distance from the electrode to the fiber. As discussed in Section 4.3, Mr. Trapa[92] had attempted to reduce the distance between fir fibers and the electrodes by screen printing silver electrodes onto solvent casted films and pressing the films, electrode sides inward, directly onto fibers. The electrodes did not have high line quality and had a tendency to crack when pressed into the fibers and this method was abandoned. This method was attempted once again, except it was decided that the electrodes should be made of a single piece of metal so that when it was pressed into the fibers it would not crack. Two methods

were attempted, metal sputtering and evaporation. Two electrode masks were made by cutting a stainless steel shim using a wire EDM process and are shown Figure 4.7:

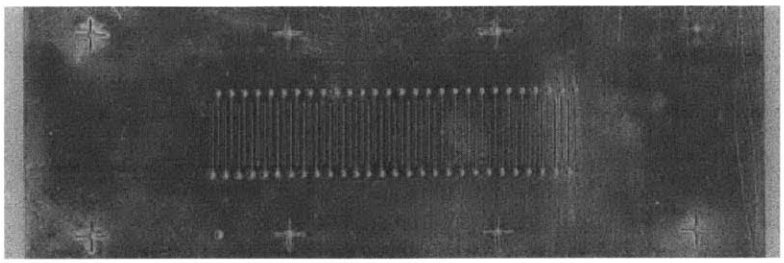

First Mask

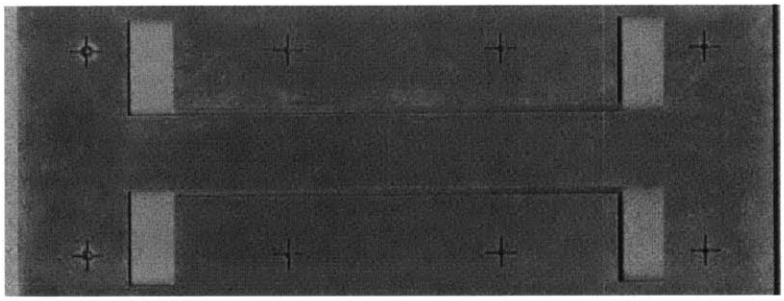

Second Mask

Figure 4.7 First and Second Masks for Printing Electrodes onto Plastic Using Sputtering and Evaporation

Several thicknesses of masks (5, 10, 15, and 20 mil) were manufactured to see the effect of mask thickness on the quality of the electrode. The electrodes were made in the following manner. First, a clean piece of plastic film was placed onto a ground steel plate. Ground steel was used due to its flatness. The first electrode mask with the fingers was placed on top and eight magnets were used to hold the mask down flat. The steel plate was then placed in the sputtering machine or evaporator and the finger were printed onto the plastic. Then the process was repeated, replacing the first mask with the second mask and aligning the crosshairs. 0.1 μm copper electrodes were manufactured using the sputtering process. Due to the small area of the sputtering targets compared size of the electrodes only a small part of the electrode could be made at once, and thus the sputtering process was abandoned.

Electrodes were also manufactured using an evaporator process. A 2000 Å aluminum thick electrodes using a custom built thermal co-evaporator at the Center for Materials Science and Engineering (CMSE at MIT) is shown below.

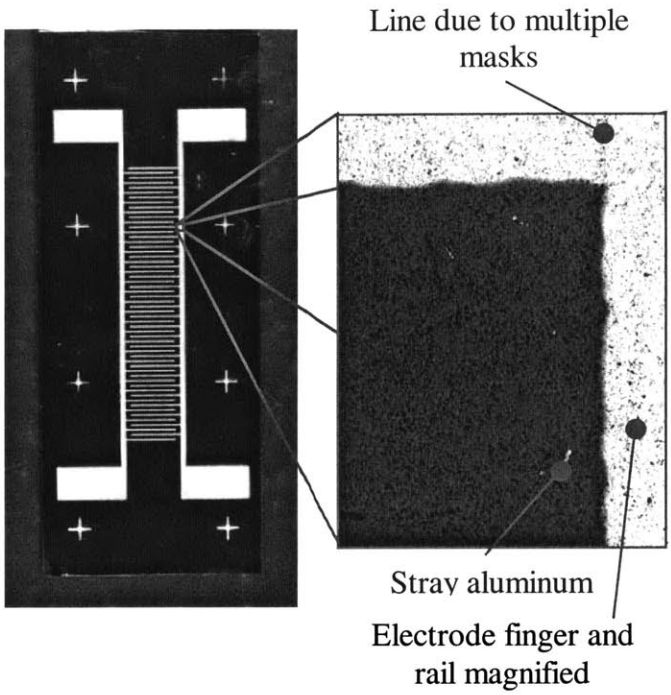

Figure 4.8 2000 Å Thick Aluminum Electrode Evaporated onto Noryl

Although the electrodes are thinner than the copper/Kapton or the silver/Kapton electrodes, tests on two specimens showed that 9800 volts are required to breakdown 2000 Å aluminum electrodes at room temperature. If thicker electrodes are required 4000 - 6000 Å thick aluminum or silver electrodes could have been possible to manufacture. Only 2 electrodes were made using this method before the evaporator required maintenance and was inoperable for several weeks.

While waiting to the evaporator to be fixed, another idea was hit upon to manufacture electrodes embedded into Noryl. This method combined the externally electroded tmAFCs with the transferred electrodes with Mr. Trapa's idea to place the electrodes directly against the fibers. Electrodes were first manufactured by transferring the electrode pattern from the Kapton to the plastic film. Then fibers could be placed between the sheets of plastic with the electrodes facing inward and heated and pressed together. The force used in the transfer process for the externally electrode tmAFCs was limited to low forces to prevent the fibers from breaking. Much higher forces could be used to make the electrode if the electrodes were made prior to making the tmAFC, thus guaranteeing the matrix flowed into the pores of the electrode. The electrodes and Noryl were sandwiched between silicon rubber in the mold. The mold was then heated to 232 °C (450 °F) with about 22.2 kN (5000 lbs) applied to the mold under a vacuum. After the mold is cooled, the Kapton is peeled off leaving the electrode pattern flush with the thermoplastic surface. The process for making the electrodes was over 95% successful. An electrode transferred to Noryl is shown below.

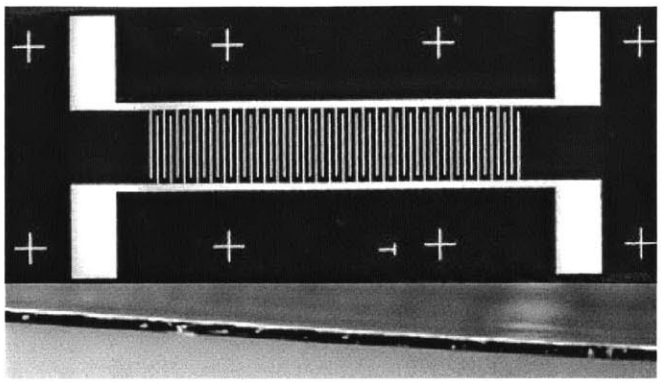

Figure 4.9 Top View and Side View of an Electrode transferred to Noryl

As can be seen in Figure 4.9, the silver transfer to the Noryl is complete.

The fibers with 5 minute epoxy was manufactured and were heated to 274 °C (525 °F) and pressed between the Noryl electrodes, with the electrode side facing the fibers as shown below:

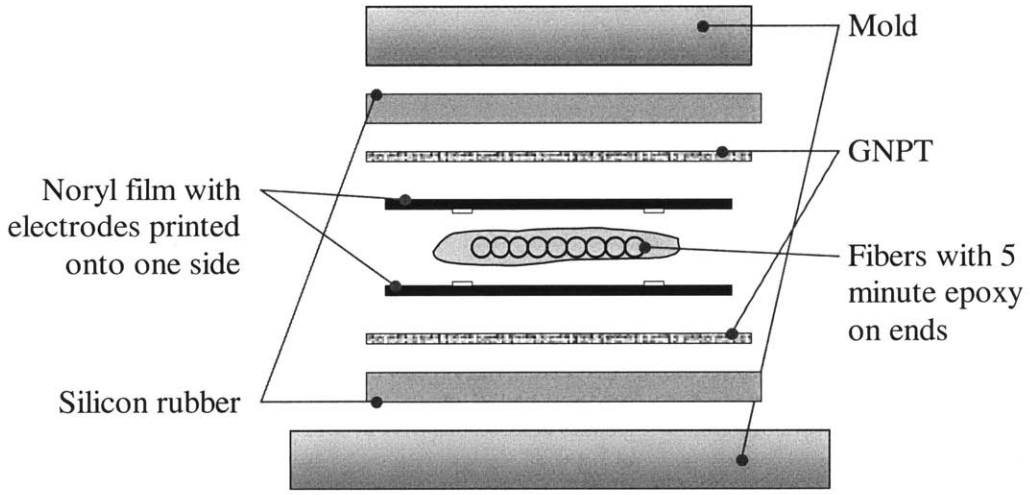

Figure 4.10 Manufacturing Method for Internally Electroded tmAFCs

Two internally electroded tmAFCs were manufactured with electrodes on either side of the film, yielding a total of four electrodes. Because the electrode was on the outside the electrodes could not be actuated without a dielectric coating on the tmAFCs. These fibers prepoled capacitance higher than any previous tmAFC (362 and 326 pF). Figure 4.11 shows a cross section of an internally and externally electroded tmAFC.

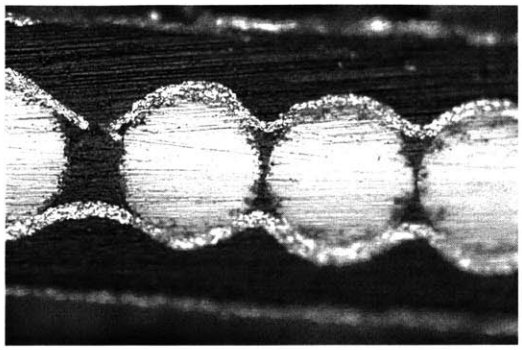

Figure 4.11 Cross Section of an Internally and Externally Electroded tmAFC

From the figure above it can be seen that the electrode are nearly touching the fibers over a large portion of the fiber. From the above picture it can also be seen that the electrodes can break at places where there are gaps between the fibers. For most of the electrode fingers seen under the microscope there was no breaks in the electrode. Figure 4.11 does not represent the majority of the electrode fingers, however it was shown to illustrate a break in the electrode. The electrodes can also break at locations where fibers cross over due to the stretching of the fibers as shown below:

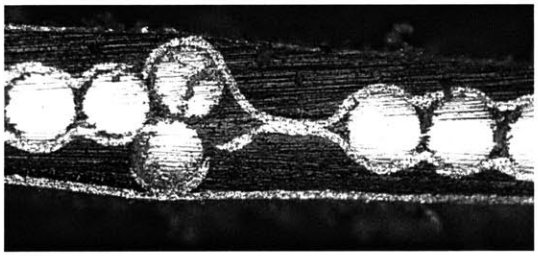

Figure 4.12 Fiber Breaks at a Fiber Cross Over in an Internally and Externally Electroded tmAFC

Noryl tmAFCs would often times have a permanent curvature after being removed from the mold. This curvature is due a lack of symmetry through the thickness in the tmAFC. When the internally and externally electroded tmAFC was flattened cracks would occur in the plastics due to the brittleness of the matrix. Due to Noryl's low heat deflection temperature, 123 °C (254 °F) (Table 4.3) and brittleness, another thermoplastic matrix material was sought.

4.5.2 Ultem 1000 Internally Electroded tmAFCs

Ultem 1000[102] (an amorphous thermoplastic polyetherimide), manufactured by General Electric Plastics was selected due to its ability to adhere to the fibers and its high usage temperature allowing Ultem tmAFCs to be used in 177 °C (350 °F) cured composite structures. Ultem 1000 usage in high temperature cured composites is limited to 200 °C (392 °F) due to its thermal deformation temperature.[103] Ultem 1000 has a repeatable unit of $C_{37}H_{24}O_6N_2$ and is shown in Figure 4.13:

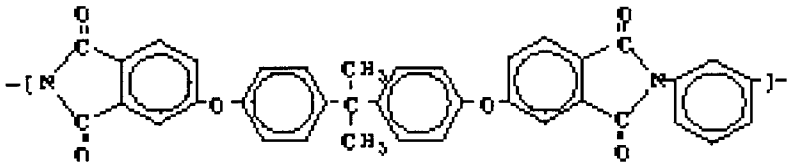

Figure 4.13 Repeating unit of Polyetherimide[104]

Material properties for Ultem 1000 are given in Table 4.4.

Table 4.4 Ultem 1000 Material Properties

Property	**Value**	**Test Method**	**Reference**
Tensile modulus at 1 mm/min	3.2 GPa	ISO R527	[105]
Compression modulus	3.31 GPa	ASTM D-695	103
Poisson's ratio	0.38	Test method not stated	[106]
Tensile strength, yield, type 1, 3.2 mm sample	105 MPa	ASTM D-638	103
Tensile elongation, yield, type 1, 3.2 mm sample	7 %	ASTM D-638	103
Tensile elongation, break, type 1, 3.2 mm sample	60 %	ASTM D-638	103
Relative dielectric constant at 100 Hz	3.15	ASTM D-150	103
Relative dielectric constant at 1 kHz	3.15	ASTM D-150	103
Dielectric breakdown strength in air 1.6 mm sample	33 kV/mm	ASTM D-149	103
Dielectric breakdown strength in oil 1.6 mm sample	28 kV/mm	ASTM D-149	103
Dielectric breakdown strength in oil 3.2 mm sample	20 kV/mm	ASTM D-149	103
Density	1270 kg/m^3	ASTM 792	103
Heat deflection temperature, 1.82mpa, 6.4mm specimen, unannealed	200 °C	ASTM D-648	103
Maximum forming temperature	316 °C	Test method not stated	[107]
Molecular weight of repeating unit	592.61 g/mol	Test method not stated	[104]

4.5.2.1 Ultem 1000 Electrode Manufacturing Procedure

The method for manufacturing thermoplastic electrodes for the Ultem tmAFCs was determined after many manufacturing experiments. The manufacturing procedure is similar to the electrodes manufactured with Noryl described in Section 4.5.1.

Electrodes for the Ultem tmAFCs were manufactured in the following manner:

1. Cut 3 sheets of 7.6 cm x 15.2 cm (3" x 6") GNPT

2. Cut 2 pieces of 4.8 mm (3/16") thick silicon rubber to the dimensions of 12.1 cm x 6.3 cm (4 ¾" x 2 ½")

3. Cut two pieces of Ultem matrix to 5.1 cm x 11.4 cm x 102 μm (2" x 4 ½" x 4 mil)

4. Clean a top and bottom electrode using acetone and methanol. This is accomplished by soaking the electrodes in a dish of acetone for about 5 to 10 minutes, then removing the electrode and spraying acetone on it, rubbing the electrode with a lint free cloth to remove any excess dirt, and then swish in a dish of methanol or isopropyl alcohol for 15 seconds. Dry the electrodes by hanging them vertically so that the solvent can drip off, taking dirt with it, in an environment where the air is constantly moving, such as a fume hood, so that dust cannot redeposit itself onto the electrodes. The electrodes should be dried until all the solvent is removed (about 30 minutes).

5. Clean the Ultem in a moving air environment using alcohol to remove grit. This is accomplished by swishing the Ultem in a dish of methanol or isopropyl alcohol for 15 seconds and then hanging them up to dry in the same manner as the electrode. Do not spray acetone on the Ultem 1000 because it degrades the polymer.

6. Place the mold in the same moving air environment as the electrodes as the Ultem. Wipe the mold using alcohol to remove grit.

7. While in the moving air environment, place the materials in the mold the mold in the following manner:

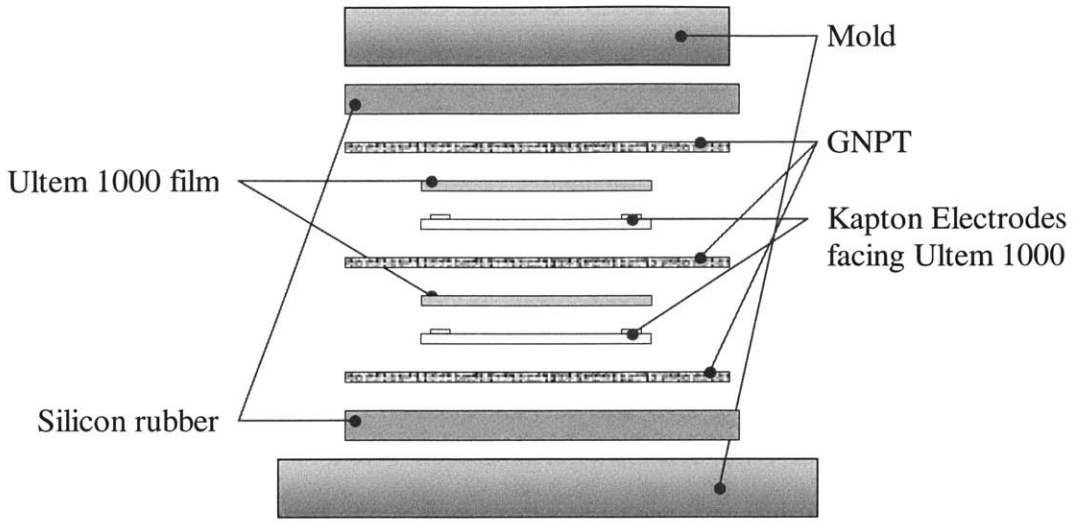

Figure 4.14 Manufacture of Ultem Electrodes

The steel mold, referred to as the "Press Plates", used for manufacturing the Ultem 1000 electrodes, is shown in Figure 4.15:

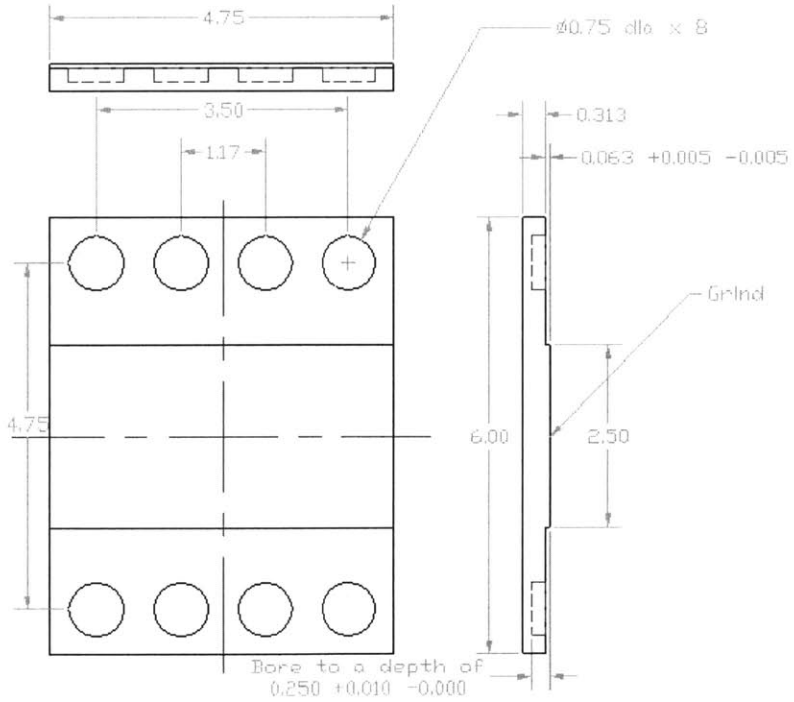

Figure 4.15 Press Plates used for Electrode Manufacturing (Dimensions in inches)

The two steel press plates were machined to form a top and a bottom for the mold, and thus the mold was symmetric through the thickness. In Figure 4.15 there are eight counter bored holes. These holes are used to hold die springs to space the mold apart during electrode manufacture. These springs prevented the mold from closing too quickly when the force is

applied. Four springs were typically used, and required about 311 – 400 N (70 - 90 lbs) to close.

8. Place the mold into the hot press and use the following cycle for bonding the two materials together:

Table 4.5 Hot Press Parameters Used for Electrode Manufacturing

Step	Temperature (°F)	Temperature rate (°F/min)	Force (lbs)	Force rate (lbs/min)	Time
1	430	500	300	32000	10 min
2	430	500	5000	32000	30 min
3	150	500	5000	32000	10 sec
4	120	500	1500	32000	10 sec
5	End	End	End	End	End

It should be noted that in Table 4.5 the temperature rate and the force rate is greater than the heaters and the hydraulics of the press can produce. The press heats at a maximum rate of about 20 °F/min, however temperature rate monotonically decreases as the temperature of the platens increases. Thus, programming the press at a temperature rate of 500 °F/min forces the hot press to heat and press should heat as fast as possible. At least 1334 N (300 lbs) is placed on the mold during at all times. If the plastic is heated to temperatures around the heat deflection temperature of the polymer, (200 °C (392 °F) for Ultem 1000, Table 4.4), the polymer will deform out of plane during heating. It is theorized that the stresses that were trapped in the film during manufacturing are relived upon reheating, thus causing deformation. Thus, an out of plane pressure must be maintained on the plastic during heating and cooling to ensure that it remains planar. Vacuum, although used for several electrode manufacturing runs, proved to be unnecessary, and was abandoned.

9. After the bonding cycle in the press, the electrodes are removed, and the Kapton is peeled from the electrode leaving the entire silver electrode embedded in the Ultem 1000. This yields the following results:

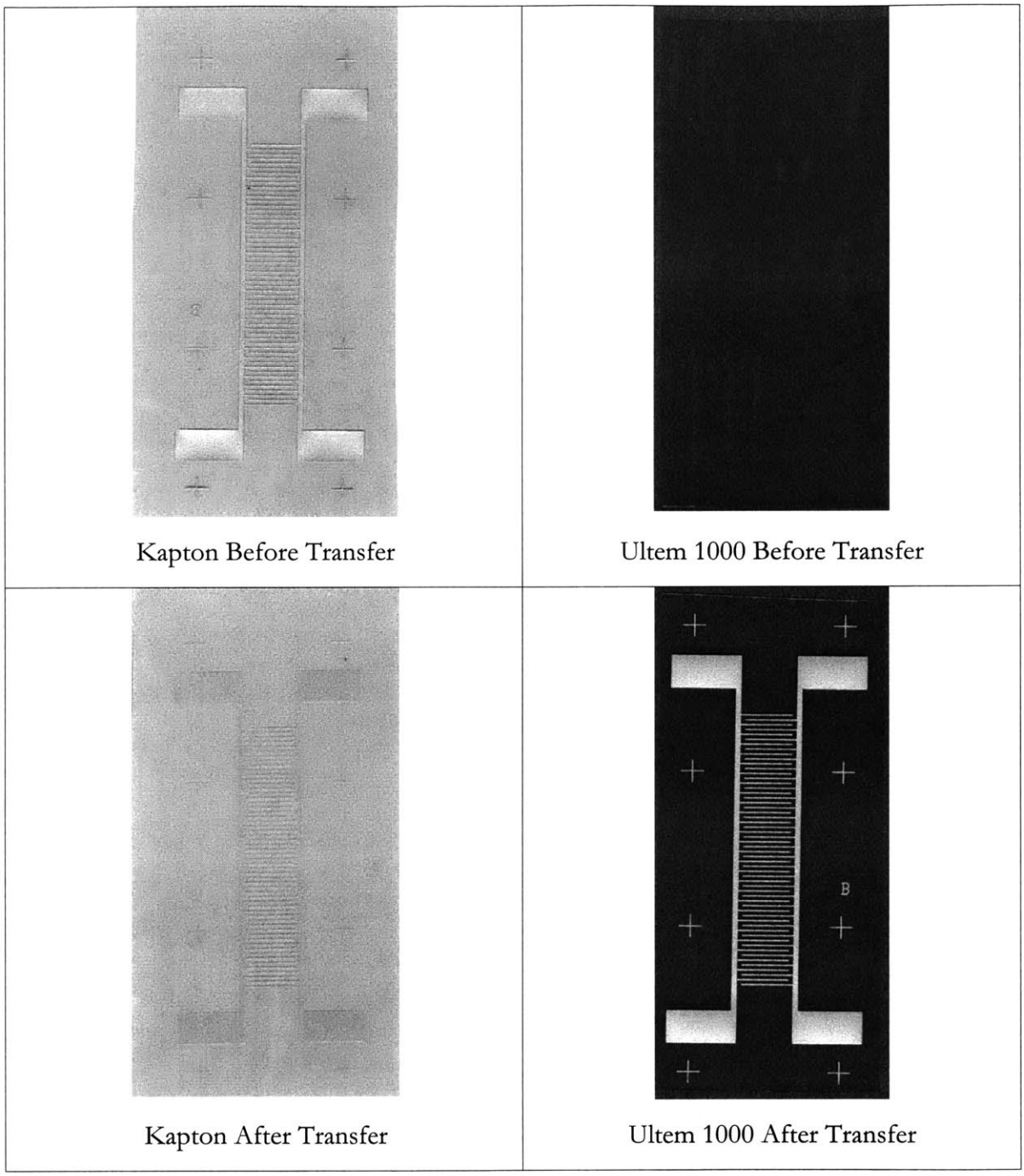

Figure 4.16 Electrode transfer from Kapton to Ultem 1000

The best transfer results occurred when the direction that the Kapton is peeled is at a 45-degree angle to the electrode fingerers. The quality of the electrode could be judged by the amount of electrode transferred. For a good quality electrode the silver would completely transfer from the Kapton to the Ultem 1000, and require a minimal amount of force to peel the Kapton off the Ultem 1000. Poor quality electrodes have some silver that remains attached to the Kapton, and require larger amount of force to peel the Kapton off

the Ultem 1000. For poor quality electrodes, the Kapton either rips or some silver remains attached to the Kapton. Typically, when some of the silver remains attached to the Kapton, it is around the corners of the electrode pads or the edges of the electrode fingers. If the above instructions are followed, then good quality electrodes will be made about 95% of the time.

When the tmAFC are manufactured, the top and the bottom electrode at put together face to face. In order to apply a voltage to the electrode a conductor needed to be bonded to the pads on the electrode. This conductor must extend outside the electrode to allow an electrical hookup. Several attempts were made using wires and pins to supply a voltage to the electrode, however the following proved to be the most reliable method.

10. Cut 4 pieces of 2.54 cm x 1.27 cm x 203 micron (1" x ½" x 8 mil) copper shim stock. If the shim is bent on the edges, use a large cylindrical weight to flatten the edges by rolling it over the copper shim. Use gloves when handling the copper because fingerprints etch the outer surface of the copper increasing their resistance.

11. Wipe the electrode surface of the thermoplastic electrodes with isopropyl alcohol. Set the thermoplastic electrodes, electrode side up, onto a piece of GNPT. Clean the copper with isopropyl alcohol also.

12. Mix some Duralco 122 conductive epoxy[108] in a pan. Place a small blob of epoxy onto the ends of two electrode pads on each electrode. The epoxy should be placed such that when one electrode is placed on top of another (face to face) none of the epoxy blobs line up.

13. Set copper strips onto the epoxy, covering only half the length of the pad. The copper should stick out of the sides of the electrode.

14. Set a piece of GNPT on top of the copper, and then set weights on top of the copper and allow to dry for 24 hours.

After the epoxy is dry and the GNPT is peeled off, the thermoplastic electrode should look similar to the following:

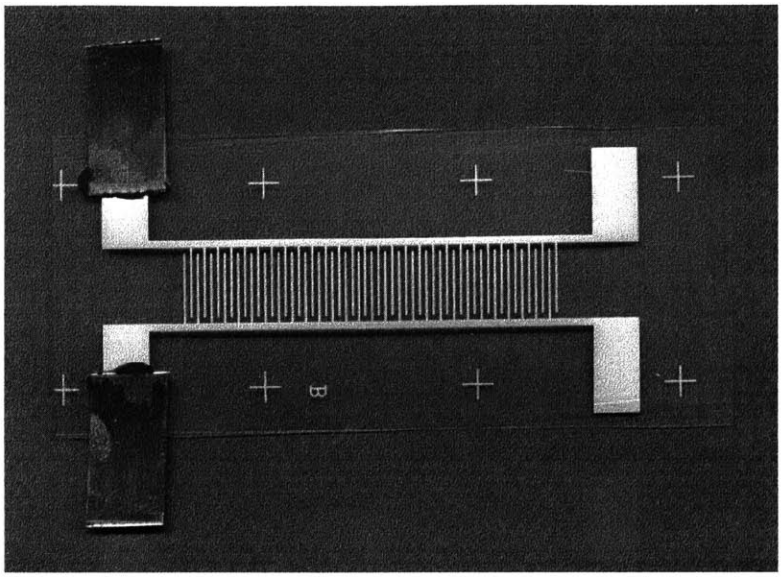

Figure 4.17 Thermoplastic Electrode with Copper Pads Bonded to it

It should be noted that several types of conductive epoxy were tried, including silver and nickel based conductive epoxies, however due to its high maximum temperature limit, 260 °C (500 °F),[109] and low viscosity, Duralco 122 conductive epoxy proved to be the best. At least 30 electrodes were manufactured using this epoxy and not once did the copper pad debond from the electrode, which happened with other conductive epoxies.

Several things are to be noted about the about the manufacture of the electrodes. First, the use of silicon rubber is very important to the manufacture of the electrodes. The silicon rubber applies a uniform pressure to the electrode. If the manufacturing is done without silicon rubber often times some areas get more pressure than others, and then the plastic does not flow into the pores of the silver electrode, and when the electrode is peeled from the Kapton the silver electrode remains attached to the Kapton. This manufacturing cycle has a tendency to degrade the silicon rubber, causing it to acquire a permanent set and the rubber becomes sticky. The shape of the set is that the center of the rubber becomes thinner than the edges. Each time the rubber is used, less and less pressure is applied to the center of the electrode because of the set, and thus the rubber should only be used about 4 or 5 times before being thrown out. It should also be noted that the cleaning of the Kapton electrode is very important to the bonding cycle. Kapton electrodes that a not cleaned according the above instructions has a tendency to not completely transfer to the Ultem 1000. This might be because dirt in the pores of the silver electrode prevent the Ultem 1000 from flowing into the electrode. It also may be that acetone degrades the bond between the Kapton and the silver electrode allowing for transfer. The Kapton with the silver electrode should be washed with methanol or isopropyl alcohol because acetone dissolves Ultem 1000 and traces of acetone on the electrodes result in a poor bond between the silver electrode and the Ultem 1000.

It should be noted that the maximum temperature used to bond the electrodes, 221 °C (430 °F), to the Ultem 1000 is between the heat deflection temperature, 200 °C (392 °F), of the Ultem 1000 (see Table 4.4) and the glass transition temperature of the Ultem 1000 measured in Section 5.2.2, 221 °C (431 °F). The quality of the bond is very sensitive to the temperature used during the bonding. Manufacturing tests were performed using slightly higher temperatures, however the Kapton could not be removed from the Ultem 1000 without damaging the polymer. It is theorized that at the maximum steady state temperature in the mold exceeded the glass transition temperature of the Ultem 1000 and the Ultem 1000 flowed into the pores of the Kapton. During cooling the Ultem solidified bonding the two together, and thus making the removal of the Kapton nearly impossible. If the temperature is too low the Ultem 1000 will not flow into the pores of the silver, and thus the two will not bond together.

If a bonding run was performed and the silver electrode did not completely stick to the Ultem 1000 and the silicon rubber seems very degraded it would be replaced for the next electrode manufacturing run. If however the silicon rubber was not degraded, the press temperature in steps 1 and 2 would be increased 2.8 °C (5 °F) on the next electrode manufacturing run. If the Kapton was difficult to remove from Ultem, the press temperature in steps 1 and 2 would be decreased 2.8 °C (5 °F) on the next electrode manufacturing run. For most electrodes manufacturing runs the press temperature was between 216 °C (420 °F) and 221 °C (430 °F). Variations in the manufacturing temperature can be attributed to variations in the ambient temperature. This indicates that the manufacturing of the Ultem electrodes can be performed in a very tight temperature range, about 218 ± 2.8 °C (425 ± 5 °F).

Because the temperature of the bonding process is so critical, the actual temperature inside the mold was investigated. When the press is operated, the heating of the platens are controlled using thermocouples embedded within the platens. The temperature commanded by the press is not the temperature between the mold. In order to determine the temperature between the plates of the mold during the electrode manufacture, two thermocouples were placed between the outer pieces of GNPT in Figure 4.14, with all other pieces removed. One thermocouple was placed in the center of the mold, and one was placed in the corner. Then the press was run in the same cycle used to manufacture the electrodes and the temperature of the press platens and thermocouples were measured. Thus, the relationship between the commanded press temperature and the temperature measured inside the mold for the electrode manufacturing cycle was determined. After this test was performed, the two thermocouples inside the mold were calibrated by boiling liquid chromatography grade water with impurities of less than 0.1 ppb and the temperature was measured using the two thermocouples. Then the water was partially frozen and the temperature was measured using the two thermocouples. It was assumed that the

temperature readout of the thermocouples could be recalibrated using a linear function. The temperatures measured using the aforementioned calibration process are given in Table 4.6.

Table 4.6 Calibration Parameters used for Figure 4.18

	Known Value	**Center Thermocouple**	**Corner Thermocouple**
Freezing Point	32 °F	47 °F	47 °F
Boiling Point	212 °F	187 °F	188 °F

Using the calibration parameters used in Table 4.6 a linear recalibration function was determined. To check the validity of the calibration process, the ambient air temperature was measured using a mercury thermometer and the thermocouples. The ambient air temperature was 75 °F when measured with the thermometer and 80 °F uncalibrated when measured with both the thermocouples. Using the calibration function, the ambient air temperature was 74.4 and 74.1 °F measured with the center and the corner thermocouples.

The relationship between the commanded press temperature and the temperature measured inside the mold using the recalibrated thermocouples for the electrode manufacturing cycle is shown in Figure 4.18.

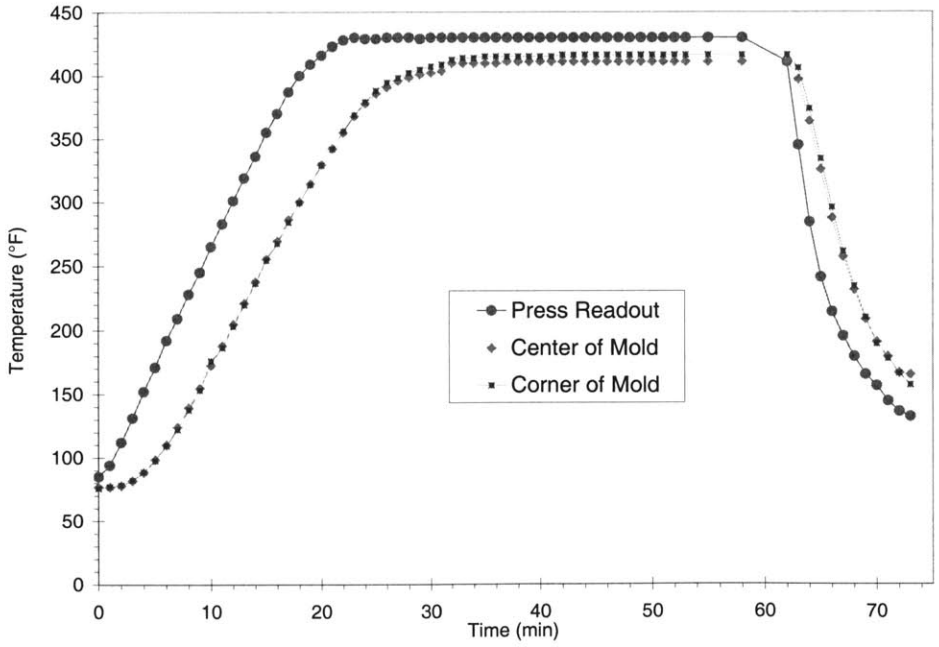

Figure 4.18 Relationship between Commanded Press Temperature and Temperature Measured inside the Mold for the Electrode Manufacturing Cycle Using the Recalibrated Thermocouples

Several things can be seen in Figure 4.18. First, the temperature in the center of the mold and the corner of the mold is essentially the same, and thus the sample can be assumed to be at a uniform temperature. Second, the temperature in the center of the mold lags the temperature of the platens of the press. This because the heat of the platens must travel through, 1 piece of GNPT, two 3/8" steel plates, 2 more pieces of GNPT, the mold, 2 pieces of silicon rubber, and 2 more pieces of GNPT. Because of all the thermal losses, the maximum temperature inside the mold is less than the maximum temperature on the platens. When the platens are commanded to be 221 °C (430 °F), at steady state, the actual temperature at the center of the mold is 213 °C (416 °F) and the edge of the mold is 210 °C (411 °F). Thus, the optimal temperature for manufacturing the Ultem 1000 thermoplastic electrodes was approximately equal to the average of the glass transition temperature, and the heat deflection temperature.

If another polymer is to be used other than the Ultem 1000 one should select a polymer with a low enough viscosity between the thermal deflection temperature and the glass transition temperature so that it can adhere to the electrode and not to the Kapton. Second, when adhering the polymer to the fibers, the glass transition temperature should be exceeded to guarantee a good quality bond. It should also be noted that the center of the mold is at a steady state temperature for approximately 20 minutes. If the electrodes were going mass produced, this time could be reduced to potentially less than a minute. Further decreases in production time could be realized if a faster heating and cooling process could be used.

Some manufacturing runs were preformed to increase the production of Ultem thermoplastic electrodes. Eight electrodes were manufactured at the same time in the same mold with no failures. This mass production of electrodes was done several times. Ten electrodes were attempted once, however the film and the GNPT shifted in the mold and some of the electrodes had no pressure on them during the cure, and the electrodes did not stick to the Ultem.

4.5.2.2 Lay-up of the tmAFC

Before the Ultem tmAFCs were manufactured, 140 μm (5.5 mil) diameter fibers manufactured by CeraNova[44] were used for the tmAFCs. These fibers had problems with straightness and were very hard to align and insure that the gaps between the fibers were small. As seen in the internally and externally electroded Noryl tmAFCs, electrode breaks could occur at small gaps between the fibers. 270 μm (10.6 mil) diameter fibers were purchased from CeraNova. These fibers were straighter and easier to align thus reducing the gaps between the fibers. These fibers were used for all the Ultem tmAFCs.

The bonding of Ultem 1000 thermoplastic electrodes to the PZT-5A fibers occurred in a manner similar to the Noryl internally electroded tmAFCs.

1. Tape a piece of GNPT to a piece of glass. Count out 37 fibers 270 μm (10.6 mil) diameter fibers and place them on the GNPT. These fibers should be approximately 15.2 cm (6") in length.

2. Line up the fibers side by side using a razor blade making sure none overlap. The gaps between the fibers should be small. Fibers that are not straight or short should be set aside and replaced with new fibers.

3. Mix some 5-minute epoxy in a pan. Using a stick, scoop up a blob of 5-minute epoxy onto the end of the stick. Spin the stick back and forth using the centrifugal force to hold the epoxy on the end of the stick.

4. Hold the stick about 2.5 cm (1") above the ends of the fibers. Allow the blob of epoxy to drip off the end of the stick onto the GNPT next to the fibers. As the epoxy is dripping, move the stick across the fibers so that epoxy covers the ends of the fibers. Never wipe the epoxy onto the fibers, nor touch the fibers with the epoxy on the end of the stick. This oftentimes makes the fibers move.

5. Cover both ends of the fibers with epoxy. The blobs of epoxy should be approximately 14 cm (5.5") apart.

6. Allow the epoxy to dry for at least 15 minutes.

7. Peel the fibers with the epoxy off from the GNPT. The fibers with the epoxy on the ends will henceforth be referred to as the "fiber mat". If necessary use a razor blade to pry the fiber mat from the GNPT.

A fiber mat comprised of 37 270 μm (10.6 mil) diameter PZT-5A fibers with 5-minute epoxy on the ends is shown in Figure 4.19.

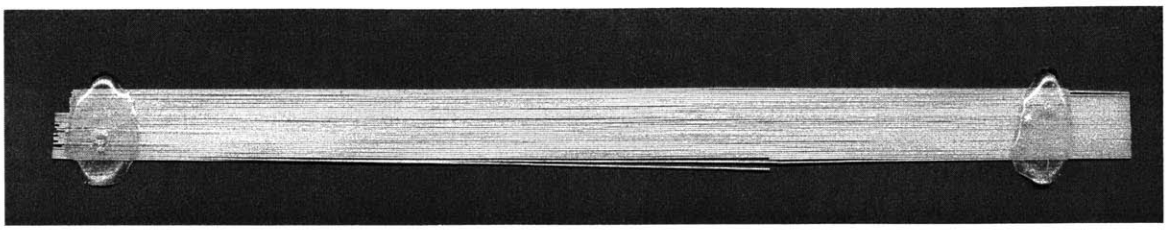

Figure 4.19 Fiber Mat Comprised of 37 270 μm (10.6 mil) Diameter PZT-5A Fibers with 5-Minute Epoxy on the Ends and Breaks in the Fibers

8. Check the fibers to make sure all the ends of the fibers are epoxied. If necessary, repair the fiber mat by applying another epoxy blob. The epoxy blobs should be at a minimum of 12.7 cm (5") apart. If they are not the fiber mat cannot be used. Also check for breaks in the center of the fibers. Breaks in the centers of the fibers, such as the ones in Figure 4.19, cannot be repaired and thus the fiber mat must be discarded.

9. Place the fiber mat into an environment where the air is constantly moving, such as a fume hood. While wearing gloves, hot the fiber mat by one of the epoxy blobs. Spray the fibers on both sides using a spray bottle of acetone followed by isopropyl alcohol. The goal is to douse the fibers to have any dirt present drip off with the solvents.

Experiments were done spraying the fibers with a can of pressurized air[110] to remove dirt and dust. Often times eyelashes would be caught between the fibers and the air could not remove them. Also using the can of pressurized air required a delicate touch, if the handle was squeezed too much the fiber mat would vibrate with too high of an amplitude, breaking the fibers.

10. Dry the fiber mat by suspending them vertically so that the solvent can drip off taking dirt with it, in an environment where the air is constantly moving, such as a fume hood, so that dust cannot redeposit itself onto the fiber mat. The fiber mat should be dried until all the solvent is removed (about 30-60 minutes).

11. Cut 2 sheets of 7.6 cm x 15.2 cm (3" x 6") GNPT

12. Cut 2 pieces of 4.8 mm (3/16") thick silicon rubber to the dimensions of 12.1 cm x 6.3 cm (4 ¾" x 2 ½")

13. Cut two pieces of Ultem 1000 to 10.2 cm x 2.5 cm x 152 μm (4" x 1" x 6 mil). One of the long sides should be cut such that is very straight, however the other three sides can be cut less exact.

14. Clean thermoplastic electrodes, the GNPT, and the Ultem 1000 strips. This is accomplished by soaking them in a of isopropyl alcohol for about 5 to 10 minutes, then spraying isopropyl alcohol onto the pieces to remove any excess dirt. Dry the pieces by hanging them vertically so that the solvent can drip off taking dirt with it, in an environment where the air is constantly moving, such as a fume hood, so that dust cannot redeposit itself onto the pieces. The pieces should be dried until all the solvent is removed (about 15-30 minutes).

15. Place the bottom portion of the mold in Figure 4.15 in the place where the fibers and the materials for the lay-up are drying (the environment where the air is constantly moving). Wipe the top surface with isopropyl alcohol to remove any dirt.

16. Lay-up the materials on the bottom portion of the mold in the following manner:

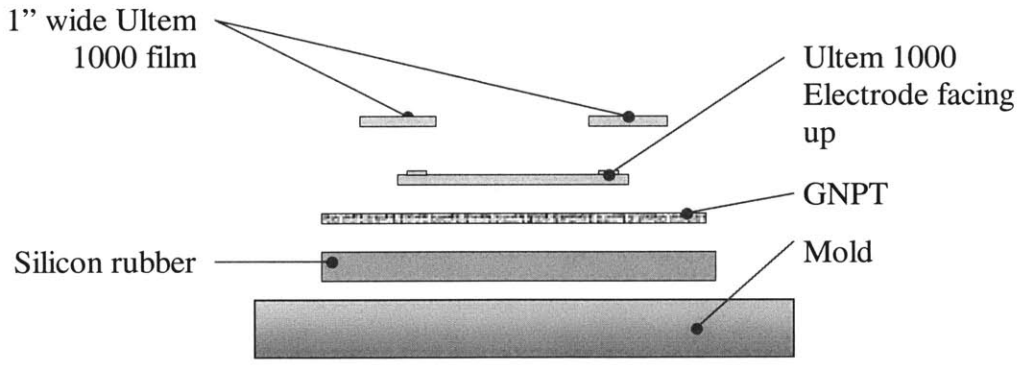

Figure 4.20 Lay-up of the Lower Portion of the tmAFC

The 1" wide Ultem 1000 film should be placed onto the Ultem 1000 electrode such that the straight edges touch the tips of the electrode fingers, as shown in the following illustration:

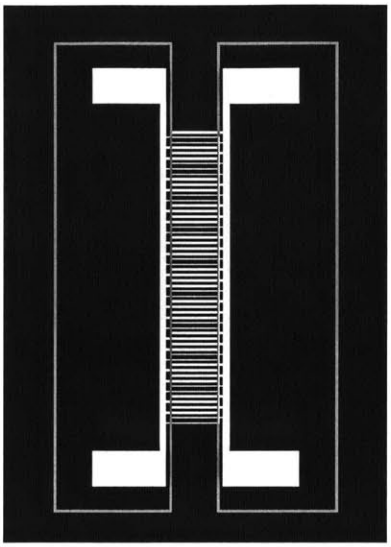

Figure 4.21 Placement of the 1" Wide Ultem 1000 Strips on the Upper Surface of the Thermoplastic Electrode

17. Using a soldering iron to poke holes between the two films, thermally weld the 1" wide Ultem 1000 strips to the electrode in several places. Do not touch the iron to areas above the electrode. Doing so could potentially cut though the electrode.

18. Rest the fiber mat on the electrode in the trough formed by the 1" wide Ultem 1000 strips. The strips prevent the fibers from moving out of the active area during the manufacturing process, thus guaranteeing that all the fibers are in the active area. The strips also prevent the electrode fingers from bending at a 90° angle when wrapping around the first and last fibers.

The mold in Figure 4.15 was constructed so that it was 12.1 cm (4.75") wide. This was to allow the epoxy on the ends of the fibers to stick out of the ends of the mold. When placing the fibers on the electrode it is best to minimize horizontal movement of the fibers. Moving the fibers back and forth on the electrode causes silver to rub off the electrode and deposit onto the fibers. This provides a potential electrical breakdown path.

19. Place the top electrode onto the fibers aligning the electrode fingers of the top and bottom electrode.

20. With a soldering iron, thermally weld the top electrode to the 1" wide strips in several places. This prevents movement of the top electrode with relation to the bottom during the bonding.

21. Place the GNTP, silicon rubber in the mold in the following manner:

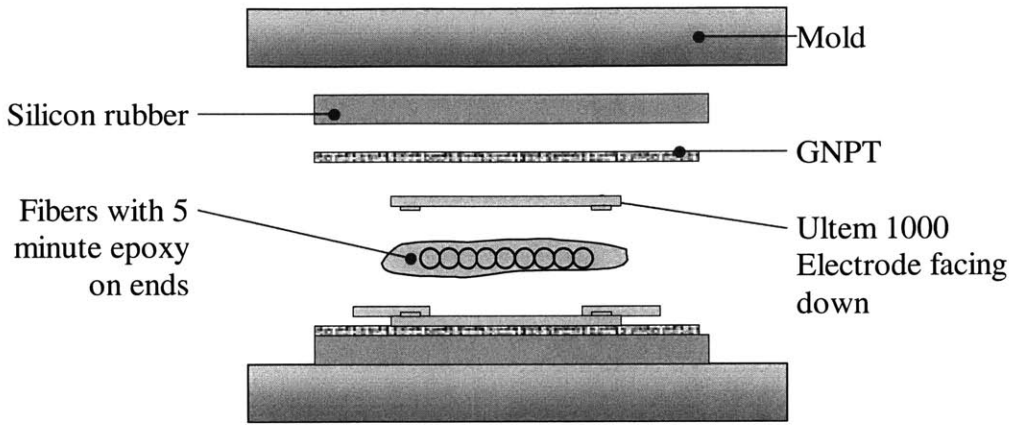

Figure 4.22 Lay-up of the Upper Portion of the tmAFC

22. Put the springs into the mold. Wipe the upper portion of the mold with isopropyl alcohol and place on top.

Many manufacturing experiments were performed to determine this procedure for manufacturing tmAFCs. The procedure described above was used for most Ultem 1000 tmAFCs. The entire lay-up should be done an environment where the air is constantly moving. This minimizes the dust and dirt that is deposited on the fibers and the electrode. Dust and dirt present on the fibers provided a dielectric breakdown path during poling, which caused breakdown in at least fifteen Ultem 1000 tmAFCs. Strict adherence to the above procedure is necessary to resolve this problem.

4.5.2.3 Bonding of the Fibers to the Electrode in tmAFCs

Before any of the tmAFCs could be manufactured, tests had to be preformed to determine the temperature and the pressure to be used for the manufacturing. Several failure modes were discovered for tmAFCs when manufacturing solvent casted tmAFCs and externally electroded tmAFCs. Each failure mode shall be listed, and if a value for the failure mode is known, it will be given.

1. The fibers fail in compression when an external pressure of approximately 689 kPa (100 psi) is applied to them.[111] This failure occurs when the pressure is applied transversely to the fibers.

2. There exists a compressive pressure at which the electrode fingers break when pressed into the fibers, as shown in Figure 4.11. This pressure should decease as the temperature

at which the electrode is pressed increases, due to the fact that the thermoplastic provides less support to the electrode when the thermoplastic is a rubbery solid or is melted. Below the glass transition temperature of the thermoplastic, the compressive failure stress of the electrode is much higher than above the glass transition temperature. This is because the thermoplastic is a glassy solid below the glass transition temperature, preventing deformation of the electrode.

3. There exists a temperature at which the thermoplastic matrix thermally fails. As will be discussed in Section 5.2.3, the temperature at which 5% of the Ultem 1000 decomposes by mass is approximately 475 °C (887 °F), depending on the heating rate.

4. There exists a temperature at which the binder in the electrode in the thermoplastic matrix thermally fails, and thus the electrode stops acting as a conductor. As discussed in Section 5.3, this temperature is greater than 316 °C (600 °F) for Ultem 1000, the limit of the apparatus used to heat the samples.

5. In order for the top and the bottom electrode to adhere to each other, the glass transition temperature must be exceeded during manufacturing of the tmAFC. For Ultem 1000, as measured in 5.2.2, the midpoint glass transition temperature is 221.4 °C (430.5 °F).

6. In order for the thermoplastic to adhere to the fibers, the thermoplastic must be melted so that it can flow into the pores of the fibers during manufacturing. When the thermoplastic is cooled down, the thermoplastic solidifies, locking into the fibers. The tmAFC does not need to be completely heated to the melt temperature of the thermoplastic. However, the thermoplastic must be heated to a high enough temperature so that the viscosity of the thermoplastic is low enough to allow it to flow into the pores of the fibers, else the electrode debonds from the fibers as shown in Figure 4.23. The temperature at which the viscosity of the thermoplastic is low enough so that it can flow into the fibers is a function of the pressure (increased pressure decreases the temperature needed), and the rate at which force is applied (the shear rate).

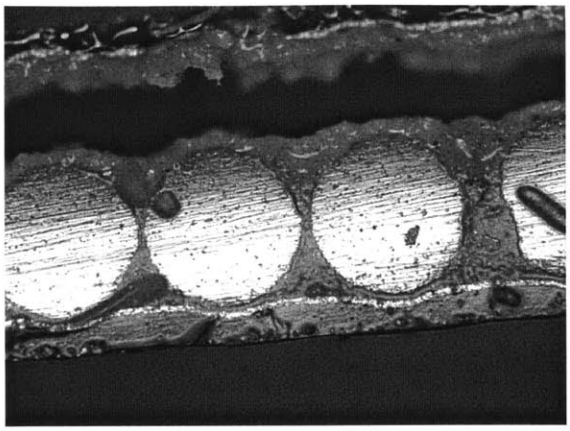

Figure 4.23 Delamination in an Ultem 1000 tmAFC

Based upon experience it has been seen that the electrode appears to fail at a lower pressure than does the fibers due to the large number of electrode breaks seen under the microscope and the relatively few fiber breaks. Using the above failure modes, a failure plot illustrating the relationship between the applied pressure during the bonding of the tmAFC versus applied temperature can be drawn:

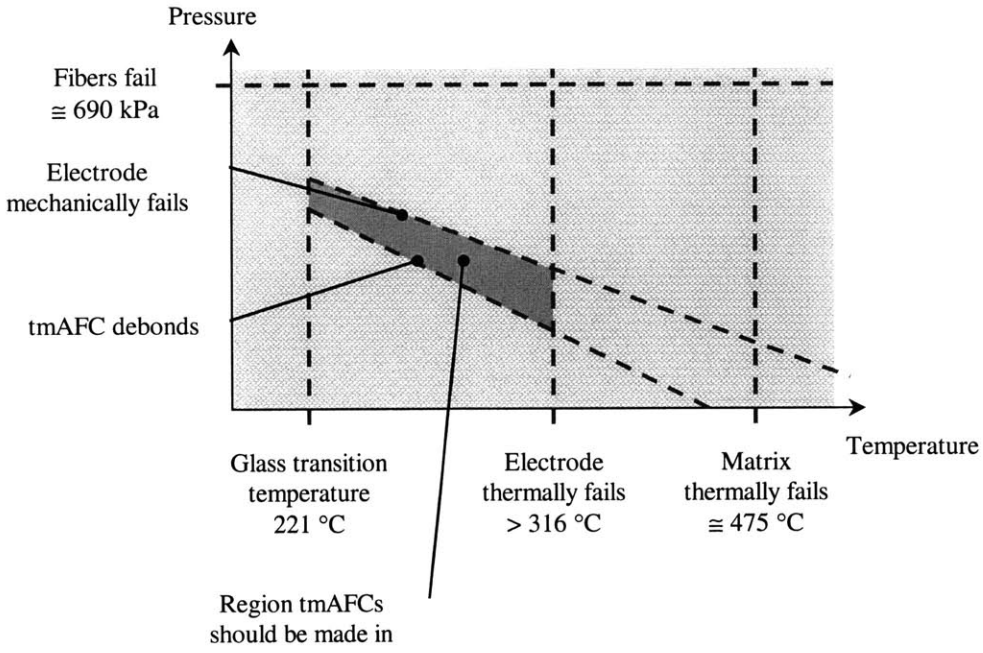

Figure 4.24 Failure Plot Illustrating the Relationship between the Applied Pressure During the Bonding of the tmAFCs versus Applied Temperature

In Figure 4.24 the pressure at which the electrode mechanically fails and the pressure at which the tmAFC debonds is shown linear with temperature. In reality is not true, however it is the most convenient way of illustrating the relationship. As can be seen in Figure 4.24,

there exists a pressure and a temperature at which tmAFCs should be manufactured, however because the pressure at which the electrode mechanically fails and the pressure at which the tmAFC debonds is unknown, the limits of this region are unknown.

Consider process of the bonding of fibers to the electrode in a tmAFC. The tmAFC is heated to a temperature above the glass transition temperature, and the electrodes and the fibers are pressed together. If this pressure just greater than is what is needed to consolidate the composite, but small enough not to break the electrode fingers, all the fingers will be intact. If all the electrode fingers are intact, then each piece of fiber between each electrode finger will receive voltage when a voltage is applied to the electrode pads, and thus the capacitance of the tmAFC will be maximized (because the fibers have a much higher capacitance than does the matrix). If the pressure is increased up to the point before a single electrode finger is broken, the capacitance of the tmAFC will not change. If the capacitance is increased further, breaking several electrode fingers, when a voltage is applied to the electrode pads, the voltage is not delivered to all the fibers, and thus the capacitance will be reduced. As the pressure is further increased, more and more electrode fingers are broken until all the fingers are broken. At this point, the capacitance of the tmAFC should be at a minimum because the only portion of the tmAFC that provides capacitance is the low dielectric matrix.

Using the layup presented in Section 4.5.2.2, several tmAFCs were manufactured using different applied pressures. The pressure is the average pressure applied to the tmAFC, equal to the maximum applied force divided by the area of the silicon rubber. After each tmAFC was manufactured, the parallel capacitance was measured. It has been seen that specimens with a high parallel capacitance (Cp) typically have a high level of free actuation[112]. Figure 4.25 is a plot of parallel capacitance and magnitude of impedance verses the applied average pressure for Ultem 1000 tmAFCs manufactured at 260 °C (500 °F).

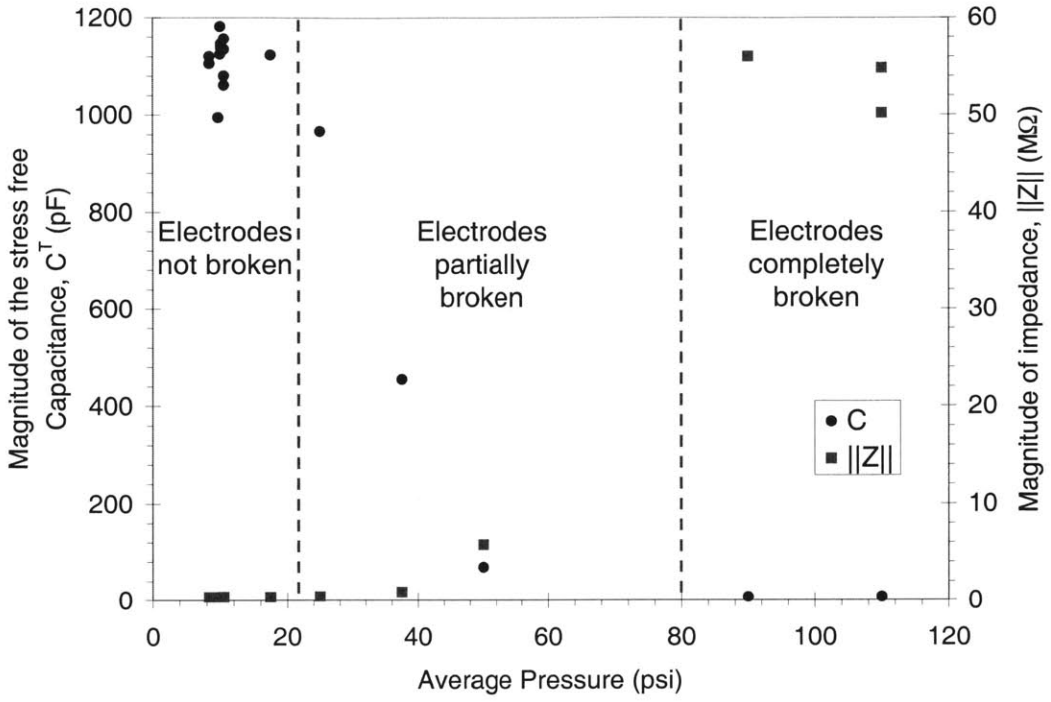

Figure 4.25 Parallel Capacitance versus Applied Pressure for Ultem tmAFCs Manufactured at 260 °C (500 °F)

It should be noted that in Figure 4.25 not all the tmAFCs were manufactured using fibers from the same batch. In addition, some manufacturing parameters were changed such as the thickness of the electrode (3 and 4 mil electrodes were used) and the length of the matrix used to bond the electrode to (4.25", 4.5", and 4.75"). These parameters were changed due to availability of materials, and attempts to fix minor manufacture problems such as the thermoplastic bonding to the side of the mold.

As can be seen in Figure 4.25, as the pressure is reduced the parallel capacitance increases and the magnitude of the impedance decreases. This increase in the parallel capacitance is because at higher load levels there is a greater chance to break fibers and the electrode. About 311 - 400 N (70-90 lbs) is required to close the mold and thus pressures less than 8.4 psi (100 lbs / (2.5" x 4.75")) was not used for manufacturing. In order to produce tmAFCs with the highest capacitance it is most desirable to manufacture tmAFCs with as low a pressure as possible, as seen in Figure 4.25. For the majority of the tmAFCs, the following cycle was used for bonding the fibers and the electrodes in the hot press:

Table 4.7 Hot Press Parameters Used for Bonding the Fibers and the Electrodes in the Hot Press

Step	Temperature (°F)	Temperature rate (°F/min)	Force (lbs)	Force rate (lbs/min)	Time
1	425	500	80	32000	10 min
2	500	3	100	32000	10 min
3	150	500	100	32000	10 sec
4	120	500	80	32000	10 sec
5	End	End	End	End	End

Figure 4.26 and Figure 4.27 shows a top view and cross section of a tmAFC.

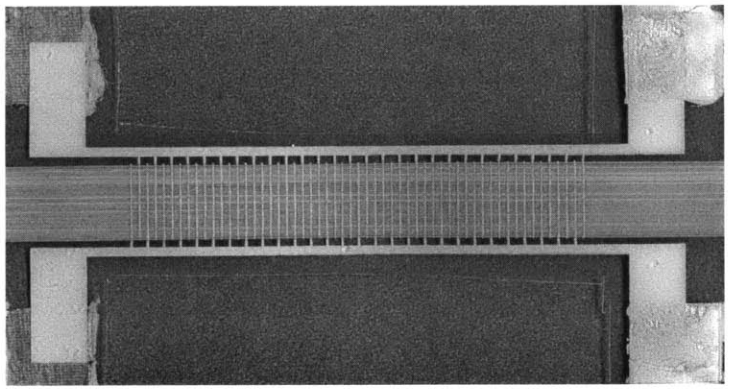

Figure 4.26 Top View of an Internally Electroded Ultem tmAFC

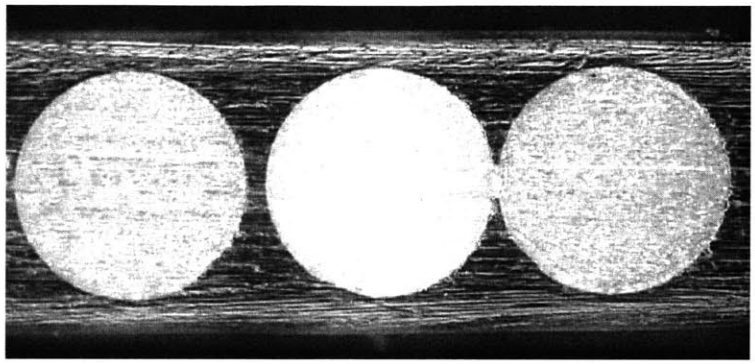

Cross section between electrodes

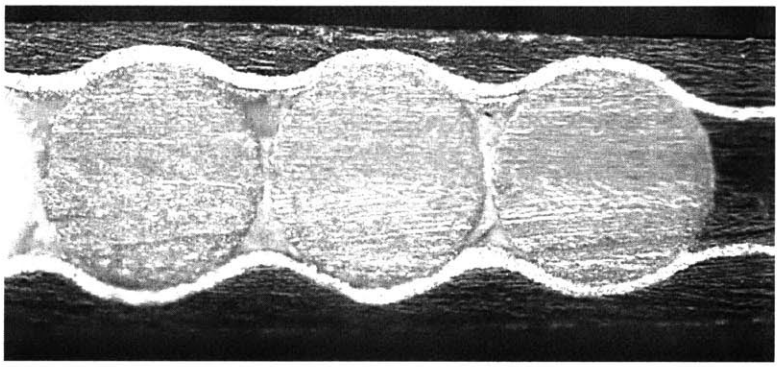

Cross section of electrodes

Figure 4.27 Cross Sections of the Fibers between the Electrodes and the Electrode of an Internally Electroded Ultem tmAFC

As can be seen in Figure 4.26 and Figure 4.27, there is intimidate contact between the fiber and the electrode. By fitting a circle Figure 4.27 and estimating where the electrode touches the fibers, using Equation 2.3, one can estimate that ξ is approximately 75% for the tmAFC. In Section 3.8.6, using material data and the finite element analysis it was predicated that for a PiezoFlex AFC $\xi > 99.4$ and $\xi < 100.1$. Thus, the tmAFC in Figure 4.27 has better electrical contact between the fibers and the electrode, and should therefore be a better actuator (see Figure 3.26), if the material stiffness and the geometry of the two actuators were the same.

Several things should be noted about bonding of the fibers to the electrode in tmAFCs.

1. Thirty-two Ultem 1000 tmAFCs were made using the mold in Figure 4.15. These were labeled in order tmAFC 1-31. Due to a record keeping error, there was two tmAFC 7's, and thus the second one was renamed tmAFC 7a. Eleven more Ultem 1000 tmAFCs

were manufactured using a mold with an internal vacuum chamber as will be shown in Figure 4.29. These tmAFCs were labeled, in-order, tmAFC A – K.

2. Most of the Ultem 1000 tmAFCs, after tmAFC 7a and prior to tmAFC 22, failed during poling due to dust and dirt being trapped between electrode fingers. The dust and the dirt provided a path for dielectric breakdown. Ultem 1000 tmAFCs made prior to tmAFC 8 were made with a coupling agent as described below. It could not be determined if the reason for these tmAFCs failing during poling was due to dust and dirt, or the coupling agent reducing the dielectric breakdown of the tmAFC.

3. tmAFCs 22-31 were made using vacuum below 686 mm of hg (27" of hg) or with no vacuum at all. This was because the vacuum chamber of the hot press had leaks. The vacuum chamber is a welded steel box open on the bottom with doors on two sides that sits atop the base which houses the hot press controls. The vacuum chamber surrounding the platens of the press and is shown in Figure 4.2. When the hot press was manufactured, the open side of the vacuum chamber was bolted to a plate that is connected to the base. Between the vacuum chamber and the plate there is a silicone sealant, such as RTV[113], which is held in place by the weight of the vacuum chamber (approximately 700 lbs). Due to the cycling of vacuum during the manufacturing of tmAFCs, the RTV seal was stressed and eventually broke in two places. As the press was used more and more the rip in the RTV increased, making a larger and larger hole. Efforts were made to plug the hole by covering it with epoxy, and other materials, however the size of the leak kept increasing. Vacuum pumps that could pull a vacuum at greater and greater flow rates were used in an attempt to counteract the leak, however the leak kept increasing. Eventually the required flow rate of the vacuum pump was so large that a vacuum pump could not be found to overcome the leak and still be driven with 110 V. The final size of the leak was approximately 1 m (3') when it was decided that the vacuum chamber could not be used anymore. It was estimated that it would cost approximately $10,000[114] and at least 1 months time to fix the leak using an o-ring. This cost was greater than the budget for the entire semester, and even if the leak was fixed there was no guarantee that there were not more leaks internally in the press (most specifically around the actuating piston that passes through the bottom of the vacuum chamber).

An attempt was made to manufacture tmAFCs with little to no vacuum and 10 tmAFCs were made in this fashion (tmAFCs 22 - 31). Although most of these tmAFCs showed a high pre-poled capacitance, every tmAFC broke down during poling. It is felt that air was trapped between the fibers during the manufacturing process, and this air would break down during poling. Voids between the fibers can be seen in Figure 4.28

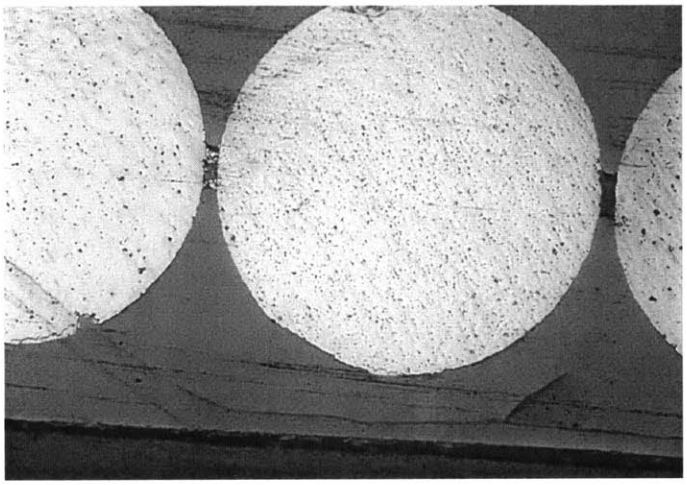

Figure 4.28 Voids and Electrical Breakdowns between Fibers in tmAFC 22

4. In an attempt to get around the problem of the leaking vacuum chamber, a new mold was manufactured. This mold was comprised of two aluminum plates similar to the press plates in Figure 4.15. A steel plate with four grooves for o-rings was placed between the aluminum plate, as shown in Figure 4.29:

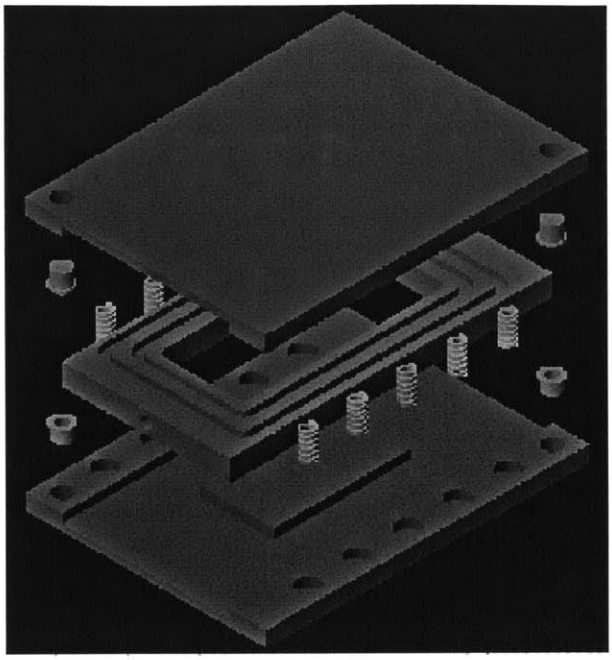

Figure 4.29 Mold with Internal Vacuum Chamber used for tmAFCs A-K

The purpose of the steel plate was to form a vacuum chamber around the tmAFCs samples. Silicon rubber o-rings were placed in the groves in the steel plate and a vacuum was drawn though the hole in the end of the steel plate. tmAFCs A – K were manufactured using the mold in Figure 4.29, and the same lay-up in Figure 4.20 and Figure 4.22. Due to budgetary concerns, only one o-ring per side was used. The mold with the internal vacuum chamber had two major drawbacks. First, the mold would squeeze together when the vacuum was applied, thus increasing the pressure on the tmAFCs. In order to minimize the squeeze that the vacuum applied, 10 die springs were placed around the outside of the mold to increase the stiffness. A second problem is that the o-rings added an unknown stiffness when attempting to close mold, and the steel plate prevented the operator from seeing the tmAFC. Thus, the pressure required to close the mold and just barely touch the sample had to be determined by trial and error. tmAFCs A – K were manufactured toward the end of the research, however the 11 samples were not enough to completely characterize the mold to the point where good tmAFCs could be made with it. It is theorized by the author that at the time that tmAFCs A – K were manufactured there was a problem with the force transducer in the press. Some samples pressed at a lower force appeared to be completely crushed, and some samples pressed at a higher force appeared to be pressed with too little force.

5. Most Ultem 1000 tmAFCs were made using a processing temperature of 260 °C (500 °F). One tmAFC (tmAFC 24) was manufactured using a processing temperature of 288 °C (550 °F), however it appeared slightly brownish in color, and its pre-poled capacitance was approximately 10% below that of tmAFCs manufactured at 260 °C (500 °F). This tmAFC was manufactured without vacuum and therefore the change in color was due to oxidation which occurred due to the lack of vacuum used for this specimen. Several tmAFCs were manufactured at 274 °C (525 °F), however the data was inconclusive whether the pre-poled capacitance changed.

6. For some tmAFCs, pieces of high temperature silicon rubber (Reference 101) were reused. It was discovered later that exposing the silicon rubber to 260 °C (500 °F) temperatures caused a permanent set in the rubber in areas of maximum stress, making the rubber thinner in the center. Thus, when the rubber was reused the actual pressure on the tmAFC was less than the pressure that was on the previous tmAFC, which may account for some of the scatter in the data in Figure 4.25. New pieces of rubber were used for most of the later tmAFCs.

7. In order to promote the adhesion between the fibers and the matrix, fibers were dipped in a solution containing coupling agent and liquid chromatography grade water with impurities of less than 0.1 ppb prior to use in the composite. These fibers were used in tmAFCs 1 - 7a. The coupling agent was Silquest A-1120 Silane[115] manufactured by Witco Corporation. The coupling agent was mixed 6% by mass with the water. tmAFCs 1 - 3 were manufactured in a manner similar to the tmAFC described in Section 4.5.2.3, except a maximum temperature of 218 °C (425 °F) was used. tmAFCs 1 - 3 had problems with delaminations so the temperature that the tmAFCs were manufactured at was increased to 260 °C (500 °F). In order to determine the minimum amount of coupling agent required five tmAFCs (tmAFCs 4 - 7a) were manufactured with 6% to 1% coupling agent by mass. In none of the tmAFCs was delaminations seen. It was then thought that perhaps the coupling agent was not responsible for the lack of delaminations, but the increase in temperature was. More tmAFCs (tmAFCs 8-31) were constructed without coupling agent and delaminations were not seen in any of them.

5. tmAFC Testing

5.1 Introduction

Several tests were performed on the constituent materials of tmAFCs, tmAFCs, and AFCs. Stress-strain tests, glass transition temperature testing, and thermal decomposition testing were performed on Ultem 1000. The decomposition temperature of silver electrodes embedded in Ultem 1000 was determined by heating the electrodes and measuring their impedance. Two tests were performed on tmAFCs, capacitance testing and actuation testing. Each will be discussed in turn.

5.2 Testing of Ultem 1000

Three tests were performed on Ultem 1000, Stress-strain tests, glass transition temperature testing, and thermal decomposition testing. Stress-strain tests were performed on Ultem 1000 to determine the Young's modulus. The glass transition temperature of Ultem 1000 was measured to determine the minimum manufacturing temperature for the electrodes. Thermal decomposition testing was performed on Ultem 1000 to determine the maximum processing temperature.

5.2.1 Young's Modulus Measurements

Five tests articles were cut from Ultem 1000 film manufactured by Westlake Plastics. The specimens had a nominal thickness of 0.051 mm (2 mil), an average width of 2.3 cm (0.89"), and a length of 30.1 cm (11.9"). The specimens were cut perpendicular to the direction that the film is unrolled. A piece of double stick tape was placed on either end of the test article 250 mm (9.84") apart. These pieces of tape were used to help align the test article in the grips of the Instron 5542 universal electromechanical testing machine[116] load frame with an initial grip separation of 250 mm (9.84"). The grips used in the testing machine were flat grips that were rubber coated (Instron part number 2710-004). The grips of the testing machine were then actuated to pre-buckle the specimen slightly and the load

was zeroed. The test specimens were then pulled at a strain rate of 0.1 mm/(mm min) and thus the rate of grip separation was 25 mm/min. The test was performed from 0 N (0 lbs) to 49.5 N (11.1 lbs) which coverers 99% of the range of the load cell used (Instron part number 2530-437). This test conformed to the ASTM D-882-97: Standard Test Method for Tensile Properties of Thin Plastic Sheeting[117]. A typical stress versus displacement plot is shown below:

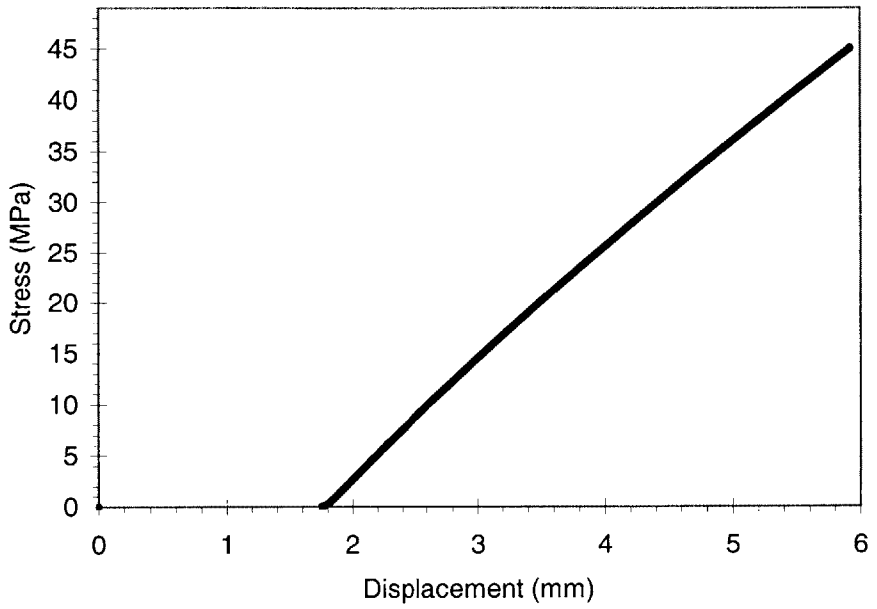

Figure 5.1 Stress versus Displacement for Ultem 1000 Specimen 3

At a displacement of about 1.8 mm in the above plot, there is a slight toe region due to the take up in slack of the specimen. In Figure 5.1, the stress in not linear with respect to displacement over the entire range of displacement. Because there is no visible yield point in the above data, it was assumed that the stress-strain relationship was given by a Ramberg-Osgood relationship (Reference 57 pages 532-535):

$$S = \frac{T}{E} + \left(\frac{T}{H}\right)^{\frac{1}{n}} \tag{5.1}$$

Where S is the strain, T is the stress, E is the Young's modulus, n is the strain hardening exponent, and H is an additional constant. In order to compensate for the toe region, data near the region of the toe was neglected. The displacement was then fitted to:

$$\frac{d - d_0}{L} = \frac{\sigma}{E} + \left(\frac{\sigma}{H}\right)^{\frac{1}{n}} \tag{5.2}$$

Where d is the displacement, d_0 is the offset in displacement due to pre-buckling the specimen, and L is the gage length of the specimen. Figure 5.2 shows the data fit for Specimen 3:

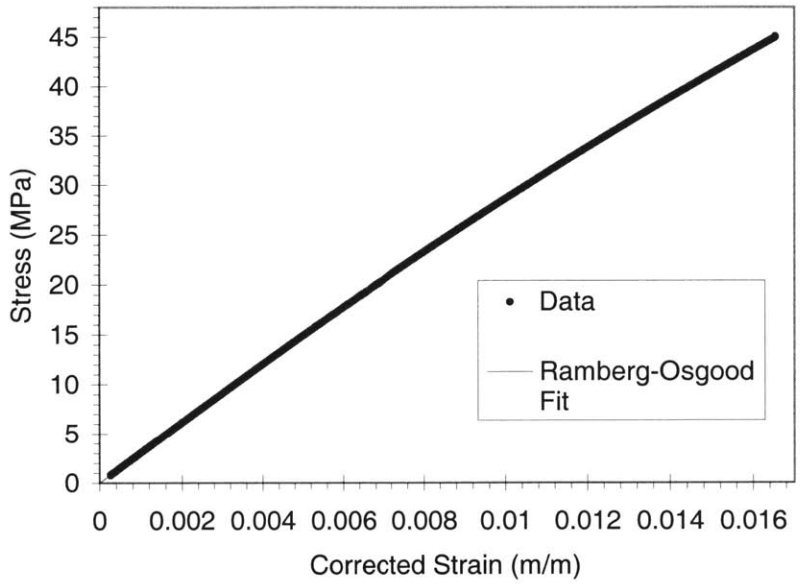

Figure 5.2 Stress versus Corrected Strain For Ultem 1000 Specimen 3

From the five specimens the average material properties were determined:

Table 5.1 Average Material Properties for Ultem 1000

Material Property	**Average**	**Standard Deviation**
E	3.12 GPa	0.082 GPa
n	0.452	0.025
H	796 MPa	103 MPa

This Young's modulus is very close to the value of 3.2 GPa as tested by General Electric (Table 4.4).

5.2.2 Ultem 1000 Glass Transition Temperature Measurement

A single sample of Ultem 1000 was measured using a Pyris 1 DSC (Differential Scanning Calorimeter) manufactured by Perkin-Elmer.[118] A sample of Indium was tested at a rate of 20 °C/min in the DSC to insure accuracy. The melting peak and the mass normalized enthalpy of fusion differed from the standard values by less than 0.2% and 0.3% and thus the DSC was considered accurate and did not require recalibration. Two Aluminum PE#0219-0041 Solid Sample Pans and lids manufactured by Perkin Elmer were

then placed in the DSC and were tested at a rate of 20 °C/min from 150 °C to 250 °C to determine a baseline curve. This baseline curve was subtracted from the Ultem 1000 data to remove the heat flow due to the sample pans.

A roll of 0.051 mm (2 mil) film of Ultem 1000 film was purchased from Westlake Plastics[99] and cut into 6.35 mm (¼") diameter pieces. These pieces were placed into a pan with a lid that was manufactured by Perkin Elmer for a sample mass of 13.716 mg. The pan with the sample was placed into the DSC on one side with an empty sample pan and lid on the other. The sample was heated from 150 °C to 250 °C at 20 °C/min to remove any thermal history. The sample was then held at 250 °C for 10 minutes and then cooled from 250 °C to 150 °C at a rate of 100 °C/min. The sample was held at 150 °C for 10 minutes and then heated from 150 °C to 250 °C at 20 °C/min. Figure 5.3 shows the endothermic heat flow as a function of temperature for the second heating ramp. For all three runs of the DSC (indium, baseline, and Ultem 1000) the samples were tested in an inert gas (helium) to prevent side reactions of the samples at high temperature. The helium purge gas was flowing at a rate of 20 ml/min.

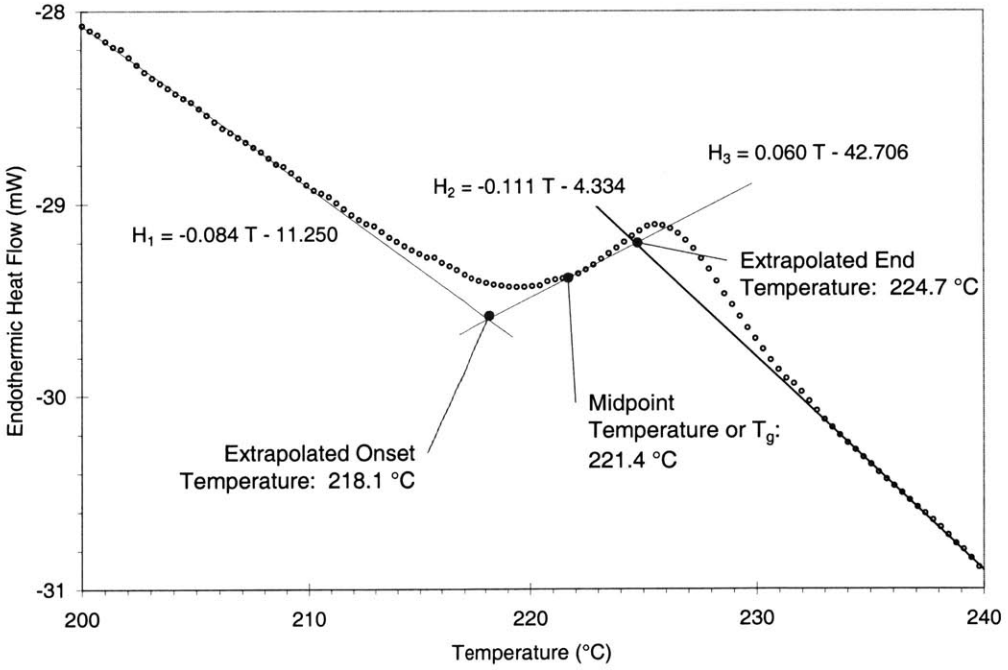

Figure 5.3 Endothermic Heat Flow versus Temperature for Ultem 1000 for the Second Heating Ramp

Ultem 1000 is an amorphous solid and thus no melting or crystallization occurs during heating. Therefore, the change in the heat flow shown in Figure 5.3 is due to a secondary transition also known as a glass transition. "Above T_g, the amorphous phase shows a high mobility leading to high elasticity and deformity. On the other had, below T_g most polymers behave like rigid solids, and are frequently brittle (glass-like)." (Reference 91

page 47) Thus, with the value of the glass transition temperature one can determine the minimum processing temperature to manufacture the tmAFCs. The glass transition temperature also provides an upper bound on the cure temperature of a composite structure that the tmAFC can be cured into. From the second heating ramp the following critical temperatures were determined for the secondary transition.

Table 5.2 Critical Temperatures determined form the Secondary Transition for Ultem 1000

Extrapolated Onset Temperature	218.1 °C (424.6 °F)
Midpoint Temperature or T_g	221.4 °C (430.5 °F)
Extrapolated End Temperature	224.7 °C(436.5 °F)

From this test the glass transition temperature, T_g, was determined to be 221.4 °C (430.5 °F) for Ultem 1000. This test conformed to the ASTM D-3418-99: Standard Test Method for Transition Temperatures of Polymers by Differential Scanning Calorimetry.[119]

5.2.3 Ultem 1000 Decomposition Kinetics

Thermogravimetric tests were performed to determine the Arrhenius activation energy for Ultem 1000 using a thermogravimetric and differential thermal analyzer, TG/DTA-320.[120] Approximately 100 test articles were punched out of Ultem 1000 film manufactured by Westlake Plastics using a punch and die set. The specimens had a nominal thickness of 0.051 mm (2 mil) and a nominal diameter of 4.76 mm (3/16"). The specimens were heated under a vacuum in a vacuum oven at 149 °C (300 °F) for over 12 hours. These drying parameters were chosen based upon the recommendations in Reference [121], which recommends drying Ultem 1000 at 149 °C (300 °F) for 4 hours. After the specimens were dried while waiting to be tested, they were placed in a jar with desiccant. Specimens remained in the desiccated jar for a maximum of three hours.

Throughout all the tests nitrogen was used as a purge gas flowing at a rate of 150 ml / min. For testing specimens at temperatures below 600 °C (1112 °F), an aluminum testing pan was used for testing (Part number SSC000E030 Open Pan Ø5[122] manufactured by Seiko). For testing specimens at temperatures above 600 °C (1112 °F), a platinum testing pan was used (Part number 50-024 PT Ø5-Pan[123] manufactured by Seiko).

Prior to testing, the TG/DTA-320 was calibrated according to the manufactures specifications. A sample of indium and a sample of zinc was tested at 5 °C / min and the melting onset temperature was determined. Using the two measured melting temperature and the known temperature points of 156.60 °C and 419.47 °C (313.88 °F and 787.05 °F), the temperature readings of the TG/DTA-320 was calibrated to the zero order and the first order. The thermogravimetric sensitivity was calibrated by testing no specimen and then a

platinum pan from 30 °C to 564.5 °C (86 °F to 1048 °F) at 40 °C / min. Using 6 points of the measured mass for these two tests, the mass readings of the TG/DTA-320 was calibrated to the zero order and the first order.

Four thermogravimetric tests were performed on Ultem 1000 for heating rates of 3, 5, 7, and 10 K / min. For each test, four pieces of Ultem 1000 film were placed into the aluminum pan. Because the pieces of plastic had a tendency to stick together and because the films were hard to manipulate with tweezers, and thus it is possible that more than four pieces were tested at a time. Two empty pans were placed in the TG/DTA-320, and once the machine had cooled below 50 °C (122 °F) and several minutes had passed, the mass was zeroed. One pan was then removed and the sample was placed into it. The sample was placed into the machine, and after several minutes had passed, the mass of each specimen was measured. The initial mass of each specimen is recorded in Table 5.3.

Table 5.3 Initial Mass and Starting Temperature for Thermogravimetric Tests of Ultem 1000

Heating Rate	3 K / min	5 K / min	7 K / min	10 K / min
Initial Mass	4652 μg	4896 μg	4650 μg	3505 μg
Starting Mass	4685 μg	4916 μg	4666 μg	3536 μg
Starting Temperature	450 °C (842 °F)	425 °C (797 °F)	450 °C (842 °F)	425 °C (797 °F)

The samples were then heated up to the starting temperature. At the starting temperature, the samples were held for 3 minutes to equilibrate in temperature and then the data was recorded at 0.5 Hz. At the end of the isothermal hold, the starting mass is measured. According to the ASTM E-1641-99: Standard Test Method for Decomposition Kinetics by Thermogravimetry,[124] the allowable sensitivity of the electrobalance is ± 50 μg. The difference between the initial and starting mass is within the allowable sensitivity. A heating rate of 10 K / min was performed first, and then a heating rate of 5 K / min. According to the ASTM E-1641-99 standard, specimens should be "equilibrated at ten times the heating rate in kelvins per minute below the known decomposition temperature." Because the decomposition temperature was not known, the samples were equilibrated at 425 °C (797 °F), which is greater than ten times the onset of decomposition. The 3 K / min and 7 K / min testes were performed next starting at 450 °C (842 °F) to reduce the testing time. The samples were heated at a controlled heating rate up to a desired level of 575 °C (1067 °F). 575 °C (1067 °F) was selected as the maximum temperature due to the temperature limit of 600 °C (1112 °F) of the aluminum pans. The machine was not commanded to go to 600 °C (1112 °F) due to a "glitch in the software or the controller that would stop the test plus or minus 20 °C before the end of the run."[125] The machine, although commanded to heat the sample to 575 °C (1067 °F), stopped heating the samples

at approximately 542 °C (1008 °F) due to a software or a controller glitch. The mass of the sample is versus temperature for temperatures above 450 °C (842 °F) is plotted in Figure 5.4.

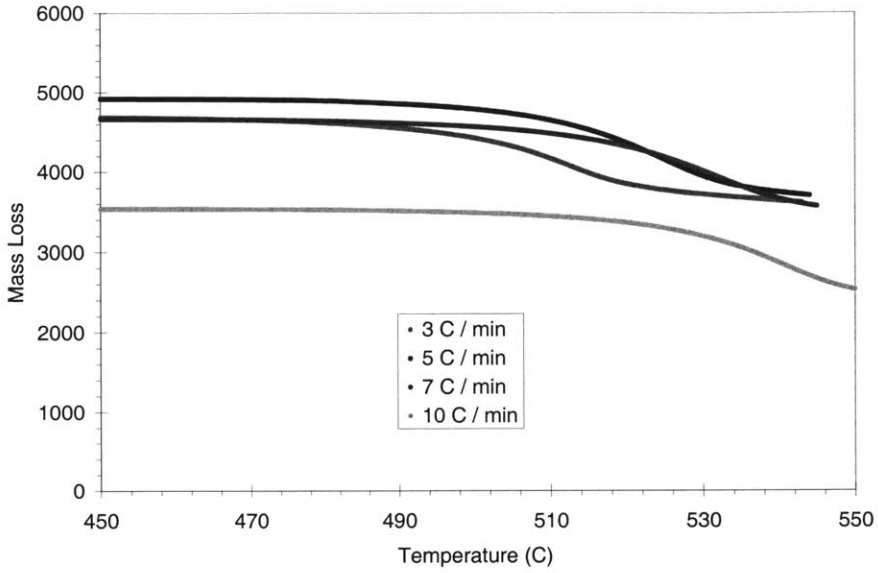

Figure 5.4 Ultem 1000 Sample Mass versus Temperature for Temperatures above 542 °C (1008 °F)

After the tests were performed it was realized in order to determine the constants for the Arrhenius reaction, the samples should have been heated up to a point where the decomposition mass was constant as a function of temperature. Previously samples had been heated up to 575 °C (1067 °F) due to the maximum temperature limit of the aluminum pans. An additional test was performed at 10 K / min using a platinum pan which had a temperature limit of greater than 1500 °C (2732 °F), the maximum temperature of the TG/DTA-320. The other three heating rates we not redone due to the prohibitive cost of the platinum pans, and the fact that if only a single reaction occurs during decomposition, the Char Yield is a constant material property[126]. The Char Yield is the fraction of nonreactive material in the sample[127], and is defined as:

$$Char\,Yield = \frac{m_F}{m_I} \tag{5.3}$$

where m_F and m_I are the initial and the final steady state mass of the specimen. The second 10 K / min test was performed in a manner similar to the previous tests, except that the starting temperature was 430 °C (806 °F) and the hold time was 2 minutes. The initial mass of the sampes was 3410 μg. The sample was heated at 10 K / min up to 1095 °C (2003 °F) at which time the test was stopped because the plastic exhaust tubing was starting to melt. A

plot of the mass versus temperature for the second 10 K / min sample is shown in Figure 5.5.

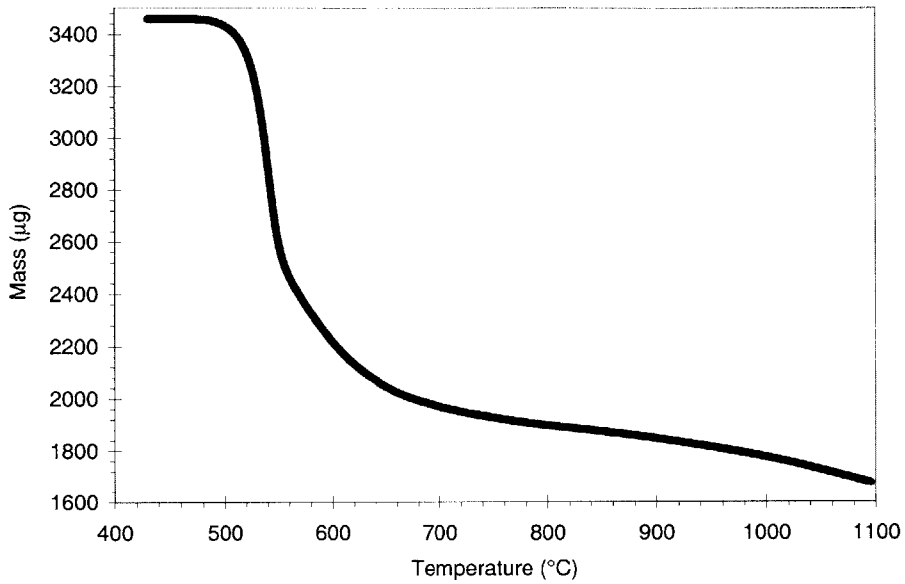

Figure 5.5 Mass versus Temperature for the Second 10 K / min Sample

As can be seen in Figure 5.5, at 1095 °C (2003 °F) the mass of the sample still had not approached a steady state. The mass appears to be approaching a steady state at 900 °C (1652 °F) when the mass loss rate starts to increase. This may indicate a second reaction taking place in the Ultem 1000 above 900 °C (1652 °F). The mass at 900 °C (1652 °F), 1846 µg, was selected to be the final mass, there by giving a Char Yield of 54.1%. Using this Char Yield, the final masses for the other four samples could be determined, and the mass loss could be determined. The mass loss versus temperature for the five samples is plotted in Figure 5.6.

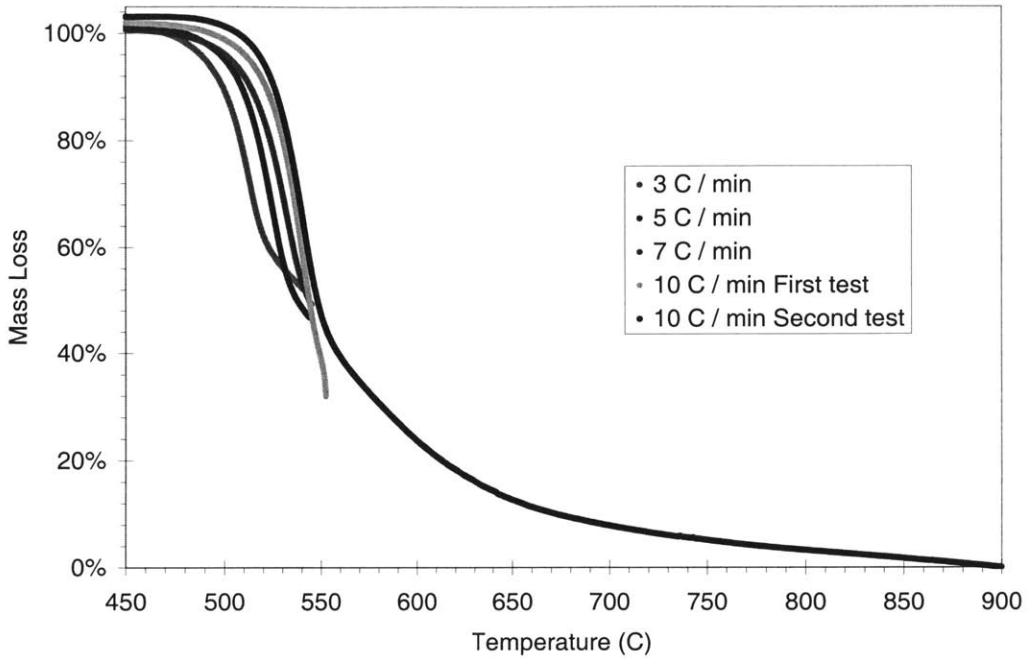

Figure 5.6 Mass Loss versus Temperature

Where the mass loss is defined as:

$$Mass\ Loss = \frac{m(T) - m_F}{m_I - m_F} \tag{5.4}$$

Where *m(T)* is the mass at temperature *T*. As can be seen from Figure 5.6, the assumption that the second 10 K / min specimen was fully decomposed at 900 °C (1652 °F) is approximately true. A second thing that should be noticed is that the two curves for the 10 K / min samples do not line up. This might be because the pans were very difficult to place in the sample holders of the TG/DTA-320 using tweezers. Because the pans are so small, sometimes the pans were placed in the sample holder a little crooked, and therefore the bottom of the pan did not touch the top of the sample holder completely, thus giving an imperfect thermal contact between the two. The arms of the sample holder are very fragile, so not much force can be applied to the sample pans to insure that they are seated correctly. The pans were placed into the sample holder using tweezers, and if it appeared that the pans were not seated correctly they were removed and placed in again. It is possible that the pans, although appeared to be seated correctly, were slightly crooked giving imperfect thermal contact. This may have occurred for the first sample tested at 10 K / min. As can be seen from Figure 5.6, the mass loss for all the samples appear to have the same shape, except for the first sample tested at 10 K / min. Therefore, the data for the first sample tested at 10 K / min was neglected from the final calculations.

The temperature at which 5%, 10%, 15% and 20% decomposition was determined for each of the curves in Figure 5.6. The decomposition temperature was determined by the mass loss at a given percent decomposition. This mass loss is given by:

$$Mass\ Loss = \frac{m_S - Percent\ Decompostion \times (m_S - m_F)}{m_I} \tag{5.5}$$

The decomposition temperature for 3, 5, 7, and 10 K / min for 5%, 10%, 15%, and 20% decomposition is given in Table 5.4.

Table 5.4 Decomposition Temperature for Different Heating Rates and Percent Decompositions

	Heating Rate			
Percent Decomposition	**3 K / min**	**5 K / min**	**7 K / min**	**10 K / min (Second Run)**
5%	479.83 °C	490.77 °C	491.53 °C	510.44 °C
10%	487.87 °C	498.60 °C	501.46 °C	516.46 °C
15%	493.20 °C	503.65 °C	507.47 °C	520.55 °C
20%	497.20 °C	507.37 °C	511.72 °C	523.65 °C

The log of the heating rate, β, is plotted versus the inverse of the decomposition temperature for 5%, 10%, 15%, and 20% decomposition in Figure 5.7.

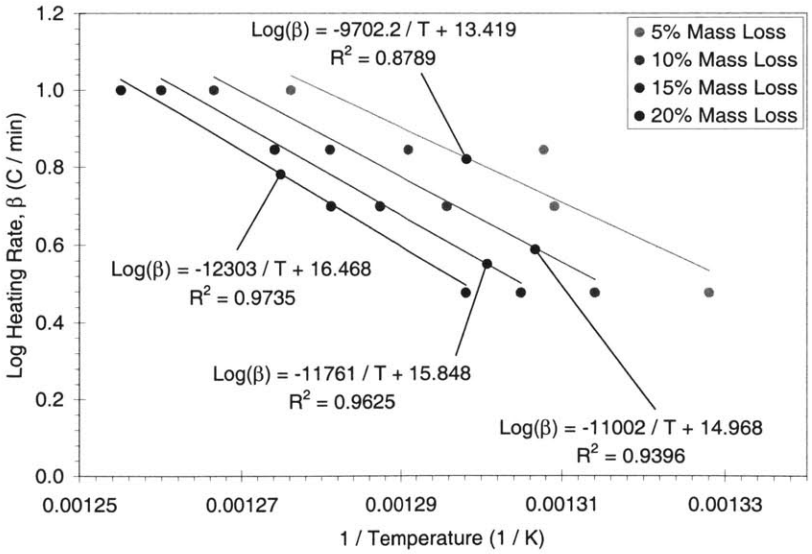

Figure 5.7 Log of Heating Rate versus the Inverse Decomposition Temperature

As can be seen in Figure 5.7, the for each mass loss rate the data falls along a single line, except for one point at each mass loss rate. This data point corresponds to a heating rate of 7 K / min. It is possible that the pan for the 7 K / min heating rate was not seated properly. Thus the data for the 7 K / min was not used in the final calculations.

The Arrhenius activation energy, E, and the pre-exponential factor, A, were calculated for Ultem 1000 using the methodology described in the ASTM E-1641-99 standard, and are given in Table 5.5.

Table 5.5 Arrhenius Activation Energy and the Pre-Exponential Factor for Ultem 1000 at for various Percent Decompositions

Percent Decomposition	**Δ Log β / Δ (1 / T)**	**Arrhenius Activation Energy, *E* (kJ / mol)**	**Uncertainty in *E* (kJ / mol)**	**Pre-exponential factor, *Ln(A)* (1 / min)**	**Uncertainty in *Ln(A)* (1 / min)**
5%	-9976	178	4	23.5 / min	0.6
10%	-10925	197	3	27.2	0.5
15%	-11575	209	3	29.6	0.4
20%	-12078	219	3	31.5	0.4

The data is not independent of the percent decomposition because the decomposition of Ultem 1000 is governed by several reactions instead of a single Arrhenius reaction. As seen in Figure 5.5, it appears that the first reaction starts at about 510 °C (950 °F) for a heating rate of 10 °C / min. A second reaction appears to occur at approximately 556 °C (1033 °F), and a third relation appears to occur at approximately 900 °C (1652 °F). However all of the data points in Table 5.5 were below where the second and third reaction occurred. As mentioned previously it was assumed that at 900 °C (1652 °F) that the reaction was complete, and the mass at this temperature was selected to be the final mass. Using this final mass the char yield was determined for each of the other heating rates and the final mass for the other heating rates was calculated. As seen in Figure 5.5, at 900 °C (1652 °F) the reaction appeared to be slowing down, however it had not fully stopped. This selection of the final mass may have caused the activation energy to not be independent of the percent decomposition.

This test conformed to the ASTM E-1641-99: Standard Test Method for Decomposition Kinetics by Thermogravimetry, except in two aspects. First, three reaction rates were used to calculate the Arrhenius activation energy instead of four as called for in the standard. Second, due to what appears to be several reactions of the Ultem 1000, it was

assumed that at 900 °C (1652 °F) that the reaction was complete, and the mass at this temperature was selected to be the final mass. This selection of the final mass may have caused the activation energy to not be independent of the percent decomposition.

It can be seen from Table 5.4 and Figure 5.6 that the temperature at which decomposition occurs is about 475 °C (887 °F), depending on the heating rate. This temperature gave an upper bound on the maximum processing temperature

5.3 Thermoplastic Electrode Testing

Silver electrodes embedded in Ultem 1000 were heated and the impedance of the electrodes was measured to determine the decomposition temperature of the electrodes. Three 76 μm (3 mil) thick Ultem 1000 electrodes were tested. First, the impedance of the samples (*R* and *X*) was tested in the HP 4194A Impedance / Gain Phase Analyzer.[128] The samples were tested at an applied rms voltage of 1 V at 1 kHz, for with 256 averages, and a integration time of "MEDIUM". Alligator clips were soldered to the top portion of a 2.54 cm x 1.27 cm x 381 μm (1" x 0.5" x 15 mil) piece of brass shim stock. Two of these shims were placed into the jaws of the 16047C Test Fixture[129] attached to the HP 4194A and clamped, leaving the alligator clips exposed to air. When testing the impedance of the electrodes, the electrodes were held in the air using the alligator clips. The alligator clips were connected to the same spot on two electrode pads. The alligator clips were connected to the pads on opposite ends of the electrode rails (Figure 2.2). For each Ultem electrode two tests can be performed, one on each electrode rail. Thus for the three samples, six tests could be performed. Five tests were performed because one of the electrode finger pads was damaged during manufacturing.

The samples were placed on a thin aluminum plate covered with GNPT. The samples were covered with GNPT and placed in the hot press, which was preheated to the desired temperature. Heating occurred at 204, 227, 249, 271, 293, and 316 °C (400, 440, 480, 520, 560, and 600 °F). Two 35.6 cm x 35.6 cm x 1.6 cm (14" x 14" x 5/8") aluminum plates were placed on top and the samples were pressed and heated for 10 minutes. It typically took about 5 minutes for the press to heat up again to the desired he temperature. After heating, the samples and the plates were removed from the press, without cooling them down. The plates and the GNPT were lifted from the sample. Two of the tested electrodes were damaged after handling after heating them at 293 °C (560 °F), leaving only 3 electrodes to test for the 293, and 316 °C (560, and 600 °F) tests. After heating, the samples were left to cool to room temperature on the aluminum plate, and then the impedance of the samples was measured in the same manner as was at room temperature.

The resistance and the reactance at 1 kHz of the Ultem 1000 electrodes, after heating for 10 minutes is shown in Figure 5.8:

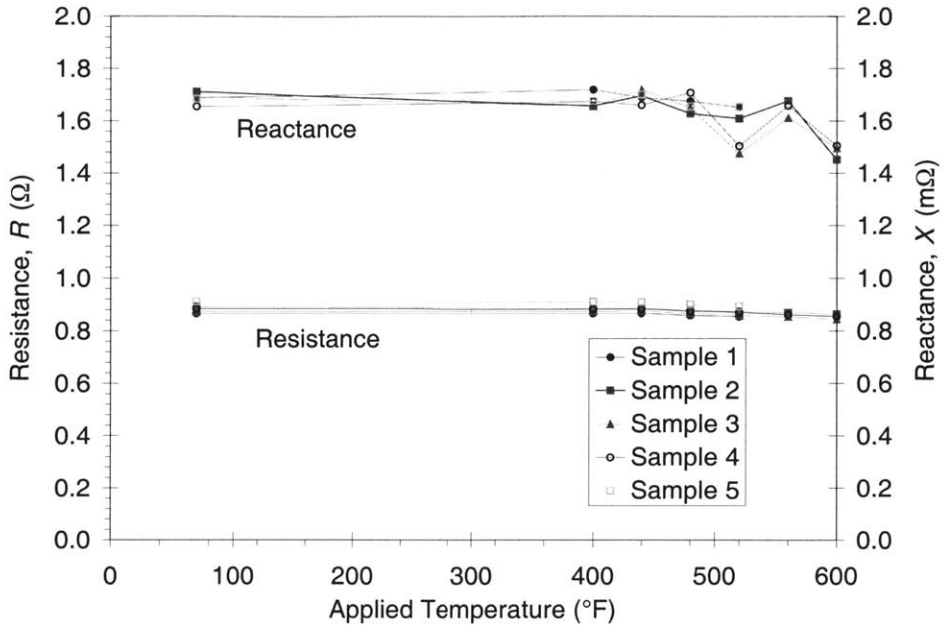

Figure 5.8 Resistance and Reactance Measured at 1 kHz of Ultem 1000 Electrodes versus Applied Temperature

As can be seen in Figure 5.8, the resistance of the samples did not change dramatically when exposed to the temperature. For the three samples that were not damaged, prior to heating, the average resistance was 0.88 Ω. After heating the average resistance of the three samples was 0.85 Ω, a percent change of –3%. The reactance of the samples did change when exposed to the temperature. Because the electrode is comprised of silver, which is a conductor, the reactance is due to stray capacitance and inductance. Small changes in the position of the electrode when testing can contribute to changes in the reactance. When the samples where heated, removed from the press, the aluminum plates lifted, and the samples were allowed to cool down, the samples would stress relieve and wrinkle. Wrinkling should not change the resistance of the electrode, however the reactance of the electrode should change. An example of this is when the impedance of a straight wire is compared to the same wire with a loop in it. For the straight wire, the resistance and the reactance should be small when measured at low frequency. When the same wire has a loop in it, the resistance should not change dramatically, however now the wire is a single loop inductor, and thus the reactance should increase.

Because there were no dramatic changes in the impedance of the Ultem 1000 electrodes after heating, it was felt that heating the electrodes below 316 °C (600 °F) does not significantly degrade the electrode.

5.4 tmAFC Testing

Two tests were performed on tmAFCs, capacitance testing and actuation testing. capacitance testing was performed on tmAFCs to determine the prepoled parallel capacitance under stress free conditions. It has been seen in the past that specimens with a high prepoled parallel capacitance have a high level of actuation. Actuation testing under stress free conditions was performed on tmAFCs and AFCs to determine level of strain output of the actuator.

5.4.1 Capacitance Testing

After each tmAFC was manufactured the parallel capacitance was measured using the CP-D measurement function of the HP 4194A Impedance / Gain Phase Analyzer. As stated earlier (Section 4.5) it has been seen that poled AFC/tmAFC specimens with a high parallel capacitance (*Cp*) typically have a high stress free actuation per unit volt. An AFC/tmAFC with a higher parallel capacitance has a smaller γ and thus will have a higher level of actuation (Figure 3.37). When fully poled the stress free relative dielectric of PZT-5A increases 24% (Reference 76, percent difference for data for k_{i3} = 0 and 0.78). AFC/tmAFCs have a lower stress free parallel pre-poled capacitance than after poling. Poling an AFC/tmAFC typically increases the stress free capacitance by about 15 to 20%. Specimens with no increase in capacitance during the poling process, or a decrease, typically breakdown or have very poor actuation when poled. Because it is known the poling increases the stress free capacitance, and that the stress free actuation is proportional to capacitance, the pre-poled capacitance can be used as an indicator to tell if the AFC/tmAFC is will produce high actuation, and thus time should be spent poling and testing the actuation of the AFC/tmAFC.

Below is a table summarizing the pre-poled parallel capacitance for the various AFC and tmAFC manufacturing methods for AFCs and tmAFCs manufactured by the author using the electrodes presented in Figure 2.2:

Table 5.6 Highest Pre-Poled Parallel Capacitance for various Manufacturing Methods for AFCs and tmAFCs manufactured by the Author

Manufacturing Method	Fiber Diameter	Highest Cp at 400 Hz.
Epoxy based AFC	140 microns	387 pF
Noryl Externally Electoded tmAFC	140 microns	28.2 pF
Noryl Internally Electoded tmAFC	140 microns	362 pF
Ultem Internally Electoded tmAFC	270 microns	1181 pF

Unfortunately, a direct comparison between the two fiber diameters is difficult because the distance between the electrode and the fibers is not known, however the relationship can be estimated. First, it is assumed that the capacitance of the AFC or tmAFC is due entirely to the fibers, and not to the matrix. The difference between the 140 and 270 microns diameter fibers is 1.93, thus the area of the 270 micron fibers is 3.72 times greater than the area of the 140 micron fibers. For all the AFCs the electrode size is the same and thus the active width of the electrodes is the same, therefore only 51.8% as many 270 micron fibers will fit between in the active are as will the 140 micron fibers, assuming that the line fraction is the same. Because the capacitance is proportional to the number of fibers times the area of the area of the fiber the following relationship can be written.

$$C \propto \text{Number of fibers} \times \text{Area of fibers}$$

$$\frac{C_{270\,\mu m\ fibers}}{C_{140\,\mu m\ fibers}} = \frac{\text{Number of 270 μm fibers}}{\text{Number of 140 μm fibers}} \times \frac{\text{Area of 270 μm fibers}}{\text{Area of 140 μm fibers}} = \frac{1}{1.93} \times \frac{3.72}{1} \quad (5.6)$$

$$C_{270\,\mu m\ fibers} = 1.93 \times C_{140\,\mu m\ fibers}$$

Thus, the capacitance of the 270 micron fibers AFCs and tmAFCs should be about 1.93 times that of the 140 micron fibers AFCs and tmAFCs. Therefore, if the Ultem tmAFCs were manufactured with 140 micron diameter fibers it would have a capacitance of about 612 pF. Therefore, the internally electroded tmAFCs with the Ultem matrix produces the highest parallel capacitance and thus should have the highest actuation. It should be noted that the AFCs and tmAFCs in Table 5.6 are listed in chronological order of manufacturing. As time progressed, the molds and the manufacturing techniques employed became better. If some of the lessons that were learned in the later manufacturing studies were applied to the earlier manufacturing studies the capacitance of the earlier manufacturing could probably be increased. More capacitance data for AFCs and Ultem tmAFCs is presented in Figure 4.25 and Appendix IV.

As time progressed, the testing rigs and capacitance testing techniques became better, thus increasing the accuracy and repeatability of the measurements. For the epoxy based AFCs and the Noryl based tmAFCs, wires were soldered, clipped using alligator clips, adhered using silver epoxy to the electrode pads. Because the leads were flexible, open compensation could not be performed directly across the AFC/tmAFC because the wires were either permanently attached, or would move when the sample was being unattached, thus altering the open capacitance of the leads. To reduce stray capacitance, the wires were often times cut to a short length, and thus the sample needed to be rested on the table to perform the measurements. The Ultem 1000 tmAFCs had metal tabs adhered to the electrode using silver or nickel epoxy, as described in Section 4.5.2.1. Alligator clips were soldered to the top portion of a 2.54 cm x 1.27 cm x 381 μm (1" x 0.5" x 15 mil) piece of brass shim stock. Two of these shims were placed into the jaws of the 16047C Test Fixture attached to the HP 4194A and clamped, leaving the alligator clips exposed to air. When

testing the capacitance of the Ultem tmAFCs, the tmAFCs were stood upright and the metal tabs of were gripped in the alligator clips. After testing the sample, an open compensation could be performed without moving the electrodes simply by removing the sampled. A short compensation could be performed by placing a brass bar across the alligator clips. This test rig proved adequate for testing of the pre-poled capacitance and the post poled capacitance of the Ultem tmAFCs. For the epoxy AFCs and the Noryl tmAFCs and some of the Ultem 1000 tmAFCs, the capacitance was measured using the Cp-D function at 400 Hz for with less than 16 averages, an integration time of "SHORT" or "MEDIUM", and an rms voltage of 0.5 Volts. For most of the Ultem tmAFCs, the admittance (*G-B*) was measured from 100 to 1000 Hz in 100 Hz increments. 256 measurements were taken at each data point and averaged, using an integration time of "LONG". An applied voltage of 1 Volt rms was used to increase the return current to the HP-4192a, making the current easier to measure. Open/short compensation was performed on most of the Ultem 1000 tmAFCs. It should be noted that despite the increases in quality of the testing rigs and improved capacitance testing techniques, the capacitance measurements typically changed a few percent when the wires or the poorer techniques were employed. This is because capacitance of AFC/tmAFC is typically between 500 pf and 1.2 nF, which is greater than the open circuit capacitance of the HP-4192a with the 16047C Test Fixture, which is on the order of 1-10 pF. The improved measurement increased the accuracy of the resistance measurements of the AFCs and tmAFCs, however because the resistance is typically very large and the meaning that the resistance plays in the actuation of the AFCs/tmAFCs is poorly understood, the resistance measurement is typically ignored. This more accurate resistance measurement was used for a new method of reducing the capacitance data is described in Appendix IV.

This test, although using the ASTM D-150-98 Standard[130] as a guideline, did not strictly follow the standard due to the fact that the capacitance due to the unguarded electrodes was not taken into account due to the odd geometry of the specimens.

5.4.2 Stress Free Actuation of tmAFCs

As mentioned in Section 3.2, one of the desirable properties to know for a distributed actuator is the *ZZ* strain per unit volt under stress free conditions. Measurement of the stress free actuation for AFCs/tmAFCs was performed using a laser interferometer.

The stress free actuation of AFCs/tmAFCs was measured using a ZMI 1000 interferometer system.[131] Specimens were placed on a flat table with one end of the specimens clamped to the table. Prior to actuation, a retro-reflector is clamped to the end opposite of the clamp. The electrical leads of the specimen are connected to a 0.1 mHz – 100 MHz PM 5138 Function Generator[132] and a Trek Model 664 10kV 20 mA amplifier.[133] Data is collected using a custom VI written for LabVIEW.[134] A detailed description of the

actuation tests can be found in Reference 58 (pages 73-86). During the test, velocity, current, and voltage data is recorded. The velocity data is converted by the system into displacement data, which is recorded.

Actuation is typically measured for comparison purposes with an applied sinusoidal voltage, V_{pp}, with no dc offset, V_{DC}, at 1 Hz. The methods used to reduce the actuation data are presented in Reference 58.

Many tmAFCs, after being manufactured, have a curvature due to residual thermal stresses. Actuation of tmAFCs cannot be measured with the above technique, because of the curvature the mirror rotates out of plane causing the laser beam not to return to the photo detector. The tmAFCs are laminated with 1 ply of E120-155 e-glass[135] on either side to reduce their curvature. Figure 5.9 shows a comparison of the peak-to-peak actuation strain, S_{pp}, for internally electroded Ultem tmAFCs laminated with 1 ply of e-glass on either side, and the peak-to-peak actuation strain for three AFCs, manufactured by Continuum Photonics laminated with 1 ply of e-glass on either side at MIT, versus peak-to-peak voltage, V_{pp}.

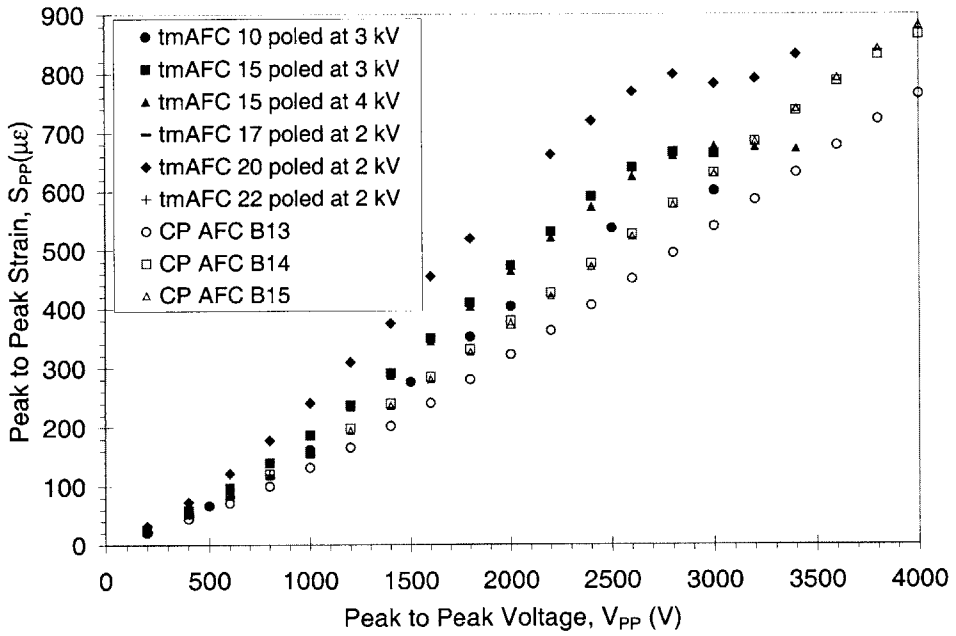

Figure 5.9 Comparison of Peak-to-Peak Actuation of Laminated tmAFCs with Laminated PiezoFlex AFCs Manufactured by Continuum Photonics actuated at 1 Hz.

Data was not recoded for tmAFC 20 poled at 2000 V for a peak-to-peak voltage of 2000 V due to an operator error. The laminated CP AFC data was measured in Reference [136].

As can be seen in Figure 5.9, the S_{pp} is essentially linear with respect to V_{pp} for low levels of V_{pp}. As V_{pp} is increased, the peak-to-peak actuation strain becomes nonlinear with

V_{pp}. As V_{pp} is increased further, the AFC/tmAFC starts to depole and the actuation strain is reduced. The tmAFCs were manufactured and poled using the following parameters.

Table 5.7 Manufacturing and Poling Parameters used for tmAFCs in Figure 5.9

Actuator	Electrode film thickness	Rubber Area	Maximum Force	Maximum Temperature	Maximum DC Poling Voltage
tmAFC 10	102 μm (4 mil)	64.5 cm^2 (10.0 in^2)	1.11 kN (250 lbs)	260 °F (500 °F)	3 kV
tmAFC 15	102 μm (4 mil)	64.5 cm^2 (10.0 in^2)	0.445 kN (100 lbs)	260 °F (500 °F)	4 kV
tmAFC 17	102 μm (4 mil)	76.8 cm^2 (11.9 in^2)	0.445 kN (100 lbs)	260 °F (500 °F)	2 kV
tmAFC 20	76 μm (3 mil)	76.8 cm^2 (11.9 in^2)	0.556 kN (125 lbs)	260 °F (500 °F)	2 kV
tmAFC 22	76 μm (3 mil)	76.8 cm^2 (11.9 in^2)	0.556 kN (125 lbs)	260 °F (500 °F)	2 kV

From Figure 5.9, it can be seen that the actuation strain several of the tmAFCs is greater than that of the CP AFCs for a given peak-to-peak voltage. Direct comparison between AFCs and tmAFCs cannot be done because the matrix material and geometry of the two actuator types are different. A comparison between the AFCs and the tmAFCs in Figure 5.9 is shown in Table 5.8:

Table 5.8 Comparison of tmAFCs with AFCs Manufactured by Continuum Photonics

AFC/ tmAFC	N_{Fibres}	W_A	LF	$N_{Fingers}$	$N_{Fingers\ Active}$	W	h	E_M
tmAFC 10	37	10.5 mm (415 mil)[a]	94.8 %	56[a]	56	1.64 cm (646 mil)	440 μm (17.3 mil)	3.2 GPa (464 ksi)[b]
tmAFC 15	37	10.5 mm (415 mil)[a]	94.8 %	56[a]	56	1.63 cm (642 mil)	416 μm (16.4 mil)	3.2 GPa (464 ksi)[b]
tmAFC 17	36	10.5 mm (415 mil)[a]	92.2 %	56[a]	54	1.68 cm (661 mil)	441 μm (17.4 mil)	3.2 GPa (464 ksi)[b]
tmAFC 20	37	10.5 mm (415 mil)[a]	94.8 %	56[a]	56	2.30 cm (906 mil)	370 μm (14.6 mil)	3.2 GPa (464 ksi)[b]
tmAFC 22	37	10.5 mm (415 mil)[a]	94.8 %	56[a]	56	1.70 cm (669 mil)	369 μm (14.5 mil)	3.2 GPa (464 ksi)[b]
AFC B13	30[c]	8.6 mm (340 mil)[d]	93.8 %	88[d]	88	1.32 cm (520 mil)[c]	342.4 μm (13.48 mil)[e]	2.9 GPa (421 ksi)[f]
AFC B14	30[c]	8.6 mm (340 mil)[d]	93.8 %	88[d]	88	1.32 cm (520 mil)[c]	342.1 μm (13.47 mil)[e]	2.9 GPa (421 ksi)[f]
AFC B15	30[c]	8.6 mm (340 mil)[d]	93.8 %	88[d]	88	1.32 cm (520 mil)[c]	342.4 μm (13.48 mil)[e]	2.9 GPa (421 ksi)[f]

a: Figure 2.2
b: Table 4.4
c: Reference 58 page 50
d: Reference 61
e: Reference 136
f: Table 2.4

In Table 5.8, N_{Fibers} is the number of fibers, W_A is the width of the active area, LF is the line fraction of fibers, $N_{Fingers}$ is the number of fingers, W is the laminated sample width, h is the non-laminated sample thickness, and E_M is the Young's modulus of the matrix. Dielectric breakdown occurred in tmAFC 17 during poling at 2300 V. The breakdown was drilled out and filled with epoxy and tmAFC 17 was repoled at 2000 V for 20 minutes at 100 °C (212 °F). All the tmAFCs were poled at 20 minutes at 100 °C (212 °F) in either heated silicon oil or in a convection oven. It should be noted that the laminated sample width for tmAFC 20 is large compared to the active width due to the fact that laminated tmAFC samples are difficult to cut, so the tmAFCs was cut a little wider to avoid crack propagation into active area. From Table 5.8, we can see that although the two actuator systems have different numbers of fibers, the line fraction of fibers is the about same. In addition, the thickness of the two-actuator systems is about the same for most of the actuators. The electrodes have the same electrode finger width and center-to-center spacing, 191 μm (7.5

mil.) and 1.14 mm (45 mil.) respectively (Figure 2.2, and Table 2.2). For the AFCs and the tmAFCs, the fiber diameter, 270 μm (Table 2.2), and the Young's modulus, 53.2 GPa (Table 2.5) is the same because the fibers were obtained from the same manufacturer.

We can compare the actuation of the two actuators by assuming that the actuators are long thin *3-3* actuators electroded at either end. From Equation **C.41**, the *ZZ* strain of a laminated AFC/tmAFC is given by:

$$S_{ZZ}^{\text{Lam}}(t)=\frac{A_F\left(Y_{33}^E\right)_F}{A_F\left(Y_{33}^E\right)_F+A_M E_M+A_K E_K+A_E E_E}\left(\Gamma_{ZZ}\right)_F V(t) \tag{5.7}$$

Where the *F*, *M*, *K*, and *E* subscripts refer to the fiber, matrix, Kapton, and E-glass respectively, and the *LAM* superscript refers to fact that the *ZZ* strain is for a laminated AFC. If both the strain and the voltage are sinusoidal (which is true for low voltages) and in-phase, then the strain and the voltage can be written as:

$$\begin{aligned} S_{ZZ}^{\text{Lam}}(t)&=\frac{S_{PP}^{Lam}}{2}E^{j\omega t} \\ V(t)&=\frac{V_{PP}}{2}E^{j\omega t} \end{aligned} \tag{5.8}$$

Inserting Equation 5.8 into Equation 5.7 yields:

$$S_{PP}^{Lam}=\frac{A_F\left(Y_{33}^E\right)_F}{A_F\left(Y_{33}^E\right)_F+A_M E_M+A_K E_K+A_E E_E}\left(\Gamma_{ZZ}\right)_F V_{PP} \tag{5.9}$$

The *ZZ* strain per unit volt for a laminated AFC/tmAFC is given by:

$$\Gamma_{ZZ}^{Lam}=\frac{S_{PP}^{Lam}(t)}{V(t)}=\frac{S_{PP}^{\text{Lam}}}{V_{PP}}=\frac{A_F\left(Y_{33}^E\right)_F}{A_F\left(Y_{33}^E\right)_F+A_M E_M+A_K E_K+A_E E_E}\left(\Gamma_{ZZ}\right)_F \tag{5.10}$$

Assuming that the actuation strain is uniform along the length of the active area of the AFC/tmAFC, Γ_{ZZ} for the fibers is given by:

$$\left(\Gamma_{ZZ}\right)_F=\frac{\left(d_{33}\right)_F}{L} \tag{5.11}$$

Assume that the fibers Γ_{ZZ} is unknown because the electrode is at an unknown distance fiber. Solving for Γ_{ZZ} of the fibers yields:

$$\left(\Gamma_{ZZ}\right)_F=\varpi\,\Gamma_{ZZ}^{Lam} \tag{5.12}$$

Where ϖ is a unit less ratio given by:

$$\varpi=\frac{\left[A_F\left(Y_{33}^E\right)_F+A_M E_M+A_K E_K+A_E E_E\right]}{\left[A_F\left(Y_{33}^E\right)_F\right]} \tag{5.13}$$

ϖ can be thought of as the reduction in the actuation of the fibers due to the passive materials in an AFC/tmAFC.

If one wanted to compare the actuation between several AFC/tmAFCs with different widths and materials, then one should compute the effective Γ_{ZZ} of the fibers for each of the actuators. Γ_{ZZ} of the fibers is an effective Γ_{ZZ} because it takes into account the distance that the electrode is from the fibers and the degree of poling of the fibers. In general, the assumption that the strain and the voltage are in phase is not true. However, this assumption was made for the AFC data taken in Reference 58, and the same assumption will be made here in order to compare the tmAFC and the AFC data.

The equations for the cross sectional areas for materials in the AFCs and tmAFCs to be used in Equation 5.13 are listed in Table 5.9:

Table 5.9 Cross Sectional Areas of Materials in the AFCs and tmAFCs.

Material	**AFC**	**tmAFC**
Fiber	$A_F^{AFC} = N_{Fibers}^{AFC}\,\pi\left(R^{AFC}\right)^2$	$A_F^{tmAFC} = N_{Fibers}^{tmAFC}\,\pi\left(R^{tmAFC}\right)^2$
Matrix	$A_M^{AFC} = h_{Unlam}^{AFC}\,W^{AFC} - A_F^{AFC} - A_K^{AFC}$	$A_M^{tmAFC} = h_{Unlam}^{tmAFC}\,W^{tmAFC} - A_F^{tmAFC}$
Kapton	$A_K^{AFC} = 2h_K^{AFC}\,W^{AFC}$	$A_K^{tmAFC} = 0$
E-Glass	$A_E^{AFC} = 2W^{AFC}\,h_E$	$A_E^{tmAFC} = 2W^{tmAFC}\,h_E$

Where the *Unlam* subscript refers to the unlaminated AFC/tmAFC, and h_K is the thickness of the Kapton. Because the e-glass has a net resin cure, the thickness times the stiffness for the e-glass is a constant (Reference 58 pages 155-159).

$$h_E\,E_E = 114\,\mu\text{m} \times 21.9\ \text{GPa} = 2.50\ \text{MN/m} \tag{5.14}$$

In Equation 5.14, the nominal thickness for e-glass is used, 114 μm (4.5 mil), instead of the actual thickness, 101 μm (3.995 mil), because the nominal thickness was used to calculate the Young's modulus of the e-glass in Reference 58 pages 155-159.[137]

In Figure 5.9, the peak-to-peak strain appears to be nonlinear with the peak-to-peak voltage. Assume that the peak-to-peak strain is a function only of peak-to-peak voltage. Taking a Maclaurin series of the laminated peak-to-peak strain about $V_{PP} = 0$ yields:

$$S_{PP}^{Lam} = S_{PP}^{Lam}\left(V_{PP}=0\right) + \left[\frac{d\,S_{PP}^{Lam}}{d\,V_{PP}}\bigg|_{V_{PP}=0}\right] V_{PP} + \left[\frac{1}{2}\frac{d^2\,S_{PP}^{Lam}}{d\,V_{PP}^2}\bigg|_{V_{PP}=0}\right] V_{PP}^2 + \cdots \tag{5.15}$$

At zero voltage, the actuation strain of the actuator is zero. The linear term in Equation 5.15 can be thought of as the piezoelectric term, and the quadratic term in Equation 5.15 can be thought of as the electrostricitve term. Thus, Equation 5.15 can be rewritten as:

$$S_{PP}^{Lam} = \Gamma_{ZZ}^{Lam} V_{PP} + m_{ZZ}^{Lam} V_{PP}^2 + \cdots \tag{5.16}$$

Where m_{ZZ}^{Lam} is the effective electrostrictive term for the laminated actuator. m_{ZZ}^{Lam} is effective in the sense that the resulting electrostrictive term may be due to high field non-linearities in the piezoelectric fibers, a decrease in the stiffness of the matrix or e-glass of the actuators as the strain is increased (Figure 5.2), or an increase in the phase difference between strain and voltage as voltage is increased. Dividing through by V_{PP} and dropping all higher order terms in Equation 5.16 yields:

$$\frac{S_{PP}^{Lam}}{V_{PP}} = \Gamma_{ZZ}^{Lam} + m_{ZZ}^{Lam} V_{PP} \tag{5.17}$$

In Equation 5.17, at low voltages, V_{PP}^2 is less than V_{PP}, thus the piezoelectric term Γ_{ZZ}^{Lam} dominates the strain. Γ_{ZZ}^{Lam} can be thought of as the low field piezoelectric term for a laminated actuator. From Equation 5.17 it can be seen that plotting the laminated peak-to-peak strain divided by the peak-to-peak voltage should yield a straight line. Replotting the data in Figure 5.9 in this manner yields:

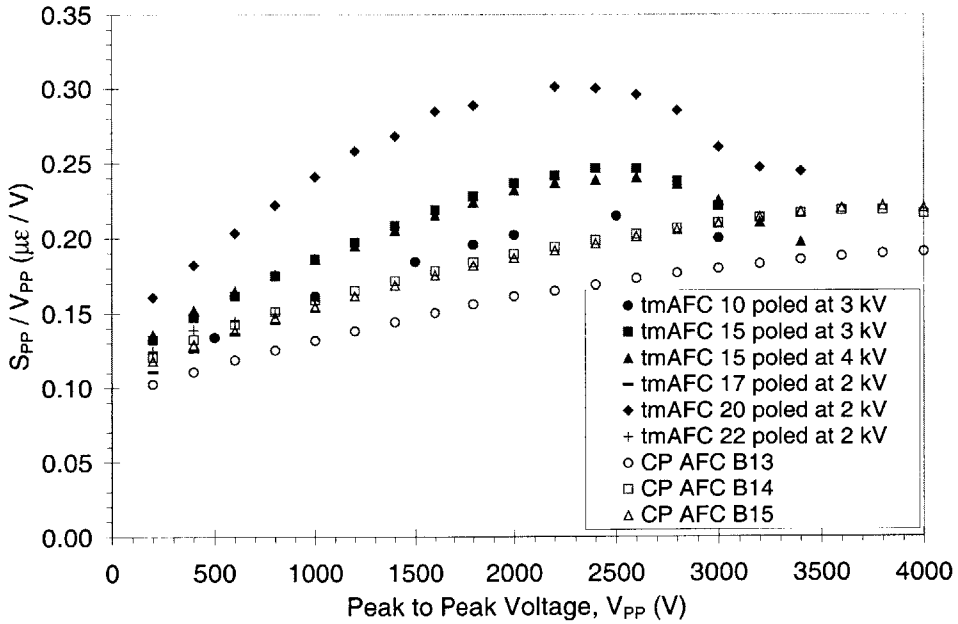

Figure 5.10 Laminated Peak-to-Peak Strain Divided by the Peak-to-Peak Voltage versus Peak-to-Peak Voltage for the Actuators in Figure 5.9

As can be seen in Figure 5.10, the laminated peak-to-peak strain divided by the peak-to-peak voltage is linear for all the actuators up to a peak-to-peak voltage of 1000 V. Above this voltage, the laminated peak-to-peak strain divided by the peak-to-peak voltage becomes non-linear due to repoling of the actuators. Using Equation 5.17, Γ_{ZZ}^{Lam} and m_{ZZ}^{Lam} can be determined for the data with a peak-to-peak voltage of between 200 V and 1000 V

Table 5.10 Actuation and Pre-poled Capacitance Data for AFCs and tmAFCs in Figure 5.9

AFC/ tmAFC	DC Poling Voltage	Virgin *Cp* Measured at 400 Hz.	Virgin *D* Measured at 400 Hz.	Γ_{ZZ}^{Lam}	m_{ZZ}^{Lam}	R^2 of Linear Fit
tmAFC 10	1 kV	966.395 pF	0.0126389	57.9 nε/V	29.7 pε/V²	0.988
tmAFC 10	3 kV	966.395 pF	0.0126389	106.0 nε/V	55.6 pε/V²	1.000
tmAFC 15	3 kV	1125.31 pF	0.0128427	119.6 nε/V	68.0 pε/V²	0.998
tmAFC 15	4 kV	1125.31 pF	0.0128427	125.0 nε/V	62.6 pε/V²	0.992
tmAFC 17	2 kV	1105.88 pF	0.0125025	103.1 nε/V	50.1 pε/V²	0.980
tmAFC 20	2 kV	1156.47 pF	0.012780	141.6 nε/V	100.4 pε/V²	0.999
tmAFC 22	2 kV	1061.82 pF	0.0144418	119.6 nε/V	39.4 pε/V²	0.960
tmAFC 22	2.5 kV	1061.82 pF	0.0144418	59.3 nε/V	81.5 pε/V²	0.996
AFC B13	?	?	?	95.9 nε/V	36.6 pε/V²	0.997
AFC B14	?	?	?	112.6 nε/V	47.6 pε/V²	0.991
AFC B15	?	?	?	110.0 nε/V	45.4 pε/V²	0.995

In Table 5.10 the parallel capacitance and the dissipation are measured prior to the samples were poled (i.e. the fibers were in the virgin state), and prior to any breakdowns in tmAFC 17. The virgin parallel capacitance and the virgin dissipation are not known for the CP AFCs. In general, the higher the virgin parallel capacitance the higher the actuation, however for the tmAFCs in Table 5.10, the number of fibers, and material thickness are different making correlation between the two difficult. Several of the tmAFCs were poled twice to see the effect of poling on the actuation. tmAFC 10 was poled at 1 kV and again at 3 kV yielding an increase in Γ_{ZZ}^{Lam} of 45%. In tmAFC 15 increasing the poling voltage from 3 kV to 4 kV with an increase in Γ_{ZZ}^{Lam} of only 4.3%. This may because the polarization for tmAFC 15 at 3 kV is nearly saturated, and thus increasing the poling voltage has almost no effect on actuation. tmAFC 22 was poled at 2 kV and 2.5 kV with a decrease in actuation of about 50%. This drop in actuation may be due to a dielectric breakdown in the sample damaging some electrode fingers or rails.

Using the data in Table 5.7 - Table 5.10, and Equation 5.12 and 5.13, the low field actuation of the fibers, $(\Gamma_{ZZ})_F$ .can be determined

Table 5.11 Comparison of Γ_{ZZ} for the Fibers of Laminated AFCs and tmAFCs

Specimen	Γ_{ZZ}^{Lam}	ϖ	$(\Gamma_{ZZ})_F$
tmAFC 10 Poled at 3 kV	106.0 nε/V	1.87	198.2 nε/V
tmAFC 15 Poled at 3 kV	119.6 nε/V	1.85	221.7 nε/V
tmAFC 15 Poled at 4 kV	125.0 nε/V	1.85	231.9 nε/V
tmAFC 17 Poled at 2 kV	103.1 nε/V	1.92	197.9 nε/V
tmAFC 20 Poled at 2 kV	141.6 nε/V	2.20	311.7 nε/V
tmAFC 22 Poled at 2 kV	119.6 nε/V	1.87	223.8 nε/V
AFC B13	95.9 nε/V	1.81	173.4 nε/V
AFC B14	112.6 nε/V	1.81	203.6 nε/V
AFC B15	110.0 nε/V	1.81	199.0 nε/V

In Table 5.11 it can be seen that all of the tmAFCs have higher reductions in the actuation of the fibers due to the passive materials, ϖ, compared to the AFCs. The tmAFCs have as high as or higher values of $(\Gamma_{ZZ})_F$ compared to the AFCs. This can be attributed to the fact that the electrodes of the tmAFCs touch the fibers over a greater area than do the AFC, and thus the tmAFCs are better actuators.

It should be noted that using data from Reference 58, the non-laminated CP AFCs B13, B14, and B15 have a low field actuation, Γ_{ZZ} of 167.8, 180.5, and 177.8 nε/V respectively, which is higher than the average AFC Γ_{ZZ} (Reference 42) of 131 nε/V. Thus, some of the laminated tmAFCs have nearly the same actuation as a non-laminated average value AFCs.

Two problems exist with comparing $(\Gamma_{ZZ})_F$ for between the AFCs and tmAFCs. First, it assumed that the AFC/tmAFC is a *3-3* actuator and thus the equations in Appendix III are applicable. In Appendix III, it is assumed that the electric field is uniform in the *Z* direction. This assumption is true for the AFC/tmAFC except under the electrodes, where the electric field is perpendicular to the electrodes. The second problem that exists when comparing $(\Gamma_{ZZ})_F$ is that in order to calculate $(\Gamma_{ZZ})_F$, $(Y_{33}^E)_F$ must be known (Equation 5.13). When one compares $(\Gamma_{ZZ})_F$ between actuators one is comparing the degree of poling between the actuators. Both $(\Gamma_{ZZ})_F$ and $(Y_{33}^E)_F$ are dependant on the degree of

poling of the fiber (Reference 76), and thus a fiber Young's modulus under shorted conditions must be assumed. A better method for comparing the actuators would be to test the shorted stiffness of the actuators to determine $\left(Y_{33}^{E}\right)_{F}$ and then use this value when calculating $\left(\Gamma_{ZZ}\right)_{F}$. This data was not known for the CP AFCs and thus $\left(Y_{33}^{E}\right)_{F}$ was not calculated.

Γ_{ZZ} was calculated for the entire AFC and tmAFC, not just the active area. In general, Γ_{ZZ} has both a real and imaginary component thus giving actuation curves with hysteresis as seen in Figure 5.11.

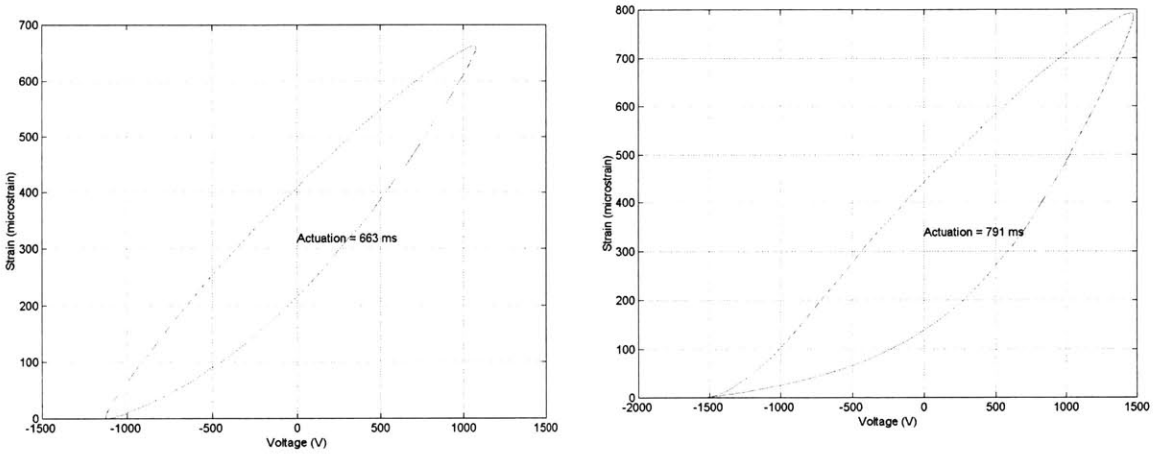

Figure 5.11 Actuation of tmAFC 20 Laminated With Two Plies of E-Glass at 2200 and 3000 Volts Peak-to-peak

Figure 5.11 shows the actuation of tmAFC 20 which was laminated with one ply of e-glass on each side, driven at 2200 and 3000 Volts peak-to-peak. At 2200 Volts peak-to-peak in the above plot an oval hysteretic actuation loop can be seen. The fact that a hysteretic loop exists for the AFC can be expanded because the piezoelectric constitutive relation contain both real and imaginary components.[83,82,138,139,140,141] As the voltage is increased to 3000 Volts peak-to-peak, one can see the onset of depoling due to the cusp at –1500 Volts. It should be noted that tmAFC 20 was poled with 2000 Volts.

The laser interferometer system for measuring displacement had several problems:

1. The displacement measured using the Zygo model 7702[142] laser used with the ZMI 1000[143] interferometer system had a serious drift issue, because velocity is integrated to determine displacement, causing errors. This limited the length of the time that the displacement could be measured because the error in displacement is cumulative.

2. The laser introduced a phase shift to the displacement data that appeared to be a function of the number of data points taken and the period. This problem was discovered when step voltage was applied to an AFC. At the moment of the switching of the voltage, both the measured voltage and the current would occur at the same time, however the step in the displacement would occur at a different time. Thus, the phase of the displacement could not be trusted, and therefore only the peak-to-peak strain could be used.

3. The laser had an internal temperature control system that would attempt to keep laser at a fixed temperature to reduce false displacement readings due to small temperature fluctuations. Internal heaters cycled on and off inside the laser changing the length of the laser slightly. This produced a periodic displacement signal of about 100 nm, which is the lower bound of the laser. Unfortunately, the displacement versus voltage plots looked very garbled for some of poorer performing AFCs/tmAFCs at lower voltages.

4. Because the current signal was so small, during actuation, the current could not be measured using the current output of the Trek Model 664 10kV 20 mA amplifier.

5. It was discovered that the Trek amplifier produced a small 60 Hz. and a 300 Hz. signal on top of the voltage signal commanded by the function generator. This caused higher harmonic actuation of the AFCs/tmAFCs, increasing the noise in the displacement signal.

6. The table used to hold the specimen and the mirror did not prevent the specimen from bending out of plane during actuation, causing problems for some specimens with slight curvatures due to manufacturing.

7. The specimens were aligned by eye with respect to the laser, and sometimes the specimens were slightly misaligned. The actuation of the specimens could be measured, the specimens removed and remounted on the table, and the actuation would be measured again with slightly different results.

As mentioned in Chapter 4, not many quality tmAFCs were manufactured due to equipment failures and monetary constraints. Those tmAFCs that survived poling without dielectric breakdown, proved to higher actuation than the average AFCs manufactured by

Continuum Photonics, despite the fact that tmAFCs have a higher matrix stiffness, and a smaller active width to sample width. This actuation data proves that tmAFCs superior to thermoset AFCs can be manufactured.

6. Summary, Conclusions and Contributions

6.1 Summary

Active Fiber Composites (AFCs) have been developed to address some of the shortcomings of monolithic piezoelectric materials. A major drawback of the AFC design is that the level of actuation of the AFCs is about 60% lower than that of the *3-3* actuation of a monolithic piezoceramic material. This is due primarily to a small layer of low dielectric matrix material trapped between the electrodes and the high dielectric fibers due to manufacturing. This dielectric mismatch causes a large voltage drop in the matrix, thereby reducing actuation. A method that has been developed to reduce this matrix gap, and thus increase actuation, is to transfer the electrode pattern onto plastic sheets, and heat and press the sheets into the fibers to make Thermoplastic Matrix Active Fiber Composites (tmAFCs). tmAFCs have simpler processing when compared to AFCs and are potentially reshapeable. The focus of this research has been to analyze, manufacture, and test tmAFCs to be used in structural control applications.

6.2 Conclusions

6.2.1 AFC Analysis

The relation between dielectric, Young's modulus, and the Poisson's ratio of the matrix material on AFC/tmAFC performance is not clearly understood. Several analyses, including rule of mixtures analyses and finite element analyses, were performed on a PiezoFlex AFC to determine the effect of the matrix material properties and the distance the electrode is from the center of the fiber on AFC material properties. These AFC properties include: the *XX* and *ZZ* strain per unit volt under stress free conditions, the *XX*, *YY*, and *ZZ* outputted stress per unit volt under strain free conditions, the shorted *ZZ* Young's

modulus, the *ZX* Poisson's ratio, and the stress free and strain free capacitance. Using this data, an electromechanical coupling coefficient, equivalent to k_{i3}^2, was calculated for a PiezoFlex AFC. For the range of matrix material properties analyzed, only the relative permittivity has an effect on the actuation performance of a PiezoFlex AFC when the electrode does not touch the fiber, $\xi > 100\ \%$. When the electrode touches the fiber, $\xi < 100\ \%$, the actuation performance of a PiezoFlex AFC is nearly independent of the matrix dielectric properties. Due to the similarity between the matrix material properties between a PiezoFlex AFC and a tmAFC, the conclusions reached for an AFC hold true for a tmAFC.

6.2.2 tmAFC Manufacturing

Solvent casted tmAFCs, externally electoded tmAFCs, and internally electoded tmAFCs have been manufactured using Kynar 2801-00 PVDF, Noryl EN265-7, and Ultem 1000 matrices. Due to the intimate contact between the electrode and the fiber, Ultem 1000 internally electroded tmAFCs have the highest levels of actuation. Internally electroded tmAFCs are manufactured by embedding a silver electrode into a piece of thermoplastic film to form a thermoplastic electrode. The piezoelectric fibers are then placed between the thermoplastic electrodes, electroded side inward, and pressed to form internally electroded tmAFCs.

6.2.3 Testing

Differential scanning calorimetry and thermogravimetric tests was used to determine the minimum and maximum temperatures for manufacturing Ultem 1000 tmAFCs. Testing indicated that manufacturing should occur between 221.4 °C (430.5 °F) and 475 °C (887 °F). Impedance testing was performed to determine at what temperature decomposition of the thermoplastic electrode would occur. Testing indicated that the thermoplastic electrode does not degrade below 316 °C (600 °F).

Capacitance testing and stress free actuation testing have been performed on tmAFCs. Ultem 1000 internally electroded tmAFCs have shown the highest levels of capacitance and actuation. The few Ultem 1000 internally electroded tmAFCs that survived poling have shown actuation exceeding that of some AFCs manufactured by Continuum Photonics, thus proving the tmAFC concept.

6.3 Contributions

6.3.1 tmAFC Manufacturing

The main contribution of this body of work is the analysis, design, manufacturing and testing of Thermoplastic Matrix Active Fiber Composites, tmAFCs. tmAFCs have simpler processing when compared to thermoset matrix AFCs and are reshapeable.

A major drawback of the AFC design is that a small layer of matrix material trapped between the gap between the electrode and the fiber drastically reduces the level of actuation of the AFC. Due to the dielectric mismatch between the low dielectric matrix and the high dielectric fibers, a large voltage drop occurs the matrix gap, thus reducing the electric field and actuation in the fiber.

Internally electroded tmAFCs have been developed to have the electrode nearly touching the fiber, thus reducing this matrix gap, and therefore increasing actuation. Internally electroded tmAFCs are manufactured by embedding a silver electrode into a piece of thermoplastic film to form a thermoplastic electrode. The piezoelectric fibers are then placed between the thermoplastic electrodes, electroded side inward, and pressed to form internally electroded tmAFCs. The few internally electroded tmAFCs that survived poling have shown actuation exceeding that of some AFCs manufactured by Continuum Photonics.

6.3.2 Thermoplastic Electrodes

A novel manufacturing technique for manufacturing silver electrodes embedded in a thermoplastic film was developed. Silver electrodes printed on Kapton were transferred to thermoplastic film by placing the two into a hot press, and heating and pressing them together. After cooling, the Kapton could be peeled off the thermoplastic film leaving the silver electrode embedded in the thermoplastic film, yielding a thermoplastic electrode with the silver electrode flush with the surface of the thermoplastic film. Thermoplastic electrodes were made using Noryl EN265-7 and Ultem 1000. Ultem 1000 thermoplastic electrodes were made with a 95% success rate. Testing indicated that the Ultem 1000 thermoplastic electrode does not degrade below 316 °C (600 °F).

6.3.3 AFC/tmAFC Analysis

Several analyses, including rule of mixtures analyses and finite element analyses, were performed on a PiezoFlex AFCs to determine the effect of changing the matrix material properties. These analyses showed that when the electrode touches the fibers, the actuation of the AFCs is about equal to that of a magnetic particle AFC (mpAFC) (Reference 45), and the actuation is nearly independent of the dielectric of the matrix. When the electrode does

not touch the fiber, the actuation is highly dependant on the dielectric of the matrix and the AFCs actuate very poorly compared to mpAFCs.

Internally electroded tmAFCs have been developed to have the electrode nearly touching the fiber, thus reducing this matrix gap, and therefore increasing actuation. tmAFCs require simpler manufacturing techniques when compared to mpAFCs, yet as shown in the finite element analysis, have nearly as high a level of actuation.

6.4 Recommendations for Future Work

6.4.1 Matrix Materials for tmAFCs

Other thermoplastic materials should be explored for use as a matrix material for tmAFCs. Polymers with a high usage temperature would allow tmAFCs to be used in higher temperature applications, and thus increasing the potential market share of tmAFCs. A good candidate for a new polymer is PEEK[144] manufactured by Vitrex USA Inc. PEEK has a continuous use temperature of 240 °C (464 °F),[145] which is higher than the glass transition temperature of Ultem 1000. Manufacturing of tmAFCs using PEEK were attempted, however it was experimentally found that the temperature limit of the press, 316 °C (600 °F), could not melt the polymer. Polymers with low mechanical loss should be investigated as well to reduce the power requirements for driving the tmAFCs.

6.4.2 tmAFC Electrodes

In order to facilitate mass production of tmAFCs, as many unnecessary manufacturing steps should be eliminated as possible. One unnecessary step is the bonding of brass or copper to the electrode pads to allow an electrical hookup to the tmAFCs. This step is currently required because using the current electrode design the thermoplastic electrodes are placed in the tmAFC face to face, with the top and bottom electrode pads aligned. Because the electrode pads are sealed in the tmAFC, there is no way to deliver a voltage to the electrode without bonding some form of conductor to the pads and sticking the conductor out of the tmAFC. The electrodes should be redesigned such that part of the electrode is exposed allowing for electrical contact, and thus eliminating an additional manufacturing step.

6.4.3 tmAFC Manufacturing

Due the fact that the force applied to the tmAFC during the bonding of the fibers to the electrode is not independent of the applied vacuum, it is recommended that tests using the mold with an internal vacuum chamber (Figure 4.29) be abandoned. Before the failure of the vacuum chamber, tests using the pressing plates (Figure 4.15) produced many high

capacitance tmAFCs, and several tmAFCs with very high actuation. If more tmAFC research is to proceed it should be using the pressing plates. This would require the vacuum chamber be fixed first.

tmAFCs were manufactured using high-temperature silicone rubber (Reference 101) sold by McMaster-Carr Supply Company. In the McMaster-Carr catalog, the rubber is listed as having a temperature limit of 316 °C (600 °F). This temperature limit appears to be temperature at which the rubber can survive at only for short periods. After used for a few cures at 260 °C (500 °F), the rubber degrades and must be discarded. A better product is Airtech 1050 Rubber manufactured by Airtech Advanced Materials Group.[146] Airtech 1050 Rubber has a temperature limit of at 316 °C (600 °F)[147] and does not appear to degrade dramatically or acquire as large a set at 260 °C (500 °F).

6.4.4 AFC/tmAFC Displacement Testing

While doing research on single crystal fiber Active Fiber Composites,[148] the author tested the displacement of AFCs using a different system than the ZMI 1000 interferometer system used in Section 5.4.2. The displacement was measured using a Nano-DVRT[149] manufactured by MicroStrain Inc. The DVRT was custom designed to measure displacements with a range of 200 μm with a minimum displacement of 25 nm. This DVRT system could measure displacements with no drift and no phase shifts, which were critical problems with the ZMI 1000 interferometer system. To supply the voltage to the AFCs, a Precision Workstation manufactured by Radiant Technologies Inc[150] connected to a Trek 609A Amplifier[151] was used. Unlike the amplifier used in Section 5.4.2 which the current signal always appeared as noise, the Precision Workstation was specifically designed to measure the current for 1pF to 50μF samples at frequencies up to 2.5 KHz.[152] Using this system polarization loops of piezoceramic samples were measured with high accuracy. A fixture was designed by the author to measure the charge and displacement of an AFC/tmAFC using the Precision Workstation and the DVRT. A methodology was developed to reduce the charge and displacement data into complex capacitance, real resistance, and complex Γ. This data was not included in the work because it was not used to take data for tmAFCs.

The DVRT system with the Precision Workstation does have several drawbacks compared to the ZMI 1000 interferometer system:

1. The Trek 609A amplifier becomes unstable above 400 Hz.

2. The Precision Workstation outputs a constant 20 to 30 mV signal, with a minimum step voltage of 20 mV. When connected to the Trek amplifier, the DC signal is amplified to 20 to 30 V, with a minimum voltage step of about 20 V.

3. The output voltage uses the *Integer* function instead of the *Round* function.

4. The Digital to Analog converter reads a minimum voltage step of 1.22 mV, limiting the minimum charge and displacement that could be measured.

5. For the *Hysteresis* and *Piezo* measurement tasks, the time period for an output voltage cycle must be less than 30 sec.

6. The maximum number of points for the voltage output must be less than 1000.

7. The minimum time difference between output voltage points is 0.01 msec, thus the time period is truncated after the second decimal place.

The AFC charge and displacement data gathered using the Precision Workstation system with the DVRT, in the authors opinion, was superior to than could be gathered using the ZMI 1000 interferometer system. The Precision Workstation system with the DVRT should be used for all AFC testing despite its drawbacks. Correct sampling size and use of intelligent input voltage cycles minimize the drawbacks of the Precision Workstation system with the DVRT.

6.4.5 Tensile Testing of AFCs and tmAFCs

In previous research, tensile testing of AFCs was performed using an Instron 8501[153] series tensile testing machine with hydraulic grips. The Instron 8501 was not an ideal system for testing AFCs with, due to the size of the sample in relation to the size of the grips, high frequency vibrations imparted onto the samples due to the hydraulic actuators, and the range and accuracy of the stroke and the force. In Section 5.2.1, the author used an Instron 5542 universal electromechanical testing machine (Reference 116) to perform tensile testing of thin sheets of polymer. Tensile tests were performed on tmAFCs to see the quality of the force and stroke data. The data proved to be of excellent quality with very low noise. This data was not included in this body of work because the test did not conform to any testing standard, nor were loading tabs applied to the tmAFC. The Instron 5542 is much easier to use and program than the Instron 8501, and it is the authors opinion that further tensile tests of AFCs and tmAFC should be performed using the Instron 5542. The Instron 5542 cannot be used to perform high frequency fatigue tests because the actuator for the Instron 5542 is operated by an electric motor, which is limited in the frequency and stroke when the force is applied.

6.4.6 Future tmAFC Concepts

Due to a plastics ability to be reshaped, it is possible that planar tmAFCs can be manufactured and then reshaped to fit the necessary application. One Ultem 1000 tmAFC when manufactured had a very large curvature in it. This tmAFC was sandwiched between steel plates, placed in an oven, and heated above the glass transition temperature for several hours to remove the thermal deformation. After removal from the oven, it was seen that the thermal deformation had been decreased by about half. Using methods such as this, tube shaped or "S" shaped tmAFCs could be manufactured.

Experiments were performed on two Ultem 1000 tmAFCs to determine if tube actuators could be made. The tmAFCs were placed on an aluminum plate covered with GNPT. An aluminum rod covered with GNPT was heated to 260 °C (500 °F). The rod was rolled over the tmAFCs transversely to the fiber direction in an attempt to make tube shaped actuators, however a large curvature could not be induced in the tmAFC. A potentially better way of making a tube shaped actuators is tape a tmAFC to an aluminum rod covered with GNPT. The rod and the tmAFC is vacuum bagged and heated in an oven above the glass transition temperature of the polymer. A vacuum is slowly pulled on the bag to cause the tmAFC to wrap around the rod thus forming a tube shaped tmAFC. In theory, if the tube was tight enough, and the electrodes survived the process, a tmAFC stack could be made.

In order to use AFCs in large-scale structural applications (such as full scale helicopter rotor blades), many AFCs are required. It is desirable to reduce the number of electrical leads to the AFCs to decrease the possibility of dielectric breakdown between the leads and reduce the required structural volume required for the leads. In order to reduce the number of electrical leads, larger volume AFCs are more desirable (larger length, width, and thickness). In order to make AFCs with a larger volume either AFCs need to be bonded and actuated together or AFCs with larger diameter fibers needs to be used. Due to the increase in the passive area due to the bond layer between the actuators, and the multiple layers of Kapton, the passive area of bonded AFCs is greater than AFCs with larger diameter fibers, and thus bonded AFCs will have smaller actuation. The strength of a fiber is inversely proportional to the area of the fiber, thus making larger diameter fiber AFCs less attractive, as seen in Reference 58 pages 62-63. Another option is to make a tmAFC using multiple layers of small diameter of fibers, with a thin layer of polymer between the layers. This would have the benefits of high strength fibers with a smaller passive area compared to AFCs bonded together. A two layer tmAFC was manufactured using the same processing discussed in Section 4.5.2.3 to determine if the possibility of manufacturing such an actuator. Between the two layers of 270 μm (10.6 mil) diameter fibers was a 76 μm (3 mil) thick layer of Ultem 1000 with an electrode on either side. This thermoplastic electrode was manufactured by embedding an electrode in a 76 μm (3 mil) thick layer of Ultem 1000 in the

same manner discussed in Section 4.5.2.1, then flipping the electrode over and embedding another electrode onto the other side. Figure 6.1 shows the cross section of the two-layer tmAFC.

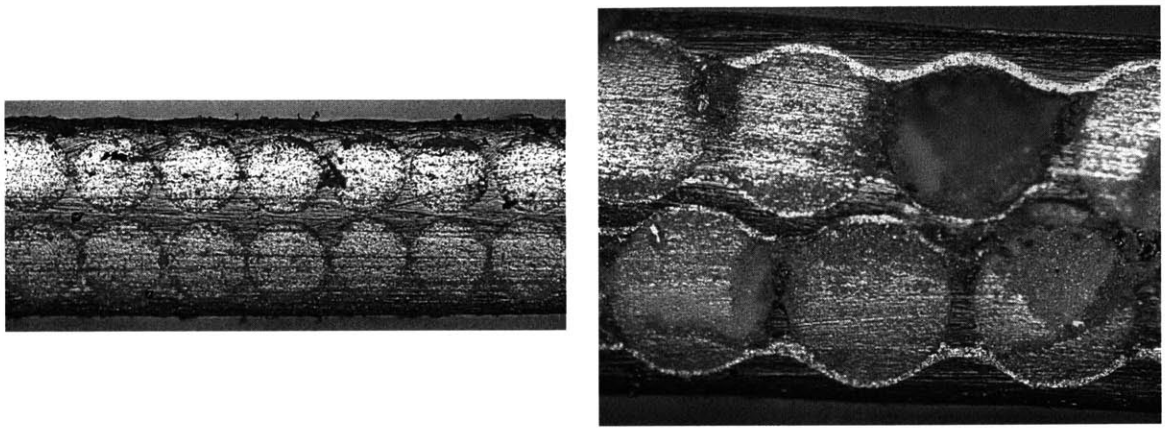

Fibers in a two layer tmAFC Electrodes in a two layer tmAFC

Figure 6.1 Fibers and electrode in a two-layer tmAFC

As can be seen in Figure 6.1, the electrodes touch each side of the fibers in the tmAFCs. When trimming the excess polymer around the sides of the tmAFC, the knife slipped cracking four rails and some fingers of the tmAFC. This tmAFC was poled at 2000 V at 100 °C (212 °F) for 20 minutes, however the tmAFC broke down after about 5 minutes where the crack in the finger was. After the tmAFC was sectioned and looked at under the microscope, it was seen that many electrode fingers were broken during the manufacturing process, most likely due to too large of a pressure being applied to the tmAFC during manufacturing. Due to the large number of fibers needed to manufacture two layer tmAFCs, only one two-layer tmAFC was manufactured.

Appendix I. Equations of Quasi-Electro-Static Electro-Elasticity

I.1 Introduction

In this Appendix the equations of electro-elasticity, which are used throughout this body of work, are presented. It is assumed that magnetic fields present in a body are negligible, and thus the quasi-electro-static approximation holds. It is also assumed that the deformation of the body is small such that the small strain approximation holds. First, the linear equations of equilibrium for a quasi-electro-static body with finite conductivity are presented. These equations are then reduced for a body with zero conductivity. Finally, the constitutive relations for a non-piezoelectric and isotropic materials are presented.

I.2 Equations of Equilibrium for a Quasi-Electro-Static Body with Finite Conductivity Undergoing Small Deformations

In Reference 89, the equations of equilibrium for a quasi-electro-static body with finite conductivity are derived for large deformations. On pages 81-82 in Reference 89, the equations of equilibrium are reduced assuming that deformations of the body are small. These equations in rectangular coordinates x,y,z, are listed below. It should be noted that x,y,z are structural and not material coordinates.

Conservation law for electric charge and current densities

$$\frac{\partial \rho_f}{\partial t} + \underline{\nabla} \bullet \underline{J}_f = 0$$

$$\frac{\partial \rho_f}{\partial t} + \frac{\partial \left(J_f\right)_x}{\partial x} + \frac{\partial \left(J_f\right)_y}{\partial y} + \frac{\partial \left(J_f\right)_z}{\partial z} = 0 \qquad \text{(A.1)}$$

Gauss' law

$$\underline{\nabla} \cdot \underline{D} = \rho_f$$
$$\frac{\partial D_x}{\partial x} + \frac{\partial D_y}{\partial y} + \frac{\partial D_z}{\partial z} = \rho_f \tag{A.2}$$

Conservation of linear momentum

$$\frac{\partial T_{xx}}{\partial x} + \frac{\partial T_{xy}}{\partial y} + \frac{\partial T_{xz}}{\partial z} + f_x = \rho \frac{\partial^2 u}{\partial t^2}$$
$$\frac{\partial T_{xy}}{\partial x} + \frac{\partial T_{yy}}{\partial y} + \frac{\partial T_{yz}}{\partial z} + f_y = \rho \frac{\partial^2 v}{\partial t^2} \tag{A.3}$$
$$\frac{\partial T_{xz}}{\partial x} + \frac{\partial T_{yz}}{\partial y} + \frac{\partial T_{zz}}{\partial z} + f_z = \rho \frac{\partial^2 w}{\partial t^2}$$

Where $\underline{J}_f$ is the conduction current density, $\underline{D}$ is the electric displacement, T is stress, ρ_f is the free charge per unit volume, ρ is the density, f is the applied body forces, and u, v, and w are the displacements in the x, y, and z directions respectively. The following additional definitions are helpful when solving the equations of equilibrium.

Definition of electric field, $\underline{E}$

$$\underline{E} = -\underline{\nabla}\varphi$$
$$\underline{E} = -\frac{\partial \varphi}{\partial x}\hat{i} - \frac{\partial \varphi}{\partial y}\hat{j} - \frac{\partial \varphi}{\partial z}\hat{k} \tag{A.4}$$

Definition of electric displacement, $\underline{D}$

$$\underline{D} = \varepsilon_0 \underline{E} + \underline{P} \tag{A.5}$$

Where φ is the electric potential, ε_0 is the permittivity of free space (8.854×10^{-12} F/m), $\underline{P}$ is the polarization vector, and $\hat{i}, \hat{j}$, and $\hat{k}$ are the unit vectors in the x, y, and z directions respectively. Under the small deformation approximation, the engineering strain, S, is given by:

$$S_{xx} = \frac{\partial u}{\partial x} \qquad S_{yy} = \frac{\partial v}{\partial y} \qquad S_{zz} = \frac{\partial w}{\partial z}$$
$$S_{yz} = \frac{\partial w}{\partial y} + \frac{\partial v}{\partial z} \quad S_{xz} = \frac{\partial w}{\partial x} + \frac{\partial u}{\partial z} \quad S_{xy} = \frac{\partial v}{\partial x} + \frac{\partial u}{\partial y} \tag{A.6}$$

Consider a surface of discontinuity between two materials, as shown below:

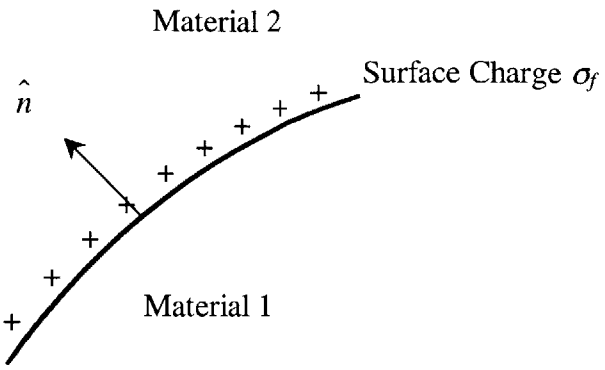

Figure I.1 Surface of Discontinuity between two Materials

In Figure I.1, $\hat{n}$ is the unit vector normal to the surface pointing in the direction from material 1 to material 2. It is also assumed in Figure I.1 that there is a free surface charge, σ_f, present between the materials. Across surfaces of discontinuity, the following must hold:

1. Displacements are continuous across a surface of discontinuity

2. The electric potential is continuous across a surface of discontinuity. This is another way of stating that:

$$\hat{n}\times(\underline{E}_2-\underline{E}_1)=0 \tag{A.7}$$

Where $\underline{E}_1$ and $\underline{E}_2$ are the electric field vectors in materials 1 and 2 respectively at the surface of discontinuity. If material 1 is a perfect conductor with a voltage V applied to it:

$$\varphi_2 = V \tag{A.8}$$

3. Stresses normal and perpendicular to the surface of discontinuity are continuous

4. The electric displacement normal to the surface of discontinuity is given by:

$$\hat{n}\bullet(\underline{D}_2-\underline{D}_1)=\sigma_f \tag{A.9}$$

Where $\underline{D}_1$ and $\underline{D}_2$ are the electric displacement vectors in materials 1 and 2 respectively at the surface of discontinuity. If material 1 is a perfect conductor then:

$$\hat{n}\bullet\underline{D}_2=\sigma_f \tag{A.10}$$

5. The charge entering, leaving, and building up on the surface must be conserved:

$$\hat{n}\bullet\left(\left(\underline{J}_f\right)_2-\left(\underline{J}_f\right)_1\right)+\frac{\partial\sigma_f}{\partial t}=0 \tag{A.11}$$

Where $\left(\underline{J}_f\right)_1$ and $\left(\underline{J}_f\right)_2$ is the conduction current density vectors in materials 1 and 2 respectively at the surface of discontinuity. Using Equation A.9, Equation A.11 can be written as:

$$\hat{n}\bullet\left[\left(\underline{J}_f\right)_2-\left(\underline{J}_f\right)_1+\frac{\partial}{\partial t}\left(\underline{D}_2-\underline{D}_1\right)\right]=0 \tag{A.12}$$

It should be noted that the total current, i, (conduction current and polarization current) though a surface S, (i is positive outward) is given by:

$$i=\oint_S\left(J_f+\frac{\partial D}{\partial t}\right)\bullet d\underline{S} \tag{A.13}$$

The charge, q, on this surface is given by:

$$i=\frac{\partial q}{\partial t} \tag{A.14}$$

I.3 Equations of Equilibrium for a Quasi-Electro-Static Body with Zero Conductivity Undergoing Small Deformations

In Reference 23, the equations of equilibrium for a quasi-electro-static body with zero conductivity under going small deformations are presented. These equations in are the same as the equations presented above for the finite conductivity case, however the conduction current density $\underline{J}_f$ is zero. Without any form of electrical conduction, there is no way for free charge per unit volume, φ_f, to build up in a body, and there is no way for free surface change, σ_f, to build up on material interfaces that are not connected to a voltage source, except in the presence of nuclear radiation. In the absence of nuclear radiation, φ_f and σ_f must be zero. Under this condition, Equation A.1 becomes redundant.

I.4 Non-piezoelectric and Isotropic Constitutive Relations

In Section 1.2.1, the constitutive equations for a piezoelectric material in engineering matrix notation is presented (Equation 1.1) and described:

$$\begin{Bmatrix} D_1 \\ D_2 \\ D_3 \\ \hline S_1 \\ S_2 \\ S_3 \\ S_4 \\ S_5 \\ S_6 \end{Bmatrix} = \left[\begin{array}{ccc:ccc:ccc} \varepsilon_{11}^T & 0 & 0 & 0 & 0 & 0 & 0 & d_{15} & 0 \\ 0 & \varepsilon_{11}^T & 0 & 0 & 0 & 0 & d_{15} & 0 & 0 \\ 0 & 0 & \varepsilon_{33}^T & d_{31} & d_{31} & d_{33} & 0 & 0 & 0 \\ \hdashline 0 & 0 & d_{31} & s_{11}^E & s_{12}^E & s_{13}^E & 0 & 0 & 0 \\ 0 & 0 & d_{31} & s_{12}^E & s_{11}^E & s_{13}^E & 0 & 0 & 0 \\ 0 & 0 & d_{33} & s_{13}^E & s_{13}^E & s_{33}^E & 0 & 0 & 0 \\ 0 & d_{15} & 0 & 0 & 0 & 0 & s_{44}^E & 0 & 0 \\ d_{15} & 0 & 0 & 0 & 0 & 0 & 0 & s_{44}^E & 0 \\ 0 & 0 & 0 & 0 & 0 & 0 & 0 & 0 & s_{66}^E \end{array}\right] \begin{Bmatrix} E_1 \\ E_2 \\ E_3 \\ \hline T_1 \\ T_2 \\ T_3 \\ T_4 \\ T_5 \\ T_6 \end{Bmatrix} \tag{A.15}$$

From Ohm's law, the conduction current density, $\underline{J}_f$, for a piezoelectric material is given by (Equation 1.13):

$$\begin{Bmatrix} (J_f)_1 \\ (J_f)_2 \\ (J_f)_3 \end{Bmatrix} = \begin{bmatrix} \sigma_{11} & 0 & 0 \\ 0 & \sigma_{11} & 0 \\ 0 & 0 & \sigma_{33} \end{bmatrix} \begin{Bmatrix} E_1 \\ E_2 \\ E_3 \end{Bmatrix} \tag{A.16}$$

For a non-piezoelectric, orthotropic material, $\underline{d}$ equals zero. Equations A.15 and A.16 can be written 15 independent material constants:

$$\begin{Bmatrix} S_1 \\ S_2 \\ S_3 \\ S_4 \\ S_5 \\ S_6 \end{Bmatrix} = \begin{bmatrix} s_{11} & s_{12} & s_{13} & 0 & 0 & 0 \\ s_{12} & s_{22} & s_{23} & 0 & 0 & 0 \\ s_{13} & s_{23} & s_{33} & 0 & 0 & 0 \\ 0 & 0 & 0 & s_{44} & 0 & 0 \\ 0 & 0 & 0 & 0 & s_{55} & 0 \\ 0 & 0 & 0 & 0 & 0 & s_{66} \end{bmatrix} \begin{Bmatrix} T_1 \\ T_2 \\ T_3 \\ T_4 \\ T_5 \\ T_6 \end{Bmatrix} \tag{A.17}$$

$$\begin{Bmatrix} D_1 \\ D_2 \\ D_3 \end{Bmatrix} = \begin{bmatrix} \varepsilon_{11} & 0 & 0 \\ 0 & \varepsilon_{22} & 0 \\ 0 & 0 & \varepsilon_{33} \end{bmatrix} \begin{Bmatrix} E_1 \\ E_2 \\ E_3 \end{Bmatrix} \tag{A.18}$$

$$\begin{Bmatrix} (J_f)_1 \\ (J_f)_2 \\ (J_f)_3 \end{Bmatrix} = \begin{bmatrix} \sigma_{11} & 0 & 0 \\ 0 & \sigma_{22} & 0 \\ 0 & 0 & \sigma_{33} \end{bmatrix} \begin{Bmatrix} E_1 \\ E_2 \\ E_3 \end{Bmatrix} \tag{A.19}$$

For a mechanically isotropic material, Equation A.17 can be written with 2 independent material constants:

$$\begin{Bmatrix} S_1 \\ S_2 \\ S_3 \\ S_4 \\ S_5 \\ S_6 \end{Bmatrix} = \frac{1}{E} \begin{bmatrix} 1 & -\nu & -\nu & 0 & 0 & 0 \\ -\nu & 1 & -\nu & 0 & 0 & 0 \\ -\nu & -\nu & 1 & 0 & 0 & 0 \\ 0 & 0 & 0 & 2(1+\nu) & 0 & 0 \\ 0 & 0 & 0 & 0 & 2(1+\nu) & 0 \\ 0 & 0 & 0 & 0 & 0 & 2(1+\nu) \end{bmatrix} \begin{Bmatrix} T_1 \\ T_2 \\ T_3 \\ T_4 \\ T_5 \\ T_6 \end{Bmatrix} \tag{A.20}$$

Where E is the Young's modulus and ν is the Poisson's ratio. For an electrically isotopic non-piezoelectric materials, Equation A.18, can be written with 1 independent material constant:

$$\begin{Bmatrix} D_1 \\ D_2 \\ D_3 \end{Bmatrix} = \begin{bmatrix} \varepsilon & 0 & 0 \\ 0 & \varepsilon & 0 \\ 0 & 0 & \varepsilon \end{bmatrix} \begin{Bmatrix} E_1 \\ E_2 \\ E_3 \end{Bmatrix} \tag{A.21}$$

Where ε is permittivity. Oftentimes, Equation A.21 will be written in terms of the relative dielectric, K:

$$\begin{Bmatrix} D_1 \\ D_2 \\ D_3 \end{Bmatrix} = \varepsilon_0 \begin{bmatrix} K & 0 & 0 \\ 0 & K & 0 \\ 0 & 0 & K \end{bmatrix} \begin{Bmatrix} E_1 \\ E_2 \\ E_3 \end{Bmatrix} \tag{A.22}$$

For an electrically isotopic non-piezoelectric material, Equation A.19 can be written with 1 independent material constant:

$$\begin{Bmatrix} (J_f)_1 \\ (J_f)_2 \\ (J_f)_3 \end{Bmatrix} = \begin{bmatrix} \sigma & 0 & 0 \\ 0 & \sigma & 0 \\ 0 & 0 & \sigma \end{bmatrix} \begin{Bmatrix} E_1 \\ E_2 \\ E_3 \end{Bmatrix} \tag{A.23}$$

Where σ is the conductivity.

Appendix II. AFC/tmAFC Constitutive Relations

II.1 Introduction

In this Appendix, the constitutive relations for the bulk material properties for an AFC/tmAFC will be determined. The reduced constitutive relations for a piezoelectric *3-3* actuator will be used for illustrative purposes.

II.2 The Reduced Constitutive Relations for a Piezoelectric Rod Poled and Actuated in the *3* Direction

Consider a rod of length L with a uniform cross section area A. The rod is electroded on two opposite ends as shown in the following figure:

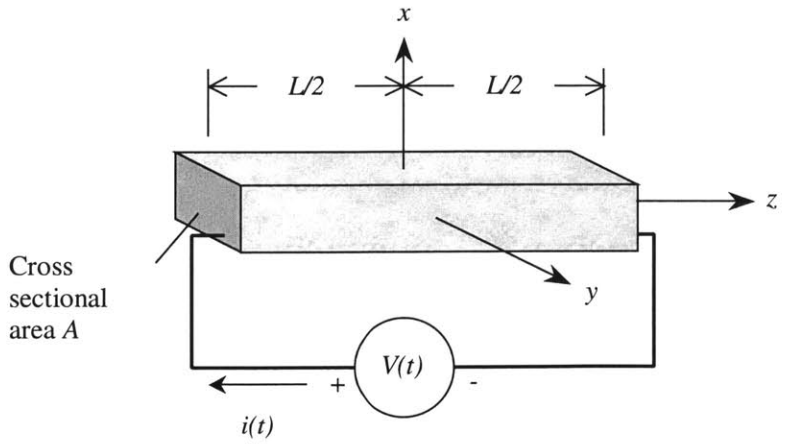

Figure II.1 Illustration of a *3-3* Actuator

The rod is connected to a voltage source $V(t)$ which supplies a current $i(t)$ to the piezoelectric material. The actuator is poled in the z direction and the majority of the electric field is in the z direction. The constitutive relations in matrix engineering form are given by:

$$\begin{aligned}\{S\} &= \left[\varepsilon^T\right]\{E\} + [d]_t\{T\} \\ \{D\} &= [d]\{E\} + \left[s^E\right]\{T\}\end{aligned} \tag{B.1}$$

Equation B.1 is expanded out in matrix form in Equation 1.2 for a Hexagonal Crystal – Class 6 mm poled ferroelectric with the polarization direction in the *3* direction. For the following discussion the piezoelectric material is assumed to be of this type.

Consider the point of view of the user of the piezoelectric rod. If the user wants to prescribe a voltage to achieve a certain level of strain or stress output, then the rod is being used as a *3-3* actuator. A user of the *3-3* actuator is then concerned about the level of voltage and current needed to achieve the desired stress and strain outputs such that the proper power supply can be selected. They are also concerned with the maximum voltage that can be applied to the actuator, the depolarization voltage, the effect of the frequency of the voltage on the output of the actuator, and the effect of temperature on the output. If the user wants to achieve a certain level of voltage or charge given an applied stress or strain, then the piezoelectric rod is being used in a sensor. If the user wants to achieve a certain level of power output (a function of voltage and current) then the piezoelectric rod is being used in an energy harvester configuration. In all these cases, the user is not concerned with the electric field or the electric displacement; they are however concerned with the voltage, charge, and current. Therefore, it is desirable to recast Equation B.1 in terms of voltage, charge, and current.

In order to recast Equation B.1 in terms of voltage, charge, and current, the positive sense of the voltage must be defined. Consider the poling process for a virgin (never has been poled) *3-3* actuator as illustrated in the following Figure.

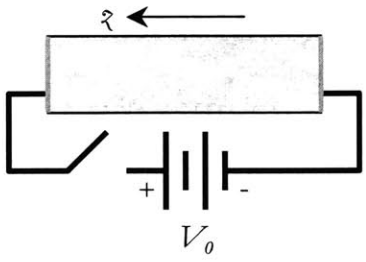

Virgin piezoelectric rod before being connected to DC voltage source, V_0

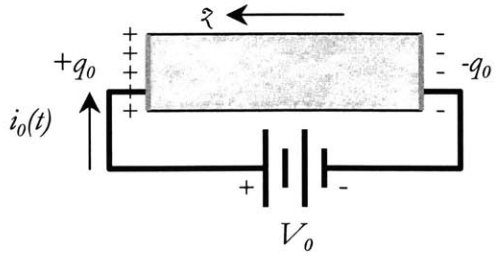

Charge rushes down wires depositing itself onto electrodes of piezoelectric rod

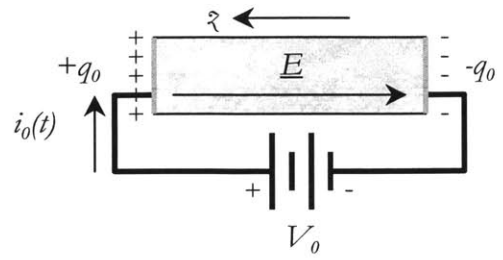

Electric field inside of piezoelectric rod forms due to separation of charge

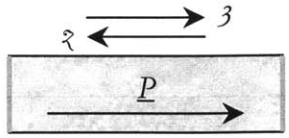

After removal of the voltage source, if electric field is strong enough, the piezoelectric material polarizes in the direction of the electric field (the *3* direction)

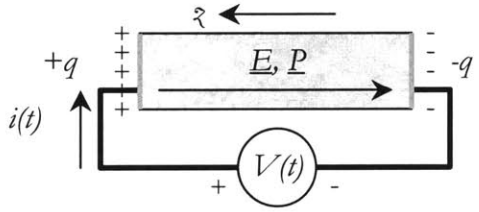

Poled piezoelectric rod connected to a time varying voltage source

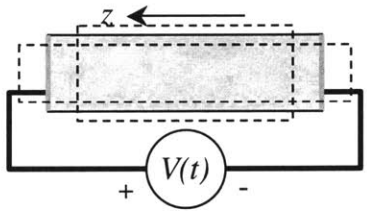

Application of an electric field in the same direction of the *3* direction causes an extension strain in the z direction. Application of an electric field in the opposite direction of the *3* direction causes a compression strain in the z direction.

Figure II.2 Illustration of the Poling Procedure and Actuation of a *3-3* Actuator

In Figure II.2 a virgin piezoelectric rod is connected to a DC voltage source, with strength V_0. As soon as the circuit is completed, charge rushes down the wires and deposits itself on the electrode. This initial movement of charge causes a large instantaneous current. The charge on the electrodes causes an electric potential to be setup inside the piezoelectric material. This electric potential, φ, is given by:

$$\varphi(x,y,z,t)=\varphi(z)=\frac{V_0}{L}z \tag{B.2}$$

Where L is the length of the actuator, and z is the longitudinal coordinate. The charge causes an electric field internally in the piezoelectric rod, $\underline{E}$, that is given by:

$$\underline{E}=-\underline{\nabla}\varphi=-\frac{\partial\varphi}{\partial x}\hat{i}-\frac{\partial\varphi}{\partial y}\hat{j}-\frac{\partial\varphi}{\partial z}\hat{k} \tag{B.3}$$

$$\underline{E}=\frac{\partial}{\partial z}\left(-\frac{V_0}{L}z\right)\hat{k}=-\frac{V_0}{L}\hat{k} \tag{B.4}$$

Where $\hat{i}, \hat{j}$ and $\hat{k}$ are the unit vectors in the x, y, and z directions respectively. The voltage is applied for some time and if the electric field is large enough, after removal of the electric field a remnant polarization $\underline{P}$ remains inside the piezoelectric rod. The direction of the remnant polarization defines the "*3*" direction or poling direction, which in this case is in the $-\hat{k}$ direction, that is opposite of the z direction. Further discussion of the poling procedure for an AFC/tmAFC is given in Section 3.4.

Now a time varying voltage source, *V(t)*, is connected to the actuator with the high voltage side connected to the wire that was previously connected to the high voltage side of the DC poling source, and the low voltage side is connected to the wire that was previously connected to the low voltage side of the DC poling source. The electric potential is given by:

$$\varphi(x, y, z, t) = \varphi(z) = \frac{V(t)}{L} z \tag{B.5}$$

The electric field is now given by:

$$\underline{E} = -\frac{V(t)}{L}\hat{k} \tag{B.6}$$

The electric field in the "*3*" direction is the projection of the electric field vector onto the vector in the direction of the poling direction, $\hat{3}$:

$$E_3 = \frac{\underline{E} \bullet \hat{3}}{\left\| \hat{3} \bullet \hat{3} \right\|} = \frac{-\frac{V(t)}{L}\hat{k} \bullet -\hat{k}}{\left\| -\hat{k} \bullet -\hat{k} \right\|} \tag{B.7}$$

$$E_3 = \frac{V(t)}{L}$$

In this case, if a positive voltage is commanded from the time varying voltage source, an electric field in the direction of the poling direction is induced, and an extension zz strain is seen. If a negative voltage is commanded from the time varying voltage source, an electric field opposite of the direction of the poling direction is induced, and a compression zz strain seen. Thus, a positive voltage direction can be defined.

A voltage in the positive direction causes an electric field
in the same direction as the poling direction in a 3-3 actuator (B.8)

This definition also allows us to define the positive and negative electrodes.

The positive electrode is the electrode that
the remnant polarization points away from (B.9)

If the *3-3* actuator is never repoled during actuation, the positive electrode is the electrode to which the high side of the voltage source was connected to during poling. In Figure II.2, the positive and negative electrodes are at $z = L/2, -L/2$ respectively. The positive direction of

the current, *i(t)*, is therefore from the high side of a voltage source connected in the positive voltage direction into the positive electrode, as shown in Figure II.2.

We will assume henceforth that stresses and strains are constant throughout the *3-3* actuator. We will also assume the actuator is actuating quasi-statically. Quasi-static actuation is defined by: "the frequency rage which there is no appreciable spatial variation in stress or electric field. The specific rage depends somewhat on the mechanical Q of the specimen, but in general the error will be less than 1% and 0.1% respectively, if the frequency is less than one tenth of 0.03 times the lowest resonant frequency of the specimen."(Reference 23 pages 38)

If these electrodes are the only electrodes used to apply voltages with, only an electric field in the *3* direction can be applied, therefore $E_1 = E_2 = 0$. Using Equations B.7 and B.8, Equation B.1 can be rewritten as:

$$D_1 = D_2 = 0$$

$$D_3 = \frac{\varepsilon_{33}^T}{L} V + d_{31} T_1 + d_{31} T_2 + d_{33} T_3$$

$$\begin{Bmatrix} S_1 \\ S_2 \\ S_3 \\ S_4 \\ S_5 \\ S_6 \end{Bmatrix} = \begin{Bmatrix} \frac{d_{31}}{L} \\ \frac{d_{31}}{L} \\ \frac{d_{33}}{L} \\ 0 \\ 0 \\ 0 \end{Bmatrix} V + \begin{bmatrix} s_{11}^E & s_{12}^E & s_{13}^E & 0 & 0 & 0 \\ s_{12}^E & s_{11}^E & s_{13}^E & 0 & 0 & 0 \\ s_{13}^E & s_{13}^E & s_{33}^E & 0 & 0 & 0 \\ 0 & 0 & 0 & s_{44}^E & 0 & 0 \\ 0 & 0 & 0 & 0 & s_{44}^E & 0 \\ 0 & 0 & 0 & 0 & 0 & s_{66}^E \end{bmatrix} \begin{Bmatrix} T_1 \\ T_2 \\ T_3 \\ T_4 \\ T_5 \\ T_6 \end{Bmatrix} \tag{B.10}$$

Where V is the time varying voltage connected in the positive voltage direction. The electric displacement is of little use to a user of a *3-3* actuator, however the charge on one of the electrodes, or the current, is. The charge on the positively electrode is given by:

$$q(t) = \int_S \left(\underline{D} \bullet \hat{n} \right) dA \tag{B.11}$$

Where $\hat{n}$ is the normal of the electrode into the piezoelectric material, and dA is the differential area of the electrode. From the definition of the "positive electrode", $\hat{n} = \hat{3}$, and therefore Equation B.11 can be written as:

$$q(t) = \int_S \left(D_3 \hat{3} \bullet \hat{3} \right) dA = \int_S D_3 \, dA = A D_3 \tag{B.12}$$

Because the same electrodes are used for the poling and actuation, only the electric displacement in the "3" direction is used in Equation B.12. The charge on the positive electrode, q, can be written as:

$$q = A\frac{\varepsilon_{33}^T}{L}V + Ad_{31}T_1 + Ad_{31}T_2 + Ad_{33}T_3 \tag{B.13}$$

The current in the positive direction, *i*, is given by:

$$i = \frac{dq}{dt} = A\frac{\varepsilon_{33}^T}{L}\frac{dV}{dt} + Ad_{31}\frac{dT_1}{dt} + Ad_{31}\frac{dT_2}{dt} + Ad_{33}\frac{dT_3}{dt} \tag{B.14}$$

The term $A\frac{\varepsilon_{33}^T}{L}$ is the stress free capacitance of the *3-3* actuator, and can be written as:

$$C^T = \varepsilon_{33}^T\frac{A}{L} \tag{B.15}$$

Thus, Equation B.1 can be written for a thin *3-3* longitudinal actuator as:

$$\begin{Bmatrix} S_1 \\ S_2 \\ S_3 \\ S_4 \\ S_5 \\ S_6 \end{Bmatrix} = \begin{Bmatrix} \frac{d_{31}}{L} \\ \frac{d_{31}}{L} \\ \frac{d_{33}}{L} \\ 0 \\ 0 \\ 0 \end{Bmatrix} V + \begin{bmatrix} s_{11}^E & s_{12}^E & s_{13}^E & 0 & 0 & 0 \\ s_{12}^E & s_{11}^E & s_{13}^E & 0 & 0 & 0 \\ s_{13}^E & s_{13}^E & s_{33}^E & 0 & 0 & 0 \\ 0 & 0 & 0 & s_{44}^E & 0 & 0 \\ 0 & 0 & 0 & 0 & s_{44}^E & 0 \\ 0 & 0 & 0 & 0 & 0 & s_{66}^E \end{bmatrix} \begin{Bmatrix} T_1 \\ T_2 \\ T_3 \\ T_4 \\ T_5 \\ T_6 \end{Bmatrix} \tag{B.16}$$

$$q = C^T V + Ad_{31}T_1 + Ad_{31}T_2 + Ad_{33}T_3 \tag{B.17}$$

$$i = C^T\frac{dV}{dt} + Ad_{31}\frac{dT_1}{dt} + Ad_{31}\frac{dT_2}{dt} + Ad_{33}\frac{dT_3}{dt} \tag{B.18}$$

Writing Equation B.1 as Equations B.16 - B.18 gives the user of the *3-3* actuator the relations between all the variables of concern. However rewriting the Equations in this manner does have the downside of making the Equations unsymmetrical.

II.3 General Reduced Constitutive Relations for a Longitudinal Actuator

As with the piezoelectric rod, the end user of a piezoelectric longitudinal actuator is concerned with the relation between stress, strain, voltage, charge, and current. Thus, it is desirable to write generalized constitutive relations similar to Equations B.16 - B.18 for a piezoelectric longitudinal actuator.

In Section II.2 the reduced constitutive relations for a piezoelectric rod poled and actuated in the *3* direction were derived. Let us consider a piezoelectric material used in a system of passive materials and passive circuit elements to actuate in a longitudinal fashion. The term "piezoelectric actuator" will be used for entire collection of passive and active

materials. The piezoelectric actuator for example could be comprised of the piezoelectric *3-3* rod shown in Figure II.1 with a passive dielectric layer acting as insulation on the outside. As another example, the piezoelectric shown in Figure II.1 could have electrodes with a finite resistance or capacitance. An AFC/tmAFC is a system of piezoelectric materials and passive materials that actuates in a longitudinal fashion. Hence, the entire AFC/tmAFC package can be referred to as a piezoelectric actuator.

As in the previous section, it will be assumed that stresses and strains are constant throughout piezoelectric actuator. It is assumed the piezoelectric actuator is actuating quasi-statically as defined in Section II.2. It is also assumed that the piezoelectric material in the actuator is poled after the actuator is manufactured (that is the piezoelectric materials are not poled prior to being integrated into the piezoelectric actuator). We can now define the "positive voltage direction"

A positive voltage outputted from a driving voltage source connected in the same manner as the poling voltage source (high side to high side) is a voltage in the positive direction (B.19)

Equation B.19 implicitly assumes that the piezoelectric materials were poled after manufacturing with the same electrodes used for actuation, and the piezoelectric materials were not depoled or repoled during its use. Equation B.19 also allows us to define the positive and negative electrodes.

The positive electrode is the electrode that the high side of the poling voltage source was connected to (B.20)

The positive direction of current is from the high side of the poling voltage source into the positive electrode.

For a piezoelectric actuator, strain is linearly proportional to stress. Because the actuator is piezoelectric, the strain is linearly proportional to the electric field, which is linearly proportional to the applied voltage. Thus, the strain for a piezoelectric actuator can be written in a manner that is similar to Equation B.16:

$$\{S\} = \left[s^V\right]\{T\} + \{\Gamma\} V$$

$$\begin{Bmatrix} S_{XX} \\ S_{YY} \\ S_{ZZ} \\ S_{YZ} \\ S_{XZ} \\ S_{XY} \end{Bmatrix} = \begin{bmatrix} s^V_{XXXX} & s^V_{XXYY} & s^V_{XXZZ} & s^V_{XXYZ} & s^V_{XXXZ} & s^V_{XXXY} \\ s^V_{XXYY} & s^V_{YYYY} & s^V_{YYZZ} & s^V_{YYYZ} & s^V_{YYXZ} & s^V_{YYXY} \\ s^V_{XXZZ} & s^V_{YYZZ} & s^V_{ZZZZ} & s^V_{ZZYZ} & s^V_{ZZXZ} & s^V_{ZZXY} \\ s^V_{XXYZ} & s^V_{YYYZ} & s^V_{ZZYZ} & s^V_{YZYZ} & s^V_{YZXZ} & s^V_{YZXY} \\ s^V_{XXXZ} & s^V_{YYXZ} & s^V_{ZZXZ} & s^V_{YZXZ} & s^V_{XZXZ} & s^V_{XZXY} \\ s^V_{XXXY} & s^V_{YYXY} & s^V_{ZZXY} & s^V_{YZXY} & s^V_{XZXY} & s^V_{XYXY} \end{bmatrix} \begin{Bmatrix} T_{XX} \\ T_{YY} \\ T_{ZZ} \\ T_{YZ} \\ T_{XZ} \\ T_{XY} \end{Bmatrix} + \begin{Bmatrix} \Gamma_{XX} \\ \Gamma_{YY} \\ \Gamma_{ZZ} \\ \Gamma_{YZ} \\ \Gamma_{XZ} \\ \Gamma_{XY} \end{Bmatrix} (V) \tag{B.21}$$

Where S is the engineering strain vector, T is the stress vector, V is the voltage drop across the piezoelectric actuator (where the voltage is applied in the positive sense), s^V is the "shorted" compliance, and Γ is a piezoelectric "strain" vector.

The actuator being considered is comprised of piezoelectric material. The current output from a piezoelectric material is linearly proportional to the stress applied to it. Because a piezoelectric material is a dielectric material, the current that passes though the piezoelectric material is proportional to the derivative of the voltage with respect to time, as is a capacitor. Typically piezoelectric materials have a resistively that is very high and therefore it can be assumed that the resistance is infinite. It is possible to construct a piezoelectric actuator with a finite resistance (a finite inductance is possible also, but will not be considered here). For a resistor the current is proportional to the voltage. Thus, the current for a piezoelectric actuator can be written in a manner that is similar to Equation B.18.

$$\begin{aligned} i &= \frac{V}{R} + C^T \frac{dV}{dt} + \lfloor \Phi \rfloor \left\{ \frac{dT}{dt} \right\} \\ i &= C^T \frac{dV}{dt} + \Phi_{XX} \frac{dT_{XX}}{dt} + \Phi_{YY} \frac{dT_{YY}}{dt} + \Phi_{ZZ} \frac{dT_{ZZ}}{dt} \end{aligned} \tag{B.22}$$

Where i is the current flowing through the actuator, R is the resistance of the piezoelectric actuator, C^T is the stress free capacitance, and Φ is a piezoelectric constant. Integrating Equation B.22 with respect to time yields the charge on the positive electrode.

$$q(t) = q(t_0) + \int_{t_0}^{t} i(T)\,dT \tag{B.23}$$

$$\begin{aligned} q(t) &= q(t_0) + C^T V(t) + \lfloor \Phi \rfloor \{T\} + \int_{t_0}^{t} \frac{V(T)}{R} dT \\ q(t) &= q(t_0) + C^T V(t) + \Phi_{XX} T_{XX} + \Phi_{YY} T_{YY} + \Phi_{ZZ} T_{ZZ} + \int_{t_0}^{t} \frac{V(T)}{R} dT \end{aligned} \tag{B.24}$$

Where t_0 is the initial time, $q(t_0)$ is the charge on the positive electrode at time t_0, and T is a dummy variable of integration. Equations B.21, B.22, and B.24 are the general reduced constitutive relations for a longitudinal actuator.

II.4 Reduced Constitutive Relations for a Rectangular AFC/tmAFC

In this section the reduced constitutive relations for an AFC/tmAFC will be derived. It is assumed the AFC/tmAFC is actuating quasi-statically as defined in Section II.2. It is also assumed that the piezoelectric fibers in the AFC/tmAFC are poled after the actuator is manufactured. As in the previous section, it will be assumed that only the global stresses and strains are of a concern, and are constant throughout the AFC/tmAFC. This is not to say the stress and strain does not vary throughout the composite. Stresses inside the AFC/tmAFC include stresses due to manufacturing, stresses due to material property mismatch during actuation, and stresses due to applied stress and strains at the boundary.

However, the only stresses and strains that the end user can control are those on the surface of the actuator. As shown in Appendix III, the material properties of the reduced constitutive relations already take into consideration the effect of internal stresses on the strain and charge output of the actuator. Thus, the stresses and strains in the constitutive relations represent the global stresses and apparent global strains on the boundary, however these stresses do not represent the actual local stress and local strain state at each point within the AFC/tmAFC.

Consider the rectangular AFC/tmAFC shown in Figure 2.1. In the active area of the AFC/tmAFC the piezoelectric fibers are poled and an application of a voltage induces an actuation strain to occur. Outside of the active area the piezoelectric fibers are not poled, and therefore act as a passive material. In terms of the needs of the end user of an AFC/tmAFC, constitutive relations for the entire actuator are desirable. However in terms of analyzing the AFC/tmAFC it is more desirable to determine constitutive relations for the active area of the AFC/tmAFC or constitutive relations for the volume surrounding a single fiber as shown in Figure 2.5. In this section, we will examine the constitutive relations for an entire AFC/tmAFC, the active area of an AFC/tmAFC, and the volume of a single fiber of an AFC/tmAFC. We will first derive the constitutive relations for the active area and of a single fiber. Using these constitutive relations, the constitutive relations for an entire AFC/tmAFC will be discussed. In each case, the constitutive relations will be of the form of Equations B.21, B.22, and B.24.

For the active area of the AFC/tmAFC the shown in Figure 2.1 the constitutive relations are given by Equation B.21:

$$\{S\}_A = \left[s^V\right]_A \{T\}_A + \{\Gamma\}_A V$$

$$\begin{Bmatrix} S_{XX} \\ S_{YY} \\ S_{ZZ} \\ S_{YZ} \\ S_{XZ} \\ S_{XY} \end{Bmatrix}_A = \begin{bmatrix} s^V_{XXXX} & s^V_{XXYY} & s^V_{XXZZ} & s^V_{XXYZ} & s^V_{XXXZ} & s^V_{XXXY} \\ s^V_{XXYY} & s^V_{YYYY} & s^V_{YYZZ} & s^V_{YYYZ} & s^V_{YYXZ} & s^V_{YYXY} \\ s^V_{XXZZ} & s^V_{YYZZ} & s^V_{ZZZZ} & s^V_{ZZYZ} & s^V_{ZZXZ} & s^V_{ZZXY} \\ s^V_{XXYZ} & s^V_{YYYZ} & s^V_{ZZYZ} & s^V_{YZYZ} & s^V_{YZXZ} & s^V_{YZXY} \\ s^V_{XXXZ} & s^V_{YYXZ} & s^V_{ZZXZ} & s^V_{YZXZ} & s^V_{XZXZ} & s^V_{XZXY} \\ s^V_{XXXY} & s^V_{YYXY} & s^V_{ZZXY} & s^V_{YZXY} & s^V_{XZXY} & s^V_{XYXY} \end{bmatrix}_A \begin{Bmatrix} T_{XX} \\ T_{YY} \\ T_{ZZ} \\ T_{YZ} \\ T_{XZ} \\ T_{XY} \end{Bmatrix}_A + \begin{Bmatrix} \Gamma_{XX} \\ \Gamma_{YY} \\ \Gamma_{ZZ} \\ \Gamma_{YZ} \\ \Gamma_{XZ} \\ \Gamma_{XY} \end{Bmatrix}_A (V)_A \tag{B.25}$$

Where the A subscript indicates that the constitutive relation are for the active area of the AFC/tmAFC, and an AFC subscript will be used to indicate the constitutive relations are for the entire AFC/tmAFC. For a single fiber, Equation B.21 can be written as:

$$\{S\}_F = \left[s^V\right]_F \{T\}_F + \{\Gamma\}_F V$$

$$\begin{Bmatrix} S_{xx} \\ S_{yy} \\ S_{zz} \\ S_{yz} \\ S_{xz} \\ S_{xy} \end{Bmatrix}_F = \begin{bmatrix} s^V_{xxxx} & s^V_{xxyy} & s^V_{xxzz} & s^V_{xxyz} & s^V_{xxxz} & s^V_{xxxy} \\ s^V_{xxyy} & s^V_{yyyy} & s^V_{yyzz} & s^V_{yyyz} & s^V_{yyxz} & s^V_{yyxy} \\ s^V_{xxzz} & s^V_{yyzz} & s^V_{zzzz} & s^V_{zzyz} & s^V_{zzxz} & s^V_{zzxy} \\ s^V_{xxyz} & s^V_{yyyz} & s^V_{zzyz} & s^V_{yzyz} & s^V_{yzxz} & s^V_{yzxy} \\ s^V_{xxxz} & s^V_{yyxz} & s^V_{zzxz} & s^V_{yzxz} & s^V_{xzxz} & s^V_{xzxy} \\ s^V_{xxxy} & s^V_{yyxy} & s^V_{zzxy} & s^V_{yzxy} & s^V_{xzyz} & s^V_{xyxy} \end{bmatrix}_F \begin{Bmatrix} T_{xx} \\ T_{yy} \\ T_{zz} \\ T_{yz} \\ T_{xz} \\ T_{xy} \end{Bmatrix}_F + \begin{Bmatrix} \Gamma_{xx} \\ \Gamma_{yy} \\ \Gamma_{zz} \\ \Gamma_{yz} \\ \Gamma_{xz} \\ \Gamma_{xy} \end{Bmatrix}_F (V)_F \tag{B.26}$$

Where the F subscript indicates that the constitutive relation is for a single fiber of an AFC/tmAFC, and S is the engineering strain. As was discussed in Section 3.4, if it assumed that the electrodes are perfectly conducting then the voltage applied to the AFC/tmAFC equals the voltage drop across the electrodes in the active area, and the voltage drop across a singe fiber, therefore:

$$(V)_{AFC} = (V)_A = (V)_F = V$$

Consider the response of a single fiber, or the active area of an AFC/tmAFC. If no stresses are applied to the body then $T = 0$. When a positive voltage is applied, the AFC/tmAFC extends in the Z direction and on average contracts or extends in the X, Y. Due to symmetry of the materials and the applied voltage, the AFC/tmAFC does not globally shear, although local shearing may occur. This indicates for both the active area and the single fiber volume that:

$$(\Gamma_{YZ})_A = (\Gamma_{XZ})_A = (\Gamma_{XY})_A = (\Gamma_{yz})_F = (\Gamma_{xz})_F = (\Gamma_{xy})_F = 0 \tag{B.27}$$

Consider the case were the AFC/tmAFC is short circuited Because the materials and the geometry of the AFC/tmAFC in the active area is symmetric in the X, Y, and Z directions, and balanced in the Z direction, when a tensile stress is applied in the XX direction the AFC/tmAFC strains only in the XX, YY, and ZZ directions, and does not globally shear. The same argument applies for a loading in the YY and ZZ directions. Therefore due to symmetry, extension and shearing for the active area are decoupled as shown in the following equation.

$$\begin{Bmatrix} S_{XX} \\ S_{YY} \\ S_{ZZ} \\ S_{YZ} \\ S_{XZ} \\ S_{XY} \end{Bmatrix}_A = \begin{bmatrix} s^V_{XXXX} & s^V_{XXYY} & s^V_{XXZZ} & 0 & 0 & 0 \\ s^V_{XXYY} & s^V_{YYYY} & s^V_{YYZZ} & 0 & 0 & 0 \\ s^V_{XXZZ} & s^V_{YYZZ} & s^V_{ZZZZ} & 0 & 0 & 0 \\ 0 & 0 & 0 & s^V_{YZYZ} & s^V_{YZXZ} & s^V_{YZXY} \\ 0 & 0 & 0 & s^V_{YZXZ} & s^V_{XZXZ} & s^V_{XZXY} \\ 0 & 0 & 0 & s^V_{YZXY} & s^V_{XZXY} & s^V_{XYXY} \end{bmatrix}_A \begin{Bmatrix} T_{XX} \\ T_{YY} \\ T_{ZZ} \\ T_{YZ} \\ T_{XZ} \\ T_{XY} \end{Bmatrix}_A + \begin{Bmatrix} \Gamma_{XX} \\ \Gamma_{YY} \\ \Gamma_{ZZ} \\ 0 \\ 0 \\ 0 \end{Bmatrix}_A V \tag{B.28}$$

The same symmetry argument holds true for a single fiber, and therefore extension and shearing will also be decoupled in Equation B.26.

In the active area, the materials are symmetric in the X, Y, and Z and balanced in the Z direction, however the principal axes for the materials are not aligned with the X, Y, Z directions for all the materials. As mentioned in Section 3.4 the *3* direction for the fiber varies from the Y direction under the electrodes to the Z direction between the electrodes. This indicates that shearing in one direction may not be decoupled with the other directions locally. However, if one considers many electrode fingers and fibers in the active area, the polarization direction appears to be primarily in the direction of the fibers, and therefore small variations in the polarization direction cancel themselves out,[154] and thus:

$$\left(s^V_{YZXZ}\right)_A = \left(s^V_{YZXY}\right)_A = \left(s^V_{XZXY}\right)_A = 0 \tag{B.29}$$

Therefore, Equation B.28 can be written as:

$$\begin{Bmatrix} S_{XX} \\ S_{YY} \\ S_{ZZ} \\ S_{YZ} \\ S_{XZ} \\ S_{XY} \end{Bmatrix}_A = \begin{bmatrix} s^V_{XX} & s^V_{XY} & s^V_{XZ} & 0 & 0 & 0 \\ s^V_{XY} & s^V_{YY} & s^V_{YZ} & 0 & 0 & 0 \\ s^V_{XZ} & s^V_{YZ} & s^V_{ZZ} & 0 & 0 & 0 \\ 0 & 0 & 0 & s^V_{YZ} & 0 & 0 \\ 0 & 0 & 0 & 0 & s^V_{XZ} & 0 \\ 0 & 0 & 0 & 0 & 0 & s^V_{XY} \end{bmatrix}_A \begin{Bmatrix} T_{XX} \\ T_{YY} \\ T_{ZZ} \\ T_{YZ} \\ T_{XZ} \\ T_{XY} \end{Bmatrix}_A + \begin{Bmatrix} \Gamma_{XX} \\ \Gamma_{YY} \\ \Gamma_{ZZ} \\ 0 \\ 0 \\ 0 \end{Bmatrix}_A V \tag{B.30}$$

In Equation B.30, contracted notation is used for the compliance matrix. "Consider a composite plate comprised of a cross weave of fibers. Although the fibers run in two directions and the fibers longitudinal axis varies sinusoidaly, on a local scale shear strains may be coupled, however when the composite is viewed in its entirety as a plate the shear strains are decoupled from each other" (Reference 154).

The active area of the AFC/tmAFC is comprised of many single fibers surrounded by matrix between two electrodes. Thus, the single fiber is a representative structure for the active area. If a stress is applied uniformly over the surface of the active area, then the same stress is applied to each individual fiber, therefore:

$$(T)_A = (T)_F \tag{B.31}$$

Using the same logic, if a uniform strain is applied to the active area then the same strain is applied to each individual fiber, and therefore:

$$(S)_A = (S)_F \tag{B.32}$$

Thus, Equation B.30 gives the relation between stress, strain, and voltage for an individual fiber or the entire active area.

$$\left[s^V\right]_A = \left[s^V\right]_F \tag{B.33}$$

$$\{\Gamma\}_A = \{\Gamma\}_F \tag{B.34}$$

Consider the relationship between charge, current and voltage presented in Equations B.22 and B.24. For a single fiber

$$q_F(t) = q_F(t_0) + C_F^T V(t) + (\Phi_{xx})_F (T_{XX})_A + (\Phi_{yy})_F (T_{YY})_A + (\Phi_{zz})_F (T_{ZZ})_A + (\Phi_{yz})_F (T_{YZ})_A + (\Phi_{xz})_F (T_{XZ})_A + (\Phi_{xy})_F (T_{XY})_A + \int_{t_0}^{t} \frac{V(T)}{R_F} dT \quad \text{(B.35)}$$

$$i_F = \frac{V}{R_F} + C_F^T \frac{dV}{dt} + (\Phi_{xx})_F \left(\frac{dT_{XX}}{dt}\right)_A + (\Phi_{yy})_F \left(\frac{dT_{YY}}{dt}\right)_A + (\Phi_{zz})_F \left(\frac{dT_{ZZ}}{dt}\right)_A + (\Phi_{yz})_F \left(\frac{dT_{YZ}}{dt}\right)_A + (\Phi_{xz})_F \left(\frac{dT_{XZ}}{dt}\right)_A + (\Phi_{xy})_F \left(\frac{dT_{XY}}{dt}\right)_A \quad \text{(B.36)}$$

In a Hexagonal Crystal – Class 6 mm poled ferroelectric with the polarization direction in the *3* direction, T_4 and T_5 stresses cause changes in the electric displacements in the *1* and *2* directions. This is because shear stresses cause shear strains which rotates the polarization vector away from the *3* direction into the *1* and *2* directions. Small shear strains do not rotate the polarization vector enough to change appreciably in *3* direction and thus small shear stresses do not cause changes in D_3. In a single fiber of an AFC/tmAFC, an applied electric field always follows the *3* direction because the same electrodes are used for poling and actuation as discussed in Section 3.4. Thus, the primary source of charge on the electrodes is due to D_3 in the fibers. In addition, in the fiber volume in Figure 2.5, the electodes at $z = 0$ are at equal potential, and the fibers at $z = L$ are at equal potential, however the two potentials are different at each end of the fibers. Thus, when a shear stress rotates the polarization vector small charge could build up on the $y = h_A/2$ electrodes, however any charge on these electrodes is countered by charge on the $y = -h_A/2$ electrodes and because the top and bottom electrodes are at equal potentials, the charges cancel out. Therefore, shear stresses do not cause charge to be generated, and thus Equations B.35 and B.36 can be written as:

$$q_F(t) = q_F(t_0) + C_F^T V(t) + (\Phi_{xx})_F (T_{XX})_A + (\Phi_{yy})_F (T_{YY})_A + (\Phi_{zz})_F (T_{ZZ})_A + \int_{t_0}^{t} \frac{V(T)}{R_F} dT \quad \text{(B.37)}$$

$$i_F = \frac{V}{R_F} + C_F^T \frac{dV}{dt} + (\Phi_{xx})_F \left(\frac{dT_{XX}}{dt}\right)_A + (\Phi_{yy})_F \left(\frac{dT_{YY}}{dt}\right)_A + (\Phi_{zz})_F \left(\frac{dT_{ZZ}}{dt}\right)_A \quad \text{(B.38)}$$

When a voltage is applied, or a stress is applied, each fiber between each electrode generates change. Due to conservation of charge, these charges sum up to give the total charge generated in the active area:

$$q_A = \sum_{i=1}^{N_{Fingers}-1} \sum_{j}^{N_{Fibers}} q_F(i,j) \quad \text{(B.39)}$$

$$i_A = \sum_{i=1}^{N_{Fingers}-1} \sum_{j=1}^{N_{Fibers}} i_F(i,j) \tag{B.40}$$

For uniform stresses, strains, and voltages, the charge and current generated by each fiber is the same, thus:

$$q_A(t) = (N_{Fingers}-1)(N_{Fibers}) q_F(t) \tag{B.41}$$

$$q_A(t) = q_A(t_0) + C_A^T V(t) + (\Phi_{XX})_A (T_{XX})_A + (\Phi_{YY})_A (T_{YY})_A + (\Phi_{ZZ})_A (T_{ZZ})_A + \int_{t_0}^{t} \frac{V(T)}{R_A} dT \tag{B.42}$$

$$i_A(t) = (N_{Fingers}-1)(N_{Fibers}) i_F(t) \tag{B.43}$$

$$i_A = \frac{V}{R_A} + C_A^T \frac{dV}{dt} + (\Phi_{XX})_A \left(\frac{dT_{XX}}{dt}\right)_A + (\Phi_{YY})_A \left(\frac{dT_{YY}}{dt}\right)_A + (\Phi_{ZZ})_A \left(\frac{dT_{ZZ}}{dt}\right)_A \tag{B.44}$$

Where:

$$C_A^T = N_{Fibers}(N_{Fingers}-1) C_F^T \tag{B.45}$$

$$R_A = \frac{R_F}{N_{Fibers}(N_{Fingers}-1)} \tag{B.46}$$

$$(\Phi_{XX})_A = N_{Fibers}(N_{Fingers}-1)(\Phi_{xx})_F \tag{B.47}$$

$$(\Phi_{YY})_A = N_{Fibers}(N_{Fingers}-1)(\Phi_{yy})_F \tag{B.48}$$

$$(\Phi_{ZZ})_A = N_{Fibers}(N_{Fingers}-1)(\Phi_{zz})_F \tag{B.49}$$

The Young's modulus will be indicated by the variable Y. At constant voltage the Young's modulus can be calculated from:

$$Y_{XX}^V = \frac{1}{s_{XX}^V} \qquad Y_{YY}^V = \frac{1}{s_{YY}^V} \qquad Y_{ZZ}^V = \frac{1}{s_{ZZ}^V} \tag{B.50}$$

The extension strains and stresses in Equation B.30 can be written as:

$$\begin{Bmatrix} S_{XX} \\ S_{YY} \\ S_{ZZ} \end{Bmatrix}_A = \begin{bmatrix} \frac{1}{Y_{XX}^V} & -\frac{\sigma_{XY}^V}{Y_{XX}^V} & -\frac{\sigma_{XZ}^V}{Y_{XX}^V} \\ -\frac{\sigma_{YX}^V}{Y_{YY}^V} & \frac{1}{Y_{YY}^V} & -\frac{\sigma_{YZ}^V}{Y_{YY}^V} \\ -\frac{\sigma_{ZX}^V}{Y_{ZZ}^V} & -\frac{\sigma_{ZY}^V}{Y_{ZZ}^V} & \frac{1}{Y_{ZZ}^V} \end{bmatrix}_A \begin{Bmatrix} T_{XX} \\ T_{YY} \\ T_{ZZ} \end{Bmatrix}_A + \begin{Bmatrix} \Gamma_{XX} \\ \Gamma_{YY} \\ \Gamma_{ZZ} \end{Bmatrix}_A V \tag{B.51}$$

Where σ^V is the Poisson ratio under a shorted condition. It should be noted that the matrix in Equation B.51 is symmetric and thus:

$$\left(\frac{\sigma_{ij}^{V}}{Y_{ii}^{V}}\right)_A = \left(\frac{\sigma_{ji}^{V}}{Y_{jj}^{V}}\right)_A \qquad i,j = X,Y,Z \qquad i \neq j \tag{B.52}$$

Equation B.30 can also be written in the form of Equation 3.48:

$$\{T\}_A = \left[c^V\right]_A \{S\}_A - \{\psi\}_A V \tag{B.53}$$

$$\begin{Bmatrix} T_{XX} \\ T_{YY} \\ T_{ZZ} \\ T_{YZ} \\ T_{XZ} \\ T_{XY} \end{Bmatrix}_A = \begin{bmatrix} c_{XX}^V & c_{XY}^V & c_{XZ}^V & 0 & 0 & 0 \\ c_{XY}^V & c_{YY}^V & c_{YZ}^V & 0 & 0 & 0 \\ c_{XZ}^V & c_{YZ}^V & c_{ZZ}^V & 0 & 0 & 0 \\ 0 & 0 & 0 & c_{YZ}^V & 0 & 0 \\ 0 & 0 & 0 & 0 & c_{XZ}^V & 0 \\ 0 & 0 & 0 & 0 & 0 & c_{XY}^V \end{bmatrix}_A \begin{Bmatrix} S_{XX} \\ S_{YY} \\ S_{ZZ} \\ S_{YZ} \\ S_{XZ} \\ S_{XY} \end{Bmatrix}_A - \begin{Bmatrix} \Psi_{XX} \\ \Psi_{YY} \\ \Psi_{ZZ} \\ 0 \\ 0 \\ 0 \end{Bmatrix}_A V \tag{B.54}$$

Where c^V is the stiffness under a shorted condition, and ψ is a piezoelectric "stress" term where:

$$\left[c^V\right]_A = \left[s^V\right]_A^{-1} \tag{B.55}$$

$$\{\Psi\}_A = \left[s^V\right]_A^{-1} \{\Gamma\}_A \tag{B.56}$$

The values for ψ can be determined using Equation B.55 from:

$$\begin{aligned}
(\psi_{XX})_A &= \left(\frac{+\Gamma_{XX}\left(s_{YY}^V s_{ZZ}^V - \left(s_{YZ}^V\right)^2\right) - \Gamma_{YY}\left(s_{ZZ}^V s_{XY}^V - s_{XZ}^V s_{YZ}^V\right) - \Gamma_{ZZ}\left(s_{YY}^V s_{XZ}^V - s_{XY}^V s_{YZ}^V\right)}{s_{XX}^V s_{YY}^V s_{ZZ}^V + 2 s_{YZ}^V s_{XZ}^V s_{XY}^V - s_{XX}^V \left(s_{YZ}^V\right)^2 - s_{YY}^V \left(s_{XZ}^V\right)^2 - s_{ZZ}^V \left(s_{XY}^V\right)^2} \right)_A \\
(\psi_{YY})_A &= \left(\frac{-\Gamma_{XX}\left(s_{ZZ}^V s_{XY}^V - s_{XZ}^V s_{YZ}^V\right) + \Gamma_{YY}\left(s_{XX}^V s_{ZZ}^V - \left(s_{XZ}^V\right)^2\right) - \Gamma_{ZZ}\left(s_{XX}^V s_{YZ}^V - s_{XY}^V s_{XZ}^V\right)}{s_{XX}^V s_{YY}^V s_{ZZ}^V + 2 s_{YZ}^V s_{XZ}^V s_{XY}^V - s_{XX}^V \left(s_{YZ}^V\right)^2 - s_{YY}^V \left(s_{XZ}^V\right)^2 - s_{ZZ}^V \left(s_{XY}^V\right)^2} \right)_A \\
(\psi_{ZZ})_A &= \left(\frac{-\Gamma_{XX}\left(s_{YY}^V s_{XZ}^V - s_{XY}^V s_{YZ}^V\right) - \Gamma_{YY}\left(s_{XX}^V s_{YZ}^V - s_{XY}^V s_{XZ}^V\right) + \Gamma_{ZZ}\left(s_{XX}^V s_{YY}^V - \left(s_{XY}^V\right)^2\right)}{s_{XX}^V s_{YY}^V s_{ZZ}^V + 2 s_{YZ}^V s_{XZ}^V s_{XY}^V - s_{XX}^V \left(s_{YZ}^V\right)^2 - s_{YY}^V \left(s_{XZ}^V\right)^2 - s_{ZZ}^V \left(s_{XY}^V\right)^2} \right)_A \\
(\psi_{YZ})_A &= (\psi_{XZ})_A = (\psi_{XY})_A = 0
\end{aligned} \tag{B.57}$$

Inserting Equation B.55 into Equation B.42 yields:

$$q_A(t) = q_A(t_0) + C_A^S V(t) + \lfloor \Lambda \rfloor_A \{S\}_A + \int_{t_0}^{t} \frac{V(T)}{R_A} dT \tag{B.58}$$

Where:

$$C_A^S = C_A^T - \lfloor \Phi \rfloor_A \{\psi\}_A \tag{B.59}$$

$$\{\Lambda\}_A = \left[c^V\right]_A \{\Phi\}_A \tag{B.60}$$

Inserting Equation B.55 into Equation B.44 yields

$$i_A = \frac{V}{R} + C_A^S \frac{dV}{dt} + \lfloor \Lambda \rfloor_A \left\{ \frac{dS}{dt} \right\}_A \tag{B.61}$$

Where C^S is the strain free capacitance, and Λ is a piezoelectric constant. Equations B.58 and B.61 are useful when determining the charge and the current for an actuator that is blocked.

The constitutive relations for the active area of an AFC/tmAFC are reprinted in the following Equations:

$$\{S\}_A = \left[s^V \right]_A \{T\}_A + \{\Gamma\}_A V \tag{B.62}$$

$$q_A(t) = q_A(t_0) + C_A^T V(t) + \lfloor \Phi \rfloor_A \{T\}_A + \int_{t_0}^{t} \frac{V(T)}{R_A} dT \tag{B.63}$$

$$i_A = \frac{V}{R_A} + C_A^T \frac{dV}{dt} + \lfloor \Phi \rfloor_A \left\{ \frac{dT}{dt} \right\}_A \tag{B.64}$$

$$\{T\}_A = \left[c^V \right]_A \{S\}_A - \{\psi\}_A V \tag{B.65}$$

$$q_A(t) = q_A(t_0) + C_A^S V(t) + \lfloor \Lambda \rfloor_A \{S\}_A + \int_{t_0}^{t} \frac{V(T)}{R_A} dT \tag{B.66}$$

$$i_A = \frac{V}{R_A} + C_A^S \frac{dV}{dt} + \lfloor \Lambda \rfloor_A \left\{ \frac{dS}{dt} \right\}_A \tag{B.67}$$

Where:

$$\left[c^V \right]_A = \left[s^V \right]_A^{-1} \tag{B.68}$$

$$\{\Psi\}_A = \left[c^V \right]_A \{\Gamma\}_A \tag{B.69}$$

$$C_A^S = C_A^T - \lfloor \Phi \rfloor_A \{\psi\}_A \tag{B.70}$$

$$\{\Lambda\}_A = \left[c^V \right]_A \{\Phi\}_A \tag{B.71}$$

and

$$\left[s^V \right]_A = \begin{bmatrix} s_{XX}^V & s_{XY}^V & s_{XZ}^V & 0 & 0 & 0 \\ s_{XY}^V & s_{YY}^V & s_{YZ}^V & 0 & 0 & 0 \\ s_{XZ}^V & s_{YZ}^V & s_{ZZ}^V & 0 & 0 & 0 \\ 0 & 0 & 0 & s_{YZ}^V & 0 & 0 \\ 0 & 0 & 0 & 0 & s_{XZ}^V & 0 \\ 0 & 0 & 0 & 0 & 0 & s_{XY}^V \end{bmatrix}_A \tag{B.72}$$

$$\lfloor \Gamma \rfloor_A = \lfloor \Gamma_{XX} \quad \Gamma_{YY} \quad \Gamma_{ZZ} \quad 0 \quad 0 \quad 0 \rfloor_A \tag{B.73}$$

$$\lfloor \Phi \rfloor_A = \lfloor \Phi_{XX} \quad \Phi_{YY} \quad \Phi_{ZZ} \quad 0 \quad 0 \quad 0 \rfloor_A \tag{B.74}$$

For a single fiber the constitutive relations are similar to Equations B.62 - B.67:

$$\{S\}_F = \left[s^V\right]_F \{T\}_F + \{\Gamma\}_F V \tag{B.75}$$

$$q_F(t) = q_F(t_0) + C_F^T V(t) + \lfloor \Phi \rfloor_F \{T\}_F + \int_{t_0}^{t} \frac{V(T)}{R_F} dT \tag{B.76}$$

$$i_F = \frac{V}{R_F} + C_F^T \frac{dV}{dt} + \lfloor \Phi \rfloor_F \left\{\frac{dT}{dt}\right\}_F \tag{B.77}$$

$$\{T\}_F = \left[c^V\right]_F \{S\}_F - \{\psi\}_F V \tag{B.78}$$

$$q_F(t) = q_F(t_0) + C_F^S V(t) + \lfloor \Lambda \rfloor_F \{S\}_F + \int_{t_0}^{t} \frac{V(T)}{R_F} dT \tag{B.79}$$

$$i_F = \frac{V}{R_F} + C_F^S \frac{dV}{dt} + \lfloor \Lambda \rfloor_F \left\{\frac{dS}{dt}\right\}_F \tag{B.80}$$

where:

$$(T)_A = (T)_F \tag{B.81}$$

$$(S)_A = (S)_F \tag{B.82}$$

$$q_A(t) = \left(N_{Fingers} - 1\right)\left(N_{Fibers}\right) q_F(t) \tag{B.83}$$

$$i_A(t) = \left(N_{Fingers} - 1\right)\left(N_{Fibers}\right) i_F(t) \tag{B.84}$$

$$\left[s^V\right]_A = \left[s^V\right]_F \tag{B.85}$$

$$\{\Gamma\}_A = \{\Gamma\}_F \tag{B.86}$$

$$\left[c^V\right]_A = \left[c^V\right]_F \tag{B.87}$$

$$\{\Psi\}_A = \{\Psi\}_F \tag{B.88}$$

$$C_A^T = N_{Fibers}\left(N_{Fingers} - 1\right) C_F^T \tag{B.89}$$

$$C_A^S = N_{Fibers}\left(N_{Fingers} - 1\right) C_F^S \tag{B.90}$$

$$R_A = \frac{R_F}{N_{Fibers}\left(N_{Fingers} - 1\right)} \tag{B.91}$$

$$\{\Phi\}_A = N_{Fibers}\left(N_{Fingers} - 1\right)\{\Phi\}_F \tag{B.92}$$

$$\{\Lambda\}_A = N_{Fibers}\left(N_{Fingers} - 1\right)\{\Lambda\}_F \tag{B.93}$$

$$C_F^S = C_F^T - \lfloor \Phi \rfloor_F \{\psi\}_F \tag{B.94}$$

The constitutive relations for an entire AFC/tmAFC should be similar to Equations B.62 - B.74, however the constitutive relations are dependant on the materials that exist outside of the active area, and the configuration of the electrodes. If the materials, geometry, and electrodes of the passive region of the AFC/tmAFC are symmetric about the *X* axis, *Y* axis, and *Z* axis the constitutive relations will be of the same form as the active area. If the materials, geometry, or electrodes are not symmetric then it is possible that extension-shear coupling, shear-shear coupling, or charge-shear coupling can occur. It

should also be noted that the material properties measured using the active area will be different from those measured for the entire AFC/tmAFC. This is because in the AFC/tmAFC fringing of the electric field occurs in the passive region between electrodes, and the stiffness of the passive region restrains the actuation of the active area somewhat. For all the AFCs and tmAFCs analyzed, fringing is neglected, and the amount of restraint due to the stiffness is approximated using the rule of mixtures, which is presented in Appendix III. Thus in this body of work, it is assumed that the constitutive relations for the AFCs/tmAFCs is of the same form as Equations B.62 - B.74.

Appendix III. Rule of Mixtures for Active Materials

III.1 Introduction

Often times in structural analysis, an engineer is presented with the material properties for components of a composite material and asked to determine the material properties for the composites. Short of finite element modeling, there exists no method for determine the exact properties of the composite, however there are many approximate methods. One of the simplest methods that can be used to estimate the composite bulk properties from the material properties of the fibers and matrix is to use the Rule of Mixtures.[63]

Consider a composite laminate composed of N materials with the X, Y and Z axes centered on the composite. Let the dimensions in the X, Y, and Z direction (thickness, width, and length) of the composite be W, b, L respectively as shown in Figure III.1. The location of each material is independent of Z. Let us assume that the materials are symmetric across the X-Z and Y-Z planes and the $Z = \pm L / 2$ faces of the composite are electoded. Each material i has a cross sectional area of A_i in the X-Y plane.

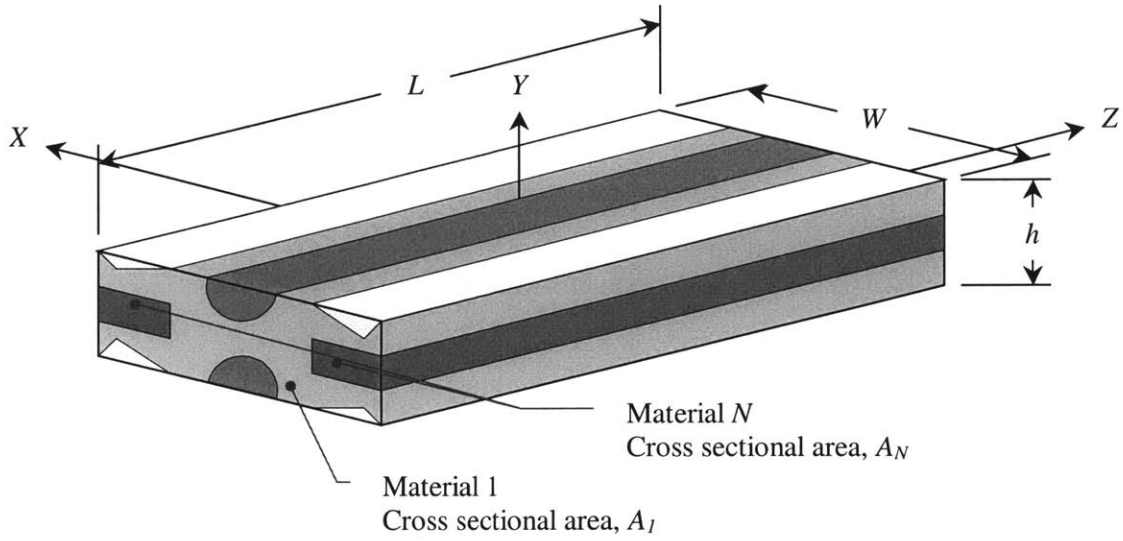

Figure III.1 Illustration of Composite Laminate Analyzed using the Rule of Mixtures

The deformation in the X, Y, and Z directions is labeled u, v, and w respectively. Each material in the composite can be piezoelectric or non-piezoelectric and each material is assumed to have no conductivity. The constitutive relations for each material i in engineering matrix form (see Equation 1.5) are given by:

$$\begin{aligned} \{E\}_i &= \left[\beta^T\right]_i \{D\}_i - [g]_i \{T\}_i \\ \{S\}_i &= [g]_{t,i} \{D\}_i + \left[s^D\right]_i \{T\}_i \end{aligned} \tag{C.1}$$

Where the i subscript indicates that the material property is for material i and the t subscript indicates the matrix is transposed. For non-piezoelectric materials $[g]_i = 0$. Let us assume that the 3 axes for each material is aligned with the Z axes of the composite, and that each material is either isotropic, or transversely isotropic with the axes of isotropy in the 3 direction. Thus if one of the materials is for example a Hexagonal Crystal – Class 6 mm poled ferroelectric then the polarization direction is also in the 3 direction and its constitutive relations are given by:

$$\begin{Bmatrix} E_1 \\ E_2 \\ E_3 \\ \hline S_1 \\ S_2 \\ S_3 \\ S_4 \\ S_5 \\ S_6 \end{Bmatrix} = \left[\begin{array}{ccc:ccc:ccc} \beta_{11}^T & 0 & 0 & 0 & 0 & 0 & 0 & -g_{15} & 0 \\ 0 & \beta_{11}^T & 0 & 0 & 0 & 0 & -g_{15} & 0 & 0 \\ 0 & 0 & \beta_{33}^T & -g_{31} & -g_{31} & -g_{33} & 0 & 0 & 0 \\ \hdashline 0 & 0 & g_{31} & s_{11}^D & s_{12}^D & s_{13}^D & 0 & 0 & 0 \\ 0 & 0 & g_{31} & s_{12}^D & s_{11}^D & s_{13}^D & 0 & 0 & 0 \\ 0 & 0 & g_{33} & s_{13}^D & s_{13}^D & s_{33}^D & 0 & 0 & 0 \\ 0 & g_{15} & 0 & 0 & 0 & 0 & s_{44}^D & 0 & 0 \\ g_{15} & 0 & 0 & 0 & 0 & 0 & 0 & s_{44}^D & 0 \\ 0 & 0 & 0 & 0 & 0 & 0 & 0 & 0 & s_{66}^D \end{array}\right] \begin{Bmatrix} D_1 \\ D_2 \\ D_3 \\ \hline T_1 \\ T_2 \\ T_3 \\ T_4 \\ T_5 \\ T_6 \end{Bmatrix} \quad \text{(C.2)}$$

For the purposes of the following calculations all of the values in equations C.1 and C.2 will be assumed to be measured at low fields and at low strains. Let us make the following assumptions:

1. The composite is very thin in the X and Y directions relative to the Z direction. ($h << L$, $W<<L$) and thus the Z direction can be considered infinite relative to the other directions.

2. Assume that no body forces are applied to the composite, and that deformations will be quasi-static.

3. Let us assume that any forces applied to the composite are applied in the 3 direction and will be only applied at the $Z = \pm L / 2$ ends.

4. Assume that any voltages will be applied at the $Z = \pm L / 2$ ends.

5. Assume that there are no applied charges on the X-Z and Y-Z faces.

6. Assume that the materials are perfectly bonded together.

From assumption 3 we can assume that there will be no inertial forces and thus mass times acceleration terms will be neglected when summing forces. From assumptions 1-5, if we make a cut anywhere in the X-Y direction the fields, stresses and strains must be the same if we cut the composite anywhere else in the X-Y direction. Thus, E, D, S, and T are independent of Z.

Let us make four further assumptions

7. Because the composite is so thin, assumption 1, it is assumed that the stresses in the *1* and *2* directions in all materials are zero, thus:

$$(T_1)_i = (T_2)_i = 0 \tag{C.3}$$

8. Because of assumptions 1 and 5 let us assume that the electric displacement in the *1* and *2* directions in each material is zero:

$$(D_1)_i = (D_2)_i = 0 \tag{C.4}$$

9. Because of the above assumptions, the fact that the materials are symmetric through the thickness of the composite and the above constitutive relations, the composite globally will not undergo bending or shearing. Since we are not looking for great accuracy in the stresses in each material let us assume that no shearing will occur in the individual materials and thus the stress, strain, electric displacement, and electric field are functions only of Z and time, t.

The constitutive relations for each material reduces to:

$$\begin{Bmatrix} E_3(t) \\ S_3(t) \end{Bmatrix}_i = \begin{bmatrix} \beta_{33}^T & -g_{33} \\ g_{33} & s_{33}^D \end{bmatrix}_i \begin{Bmatrix} D_3(t) \\ T_3(t) \end{Bmatrix}_i \tag{C.5}$$

The strain in the *3* direction, S_3, is given by:

$$\{S_3(t)\}_i = \frac{\partial w_i(z,t)}{\partial z} \tag{C.6}$$

Where w_i is the displacement in the Z direction in material i. The electric field in the *3* direction is given by:

$$\{E_3(t)\}_i = -\frac{\partial \varphi_i(z,t)}{\partial z} \tag{C.7}$$

Where φ_i is the electric potential in the Z direction in material i. Let us assume that the independent variables of the displacement and the potential can be separated:

$$w_i(z,t) = \left[Z_w(z)T_w(t)\right]_i \tag{C.8}$$

$$\varphi_i(z,t) = \left[Z_\varphi(z)T_\varphi(t)\right]_i \tag{C.9}$$

When the composite is cut in the X-Y plane, in order for every section to have the same strain field and electric field then the following must be true:

$$w_i(z,t) = (C_1 + C_2 z)_i e^{j\omega t} \tag{C.10}$$

$$\varphi_i(z,t) = (C_3 + C_4 z)_i e^{j\omega t} \tag{C.11}$$

Where C_{1i} C_{2i}, C_{3i}, and C_{4i} are constants for material i and the displacements and potentials are assumed to be harmonic. From assumption 6, because the materials are perfectly bonded together at each point Z the displacements must be the same. Therefore:

$$w_1(z,t) = w_2(z,t) = \cdots = w_i(z,t) = \cdots = w_N(z,t) = w(z,t) \tag{C.12}$$

In order for this to be true:

$$w(z,t) = (C_1 + C_2 z)e^{j\omega t} \tag{C.13}$$

In the above equation the subscripts have been dropped. By a similar argument we can write the potential in material *i* as:

$$\varphi(z,t) = (C_3 + C_4 z)e^{j\omega t} \tag{C.14}$$

Because each material is perfectly bonded together, when the composite is strained in the *Z* direction each material must undergo the same amount of *w* deformation at every time *t*. Thus, the strain in the *3* direction for each material will be equal:

$$\{S_3(t)\}_1 = \{S_3(t)\}_2 = \cdots = \{S_3(t)\}_N = S_3(t) = C_2 e^{j\omega t} \tag{C.15}$$

By the same arguments, the electric field in the *3* direction for each material will be also be equal:

$$\{E_3(t)\}_1 = \{E_3(t)\}_2 = \cdots = \{E_3(t)\}_N = E_3(t) = -C_4 e^{j\omega t} \tag{C.16}$$

The constitutive relations, Equation C.5, for each material reduce to:

$$\begin{Bmatrix} D_3(t) \\ T_3(t) \end{Bmatrix}_i = \left(\frac{1}{s_{33}^D \beta_{33}^T + g_{33}^2} \begin{bmatrix} s_{33}^D & g_{33} \\ -g_{33} & \beta_{33}^T \end{bmatrix}_i \right) \begin{Bmatrix} E_3(t) \\ S_3(t) \end{Bmatrix} \tag{C.17}$$

These material constants can also be converted to the material constants in Equation 1.1:

$$\begin{Bmatrix} (D_3(t))_i \\ S_3(t) \end{Bmatrix} = \begin{bmatrix} \varepsilon_{33}^T & d_{33} \\ d_{33} & s_{33}^E \end{bmatrix}_i \begin{Bmatrix} E_3(t) \\ (T_3(t))_i \end{Bmatrix} \tag{C.18}$$

$$(\varepsilon_{33}^T)_i = \left(\frac{1}{\beta_{33}^T} \right)_i \qquad (d_{33})_i = \left(\frac{g_{33}}{\beta_{33}^T} \right)_i \qquad (s_{33}^E)_i = (s_{33}^D)_i + \left(\frac{(g_{33})^2}{\beta_{33}^T} \right)_i \tag{C.19}$$

$$(Y_{33}^E)_i = \frac{1}{(s_{33}^E)_i} \tag{C.20}$$

All of the values in Equation C.18 are assumed to be measured at low fields and low strains. Another constant, the coupling coefficient can be determined form the above constants:

$$(k_{33}^2)_i = \left(\frac{d_{33}^2}{\varepsilon_{33}^T s_{33}^E} \right)_i = \left(\frac{g_{33}^2}{s_{33}^D \beta_{33}^T + g_{33}^2} \right)_i \tag{C.21}$$

Thus, we can write Equation C.17 as:

$$\begin{Bmatrix} D_3(t) \\ T_3(t) \end{Bmatrix}_i = \begin{bmatrix} (1-k_{33}^2)\varepsilon_{33}^T & d_{33} Y_{33}^E \\ -d_{33} Y_{33}^E & Y_{33}^E \end{bmatrix}_i \begin{Bmatrix} E_3(t) \\ S_3(t) \end{Bmatrix} \tag{C.22}$$

Let us apply a force, *F(t)*, in the *3* direction on the $Z = \pm L / 2$ ends. Then by summing forces in the *Z* direction at $Z = L/2$:

$$F(t) - \int_{A_1} \{T_3(t)\}_1 \, dx\, dy - \int_{A_2} \{T_3(t)\}_2 \, dx\, dy - \cdots - \int_{A_N} \{T_3(t)\}_N \, dx\, dy = 0 \tag{C.23}$$

$$\sum_{i=1}^{N} A_i \{T_3(t)\}_i = F(t) \tag{C.24}$$

Inserting the constitutive relations for T from Equation C.22 into Equation C.24:

$$S_3(t) \sum_{i=1}^{N} A_i \left(Y_{33}^E\right)_i - E_3(t) \sum_{i=1}^{N} A_i \left(d_{33} Y_{33}^E\right)_i = F(t) \tag{C.25}$$

III.2 Composite under Short Circuit Condition with a Time Varying Force

Let us consider the case where the electrodes at $Z = \pm L / 2$ are shorted and a time varying force is placed on the composite. Thus, the electric field in the *3* direction is given by:

$$E_3(t) = 0 \tag{C.26}$$

Therefore, we can write:

$$S_3(t) \sum_{i=1}^{N} A_i \left(Y_{33}^E\right)_i = F(t) \tag{C.27}$$

The average applied stress in the composite is given by:

$$\left(T_3(t)\right)_{Average} = hW\, F(t) \tag{C.28}$$

Thus

$$S_3(t) = \frac{hW}{\sum_{i=1}^{N} A_i \left(Y_{33}^E\right)_i} \left(T_3(t)\right)_{Average} \tag{C.29}$$

Thus, we can write the average Young's modulus in the *3* direction under a shorted condition as:

$$\left(Y_{33}^E\right)_{Composite} = \frac{1}{hW} \sum_{i=1}^{N} A_i \left(Y_{33}^E\right)_i \tag{C.30}$$

III.3 Composite under an Open Circuit Condition with a Sinusoidal Force

Let us look as the case where the composite is placed under a sinusoidal force with an open circuit condition at the ends. The current entering the $Z = -L / 2$ electrode is given by:

$$i(t)=\oint_A\left(\frac{\partial D_3(t)}{\partial t}\right)dA=\sum_{i=1}^{N}A_i\frac{\partial\left(D_3(t)\right)_i}{\partial t}= \\ =\frac{\partial}{\partial t}\left(\sum_{i=1}^{N}A_i\left(d_{33}Y_{33}^E\right)_i S_3(t)+\sum_{i=1}^{N}A_i\left(\left(1-k_{33}^2\right)\varepsilon_{33}^T\right)_i E_3(t)\right)=0 \tag{C.31}$$

Which in the open circuit condition the current is zero. Since $S_3(t)$ and $E_3(t)$ are harmonic with frequency ω:

$$0=j\omega\left(\sum_{i=1}^{N}A_i\left(d_{33}Y_{33}^E\right)_i S_3(t)+\sum_{i=1}^{N}A_i\left(\left(1-k_{33}^2\right)\varepsilon_{33}^T\right)_i E_3(t)\right) \tag{C.32}$$

or

$$E_3(t)=-\frac{\sum_{i=1}^{N}A_i\left(d_{33}Y_{33}^E\right)_i}{\sum_{i=1}^{N}A_i\left(\left(1-k_{33}^2\right)\varepsilon_{33}^T\right)_i}S_3(t) \tag{C.33}$$

Thus, we can substitute this back into Equation C.25:

$$S_3(t)=\frac{hW\left(T_3(t)\right)_{Average}}{\left[\sum_{i=1}^{N}A_i\left(Y_{33}^E\right)_i+\frac{\left[\sum_{i=1}^{N}A_i\left(d_{33}Y_{33}^E\right)_i\right]^2}{\sum_{i=1}^{N}A_i\left(\left(1-k_{33}^2\right)\varepsilon_{33}^T\right)_i}\right]} \tag{C.34}$$

Thus, we can write the average sttiffness in the *3* direction under a open circuit condition as:

$$\left(Y_{33}^D\right)_{Composite}=\frac{\left[\sum_{i=1}^{N}A_i\left(\left(1-k_{33}^2\right)\varepsilon_{33}^T\right)_i\right]\left[\sum_{i=1}^{N}A_i\left(Y_{33}^E\right)_i\right]+\left[\sum_{i=1}^{N}A_i\left(d_{33}Y_{33}^E\right)_i\right]^2}{hW\left[\sum_{i=1}^{N}A_i\left(\left(1-k_{33}^2\right)\varepsilon_{33}^T\right)_i\right]} \tag{C.35}$$

$$\left(Y_{33}^D\right)_{Composite}=\left(Y_{33}^E\right)_{Composite}+\frac{\left[\sum_{i=1}^{N}A_i\left(d_{33}Y_{33}^E\right)_i\right]^2}{hW\left[\sum_{i=1}^{N}A_i\left(\left(1-k_{33}^2\right)\varepsilon_{33}^T\right)_i\right]} \tag{C.36}$$

III.4 Free Actuation of a Composite under a Sinusoidal Voltage

A third case of interest is the free actuation of the composite under a sinusoidal voltage applied at the $Z = \pm L / 2$ ends. Let us assume that the voltage at $Z = L / 2$ is zero and at $Z = -L / 2$ the voltage is given by:

$$\varphi\left(z=-\frac{L}{2},t\right)=V_0\,e^{j\omega t} \tag{C.37}$$

Thus, we can write the voltage in the composite as:

$$\varphi(z,t)=V_0\left(\frac{L-2z}{2L}\right)e^{j\omega t} \tag{C.38}$$

The electric field is given by:

$$E_3(t)=-\frac{\partial\varphi(z,t)}{\partial z}=\frac{V_0}{L}e^{j\omega t} \tag{C.39}$$

Thus we can write using Equation C.25:

$$F(t)=S_3(t)\sum_{i=1}^{N}A_i\left(Y_{33}^E\right)_i-\frac{V_0}{L}e^{j\omega t}\sum_{i=1}^{N}A_i\left(d_{33}\,Y_{33}^E\right)_i \tag{C.40}$$

Under free actuation no stress is applied to the composite, thus *F(t)* is zero, however there is stress internally in the composite due to the mismatch in material stiffness and properties:

$$S_3(t)=\frac{V_0}{L}e^{j\omega t}\frac{\sum_{i=1}^{N}A_i\left(d_{33}\,Y_{33}^E\right)_i}{\sum_{i=1}^{N}A_i\left(Y_{33}^E\right)_i}=\frac{\sum_{i=1}^{N}A_i\left(d_{33}\,Y_{33}^E\right)_i}{\sum_{i=1}^{N}A_i\left(Y_{33}^E\right)_i}E_3(t) \tag{C.41}$$

Appendix IV. Power Absorbed by an AFC/tmAFC for Low Electric Fields

IV.1 Introduction

In this Appendix, a derivation is presented for the power absorbed by an AFC/tmAFC for low electric fields. The purpose of this Appendix is two fold. First, this derivation is presented to highlight the electrical behavior of the AFC/tmAFC as a function of frequency. Second, the derivation is presented to explain the method of measuring capacitance of the AFC/tmAFC that differs from previous work (Reference 34 pages 159-160).

IV.2 Model of an AFC as a Complex Resistor and Complex Capacitor in Parallel

Considerer the capacitor and a resistor in parallel shown in Figure IV.1:

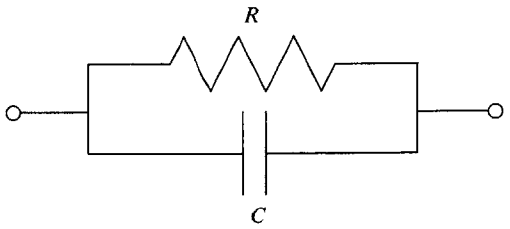

Figure IV.1 Resistor and Capacitor in Parallel

Assume that that the resistor and capacitor has both real and imaginary parts:

$$R = R_R - j R_I$$
$$C = C_R - j C_I \tag{D.1}$$

Where R is the complex resistance, C is the complex capacitance. The subscripts R and I indicate the real and imaginary portions of the value and j is the square root of -1. It is assumed that the imaginary portion of the capacitance and resistance are multiplied by a -1 to make each of the terms in Equation D.1 positive when fitted to most experimental data, as will be shown in Equation D.9. As mentioned in Section 2.3.4, a specimen can have a complex capacitance if the permittivity of the material can be modeled as a complex number. Although not mentioned extensively in literature, a specimen can have a complex resistance if the conductivity of the material is complex.[155] Furthermore, "there is nothing in nature to preclude the existence of a complex conductivity".[156]

The definition of the admittance, Y, is given by:

$$Y = G + j B \tag{D.2}$$

Where G is the conductance and B is the susceptance. For a material that can be modeled as a resistor and capacitor in parallel, the admittance is given by:

$$Y = \frac{1}{R} + j \omega C \tag{D.3}$$

Where ω is the radial frequency. Inserting Equation D.1 into Equation D.3, the admittance is given by:

$$Y = \frac{R_R}{\left(R_R^{\,2} + R_I^{\,2}\right)} + \omega C_I + j\left(\frac{R_I}{\left(R_R^{\,2} + R_I^{\,2}\right)} + \omega C_R\right) \tag{D.4}$$

There are several things to notice about the admittance in Equation D.4. Both the real and the imaginary parts are linear with frequency. In addition, both the real and imaginary parts of the admittance are non-zero at $\omega = 0$. AFC B40 manufactured by CP, was placed in a HP-4192a impedance analyzer (Reference 128) and the admittance versus frequency was measured, as shown in Figure IV.2.

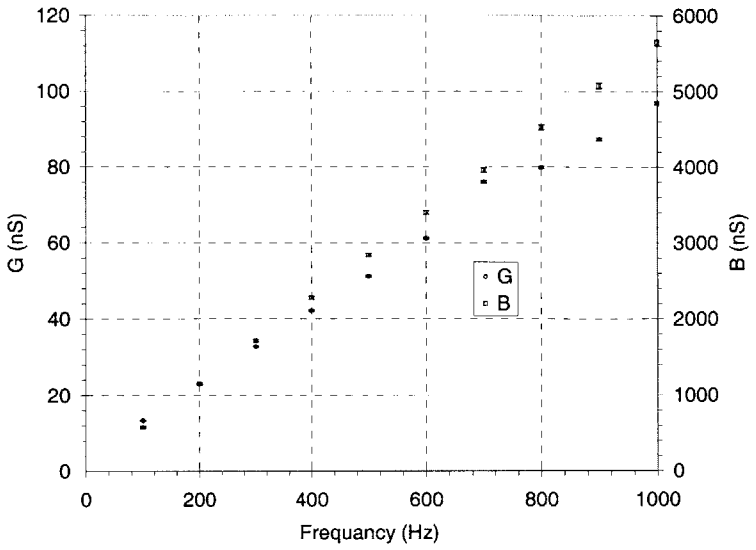

Figure IV.2 Admittance and Error Bars versus Frequency for AFC B40 Manufactured by CP

G and *B* for low frequencies up to about 700 Hz. are both linear with respect to frequency and both appear to have a small but non-zero intercept. At about 700 Hz. it appears that a resonance occurs in the AFC that seems to affect the conductance but not the susceptance. For the data in Figure IV.2 and the following figures, 256 measurements were taken at each data point and averaged, and the integration time on the HP-4192a was set to "LONG". Increasing the number of measurements averaged increases the precision of the measurement. Also increasing the integration time from "SHORT" to "MEDIUM" to "LONG" increases the precision of the measurement. An rms voltage of 0.5 Volts was used for all measurements, unless noted. Increasing the rms voltage, from 0.5 to the maximum of 1 V_{RMS} for the HP-4192a, does not change the data significantly. However, a large applied voltage allows for a large current signal, making it easier for the HP-4192a to measure. For frequencies below 1 kHz, open-short compensation only slightly changes the measured quantities. However, as frequency is increased open-short compensation becomes necessary.

The error bars in Figure IV.2 is the measurement accuracy calculated for both *G* and *B* using the equations given in Reference.[157] These Equations are for an integration time of "MEDIUM", and greater than four sample averages, and an voltage level of 1 Volt rms. These measurements were performed for a longer time with significantly more averages so that the actual measurement accuracy error in both *G* and *B* should be less.

For the AFC, for low voltages we can write:

$$G^{AFC} = \frac{R_R^{AFC}}{\left(R_R^{AFC^2} + R_I^{AFC^2}\right)} + \omega C_I^{AFC}$$
$$B^{AFC} = \frac{R_I^{AFC}}{\left(R_R^{AFC^2} + R_I^{AFC^2}\right)} + \omega C_R^{AFC} \tag{D.5}$$

The impedance, Z is defined as:

$$Z = \frac{1}{Y} = R + jX \tag{D.6}$$

Where R is the resistance and X is the reactance. The resistance and the reactance for the AFC is then given by:

$$R^{AFC} = \frac{G^{AFC}}{G^{AFC^2} + B^{AFC^2}}$$
$$X^{AFC} = -\frac{B^{AFC}}{G^{AFC^2} + B^{AFC^2}} \tag{D.7}$$

Assume that two lines can be fitted to the conductance and the susceptance data:

$$G_{Fit} = G_m \omega + G_b$$
$$B_{Fit} = B_m \omega + B_b \tag{D.8}$$

Where the *FIT* subscript indicates that the data is fitted, the *m* subscript indicates the slope and *b* represents the intercept. Comparing Equation D.5 and Equation D.8 the real and imaginary resistance and capacitance can be determined from the fitted data.

$$C_R = B_m$$
$$C_I = G_m$$
$$R_R = \frac{G_b}{G_b^2 + B_b^2}$$
$$R_I = \frac{B_b}{G_b^2 + B_b^2} \tag{D.9}$$

It should be noted based upon experimental observation, G_m, B_m, G_b, and B_b are typically positive for admittance measurements of tmAFCs and AFCs. Therefore, when defining the capacitance and the resistance in Equation D.1, a negative sign was included in front of the imaginary portion of the capacitance and the resistance to make the values of R_R and R_I positive quantities.

Using above data in the 100 Hz. to 500 Hz. data range and Equation D.9, we can determine R_R, R_I, C_R, and C_I, for this AFC, as shown in Table IV.1.

Table IV.1 Complex Resistance and Complex Capacitance for AFC B40 Manufactured by CP

Quantity	Value
R_R	17.15 MΩ
R_I	62.77 MΩ
C_R	899.4 pF
C_I	51.08 pF

Using the values in Table IV.1 we can predict G and B as a function of frequency for AFC B40 Manufactured by CP.

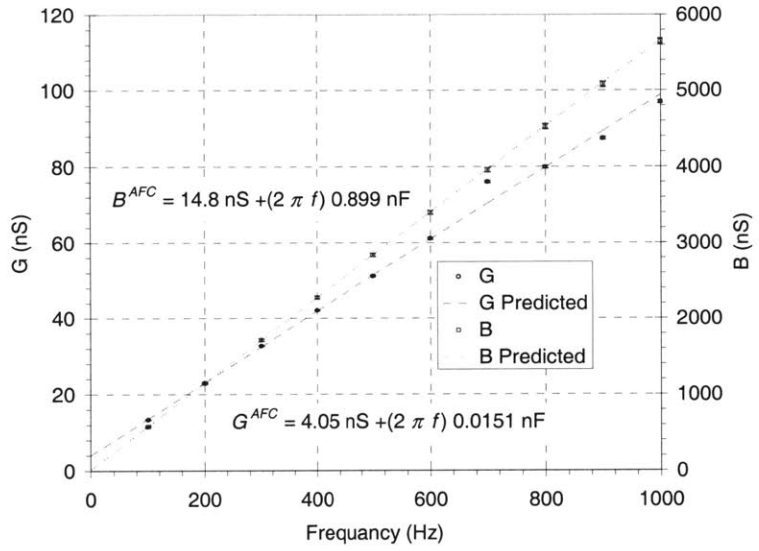

Figure IV.3 Admittance, Error Bars, and the Prediction of Admittance versus Frequency for AFC B40 Manufactured by CP for Frequencies between 100 and 1000 Hz.

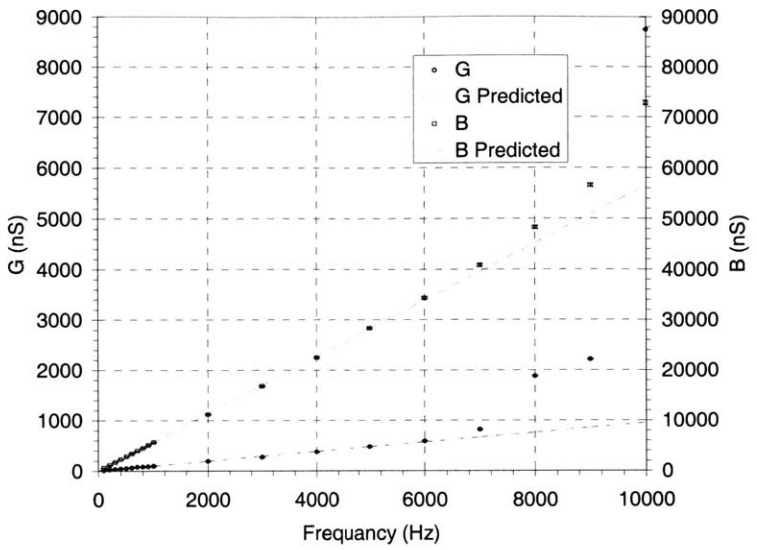

Figure IV.4 Admittance, Error Bars, and the Prediction of Admittance versus Frequency for AFC B40 Manufactured by CP for Frequencies between 100 and 10,000 Hz.

The theory that the admittance of an AFC is given by capacitor with both a real and imaginary portion and a resistor with both a real and imaginary portion in parallel predicts the response of an AFC fairly well over a large frequency range, as can be seen in Figure IV.3 and Figure IV.4. The author has seen that Equation D.5 fits the low field admittance behavior (typically below 500 Hz.) of an AFC or a tmAFC, using PZT-5A and lead free piezoelectric fibers. Equation D.5 also fits the low field admittance behavior of an MFC[48] (two specimens tested). For several tmAFCs, and one of the MFCs the intercept of the conductivity was negative. For a frequency range of 100 Hz. to 500 Hz., the R^2 value for the conductance 0.9998 and the R^2 value for the susceptance 1.0000. Although data for a CP AFC is for this example, these methods hold true for other types of AFC. Two electrical resonances occur in AFC B40, one at about 700 Hz. and one greater that 10,000 Hz. Equation D.5 appears to hold true up to about 5,000 Hz.

Another CP acturator, specimen AHZ-14, was tested in the HP-4192a impedance analyzer from a frequency of 100 Hz to 1 MHz. In order to reduce the measurement error over the entire frequency range a four-terminal pair[158] configuration was used to measure the impedance of the specimen. In order to minimize electric fields in the specimen and wiring due to surrounding equipment, the specimens were placed within an aluminum box, which was grounded to the ground of the coax cables of the instrument. Suggestions for designing the box were given in Reference 158. To minimize stray measurements between the leads of the box connected to the specimen, a ground plane was placed between the specimen separating the leads of the box and the rails of the specimen. The impedance of the box without the specimen in an open circuit condition and then in a shorted condition was measured over the desired frequency range using the same conditions used to measure the

sample to compensate for the impedance of the box. The admittance of Specimen AHZ-14 was measured using 1 V_{RMS} using the following parameters:

Table IV.2 Complex Resistance and Complex Capacitance for AFC B40 Manufactured by CP

Frequency Range	**Frequency Step Between Measured Points**	**Number of Cycles Averaged**	**Integration Time**
100 Hz to 1 kHz	100 Hz	256	Long
1 kHz to 10 kHz	100 Hz	16	Long
10 kHz to 100 kHz	500 Hz	8	Long
100 kHz to 1 MHz	5 kHz	8	Long
8 kHz to 12 kHz	10 Hz	4	Long
31 kHz to 35 kHz	10 Hz	4	Long

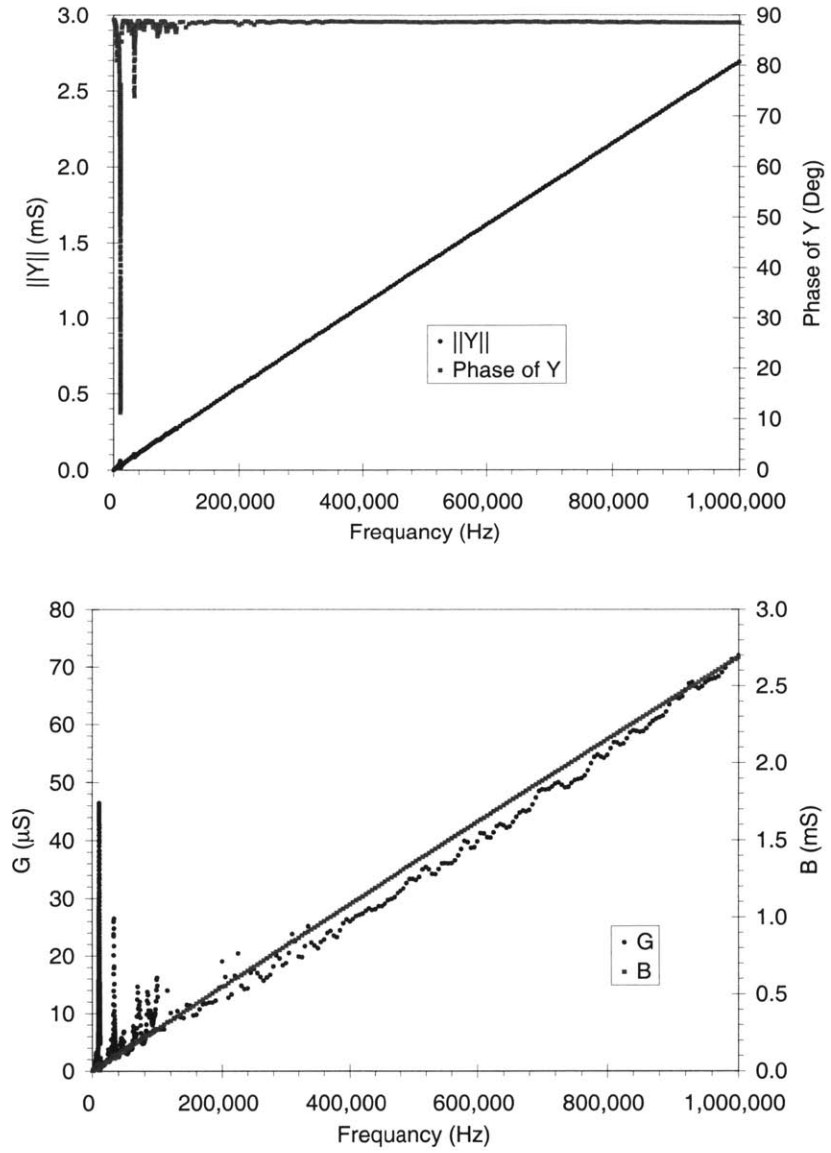

Figure IV.5 Admittance for Specimen AHR-14, Manufactured by CP, for Frequencies between 100 Hz. to 1 MHz.

In Figure IV.5 several things are evident. First it can be seen that the magnitude of the admittance appears to be linear with frequency, and phase angle is nearly constant over the entire frequency range, except at several resonance's.

In order to test the theory that the admittance of an AFC is given by capacitor with both a real and imaginary portion and a resistor with both a real and imaginary portion in parallel at frequencies below 100 Hz., specimens B40 and AHR-10 were tested in an

Schlumberger Technologies 1260 Impedance/Gain-Phase Analyzer.[159] The second AFC, also manufactured by CP, was laminated a ply of e-glass of on either side at MIT. The Schlumberger Technologies 1260 Impedance/Gain-Phase Analyzer has a frequency range of 10 μHz to 32 MHz, however the sensitivity of the impedance analyzer is drastically reduced at lower frequencies.[160]

Specimens B40 and AHR-10 were placed within the 1260 Impedance/Gain-Phase Analyzer and the impedance was measured over a frequency range of 1 Hz. to 1000 Hz. using 5 frequency steps per decade. The impedance was measured using a 3 volt amplitude signal for 1000 cycles at each frequency step, with a 50 cycle interval per frequency measurement. The admittance for specimens B40 and AHR-10 for frequencies between 1 Hz. to 1000 Hz. is shown in Figure IV.6 and Figure IV.7.

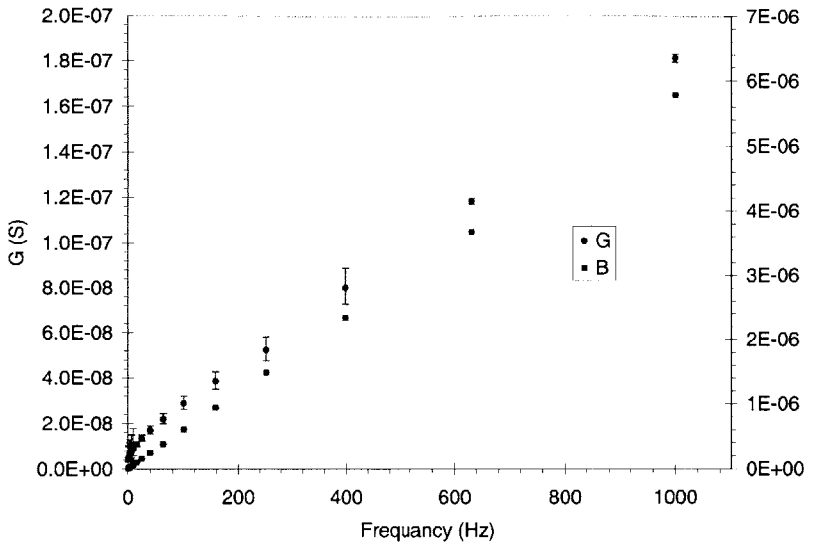

Specimen B40

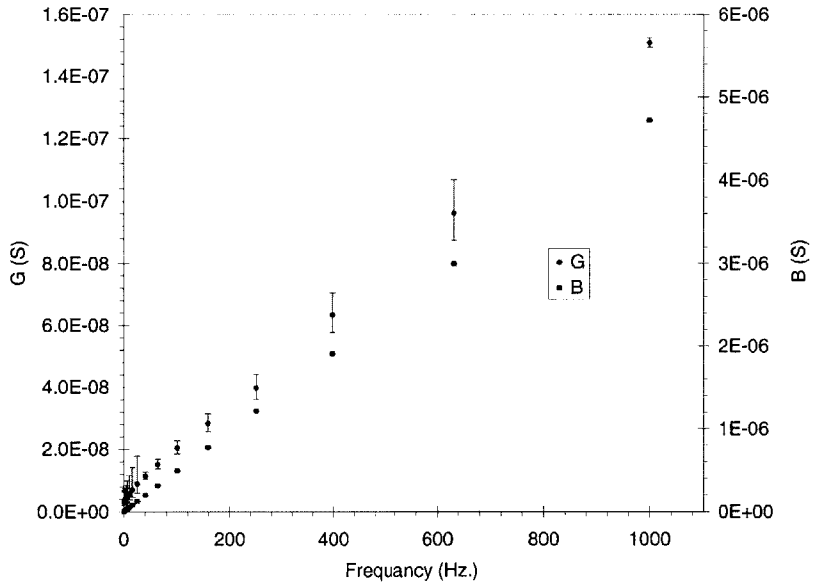

Specimen AHR-10

Figure IV.6 Admittance and Error Bars for Specimens B40 and AHR-10, Manufactured by CP, for Frequencies between 1 Hz. to 1000 Hz.

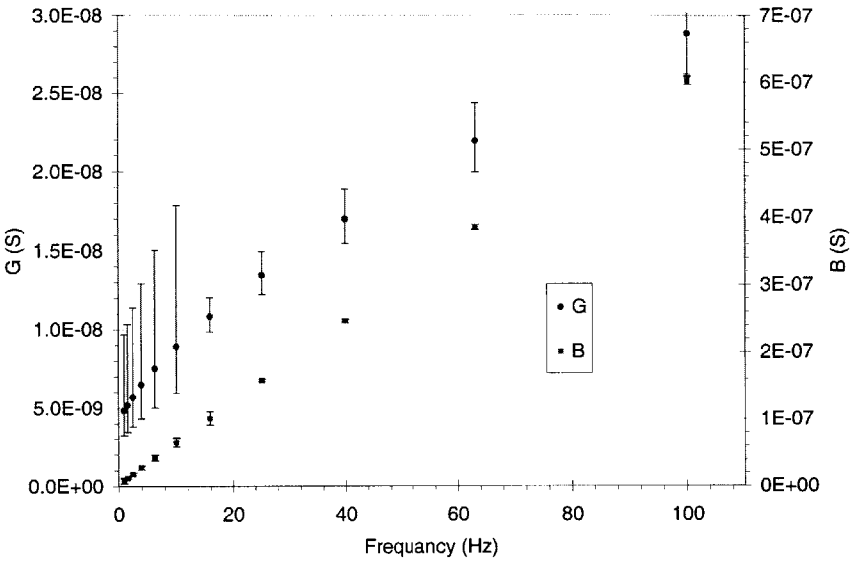

Specimen B40

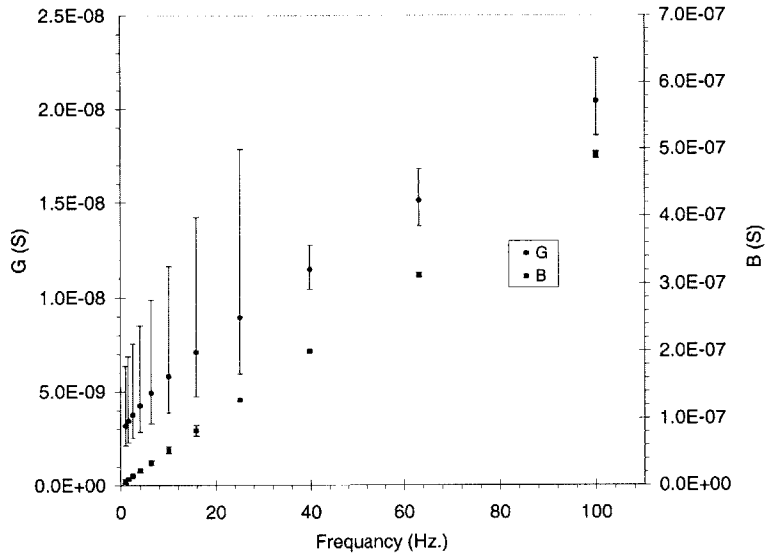

Specimen AHR-10

Figure IV.7 Admittance and Error Bars for Specimens B40 and AHR-10, Manufactured by CP, for Frequencies between 1 Hz. to 100 Hz.

Several things can be seen in Figure IV.6 and Figure IV.7. It should be noted that the data for the susceptance, *B*, for both samples is linear with respect to frequency. At a frequency of 300 Hz. internal switching of the electronics of the 1260 Impedance/Gain-Phase Analyzer occurs. This causes the values in the vicinity (about ±50 Hz.) of 300 Hz. to be in error slightly. This was confirmed by measuring the capacitance of a highly accurate 1 nF capacitor. As the frequency is reduced below about 100 Hz., the conductance, *G*, appears to deviate from the linear form, as shown above. As the frequency is reduced, the

error of the Impedance Analyzer drastically increases, as indicated by the error bars in Figure IV.6 and Figure IV.7. For example for a 1 nF capacitor, for a frequency range of about 150 Hz. to 1000 Hz. the capacitance measurement error is 0.2%, 15 Hz. to 150 Hz. the capacitance measurement error is 1%, 1.5 Hz. to 15 Hz. the capacitance measurement error is 10%, and below 1.5 Hz the error is greater than 10%[160]. Extrapolating from the errors given in a chart in 160, for a 1 nF capacitor between 0.15 Hz and 1.5 Hz the capacitance measurement error is between 50% and 100%. In the above figures, the extrapolated error for the resistance and the capacitance is graphed as 50% error. For a frequency range of 1 μHz. to 10 kHz., a resistor with a resistance between 100 kΩ and 1MΩ, the measurement error in the resistance is 0.2%, for a resistance between 1 MΩ and 10 MΩ, the measurement error in the resistance is 1%, for a resistance between 10 MΩ and 100 MΩ, the measurement error in the resistance is 10%.[160] For resistors with resistances greater than 100 MΩ, extrapolating from the errors given in a chart in 160, the measurement error is between 50% and 100%. Given the above discussion, it was assumed that the AFC can be modeled as a resistor and capacitor in parallel, and thus the error in G and B, G_{Error} and B_{Error}, could be modeled by inserting the measured values plus or minus the measurement error of the resistance and the capacitance, R_{Error} and C_{Error}, into Equation D.5, ignoring the imaginary terms.[161] The error for G and B is then given by:

$$G_{Error} = \frac{\mp R_{Error}}{R_{Measured}\left(1 \pm R_{Error}\right)} \qquad (D.10)$$

$$B_{Error} = \pm \omega C_{Measured} C_{Error}$$

In Figure IV.6 and Figure IV.7it can be seen that although the error below for the lower frequencies increases dramatically, the data forms a continuous curve. The measurement error discussed in Reference 160 might be for a single measurement. 1000 measurements were taken at each frequency, and the measurement errors may have canceled each other out.

The complex resistance measured in the above measurements is due to one or a combination of several possibilities. First, it is possible for the AFC that the conductivity of one of the materials is complex. Second, because the impedance is so large for the specimens it is possible that the measured complex resistance is due to limitations of the machine. However, open and short compensation was performed and the calculated errors were very small. Third, the polarizability of each material in the AFC/tmAFC may be separated into four different parts, electronic, ionic, orientational, and interfacial polarization with each providing a contribution to the total polarization of the material over different frequency ranges.[162] Between 100 Hz and 1 MHz it is possible that several of these polarization mechanisms dominate, however at lower frequencies at different set of polarization mechanisms dominate causing the material to appear to have what appears to be a complex resistance. Fourth, in Reference 89 an AFC is modeled as a resistor and a

capacitor in parallel which in series with a resistor and a capacitor in parallel, a series lossy capacitor. The admittance for this circuit is derived in Reference [163]. In this circuit three distinct regions exists, a mostly capacitive region for high frequencies, a mostly resistive region for low frequencies, and a transition region. For an AFC the mostly capacitive region could be less than 100 Hz, and thus using the HP Analyzer, the admittance data could appear in a linear from with both *G* and *B* with an offset, and thus the mostly resistive region and the transitions region would never be seen. This is the most likely reason for the complex resistance, however the author could neither prove nor disprove the series lossy model due to a lack of accurate equipment that could measure below 100 Hz.

IV.3 *Cp-D* Measuring of an AFC/tmAFC

In Reference 34, *Cp-D* values for AFCs are measured in the HP-4192a at 400 Hz., where *Cp* is the parallel capacitance and *D* is the dissipation factor. In this case the HP-4192a assumes that the article being measured is a capacitor in parallel with a resistor, both which only have real portions. This case is the same as the previous case except that in Equation D.5 C_I and R_I are assumed to be zero.

In order to determine how C_R and R_R are functions of *Cp* and *D* first let us look at Equations D.1, D.2 and D.3. The admittance, if it is assumed that C_I and R_I are zero, is given by:

$$Y = G + jB = \frac{1}{R_R} + j\omega C_R \tag{D.11}$$

Thus conductance and the susceptance is given by:

$$G_{AFC} = \frac{1}{R_R} \tag{D.12}$$

$$B_{AFC} = \omega C_R$$

Thus, a measurement of the admittance at any frequency gives the real resistance and the imaginary capacitance. *Cp* is equivalent to the real capacitance.

$$C_R = Cp \tag{D.13}$$

D, the dissipation factor, is defined as:

$$D = Tan(\delta) = \frac{R}{|X|} = \frac{G}{|B|} = \frac{1}{Q} \tag{D.14}$$

Where Q is the quality factor and δ is the angle between the imaginary axis and line that connects the origin to the impedance when the impedance is plotted in the complex plane as shown in Figure IV.8.

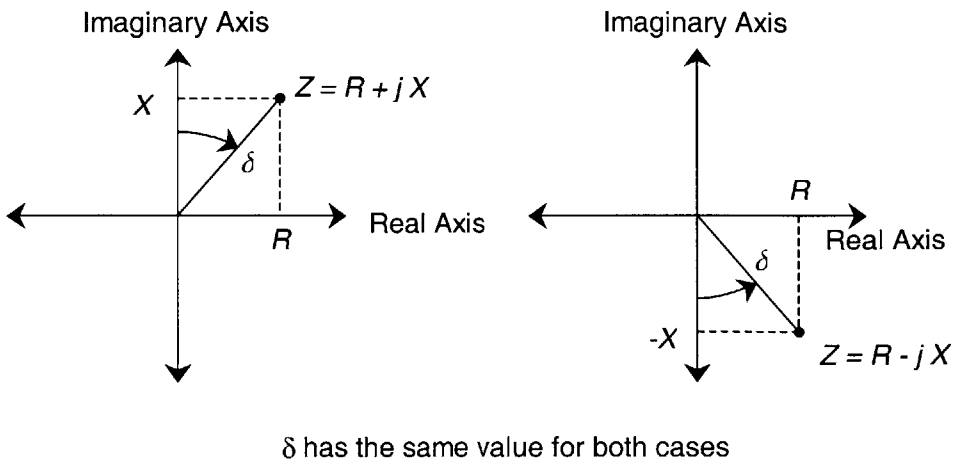

Figure IV.8 Definition of the Angle δ

Thus, the dissipation factor is given by:

$$D = \frac{R}{|X|} = \frac{1}{C_R R_R \omega} \tag{D.15}$$

Therefore, the real resistance is determined from:

$$R_R = \frac{1}{Cp\, D\, \omega} \tag{D.16}$$

Using Equation D.7 and setting R_I and C_I to zero yields.

$$R_{AFC} = \frac{R_R}{1 + C_R^2 R_R^2 \omega^2} = D\left|X_{AFC}\right| = \frac{D}{\omega Cp\left(1 + D^2\right)}$$
$$X_{AFC} = -\frac{C_R R_R^2 \omega}{1 + C_R^2 R_R^2 \omega^2} = -\frac{1}{\omega Cp\left(1 + D^2\right)} \tag{D.17}$$

The real resistance and the real capacitance was measured for AFC B40 manufactured by CP using Cp and D at 400 Hz., and the results are given in Table IV.3.

Table IV.3 Real Resistance and Real Capacitance from Cp and D at 400 Hz. for AFC B40 Manufactured by CP

Quantity	**Value**
R_R	23.74 MΩ
R_I	0
C_R	905.5 pF
C_I	0

Plotting the data in Table IV.3 versus frequency

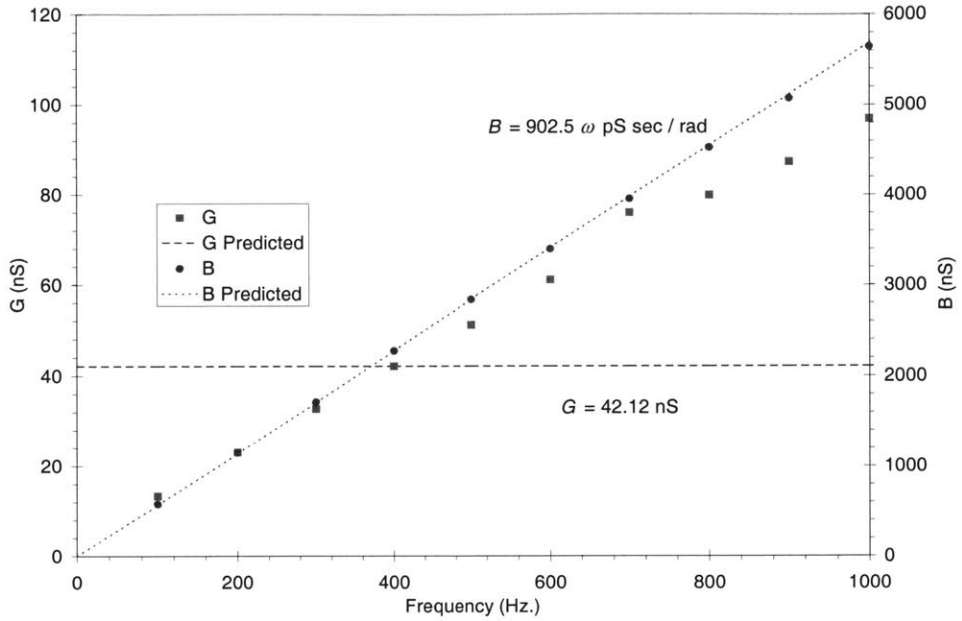

Figure IV.9 Admittance and the Prediction of Admittance using *Cp* and *D* at 400 Hz. versus Frequency for AFC B40 Manufactured by CP for Frequencies between 100 and 1000 Hz.

From Figure IV.9, we can see that measuring Cp-D for an AFC or tmAFC does not accurately predict the low field conductance of an AFC. Comparing the data in Table IV.1 and Table IV.3 we can see that the value for the capacitance differs by about 0.7% (0.7 % = 905.5/899.4 – 1) and resistance differs by about 38% (38 % = 23.74/17.15 – 1). Therefore, a single measurement of Cp-D cannot be used to adequately describe the low field behavior of an AFC/tmAFC as was done in Reference 34.

IV.4 Model of an AFC as a Real Resistor and a Complex Capacitor in Parallel

In References 4 (pages 63-74), an AFC was modeled as a complex capacitor in parallel with a real resistor. The results of this case are the same as the model of an AFC as a complex resistor and complex capacitor in parallel however R_I is zero. Setting R_I equal to zero in Equation D.5 yields:

$$G_{AFC} = \frac{1}{R_R} + \omega C_I$$
$$B_{AFC} = \omega C_R \qquad \text{(D.18)}$$

Using Equation D.18 to fitting the data for frequencies between 100 and 500 Hz. in Figure IV.2 for AFC B40 manufactured by CP yields:

Table IV.4 Real Resistance and Complex Capacitance for AFC B40 Manufactured by CP

Quantity	**Value**
R_R	246.9 MΩ
R_I	0
C_R	905.8 pF
C_I	15.1 pF

Plotting Equation D.18 using the data in Figure IV.3 yields:

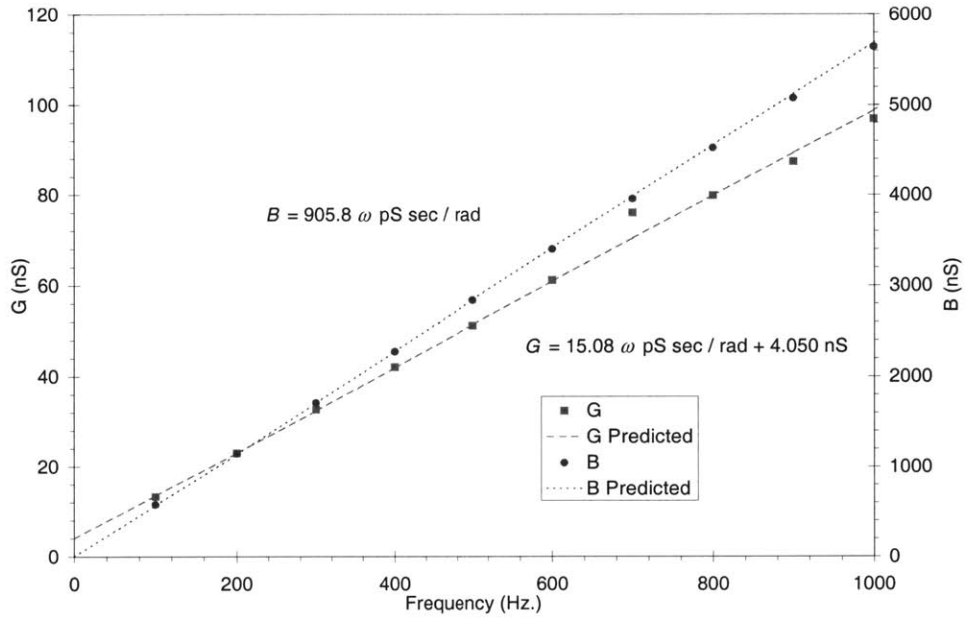

Figure IV.10 Real Resistance and Complex Capacitance versus Frequency for AFC B40 Manufactured by CP

For a frequency range of 100 to 500 Hz., the R^2 value for the conductance 0.99980 and the R^2 value for the susceptance 0.99993. The model that predicts that the AFC can be modeled as a complex capacitor in parallel with a real resistor, does yield a high R^2 for AFC B40, however it does not model other AFCs and MFCs as well. The measured resistance is 246.9 MΩ, which is nearly four time greater than the magnitude of the resistance for the model of complex resistor in parallel with the complex capacitor, in Section IV.2. In Section IV.2, the magnitude of R equals 65.07 MΩ ($= \sqrt{R_R^2 + R_I^2}$).

IV.5 Power Absorbed by an AFC/tmAFC

We can determine the power absorbed by the AFC using the circuit in Figure IV.1 and resistance and capacitance in Equation D.5. If it assumed that the voltage applied to the AFC is given by:

$$\begin{aligned} V &= V_0 Cos(\omega t) \\ V &= \mathrm{Re}\left(V_0 e^{j\omega t}\right) = V_0 \angle 0 \end{aligned} \tag{D.19}$$

Where V_0 is the amplitude of the voltage signal and not the rms amplitude. The final term in Equation D.19 is in phasor notation[164], which shall also be used in the next equation. The complex current is given by:

$$I = YV = \left(\frac{R_R}{\left(R_R{}^2 + R_I{}^2\right)} + \omega C_I + j\left(\frac{R_I}{\left(R_R{}^2 + R_I{}^2\right)} + \omega C_R \right) \right) \times \left(V_0 \angle 0\right) \tag{D.20}$$

The apparent power is defined as:

$$S = \frac{1}{2} V I^*$$

Where the star superscript represents the complex conjugate. The real average power absorbed by the AFC is given by:

$$P = \mathrm{Re}(S) = \frac{1}{2} V_0^2 \left(\frac{R_R}{R_R^2 + R_I^2} + \omega C_I \right) \tag{D.21}$$

It should be noted that P is the average of the instantaneous power, $p(t)$, over many cycles:

$$P = \lim_{n \to \infty} \frac{1}{nT} \int_{t_0}^{t_0 + nT} p(t) dt \tag{D.22}$$

Where n is the number of cycles and T is the period of the voltage. The imaginary portion of the complex power, Equation D.20, is known as the reactive power, Q, and is given by:

$$Q = \mathrm{Im}(S) = -\frac{1}{2} V_0^2 \left(\frac{R_I}{R_R^2 + R_I^2} + \omega C_R \right) \tag{D.23}$$

The magnitude of the average complex power, Equation D.20, is given by:

$$\|S\| = -\frac{1}{2} V_0^2 \sqrt{\left(\frac{R_I}{R_R^2 + R_I^2} + \omega C_R \right)^2 + \left(\frac{R_R}{R_R^2 + R_I^2} + \omega C_I \right)^2} \tag{D.24}$$

Again, Equation D.24 is not the instantaneous magnitude of the complex power, but is the average of many cycles. In Figure IV.11, the average power absorbed divided by the magnitude of the voltage squared is plotted for AFC B40:

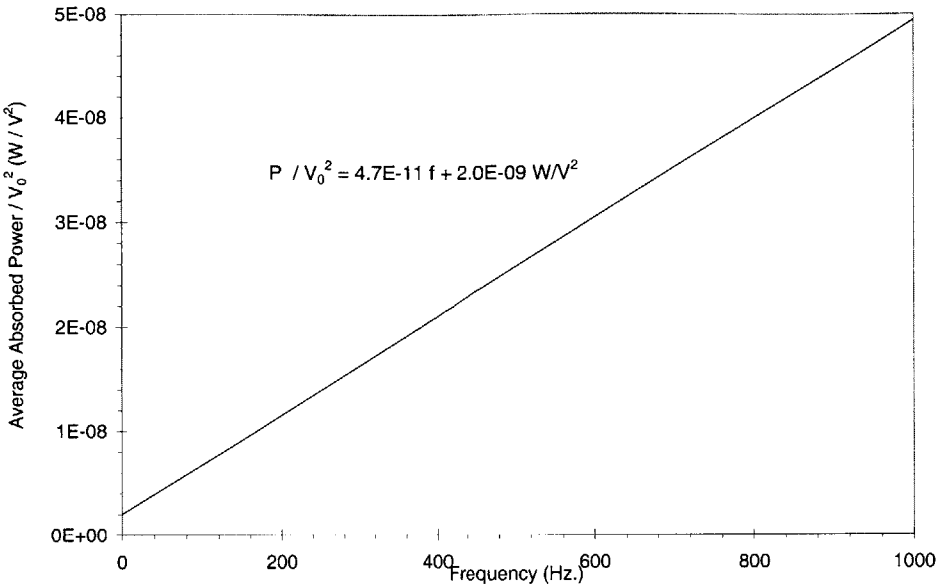

Figure IV.11 $P / (V_0)^2$ vs. Frequency for AFC B40 Specimen from CP

The above data was measured using a peak-to-peak voltage of 0.5 volts rms. When the AFC is exposed to higher fields the admittance of the AFC changes due to the fact that the material constants are a function of electric field. Therefore, the high field behavior of the AFC is not captured with this model.

7. References

[1] Jain, A. K., Sirkis, J. S., "Continuum Damage Mechanics in Piezoelectric Ceramics", Adaptive Structures and Composite Materials: Analysis and Application, ASME 1994 International Mechanical Engineering Congress and Exposition, Chicago, Illinois, Nov. 6-11, pages 47-58.

[2] Active Control eXperts Inc., Cambridge, Massachusetts.

[3] Rodgers, J.P., "Development of a Integral Twist-Actuated Rotor Blade for Individual Blade Control", Ph.D. Thesis, Massachusetts Institute of Technology, October 1998.

[4] Schmidt, M.C., "Development of Integral Actuation Technology for Composite Rotorcraft Structures", Master Thesis, Massachusetts Institute of Technology, December 2000.

[5] Sanjoon, S., "Design, Manufacturing, and Testing of an Active Twist Rotor", Master Thesis, Massachusetts Institute of Technology, 1999.

[6] Sanjoon, S., "Integral Twist Actuation of Helicopter Rotor Blades for Vibration Reduction", Ph.D. Thesis, Massachusetts Institute of Technology, August 2001.

[7] Du Plessis, A.J., "Modeling and Experimental Testing of Twist Actuated Single Cell Composite Beams for Helicopter Blade Control", Master Thesis, Massachusetts Institute of Technology, February 1996.

[8] Bingham, B.S., "Structural-Acoustic Design and Control of an Integrally Actuated Composite Panel", Master Thesis, Massachusetts Institute of Technology, 1998.

[9] Savran, C.A., "Broadband Active Structural Control Using Collocated Piezoelectric Sensors and Actuators", Master Thesis, Massachusetts Institute of Technology, 2000.

[10] Fripp, M.L., "Weighted Arrays for Modal Isolation and Active Control of Complex Structures", Ph.D. Thesis, Massachusetts Institute of Technology, June 2000.

[11] Kyung Yeol, S., "Active Control of Radiated Noise - Design and Implementation", Ph.D. Thesis, Massachusetts Institute of Technology, October 2001.

[12] K2 "Four" Ski, K2 Inc., Los Angeles, California.

[13] "Mapple Siege" Water Ski, Active Control eXperts, Cambridge, Massachusetts.

[14] "K2 Electra Series" Snowboard, K2 Inc., Los Angeles, California.

[15] "Copperhead ACX" Baseball Bats, Worth Sports, Tullahoma, Tennessee.

[16] "Smart Shock", K2 Inc., Los Angeles, California.

[17] Janos, B.Z. and Hagood, N.W., "Smart Materials and Structures Technological Feasibility and Policy Assessment", AMSL report # 00-4, Active Materials and Structures Laboratory, Massachusetts Institute of Technology, June 2000.

[18] "Standard on Piezoelectric Crystals, 1949", The Institute of Radio Engineers Inc., Proceeding of the I.R.E. (Including the WAVES and ELECTRONS Section) Volume 37 Number 12, New York, New York, 1949, pages 1378-1395.

[19] "IRE Standards on Piezoelectric Crystals-The Piezoelectric Vibrator: Definitions and Methods of Measurment, 1957", The Institute of Radio Engineers Inc., Proceeding of the I.R.E. Volume 45 Number 3, New York, New York, 1957, pages 353-358.

[20] "IRE Standards on Piezoelectric Crystals: Determination of the Elastic, Piezoelectric, and Dielectric Constants-The Electromechanical Coupling Factor, 1958", The Institute of Radio Engineers Inc., Proceeding of the IRE Volume 46 Number 4, New York, New York, 1958, pages 764-778.

[21] "IRE Standards on Piezoelectric Crystals: Measurements of Piezoelectric Ceramics, 1961", The Institute of Radio Engineers Inc., Proceeding of the IRE Volume 49 Number 7, New York, New York, 1961, pages 1161-1169.

[22] "Standard Definitions and Methods of Measurement for Piezoelectric Vibrators IEEE Std 177-1966", The Institute of Electrical and Electronics Engineers Inc., New York, New York, 1966.

[23] "IEEE Standard on Piezoelectricity ANSI/IEEE Std 176-1987", The Institute of Electrical and Electronics Engineers Inc., New York, New York, 1988.

[24] Draft 1 of "IEEE Standard on Loss in Acoustic Materials", The Institute of Electrical and Electronics Engineers Inc., New York, New York, Unpublished.

[25] "Military Standard Piezoelectric Ceramic Material and Measurements Guidelines for Sonar Transducers MIL-STD-1376B(SH)", Department of Defense, United States of America, Washington DC, 1995.

[26] Sherrit S., Private communication on research into the possibility that the conduction current for a piezoceramic is dependant on stress, Science and Technology Development Section, Jet Propulsion Laboratory, Spring 2002.

[27] PZT-5A and PZT-5H Piezoceramics, Morgan Electro Ceramics, Southampton, England

[28] Mattuat, O. E., Berlincourt ,D., Kikuchi, Y. and Meitzler, A.H., "Ultrasonic Transducer Materials", Plenum Press, New York, New York, 1971, pages 102-109.

[29] Jaffe, B., Cook, W.R., and Jaffe, H., "Piezoelectric Ceramics", R.A.N. Publishers, Marietta, Ohio, 1971, Page 146.

[30] "Military Standard Piezoelectric Ceramic Material and Measurements Guidelines for Sonar Transducers MIL-STD-1376B, Notice 1, 13 July 1999", Department of Defense, United States of America, Washington DC, 1999.

[31] "QuickPack" Actuator, Active Control eXperts Inc., Cambridge, Massachusetts.

[32] http://www.acx.com/lab/quickpack.html, Active Control eXperts Inc., Cambridge, Massachusetts.

[33] "QuickPack QP10N and QuickPack QP45W" Actuator, Active Control eXperts Inc., Cambridge, Massachusetts.

[34] Bent, A.A., "Active Fiber Composites for Structural Actuation", Ph.D. Thesis, Massachusetts Institute of Technology, January 1997, page 24.

[35] Janos, B.Z. and Hagood, N.W., "Distributed Actuator Systems Based On Piezoceramics", Proceeding of the 7th International Conference on New Actuators, ACTUATOR 2000, June 2000.

[36] "PowerAct " strain actuator, Midé Technology Corporation, Medford Massachusetts.

[37] "QuickPack IDE Strain Actuator" model number QP10Ni, Active Control eXperts Inc., Cambridge, Massachusetts.

[38] "QuickPack IDE Strain Actuator" model number QP10Ni datasheet, November 29 2000 version, Active Control eXperts Inc., Cambridge, Massachusetts.

[39] Bent, A.A. and Hagood, N.W., "Anisotropic Actuation with Piezoelectric Fiber Composites", Journal of International Material Systems and Structures,3 [6] 338, 1995.

[40] Bent, A.A. and Hagood, N.W., "Improved Performance in Piezoelectric Fiber Composites Using Interdigitated Electrodes", Paper No. 2441-50, SPIE Proceedings of the 1995 North America Conference on Smart Structures and Materials, San Diego, California , 1995.

[41] Continuum Photonics, Inc. (formally Continuum Control Corporation, Inc.), Billerica, Massachusetts.

[42] PiezoFlex by Continuum Datasheet Rev 1.0 – AP 8/00, Continuum Photonics, Billerica, Massachusetts.

[43] Kapton Type 100 HN Film, DuPont High Performance Films, Circleville, Ohio.

[44] CeraNova Corporation, Franklin, Massachusetts.

[45] Janos, B.Z., "Design, Development, and Characterization of Magnetic Particle Active Fiber Composites", Ph.D. Thesis, Massachusetts Institute of Technology, June 2001, page 63.

[46] Hagood, N.W., Private communication on the manufacturing time for PiezoFlex AFCs, Active Materials and Structures Laboratory, Massachusetts Institute of Technology, December 2001.

[47] Janos, B.Z. and Hagood, N.W., "Overview of Active Fiber Composites Technologies", Proceeding of the 6th International Conference on New Actuators, ACTUATOR 98, 1998.

[48] Wilkie, W.K., et. al. "Low-Cost Piezocomposite Actuator for Structural Control Applications", SPIE's 7th Annual International Symposium on Smart Structures and Materials, Newport Beach, CA, 2000.

[49] Lynch, T., "Smart Ceramics Transform Structural Shapes", The Industrial Physicist, December 2001/January 2002, pages 10-11.

[50] Wilkie, K.W., Private communication on the material properties of LaRC-MFC Actuators, Structural Dynamics Branch, NASA Langley Research Center, February 2002.

[51] PZT 3195HD Piezoceramic, CTS Wireless Components Piezoelectric Products, Albuquerque, New Mexico.

[52] "PZT Piezoelectric Materials Technical Data (Typical Values)" 4/2000 Technical Bulletin, CTS Wireless Components Piezoelectric Products, Albuquerque, New Mexico, 2000.

[53] Janos, B.Z. and Hagood, N.W., "Magnetic Particle Doping for Anisotropic Matrix Materials in Active Fiber Composites", Smart Structures and Materials 1999, SPIE Paper 3675-02, 1999.

[54] Mueller, U.C., "Feasibility Study on Conductive Polymers as Matrix Materials in Active Fiber Composites (AFCs)", AMSL report number 01-04, Active Materials and Structures Laboratory, Massachusetts Institute of Technology, November 2000.

[55] Hernandez, V.L. Private communication on the feasibility of manufacturing a cpAFC, Active Materials and Structures Laboratory, Massachusetts Institute of Technology, May 2001.

[56] http://www.gepolymerland.com/research/glossary/techgloss.html#e, General Electric Plastics, Pittsfield, Massachusetts.

[57] Dowling, N.E., "Mechanical Behavior of Materials", Prentice-Hall Inc., Englewood Cliffs, New Jersey, 1993, page 100.

[58] Wickramasinghe, V.K., "Characterization of Active Fiber Composite Actuators for Helicopter Rotor Blade Applications", Master Thesis, Massachusetts Institute of Technology, March 2001.

[59] DuPont bulletin GS-96-7", DuPont High Performance Films, Circleville, Ohio.

[60] "DuPont (8/95) 231302B" Datasheet, DuPont High Performance Films, Circleville, Ohio.

[61] "AFC New Dimensioned.dwg" CAD Drawing, Continuum Photonics, Inc., Billerica, Massachusetts, available from the author upon request.

[62] Wickramasinghe, V.K, Private communication on the scatter in the data for PiezoFlex open circuit chord modulus, Active Materials and Structures Laboratory, Massachusetts Institute of Technology, 2001.

[63] Jones, R.M., "Mechanics of Composite Materials", Taylor & Francis, 1975, pages .90-97.

[64] EPON resin 9405/ EPI-CURE curing agent 9470 epoxy, Shell Chemicals, Houston, Texas.

[65] "SC:856-94" Datasheet, Shell Chemicals, Houston, Texas.

[66] "ASTM E-1356-98 Standard Test Method for Assignment of the Glass Transition Temperatures by Differential Scanning Calorimetry or Differential Thermal Analysis",

Annual Book ASTM Standards, Philadelphia, Pennsylvania, American Society for Testing and Materials, 2000.

[67] Pizzochero, A., Private communication on the matrix material properties of PiezoFlex AFCs, Continuum Photonics, Inc., Billerica, Massachusetts, 1999.

[68] Berlincourt, D., Krueger, H.H.A., and Near, C., "Technical Publication TP-226 Properties of Piezoelectricity Ceramics, Properties of Morgan Electro Ceramic Ceramics", MorganElectro Ceramics, http://www.morgan-electroceramics.com, page 4.

[69] Baerwald, H.G., "Eigen Coupling Factors and Principal Components, The Thermodynamic Invariants of Piezoelectricity", 1960 IRE International Convention Record, Part 6, New York, New York, pages 205 – 211.

[70] Berlincourt, D.A., and Brunarski, F., "Dependence of the Parameters of a Piezoelectric Ceramic on Polarization", Internal Clevite Corporation Engineering Memorandum No. 60-11, Clevite Corporations, Cleveland Ohio, November 18, 1960.

[71] Berlincourt, D.A., Curran, D.R., and Jaffe, H., "Piezoelectric and Piezomagnetic Materials and Their Function in Transducers", Physical Acoustics, Principals and Methods, Volume I-Part A, Academic Press, New York, 1964, pages 192-195.

[72] http://www.piezo.com/psi5a4.html, Piezo Systems Inc, Cambridge, Massachusetts.

[73] Morgan Electro Ceramics, Southampton, England.

[74] Name withheld, Private communication about the approximate poling procedure for Morgan Electro Ceramics PZT 5A, Morgan Electro Ceramics, June 2001.

[75] Zhang, Q.M., et. al, "Change of the Weak-Field Properties of Pz(ZrTi)O3 Piezoceramics With Compressive Uniaxial Stress and its Links to the Effect of Dopants on the Stability of the Polarizations in the Materials", J. Mater. Res. Vol 12 No. 1, Jan 1997.

[76] Berlincourt, D.A., "Variation of Electroelastic Constants of Polycrystalline Lead Titanate Zirconate with Thoroughness of Poling", The Journal of the Acoustical Society of America, Volume 36, Number 3, March 1964.

[77] "Technical Publication TP-224 Piezoelectric Coupling", Morgan Electro Ceramics, http://www.morgan-electroceramics.com, pages 1-2.

[78] Ikeda, T., "Fundamentals of Piezoelectricity", Oxford University Press, New York, 1996, pages 18-21.

[79] Berlincourt, D.A., Curran, D.R., and Jaffe, H., "Piezoelectric and Piezomagnetic Materials", Physical Acoustics Principals and Methods, Volume I-Part A, Academic Press, New York, 1964, page 192-195.

[80] Baerwald, H.G., "Eigen Coupling Factors and Principal Components, The Thermodynamic Invariants of Piezoelectricity", IRE International Convention Record Part 6, The Institute of Radio Engineers, 1960.

[81] Dunn, C.T., "A Partial Explanation of the Invariant Coupling Coefficient", unpublished, available from the author upon request.

[82] Sherrit, S., and Mukherjee, B.K, " The Use of Complex Material Constants to Model the Dynamic Response of Piezoelectric Materials", IEEE Ultrasonics Symposium, 1998, pages 633-640.

[83] Holland, R., "Representation of Dielectric, Elastic, and Piezoelectric Losses by Complex Coefficients", IEEE Transactions on Sonics and Ultrasonics, Vol SU-14, No. 1, January 1967, pages 18-20.

[84] "Military Standard Piezoelectric Ceramic Material and Measurements Guidelines for Sonar Transducers MIL-STD-1376B(SH)", page 31.

[85] BM500 material data, http://www.sensortech.ca/bm500.html, Sensor Technology Limited, Collingwood Ontario, Canada.

[86] EBL#2 material data, http://www.staveleyndt.com/prodset4.htm, Staveley NDT Technologies, Kennewick, Washington.

[87] 5A4E material data, http://www.piezo.com/psi5a4.html, Piezo Systems Inc, Cambridge, Massachusetts.

[88] ANSYS version 5.6.1, Ansys Inc., Canonsburg, Pennsylvania.

[89] Harper, J.E., "Analysis of Nonlinear Electroelastic Continua with Electrical Conduction", Master Thesis, Massachusetts Institute of Technology, May 1999, pages 97-101.

[90] Pizzochero, A., Private communication on the material properties of PiezoFlex AFCs, Continuum Photonics, Inc., Billerica, Massachusetts, April 2002.

[91] Ram, A, "Fundamentals of Polymer Engineering", Plenum Press, New York, New York, 1997, page 92.

[92] Trapa, P., Private communication on the history of tmAFC development, Active Materials and Structures Laboratory, Massachusetts Institute of Technology.

[93] Kynar 2801-00 Vinylidene Fluoride Resin, Elf Atochem North America Inc., Philadelphia, Pennsylvania.

[94] "Kynar & Kynar Flex PVDF Performance Characteristics & Data", datasheet #ADV 010108 7.5M C&Q 9/01, ATOFINA Chemicals, Inc., Philadelphia, Pennsylvania, 2001.

[95] 5-Minute Epoxy 5-208/20845, Devcon, Riviera Beach, Florida.

[96] Teflon Coated Glass Fabric Electrical Grade, TCGF-EHV (GNPT), American Durafilm Company, Inc., Holliston, Massachusetts.

[97] Hot Press, Model Number MTP 1301, Tetrahedron Associates, Inc., San Diego, California.

[98] Noryl EN265-701, General Electric Plastics, Pittsfield, Massachusetts.

[99] Westlake Plastics, Lenni, PA.

[100] http://www.geplastics.com/NASApp/dfss/matsel?pageId=Frame

[101] High-Temperature Silicone Rubber, McMaster-Carr Supply Company, New Brunswick, New Jersey.

[102] Ultem 1000, General Electric Plastics, Pittsfield, Massachusetts.

[103] "Ultem PEI Resin, Ultem ULT-3061 (10/97) CA Datasheet", General Electric Plastics, Pittsfield, Massachusetts.

[104] http://www.polymerprocessing.com/polymers/PEI.html, PolymerProcessing.com.

[105] "Ultem Profile release 09/1998 Ultem Eng/3M/0998" Datasheet, General Electric Plastics, Pittsfield, Massachusetts.

[106] "GE Engineering Thermoplastics Design Guide", General Electric Plastics, Pittsfield, Massachusetts.

[107] "GE Engineering Thermoplastics Processing Guide" GEDEX152 (1/00) Sage, General Electric Plastics, Pittsfield, Massachusetts.

[108] Duralco 122 Room Temperature curing, 500 °F Conductive Epoxy, Cotronics Corp., Brooklyn, New York.

[109] "High Temperature Adhesives and Material Instructional Handbook" volume 99-37 1999, Cotronics Corp., Brooklyn, New York, 1999.

[110] Dust-Off Plus Model DPNR, Falcon Safety Products, Inc., Branchburg, New Jersey.

[111] Pizzochero, A., Private communication on the compressive failure pressure of PZT-5A fibers, Continuum Photonics, Inc., Billerica, Massachusetts, 1999.

[112] Pizzochero, A., N.W., "Residual Actuation and Stiffness Properties of Piezoelectric Composites: Theory and Experiment", Master Thesis, Massachusetts Institute of Technology, February 1998, page 128.

[113] RTV Silicone Sealant, General Electric Company, Fairfield, CT

[114] Robertson, D., Private communication on the cost to fix the vacuum leaks in the hot press, Active Materials and Structures Laboratory, Massachusetts Institute of Technology.

[115] Silquest A-1120 Silane, Witco Corporation, Greenwich, CT.

[116] Instron 5542 universal electromechanical testing machine load frame, Instron Corporation, Canton, Massachusetts.

[117] "ASTM D-882-97: Standard Test Method for Tensile Properties of Thin Plastic Sheeting", Annual Book ASTM Standards, Philadelphia, Pennsylvania, American Society for Testing and Materials, 2000.

[118] Pyris 1, Perkin Elmer, Wellesley, Massachusetts.

[119] "ASTM D-3418-99: Standard Test Method for Transition Temperatures of Polymers by Differential Scanning Calorimetry", Annual Book ASTM Standards, Philadelphia, Pennsylvania, American Society for Testing and Materials, 2000.

[120] Seiko model TG/DTA-320 thermogravimetric and differential thermal analyzer, Perkin-Elemer Instruments, Shelton, Connecticut.

[121] "GE Engineering Thermoplastics PROCESSING GUIDE Injection Molding Ultem PEI Resin" ULT-210D (2/98) CA Datasheet, General Electric Plastics, Pittsfield, Massachusetts, pages 11-7 to 11-8.

[122] Aluminum pan Seiko part number SSC000E030 Open Pan Ø5, Perkin-Elemer Instruments, Shelton, Connecticut.

[123] Platinum pan Seiko part number 50-024 PT Ø5-Pan, Perkin-Elemer Instruments, Shelton, Connecticut.

[124] "ASTM E-1641-99: Standard Test Method for Decomposition Kinetics by Thermogravimetry", Annual Book ASTM Standards, Philadelphia, Pennsylvania, American Society for Testing and Materials, 2000.

[125] McClure, T., Private communication on the problem with early shutdown of the temperature cycle of the Seiko TG/DTA-320, Center for Materials Science and Engineering, Massachusetts Institute of Technology, May 2001.

[126] Strauss, E.L, "Polymer Degradations Processes in Ablation", Aspects of Degradation and Stabilization of Polymers, Elsevier Scientific Publishing, New York, New York, 1978.

[127] Crews, L.K., "High Temperature Degradation of Graphite/Epoxy Composites", PhD Thesis, Massachusetts Institute of Technology, August 1998, pages 82-91.

[128] HP 4194A Impedance / Gain Phase Analyzer, Hewlett Packard, Palo Alto, California.

[129] 16047C Test Fixture, Hewlett Packard, Palo Alto, California.

[130] "ASTM D-150-98 Standard Test Methods for AC Loss Characteristics and Permittivity (Dielectric Constant) of Solid Electrical Insulation", Annual Book ASTM Standards, Philadelphia, Pennsylvania, American Society for Testing and Materials, 2000.

[131] ZMI 1000, Zygo Corporation, Middlefield, Connecticut.

[132] 0.1 mHz – 100 MHz PM 5138 Function Generator, Phillips, Germany.

[133] Model 664 10kV 20 mA amplifier, Trek Inc., Medina, New York.

[134] LabVIEW version 5.1, National Instruments Corporation, Austin, Texas.

[135] Hexcel E120-155 prepreg cloth, Pleasanton, California.

[136] Wickramasinghe, V.K., "VppSweepData.xls", Microsoft Excel Workbook, Massachusetts Institute of Technology, available from the author upon request.

[137] Wickramasinghe, V.K, Private communication on calculation of the Young's modulus of e-glass, Active Materials and Structures Laboratory, Massachusetts Institute of Technology, 2001.

[138] Draft 1 of "IEEE Standard on Loss in Acoustic Materials", pages 19-37.

[139] Alemany, C., Pardo, L., Jiménez, B., Carmona, F., and Mendiola, J., "Automatic Iterative Evaluation of Complex Material Constants in Piezoelectric Ceramics", Journal of Physics D, Applied Physics 27 (1994), pages 148-155.

[140] Alemany, C., González, A.M., Pardo, L., Jiménez, B., Carmona, F., and Mendiola, J., "Automatic Determination of Complex Constants of Piezoelectric Lossy Materials in the Radial Mode", Journal of Physics D, Applied Physics 28 (1995), pages 945-956.

[141] González, A.M, and Alemany, C., "Determination of the Frequency Dependence of Characteristic Constants in Lossy Piezoelectric Materials", Journal of Physics D, Applied Physics 29 (1996), pages 2476-2482.

[142] Zygo model 7702 leaser head 3 mm, Zygo Corporation, Middlefield Connecticut.

[143] ZMI-1000 chassis, Zygo Corporation, Middlefield Connecticut.

[144] PEEK polymer, Victrex USA Inc., Greenville, South Carolina.

[145] "High Performance Films" datasheet, Westlake Plastics Company, Lenni, Pennsylvania.

[146] Airtech 1050 rubber, Airtech Advanced Materials Group, Huntington Beach, California.

[147] Airtech 1050 Datasheet 2-28-97, Airtech Advanced Materials Group, Huntington Beach, California.

[148] Single Crystal Piezoelectric Fiber Materials, Development, Devices, and Demonstration, Government Program Managers Wu, S, and Smith, W.AFOSR-DARPAGrant Number F49620-99-2-0332,

[149] Nano-DVRT, MicroStrain, Inc, Burlington, Vermont.

[150] Precision Workstation, Radiant Technologies Inc., Albuquerque, NM.

[151] Trek 609A Amplifier, Trek, Inc, Medina, New York.

[152] "Precision Workstation" hardware specifications, http://www.ferrodevices.com/ppwork.html.

[153] Instron 8501 series tensile testing machine, Instron Corporation, Canton, Massachusetts.

[154] Dugundji, J., Private communication on the coupling of shear strains in a composite with locally varying material properties, Technology Laboratory, for Advanced Composites, Massachusetts Institute of Technology, February 2002.

[155] Sherrit, S., Private communication on the existence of complex conductivity, Science and Technology Development Section, Jet Propulsion Laboratory, November 2001.

[156] Zahn, M., Private communication on the existence of complex conductivity, Laboratory for Electromagnetic and Electronic Systems, Massachusetts Institute of Technology, November 2001.

[157] "Reliable Impedance and Transmission Measurements with an Intelligent Analyzer" Technical Data Sheet for the HP 4194A Impedance/ Gain-Phase Analyzer, Hewlett Packard, Palo Alto, California, June 1985, pages 14 to 15.

[158] Honda, M., "The Impedance Measurement Handbook A Guide to Measurement Technology and Techniques", 1/90 5950-300 Edition, Yokogawa-Hewlett-Packard, 1990.

[159] 1260 Impedance/Gain-Phase Analyzer, Schlumberger Technologies Instruments Division, Hampshire, England.

[160] "1260 Impedance/Gain-Phase Analyzer" SI/MDV006/Issue 04/FD8990F Datasheet, Schlumberger Technologies Instruments Division, Hampshire, England, 1993.

[161] Dugundji, J., Private communication on the methodology for determining the error in G and B, Technology Laboratory for Advanced Composites, Massachusetts Institute of Technology, June 2001.

[162] Kittel, Charles, "Introduction to Solid State Physics Second Edition", John Wiley & Sons Inc., New York, New York, 1953, pages 164 - 172.

[163] Zahn, M., "Electromagnetic Field Theory: a problem solving approach", Krieger Publishing Company, Malabar, Florida, 1979, pages 184-189.

[164] Hayt Jr., W.H. and Kemmerly, J.E., "Engineering Circuit Analysis Fourth Edition", McGraw-Hill Book Company, New York, New York, 1986, pages 617 - 627.